Department of Spatial Sciences

Semi-automated Geomorphological Mapping Applied to Landslide Hazard Analysis

Andrew Hansen

This thesis is presented for the Degree of
Doctor of Philosophy
of
Curtin University of Technology

July 2007

Declaration

To the best of my knowledge and belief this thesis contains no material previously published by any other person except where due acknowledgment has been made.

This thesis contains no material which has been accepted for the award of any other degree or diploma in any university.

Signature: …….

Date: ……...

ABSTRACT

Computer-assisted three-dimensional (3D) mapping using stereo and multi-image ("softcopy") photogrammetry is shown to enhance the visual interpretation of geomorphology in steep terrain with the direct benefit of greater locational accuracy than traditional manual mapping. This would benefit multi-parameter correlations between terrain attributes and landslide distribution in both direct and indirect forms of landslide hazard assessment. Case studies involve synthetic models of a landslide, and field studies of a rock slope and steep undeveloped hillsides with both recently-formed and partly degraded, old landslide scars. Diagnostic 3D morphology was generated semi-automatically both using a terrain-following cursor under stereo-viewing and from high resolution digital elevation models created using area-based image correlation, further processed with curvature algorithms.

Laboratory-based studies quantify limitations of area-based image correlation for measurement of 3D points on planar surfaces with varying camera orientations. The accuracy of point measurement is shown to be non-linear with limiting conditions created by both narrow and wide camera angles and moderate obliquity of the target plane. Analysis of the results with the planar surface highlighted problems with the controlling parameters of the area-based image correlation process when used for generating DEMs from images obtained with a low-cost digital camera. Although the specific cause of the phase-wrapped image artefacts identified was not found, the procedure would form a suitable method for testing image correlation software, as these artefacts may not be obvious in DEMs of non-planar surfaces.

Modelling of synthetic landslides shows that Fast Fourier Transforms are an efficient method for removing noise, as produced by errors in measurement of individual DEM points, enabling diagnostic morphological terrain elements to be extracted. Component landforms within landslides are complex entities and conversion of the automatically-defined morphology into geomorphology was only achieved with manual interpretation; however, this interpretation was facilitated by softcopy-driven stereo viewing of the morphological entities across the hillsides.

In the final case study of a large landslide within a man-made slope, landslide displacements were measured using a photogrammetric model consisting of 79 images captured with a helicopter-borne, hand-held, small format digital camera. Displacement vectors and a thematic geomorphological map were superimposed over an animated, 3D photo-textured model to aid non-stereo visualisation and communication of results.

ACKNOWLEDGEMENTS

I would like to acknowledge the assistance provided by many organisations and people who have directly and indirectly facilitated completion of this dissertation. Drs. Derek Lichti and Stuart Gordon, and Mr Gregg Winter assisted in fieldwork at the Mountain Quarry in Boya, Western Australia; Mr Alvin W-c Cheung, Ms Angie Chan and Dr Mark Ruse assisted in the topographic survey of the One Rise More landslide in Hong Kong. Mr Jonathan Thompson assisted in the survey of the Cloudy Hill landslide in Hong Kong. Mr Y.C. Chan and Mr H.N. Wong of the Geotechnical Engineering Office, Government of Hong Kong SAR, facilitated the research by supporting the provision of high resolution aerial photographic and digital topographic survey data supplied by the Lands Department, Government of Hong Kong SAR. My twin brother, Laurence, has supplied much needed support and encouragement for many aspects of my research and with my career.

Three men have significantly influenced my studies and career in the field of applied geomorphology; Dr John C. Doornkamp at the University of Nottingham, Professor Denys Brunsden at the University of London King's College and Dr Earl E. Brabb of the U.S. Geological Survey in Menlo Park, California. Their influence cannot be underestimated and I am grateful for their support.

The research has been partly funded by a Curtin University Postgraduate Scholarship. Supervision of the research work in this dissertation was carried out on behalf of the University during the first year by Dr Robert Hickey, and subsequently by Drs. Derek D. Lichti and Robert J. Corner. Thanks are due to all three of them for their efforts and their patience.

Lastly, thanks are due to my wife Nina, and son David, for enduring the long gestation period for this research. I would also like to record the enormous debt of gratitude that I owe to my parents, Hazel and Vic Hansen, and to my parents-in-law Ruth and Peter Reed, who supported my academic endeavours and career over the years.

Andrew Hansen
Perth
July 2007

TABLE OF CONTENTS

Chapter **Page**

Chapter **Page**

Chapter **Page**

Chapter **Page**

Chapter **Page**

Chapter **Page**

LIST OF FIGURES

Figure **Page**

Figure **Page**

Figure **Page**

LIST OF TABLES

Table **Page**

Chapter 1

INTRODUCTION

1.1 Landslides and the Application of Photogrammetry to Geomorphology

Landslides are widely recognised as causing significant disruption to human and socio-economic activities in both developed and developing countries (e.g., Brabb and Harrod, 1989). Techniques developed to assess the hazard arising from slope instability range from engineering studies concentrating on the properties and mechanics of the materials (c.f., shear strength: Skempton, 1964; pore pressures: Skempton 1954; stability analyses: Janbu, 1954; Bishop, 1955) to national inventories of landslide-prone terrain (e.g., Radbruch-Hall et al., 1979). Comprehensive reviews of landslide hazard assessment techniques have been provided by Hansen (1984a), Varnes (1984) and Soeters and van Westen (1996). Soeters and van Westen (1996, p. 129) note that:

> *'Considering the many terrain factors involved in slope instability, the practice of landslide hazard zonation requires:*
>
> - *a detailed inventory of slope instability processes, the study of these processes in relation to their environmental setting,*
> - *the analysis of conditional and triggering factors, and*
> - *a representation of the spatial distribution of these factors.'*

A feature common to all these procedures is the correct co-location of the factors within the coordinate system of the analytical procedure using the different attributes. Coordinate systems used for these analyses are summarised in Table 1.1. With two-dimensional (2D) coordinates for attribute storage, morphometric attributes such as slope gradient or aspect must be determined separately and stored as discrete attribute values within the units of the storage system. This would be an array for a raster database or a polygon with single values.

Terrain shape, as described by slope gradient and aspect, has been used in multi-parametric methods of landslide susceptibility assessment since the 1970s (e.g., Brabb et al., 1972). More recently, complex shape attributes using various forms of terrain curvature have been proposed and tested (e.g., Gao, 1992).

Table 1.1 Coordinate systems available for slope stability analysis

Number of Dimensions (D) of Measured Points	Application	Content
2D: horizontal and vertical	Geotechnical methods of slope stability analysis	Measured or inferred surfaces denoting changes in physical properties including terrain, subsurface material boundaries, transient and permanent hydrological boundaries
2D (or **2.5D**): Eastings, Northings and labelled height (contour strings)	Cartography / GIS	2D polygon and vector overlays of terrain and environmental attributes and direct or indirect measures of landslide distribution; elevation is limited to labelled contours
3D: X, Y with fully attributed Z; may be independent of map coordinate system	Photogrammetry / GIS	Measured points, lines and polygons representing attributes have independent values in a coherent 3D model allowing multi-directional visualisation

Geomorphological interpretations are based on an assessment of landforming processes that are ongoing, or have been active in the past; this interpretation often relies heavily on the recognition of past processes from diagnostic landform features. Consequently, accurate interpretation and description of geomorphology depends heavily on observation that commonly takes place during fieldwork and stereoscopic observation of aerial photographs (Demek, 1972; Demek and Embleton, 1978). When direct observation and mapping is replaced by digital representations of the terrain, the ability to interpret landforms, either quantitatively or qualitatively, depends on the quality of the topographic data used to derive the morphology.

Landslide hazard assessment can be performed using direct and indirect methods (Hansen, 1984a). Direct methods use maps of landslides and related terrain conditions to subjectively determine susceptibility to landsliding; indirect methods use deterministic or statistical models based on correlations between environmental and geological factors, and are suited to automated analysis in geographic information systems (GIS). Both analytical and subjective methods of landslide hazard assessment require as source data information on the distribution and typology of landforms resulting from slope instability (e.g., failure scars and debris trails) and the distribution and characterisation of various landforms that may reflect

surface and subsurface materials and properties that control slope stability (e.g., hydrology; weathering; erosion, transportation and deposition of slope-forming materials). Questions have been raised about the validity of some hazard zoning studies based on process models applied through a GIS; in this context, Parry et al. (2005) support expanding the application of subjective assessment based on engineering judgement. The increased application of 3D measurement technologies to remotely-sensed imagery will enhance the precision of landslide and terrain inventories on which both direct and indirect hazard studies are based.

With development and increasing availability of low-cost digital photogrammetric technologies, "softcopy" processing of digital stereo- and multi-image photogrammetric models is now more available to practitioners in pure and applied geomorphological research (e.g., Lane et al., 1998), and these techniques are being taken into professional practice. These technologies will be applied using readily available data sources such as consumer-grade digital cameras and paper prints converted to digital format using low-cost desktop scanners (e.g., Fraser, 1998; Chandler, 2001). The spatial fidelity of data obtained from such sources is less rigorous than for conventional topographic survey applications that use high quality, large- and medium-format metric cameras and photogrammetric-quality scanners.

1.2 Photogrammetry and Geomorphological Mapping

This dissertation identifies, assesses and adapts appropriate techniques and data processing methods to expand the use of digital photogrammetry and digital terrain model (DTM; set of 3D point data, usually as a triangulated irregular network, TIN) / digital elevation model (DEM; 3D point data in a regularly-spaced grid) processing for geomorphological mapping in hilly and mountainous terrain. Where previous photogrammetrically-oriented geomorphological studies have concentrated on collecting DTMs or particle size information such as river bedloads and soil surfaces (e.g., Chandler, 1999, 2001; Carbonneau et al., 2003), the emphasis within this dissertation is on the integration of digital photogrammetry with the identification and spatial representation of landforms specifically relevant to slope stability.

Geomorphological mapping is a two-stage process of landform analysis and representation. The initial stage involves (i) the observation, analysis and

interpretation of landforms into their component elements according to a defined classification, and (ii) the cartographic representation of those elements. The latter requires designation of symbology that represents various aspects of the origin and materials of objects that form topographic elements of landforms. Cartographic representation of this symbology is traditionally 2D on maps and plans (Table 1.1), although schemes have been devised to allow depth and multiple layers to be depicted. The function of photogrammetry is to obtain an estimate of the three-dimensional (3D) coordinates of a target point by geometric comparison with known control points through measurement of the location of the object on one or more images. Additional functions that may be included within proprietary photogrammetric software packages use various forms of image correlation and or image geometry to locate or automatically measure point coordinates on the surface of the objects within the image. The direct use of photogrammetry for geomorphological mapping provides the opportunity to create and manipulate 3D geomorphological maps with enhanced visualisation capabilities.

This dissertation describes studies carried out to evaluate the ways in which aerial and terrestrial photogrammetry can be applied to the semi-automated generation of morphological and geomorphological digital data layers that can be viewed as 3D visual models or reproduced as 2D cartographic products (i.e., conventional geomorphological maps). Integration is achieved both directly, through stereo-assisted morphological and geomorphological mapping, and as a two-stage process including DEM/DTM generation and subsequent derivation of terrain attributes. The work extends existing studies where the prime focus has been the use of photogrammetry for measurement or the production of DEMs (e.g., Lane et al., 1998), combining this with other studies where DEMs have been processed to derive topographic attributes including slope gradient, aspect and curvature (e.g., Wood, 1996).

1.3 Research Objectives

1.3.1 Aims of the Research

The major focus of this dissertation is to identify the extent to which geomorphological mapping can be automated through adapting and applying digital

photogrammetric techniques. This research used photogrammetric data collection and DEM processing methods to capture a range of morphometric, geologic and geomorphic information with an emphasis on terrain attributes relevant to the assessment of slope stability and landslide hazard. Throughout the investigation, the emphasis was on the characterisation of the terrain through landform measurement and identification, allowing the synthesis of digital photogrammetry and terrain mapping technologies. The results included raw landform morphometry and geomorphological maps collected using softcopy photogrammetry as stereo pairs and multi-image models derived from large and small format aerial photography and terrestrial photography using consumer grade cameras.

The research had four objectives:

(a) Evaluate the sources of digital terrain images that can be used in digital photogrammetric processing to generate DEMs appropriate for geomorphological investigations of sloping terrain;
(b) Develop DEM processing options that identify landforms relevant to slope stability;
(c) Evaluate and develop the main digital photogrammetric technologies in relation to their usefulness for reducing the significant amount of operator variability that occurs in the interpretation of landforms and the production of geomorphological maps;
(d) Develop computer aided drafting (CAD) technologies in conjunction with digital photogrammetry for the depiction of landforms relevant to slope stability.

This study has focused on the integration of photogrammetric and geomorphological mapping technologies. The initial hypothesis to be tested is:

That morphological and geomorphological maps relevant to slope stability can be efficiently generated using digital photogrammetry, DEM and CAD processes to a ground precision appropriate to the use of the data.

1.3.2 Components of the Research

This investigation has the following major components:

(a) Review the rationale for geomorphological mapping to identify areas where photogrammetric processing and products can and cannot be applied;
(b) Review the data collection and processing streams available within photogrammetry to identify appropriate ways to integrate the processes into geomorphological mapping;
(c) Conduct case study investigations using both stereo and multi-image digital photogrammetric technologies on image data collected as medium and high quality scanning of paper prints and film negatives, and low and medium-cost digital cameras;
(d) Assess the suitability and limitations of photogrammetric technology for landform measurement when using source data of varying spatial fidelity;
(e) Consider processing techniques to extract morphological information from photogrammetric results and enhance it by the addition of geomorphological interpretation.

1.3.3 Significance and Benefits of the Research

Geomorphological mapping techniques have been applied to many fields of terrain and natural hazard assessment as a supplement to topographic data sources (Griffiths and Edwards, 2001). Digital photogrammetry has been identified as a method of improving the range and accuracy of geomorphological data collection (Chandler, 1989, 2001; Lane, 1994; Lane et al., 1998). Lane et al. (2000) note that geomorphological measurement can be quantified by using automated 3D point extraction methods on raw images which allow measures of elevation error to be generated in conjunction with the DEM. This reduces the reliance on digital data obtained from published sources such as printed maps or external mapping organisations; the quality of such data may be unknown, and it may be used for purposes beyond those originally intended (Fryer et al., 1994; McCullagh, 1998; Wise, 1998). Lane et al. (2000) conclude that automated point extraction methods can generate DEMs with precisions generally adequate for geomorphological research (see Chapter 3) in areas of smooth terrain, but caution that further research is needed in areas of complex and rough topography and for different spatial scales. This dissertation describes the results of studies to generate and process high resolution DEMs with grid spacings ranging from 25m to under 0.2m in steep,

undulating terrain with large areas of slope with gradients greater than 25°, as is often the case for landslide-prone hillsides, to test semi-automated landform identification methodologies as a component of geomorphological mapping.

The case studies found that, while the use of photogrammetric technologies can significantly improve the capture of morphological data, the integration of geomorphological interpretation was only partly successful. This was mainly because geomorphological interpretation of complex landforms is highly subjective. However, the integration of morphological and geomorphological symbology into computer-driven photogrammetric (softcopy) systems significantly aids the mapping process due to the ability of the operator to dynamically visualise, place and edit the interpretation draped over the 3D landforms.

Towards the end of the research, and after the field case studies had been completed, anomalous behaviour was identified in one of the softcopy photogrammetry systems used to compile the morphological and geomorphological maps. Further testing using a smooth, highly textured granite slab revealed that the softcopy system will generate sub-optimal results unless the operating parameters are carefully selected; some parameter choices required for images captured with low cost camera systems, may fall outside ranges considered normal for those captured with large format aerial camera systems. This testing has established that use of a smooth, highly textured target can prove valuable for identifying systematic errors in both camera and lens systems and the photogrammetric algorithms, as well as defining operational limitations on the use of photogrammetric systems for the measurement of sloping planes. The planar target tests were performed only on imagery obtained with small format digital cameras that are known to contain greater amounts of lens distortion than high precision, large format aerial cameras; while unresolved lens distortion may be one of the factors leading to this anomalous behaviour, this has not been conclusively proven.

1.3.4 Audience

This dissertation has been written from the perspective of an Earth scientist applying softcopy photogrammetric and other techniques more commonly used for topographic surveying. The intended audience for this research is the wider Earth

science community which should consider the benefits and constraints of using softcopy photogrammetric technologies for improving the productivity and scope of landform analysis. With this in mind, the dissertation contains some discussion of the constraints and opportunities that may apply when using photogrammetric methods for both field- and laboratory-scale landform mapping and measurement. As a multi-disciplinary study, a glossary of technical terms has been added as Appendix A to aid use by readers not familiar with photogrammetry or geomorphology. Some reference to photogrammetric processing theory is made to aid consideration of the technology's application to geomorphology and landform measurement.

1.3.5 Contributions of the Dissertation

The research carried out for this dissertation has extended understanding of the ways in which a mature technology within the field of geomatics can be applied to Earth science. The specific developments resulting from this investigation are:

(a) Removal of high frequency noise from digital images using Fast Fourier Transforms (FFTs) improves correlations achieved when using area-based image matching; this is particularly useful when using images captured using low cost desktop scanners;

(b) High resolution DEMs generated directly from imagery within a softcopy system can better represent terrain morphology than DEMs generated from comparably-scaled contour data, especially when the DEMs are smoothed to remove random noise generated by the measurement system. Smoothing can be achieved by applying FFTs or other low pass filters;

(c) Curvature algorithms applied to the smoothed DEMs can be used to identify prominent morphological features in the terrain, particularly both recently-formed and degraded landslide scars;

(d) Co-observation of these 3D morphological features superimposed over stereo terrain imagery and viewed by experienced observers, assists in the interpretation of landslide boundaries and other geomorphological features;

(e) Large variations in measurement accuracy have been quantified for points on planar surfaces with regard to changes in stereo-camera axis separation and the orientation of the target plane relative to the camera axes;

(f) Multi-image photogrammetric models can be created to measure and visualise landslide scars and similar landforms using low cost software and cameras; combining long and short range terrestrial imagery allows georeferenced, high resolution ground models to be created to aid laboratory-based feature interpretation and mapping;

(g) 3D photo-textured point clouds can be viewed with softcopy systems or animated to allow visual appreciation of 3D morphological, geomorphological and thematic products.

This dissertation has been structured to provide a set of instructive notes and explanatory case studies that demonstrate the techniques and adaptations needed for Earth scientists to use softcopy photogrammetric systems for the compilation of geomorphological and related thematic maps in steep terrain. Some of the developments also apply to the use of softcopy photogrammetry to geomorphological model studies.

1.4 Thesis Structure

The thesis is divided into ten chapters. The initial focus in Chapters 2 to 5 is on the two component methodologies, geomorphological mapping and photogrammetry, together with strategies for extracting morphological and geomorphological features. The second section of the thesis in Chapters 6 through 9 contains case studies where photogrammetric and geomorphological technologies are integrated and compared to existing methodologies.

Chapter 2 contains a review of geomorphological mapping and landslide hazard assessment, highlighting those components where the application of digital photogrammetry is most likely to be beneficial. Using examples from the case studies, Chapter 3 discusses the components of digital image capture and photogrammetric processing that need to be understood for effective use of the technology in hillslope geomorphology. Chapter 4 examines the calibration of the automated point measurement algorithm implemented within a proprietary softcopy photogrammetric system used for several of the case studies, and investigates a measurement artefact that appears to have degraded the accuracy of results in some of the case studies. The integration of these technologies is considered in Chapter 5.

To test data extraction methods, a landslide scar was simulated in a gridded DEM by an ellipsoid intersecting multiple sloping planes representing the ground surface and two rock slopes within the landslide scar. The DEM was degraded by the addition of random noise, and used to test automated morphometric mapping strategies incorporating various low band pass and edge detection filters. Noise removal using Fast Fourier Transforms (FFTs) with edge detection using curvature algorithms proved most effective at delineating the component landform elements within the simulated landslide scar.

Chapters 6 and 7 describe the procedures and results obtained when high resolution mapping was carried out over small field sites of $<1km^2$. A study using close-range, stereo and multi-image photogrammetry on a near-vertical rock face in a disused quarry to the east of Perth, Australia is described in Chapter 6; Chapter 7 presents an investigation where stereo photogrammetry was used to map several partly revegetated debris flow scars at One Rise More in Hong Kong. Chapter 8 considers the use of multi-image photogrammetric modelling of a 40-year old debris flow scar at One Rise More and a recently-formed debris flow scar at Cloudy Hill, also in Hong Kong.

Chapter 9 describes the investigations at a large man-made slope which is severely disrupted by a slow-moving landslide at Chainage 23+800, Simpang Pulai to Lojing Highway, Malaysia. A detailed 3D geomorphological map was compiled from 79 photographs obtained from a helicopter with a small format, hand-held digital camera. Results include determining the movement dynamics of the landslide, and visualisation with a 3D photo-textured point cloud with a ground resolution of 10cm.

Chapter 10 summarises the results of the case studies in the context of the aims of the research with recommendations for future development. The dissertation closes with the cited references. A glossary of technical terms is given in Appendix A, while Appendix B contains a 3D animation of the landslide displacement mapping and partial geomorphological map of the landslide at Chainage 23+800, Simpang Pulai – Lojing Highway in Malaysia.

Chapter 2

GEOMORPHOLOGICAL MAPPING AND LANDSLIDE HAZARD ASSESSMENT

2.1 The Role of Mapping in Geomorphology

Osterkamp and Hupp (1996) argue that geomorphology is an example of a composite science (Kuhn, 1970), which can be defined as (Osterkamp and Hupp, 1996, p. 417) *'a discipline with specific and generally agreed-upon goals requiring various scientific and technological approaches of investigation to meet those objectives. A goal of geomorphology, for example, is a genetic interpretation of landforms, and techniques of physics, chemistry, biology and engineering are employed to develop interpretations'*. Osterkamp and Hupp (1996) further argue that composite sciences are able to readily include methodologies and structures from other complex and basic sciences, have diverse inputs and are typically more applied than the basic sciences. Within this framework, the adoption into geomorphology of metrological technologies is a logical development to solve specific methodological needs.

The study of geomorphology seeks to understand the spatial distribution of landforms and landforming processes. This requires measurement of topographic form, constituent materials, causative processes, and consideration of the compounding effects of time on all three. All four components form continuous entities with varying degrees of correlation; records of all four are subject to measurement, sampling and interpretation error, resulting in uncertainty. While the ground surface is more or less continuously visible, depending on the viewing system and intervening objects, measurement will occur at discrete locations. Locating subsurface objects is more difficult but can be achieved by extrapolation from surface measurements, or by employing some procedure that renders the ground less opaque (e.g., ground penetrating radar). Measuring and cataloguing a material's chemical and physical properties are more difficult; samples have to be collected, tested and the results interpolated between sampling sites. Geomorphological processes operate at micro to macro scales; they can range from slow and continuous to rapid and episodic; and they can have acted at different rates over time (Schumm and Lichty, 1965; Thornes and Brunsden, 1977).

2.1.1 Manual Geomorphological Mapping

While natural (and man-made) landscapes are complex associations of form, materials and landforming processes, the science of geomorphology has developed techniques to identify, simplify and portray the inherent complexity of the spatial and temporal associations of geomorphological entities. The oldest, most ubiquitous and arguably still most valuable geomorphological technique is simply to observe the landscape and record what is seen. But to record observations succinctly requires interpretation and classification, and the ability to interpret landscapes depends on experience (based on prior similar observations) and analysis of the observed or otherwise measured components (Crofts, 1981).

Most investigations concerned with collecting information about the spatial distribution of geomorphological features within an area commence with an initial postulate about the types of landform likely to be present; this will take the form of a conceptual model of the types and sequence of landforms, their constituent materials and the geomorphological processes that may have occurred in the past or are continuing to modify the landforms and materials. This is necessary, as with any investigation, to ensure that adequate information is gathered during the data collection exercise to allow description, analysis, categorisation and discrimination of the results. In the case of landform, material or process phenomena, the database will need to have spatial information stored together with the attribute description or value; this can be collected as lists (e.g., checklists), hardcopy maps or digital records. As the data collection exercise progresses, the scope of the data being collected should be reviewed and, if necessary, amended in view of the ongoing findings. In the case of geomorphological mapping, it may be necessary to add or amend items in the legend, or an interpretation should be changed if detailed observation or measurement indicates that the initial assumptions are incorrect or inadequate. Once data collection is complete, initial generalisations must be reviewed to ensure that assumptions about landform sequence, materials and causative processes are substantiated by the observations.

During mapping, observations are usually recorded onto a basemap (if this exists) or annotated onto an aerial photograph or orthophoto. An important technique used in geomorphology is aerial photograph interpretation (API; photogeology), in which

landforms are interpreted remotely by observation, normally using stereo pairs of vertical aerial photographs (e.g., Ray, 1960; Beaumont, 1979; Lillesand and Kiefer, 1979; Verstappen and van Zuidam, 1968; Verstappen, 1983). Unless some form of optical transfer device is being used (e.g., transferscope), manual transfer of stereo-observations onto an existing basemap requires some visual clue as to the correct location of the feature to be plotted. In areas away from prominent landmarks or vegetation boundaries that might be included on topographic or special purpose maps, contours are usually the only source of information shown on the base map for indirect orientation. The usefulness of contours depends on their vertical separation relative to the local terrain; while a particular contour interval may be adequate in hilly terrain, the same interval is likely to result in contours too widely spaced for effective use in low gradient terrain such as floodplains (see Chapter 2.7.2). When mapping geomorphology in areas without an existing topographic map, the first stage of the investigation, should funding allow, is to prepare one of the area to use as a basemap. In recent years, the availability of orthophotos (e.g., Chapter 2.7.3) and global positioning system (GPS) tracking have improved the ability to identify the location of specific observations.

2.1.2 GIS: Terrain and Vector Visualisation

The shape of an object can be defined by sets of points, lines, polygons and surfaces. Representation of these objects in terrain-related databases can take two forms: regular grids of points (rasters) and irregularly-spaced 2D or 3D points forming vectors (Burrough and McDonnell, 1998). Computer-aided drafting (CAD) systems normally use vector storage, as this is most analogous with the traditional points and lines visible on hand-drawn or printed maps. Rasters are best suited to images and other continuous variables. Software development in proprietary systems in the fields of CAD (e.g., MicroStation (Bentley, 2005); AutoCAD (AutoDesk, 2005)), GIS (e.g., Arc/Info (ESRI, 2005); ER Mapper (ER Mapper, 2005)) and remote sensing allow overlapping display (but not analysis) of both vectors and rasters without the necessity to convert files between the two data types.

The production of orthophotos requires the perspective and optical distortions present in an image to be removed (i.e. rectified) so that the features on the image conform to a defined geographic coordinate space. Conversely, a rectified image can

be draped over a 3D model to allow visualisation of the image features in relation to their topographic setting. These 3D visualisations can be generated within GIS systems such as Arc/Info and ER Mapper., and for the past few years, stereo viewing is being incorporated (e.g., Leica Geosystems's StereoAnalyst for ArcGIS (Leica, 2007)). Softcopy photogrammetric systems allow 3D visualisation of the terrain either as stereo pairs, (e.g., Socet Set (LH Systems, 2007); Z/I Imaging (ZI, 2007); uSMART (SmartTech, 2007)) or as multi-image collections (e.g., PhotoModeler (EOS, 2003)), with points and vectors draped across the images. Applying perspective distortion to 3D points and vectors during superimposition over both images under stereo viewing allows them to be viewed within the stereo model. This presents the opportunity for integrating terrain visualisation and geomorphological interpretation technologies.

Before considering methods of data representation, techniques for identifying and recording the shape and geomorphological characteristics of the terrain will be reviewed. These are divided into morphological and geomorphological mapping.

2.2 Morphological and Geomorphological Mapping

2.2.1 Morphological Mapping

As an alternative to depicting the shape of the terrain by contours, morphological mapping is a specific technique that identifies breaklines between areas of ground with similar properties (Figure 2.1). The technique was developed by Waters (1958) and extended by Savigear (1965). Elements of morphology are included in the engineering geology mapping legend of the Geological Society Engineering Group Working Party (Anon, 1972, 1982), although purely morphological symbols (e.g., convex break in slope) are not easily distinguished from those with implicit genetic connotations (e.g., convex break in slope forming the upper and side boundaries of a landslide scar).

The rate of change of gradient at breaklines is reflected by using a continuous line for sharp breaks in slope, with a dashed line used for gently curving changes (Figure 2.1). A 'V' symbol is placed along breaks or changes in slope with the open end uphill. A diamond or a cross superimposed on a breakline represents a ridge or

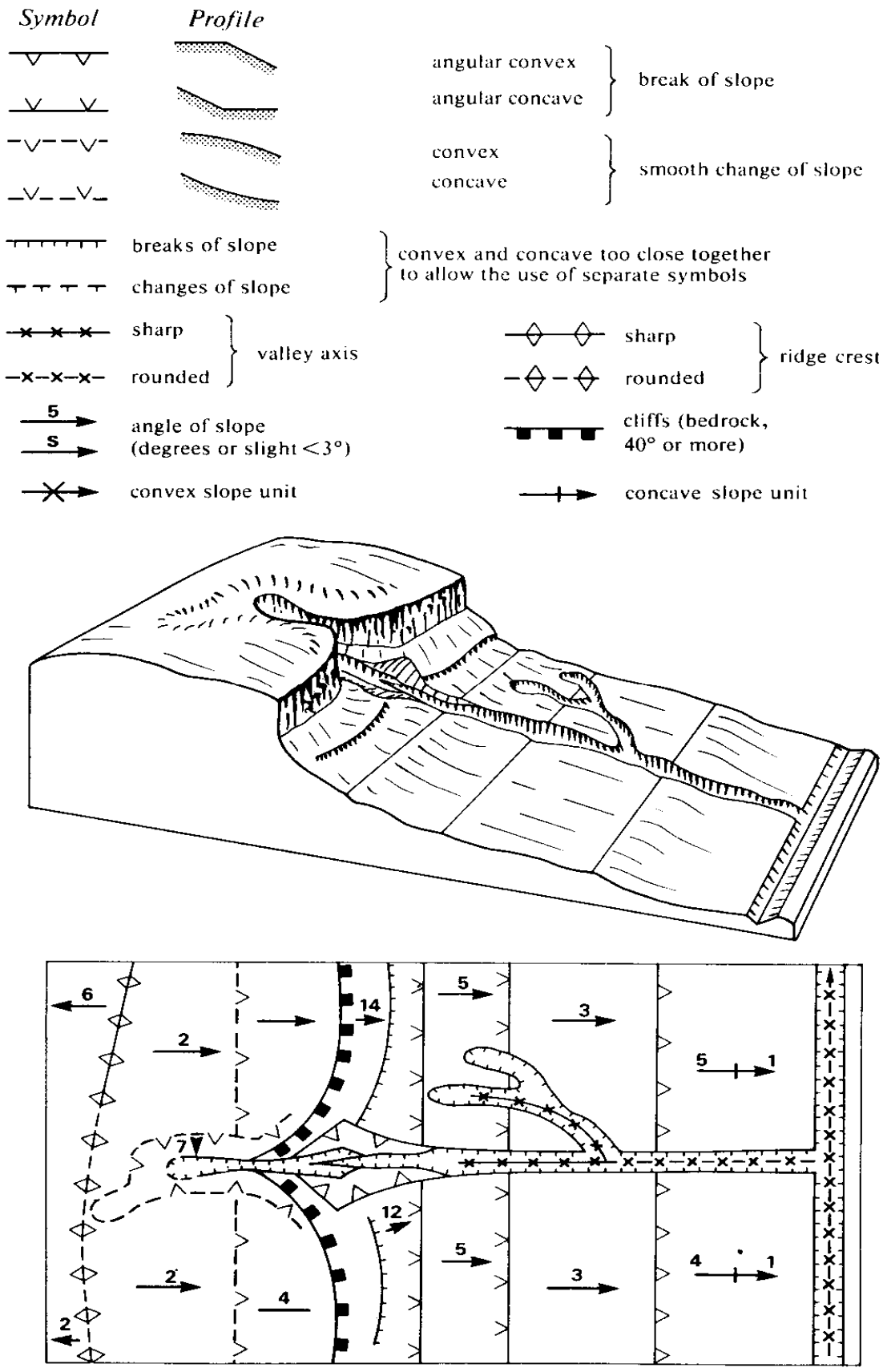

Figure 2.1 The technique of morphological mapping (after Savigear, 1965, reproduced in Cooke and Doornkamp, 1974)

valley respectively. A line with perpendicular ticks is used where a convex and concave break or change in slope lie too close together for separate depiction at the mapping scale. A variant for cliffs (for which a suitable definition might be *'exposed bedrock with a slope gradient of >40 º'*) uses small rectangles instead of ticks.

The two properties of terrain morphology are gradient and curvature. Algorithms to derive both these attributes from a DEM (or through a TIN-based DTM resampled to a DEM) are available in many GIS software packages (e.g., Arc/Info, ER Mapper). The depiction of terrain or landform morphology is particularly amenable to full or semi-automation and procedures for this will be examined later in this dissertation; for example, Figure 6.8 shows an example where morphological mapping symbology has been used to identify the boundaries of rock surfaces.

2.2.2 Geomorphological Mapping

In addition to morphological information, geomorphological maps should include information about the lithology, geological structure, causative processes, and where possible, age and activity of those processes. The complexity of landform information that can be portrayed will depend on the scale of the map relative to the size of the landforms being mapped as well as cartographic and reproduction criteria; consequently, there are many different approaches to geomorphological mapping (Crofts, 1981; Lee, 2001). At regional scales (e.g., 1:250,000 to 1:1 million), the mappable units are associations of landforms with similar surface form (e.g., land systems maps: Christian and Stewart, 1968; Cooke and Doornkamp, 1974). Medium-scale mapping (e.g., 1:10,000 to 1:50,000 scale) is necessary to differentiate individual landforms such as escarpments, landslides, rivers and dunes. Individual landform elements such as failed blocks within a landslide, rockfalls and erosion gullys, would require mapping at detailed scales of 1:2500 or 1:1000. General purpose geomorphological maps such as those for national terrain inventories (e.g., Klimazewski, 1956; 1982) can be very complex (Lee, 2001); therefore special purpose maps may include only a selected range of landforms, materials and geomorphological processes relevant to the problem to be solved. This is the rationale behind the "Geotechnical Land Use Maps" that show classes of terrain hazard in Hong Kong (Styles and Hansen, 1989).

Using the concept of limiting equilibrium (e.g., Bishop, 1955), slope failures occur when the sum of the mobilising forces (e.g., mass of the soil, rock, groundwater and superimposed loads) exceeds the sum of the resisting forces (e.g., shear strength of the slope-forming materials). Although a landslide may be a discrete landform, both the mobilising and resisting factors affecting slope stability vary across hillsides, depending on the distribution of materials and landforms. Therefore, when used for landslide hazard studies, detailed geomorphological maps should depict all the landforms present within the survey area that identify the distribution of material properties and landslide triggering factors (e.g., hillslope hydrology; Zaruba and Mencl, 1976).

Crofts (1981) considers that the strength of the technique lies in the range of landforms that can be identified; however, this will depend on the experience and ability of the operator to recognise the full suite of landforms present; for the same reason, the greatest problem with geomorphological mapping is operator variability (Crofts, 1981). For special purpose investigations, the operator can make a subjective decision not to include certain landforms if they are judged irrelevant to the problem at hand (Crofts, 1981). This is particularly true of engineering-related mapping, where processes acting at very local scales with tiny cumulative effects within the design life of the structure or project, for example soil creep, would have negligible effects on a structural foundation, whereas a landslide may be devastating. On the other hand, recognition of small processes such as sheet, rill and gully erosion may be significant if they have the ability to damage smaller but important structural components such as drains, or if they allow joint sets in a rock face to open.

Geomorphological mapping is well developed in Europe, where the techniques have been widely used for planning and urban expansion since the 1950s (Cooke and Doornkamp, 1974; Crofts, 1981). Gilewska (1976), Klimazewski (1982), and Salomé and van Dorsser (1982; 1985) present comparisons of different geomorphological mapping systems. Three widely-recognised mapping legends are:

(a) Demek (1972), who describes large scale methods and the International Geographical Union (IGU) legend;
(b) Demek and Embleton (1978) extend the mapping techniques to medium scale;

(c) Verstappen and van Zuidam (1968; and more recently, van Zuidam, 1986) describe the International Training Centre for Aerial Survey (ITC) system of geomorphological mapping.

Verstappen (1983; and van Zuidam, 1968; Cooke and Doornkamp, 1974) distinguishes between three types of geomorphological map:

(a) Morphographic maps – contain landforms where the shapes are implicit in the name, e.g. drumlins;

(b) Morphogenetic maps – where emphasis is on the origin and development of the landform; the map legend should contain the genetic description. Landform and materials need to be shown because of the close link with process;

(c) Morphochronologic maps – where subdivisions are based on the time of initiation of the landform. The main distinction will be between landforms resulting from currently active processes and those which are no longer significant, for example, valleys resulting from glacial downcutting in areas that are now deglaciated.

Two examples of geomorphological maps are given at Figures 2.2 and 2.4, and their respective legends at Figures 2.3 and 2.5. These demonstrate the variations of mapping style possible when recording terrain information at scales ranging from 1:1,000 to 1:10,000. The first example depicts some mountainous terrain landforms recorded in part of the Italian Alps using in the 1:10,000 scale mapping system developed by the Alpine Geomorphology Research Group (AGRG) at the University of Amsterdam (de Graaff et al., 1987). The three main cartographic elements are:

(a) Form – point or line symbols define the boundaries of individual landforms;

(b) Material – area symbols;

(c) Process and Time – colour is used to designate the genetic origin of the landform (e.g., fluvial or glacial, etc.), and the time when those processes were active (e.g., presently active, or a relict from the Pleistocene glaciation).

Sections of Figure 2.2 have been drawn to demonstrate the method of construction of the map, and Figure 2.3 shows part of the legend used. The first stage (Figure 2.2a) contains only the hydrographical elements, including rivers, streams and overland flow. In the second stage (Figure 2.2b), the landform shape elements are added, such as the major breaks in slope, including landslide scars, escarpments, and annotated

with selected slope gradients. Thirdly, the dominant surface materials are depicted by symbology (Figure 2.2c), and finally, the elements of the map are colour-coded according to the genetic processes giving rise to the landform and materials. This mapping system does not include explicit information relating to either the age or current level of activity for each of the landforms, although the age can be interpreted from the nature of some of the landforms, e.g., the ice-marginal deposits in an area which is not currently glaciated. However, there is no indication if the landslides are active or relict features.

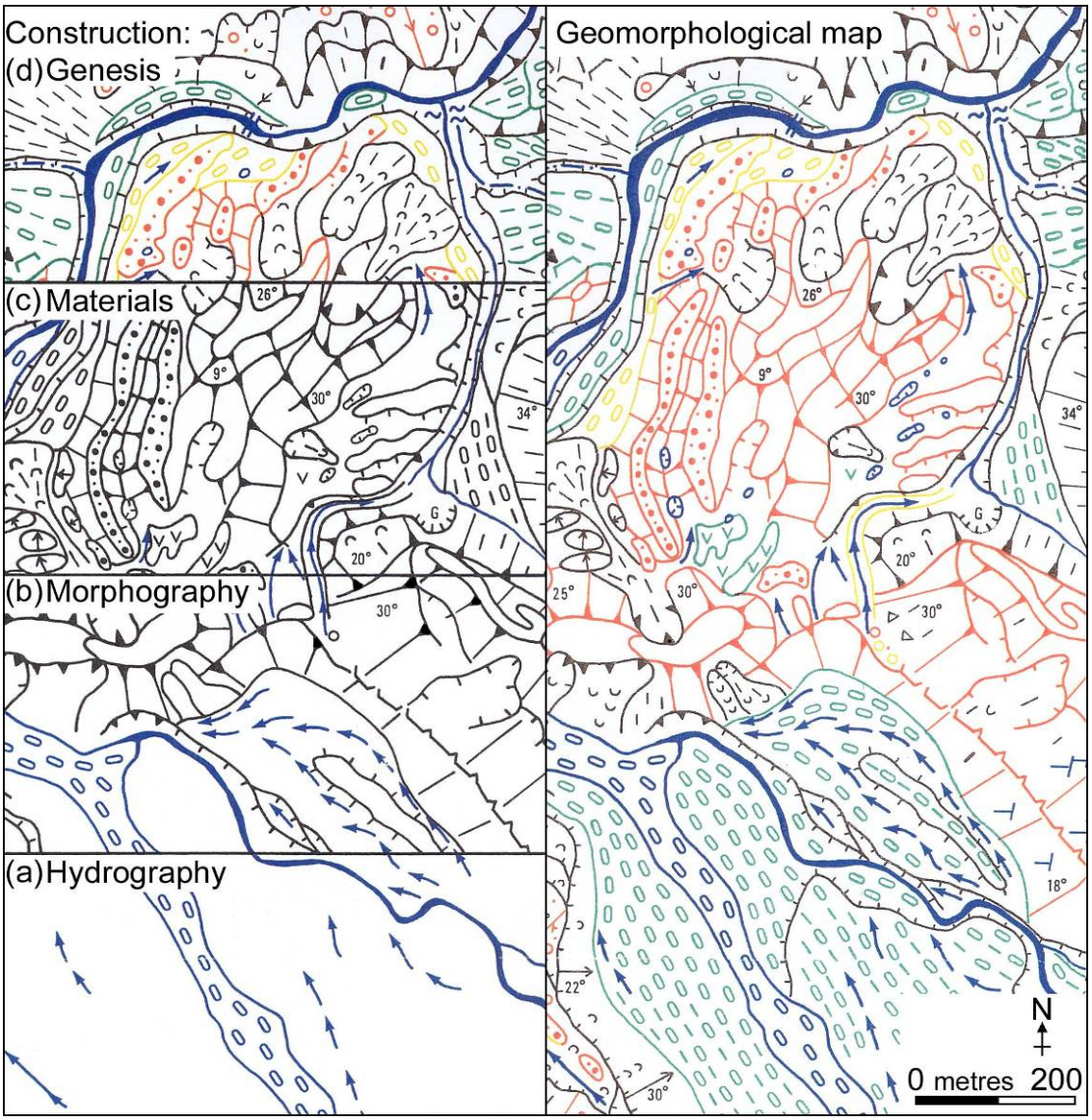

Figure 2.2 Construction of the 1:10,000 scale AGRG geomorphological map (after de Graaff et al., 1987)

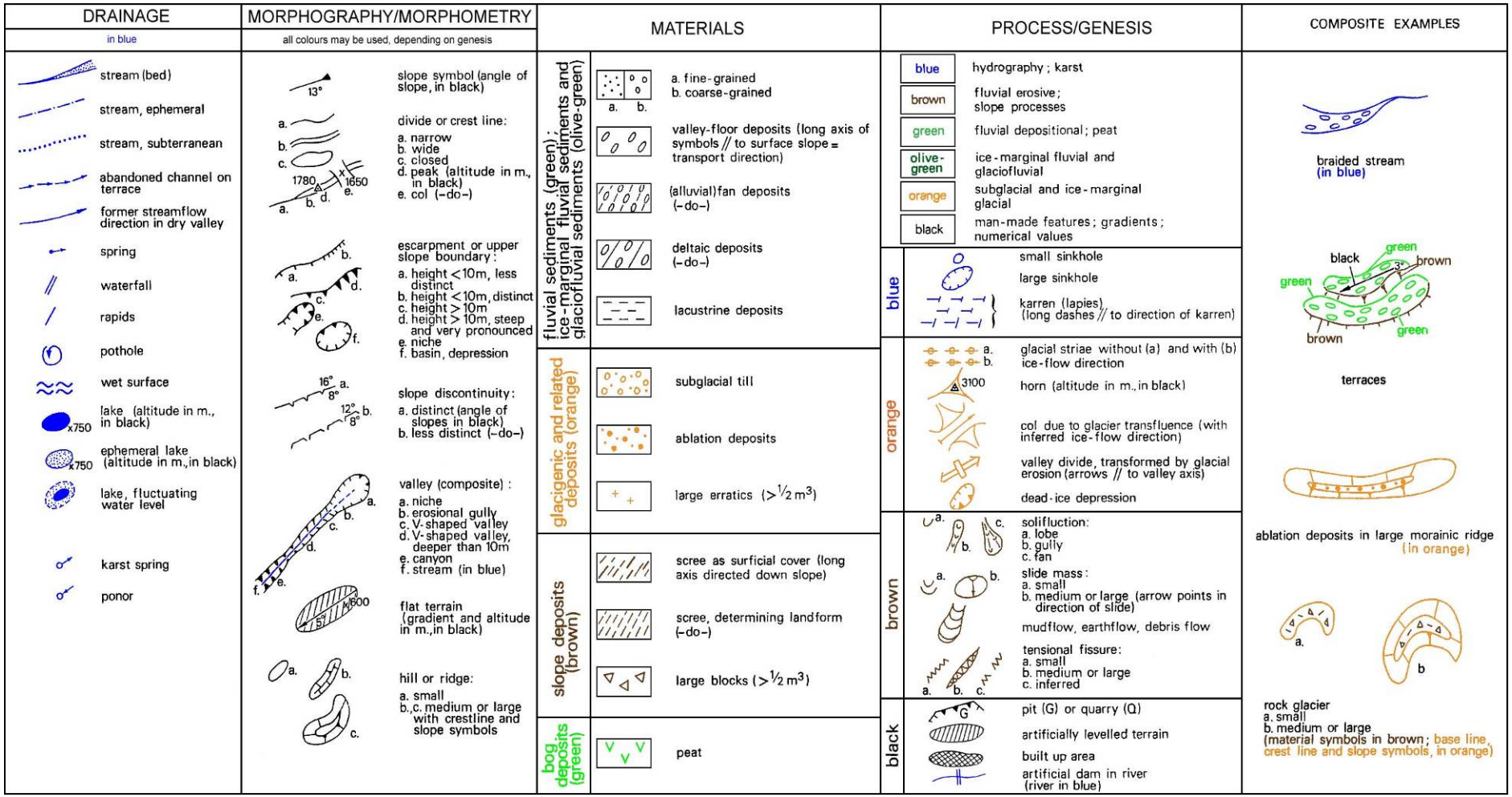

Figure 2.3 Geomorphological mapping legend, AGRG (after de Graaff et al., 1987)

With the second example (Figure 2.4), Terhorst and Kirschhausen (2001) present an example of a detailed, 1:1000 scale, landslide-oriented geomorphological map designed for the German MABIS landslide mapping project; the associated mapping legend is shown in Figure 2.5.

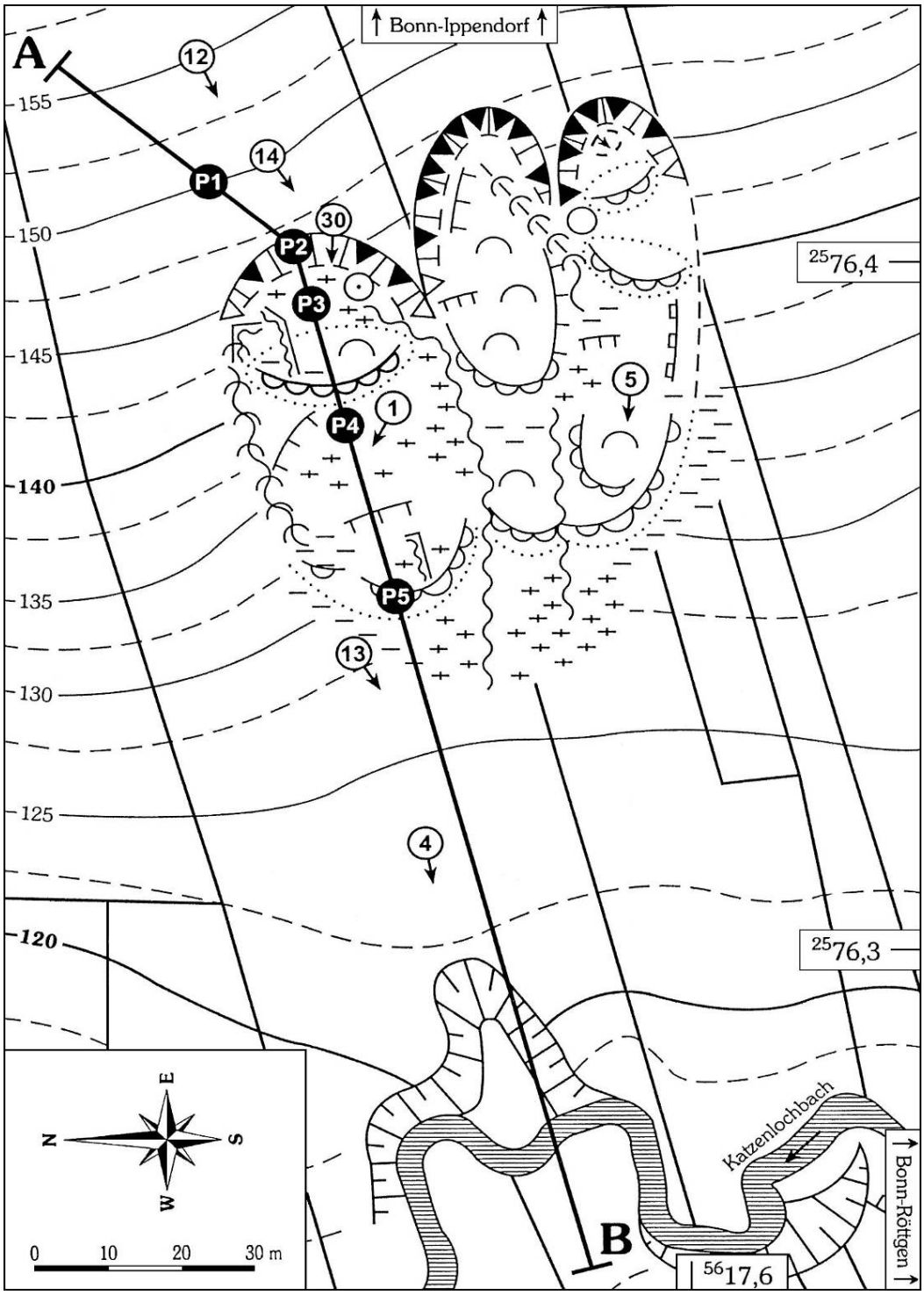

Figure 2.4 1:1000 scale landslide-oriented geomorphological map (from Terhorst and Kirschhausen, 2001)

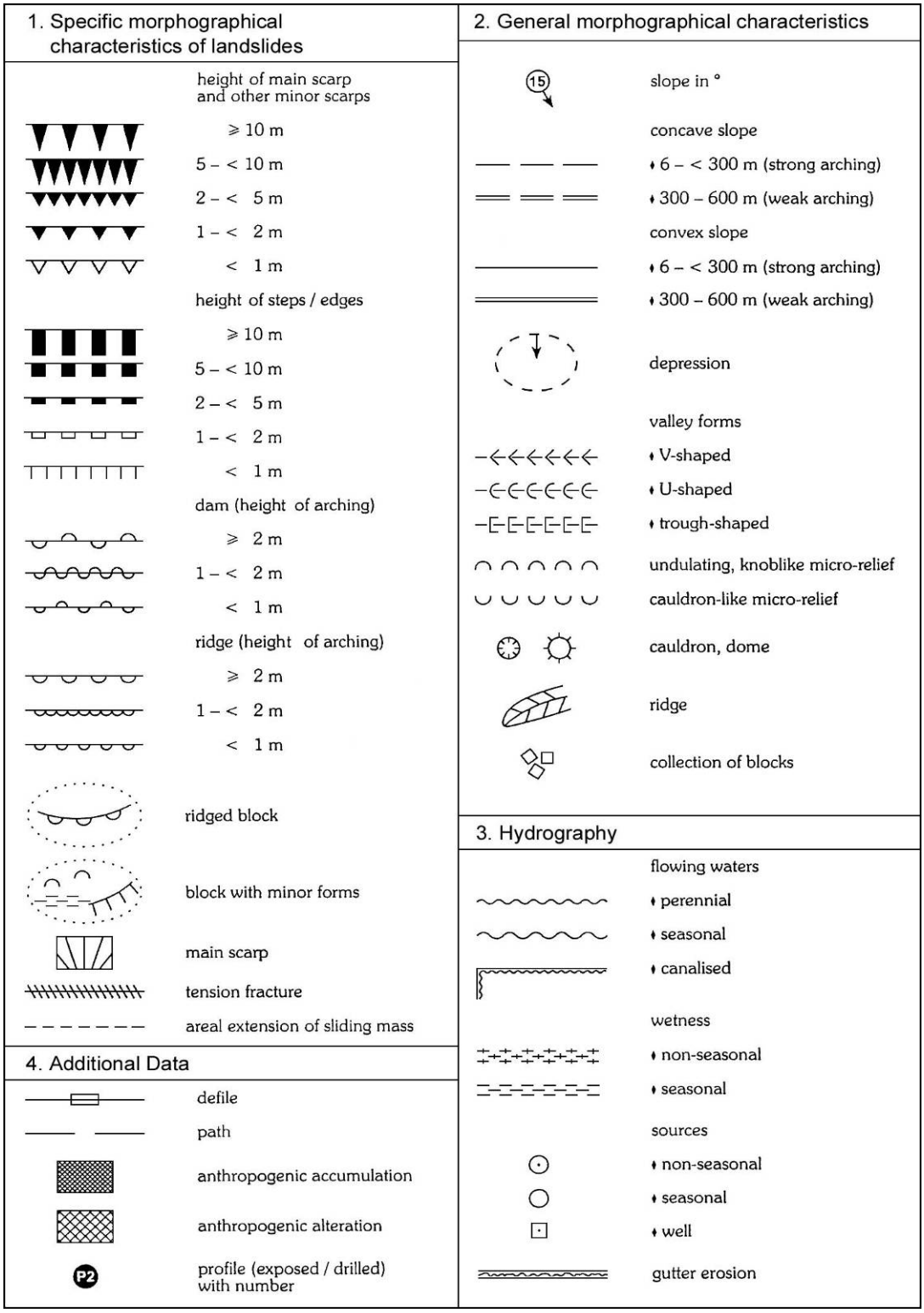

Figure 2.5 Legend for <1:2,500 scale landslide-oriented geomorphological maps (from Terhorst and Kirschhausen, 2001)

The landslide complex shown in Figure 2.4 consists of three bowl-shaped depressions with headwalls between 2 and 5m high (this is confirmed by reference to the 2.5m interval contours adjacent to the landslides), with additional, partly

degraded rotational landslide blocks that have moved downslope from the initial failure site. This mapping legend does not identify the boundaries of the minor features such as the zones of wetness, but allows the major dimensions of the landslide features to be identified to a horizontal accuracy of approximately 2m. A series of downslope cross sections are necessary to provide lithologic and subsurface information.

Terhorst and Kirschhausen (2001) incorporate partial computerisation of the mapping process by using symbology generated using CorelDraw and AutoCAD software. Recognising that conventional geomorphological mapping legends (e.g., Figures 2.3 and 2.5) are dominated by point and line symbols and are consequently unsuitable for use in a polygon-based GIS, van Westen et al. (2003) developed a two-layer scheme to overcome this limitation. The resulting 1:5000 scale mapping scheme for the 20.8km^2 Alpago test area of the Italian Alps, uses a main layer describing the genesis, material types and chronological information for 52 geomorphological units, with 81 subunits identified in the second layer. Each subunit consists of a single landform for which the genesis and shape information is given. For landslides, information on the relative age of the movement and main causal factors are included in the main unit, with the description of landslide components and activity given in the subunits. In their study, van Westen et al. (2003) compare a subjective landslide susceptibility map compiled by experts using direct mapping during fieldwork, with six types of susceptibility map compiled using different numbers of terrain attributes processed using Bonham-Carter's (1994) weights of evidence method. Results show that:

(a) The spatial prediction capacity for landsliding is improved by the inclusion of more geomorphological information;

(b) Use of the main geomorphological units provide the optimum prediction capacity, as the subunits tend to produce very detailed maps that highlight the existing pattern of landslides, rather than the adjacent areas where there would be a higher risk of landslides in the future;

(c) When comparing the direct and indirect susceptibility maps, the inclusion of geomorphological units improves the prediction rate of landsliding from 52% when using only slope gradient and lithology, to 76%.

2.3 Conceptual Models and Geomorphological Paradigms

When mapping landforms, the observer will have in mind a conceptual model of the landform elements and how they are likely to be distributed across the landscape. Conceptual models of landscape development have aided geomorphological interpretation for over one hundred years. In his 'Geographical Cycle', Davis (1899) considered the erosional sequence of landforms to include an initial uplift of mountains followed by progressive erosion by wind and water, ultimately to create a gentle slope, the peneplain. Osterkamp and Hupp (1996) identify the paradigm that considers landscapes as a composite of evolutionary, time-dependent features to be a modified form of Darwin's (1859) concept of evolution. Davis's Geographical Cycle was developed for humid, temperate climates, and uses for genetic emphasis the sequence: geological structure, process and stage (Garner, 1974). Alternative landform sequences have been proposed, including Penck (1924) and King (1953; 1962) for other climatic environments (Higgins, 1975). King, for example, places the emphasis on landform origins on stage, ahead of process and structure (Garner, 1974). Penck (1924) in Europe, and independently, Meyerhoff (1940, quoted in Meyerhoff, 1975) in New England, USA, recognises the influence of a dynamic Earth with polycyclic landform sequences affected by major climatic change.

Schumm (1976) and Schumm and Lichty (1965) consider that models of geomorphic evolution are oversimplified and unsatisfactory for short-term interpretation of landform change. Schumm argues (1973; 1976) that landscapes are complex systems that can react to change with gradual and or episodic responses. As a corollary to the concept of geomorphic thresholds, Schumm (1973) observes that rejuvenation within a catchment creates a complex response within the fluvial system, where long periods of relative stability can be punctuated by short episodes of erosion.

Anderson and Burt (1981) classify the Davisian (Davis, 1899) and other temporal models of landform explanation as examples of the inductive scientific method. They add that, while application of these models in the first half of the 20th century reached the status of a paradigm in which geomorphological problems could be organised, the models also fail to answer more problems than they explain, creating the conceptual environment for paradigm replacement (Kuhn, 1962). By the second

half of the 20th century, debate on temporal landform sequences had been largely superseded by systems theory, pioneered through the application of statistical methods by Strahler (1950) and more directly by Chorley (1962). The introduction of statistical analysis as a means of hypothesis testing in geomorphology heralded the wider application of the deductive scientific method within a more quantitative approach. Through a focus on geomorphological processes and rates, the investigation of landform dynamics is able to encompass both long- and short-term changes, together with large and small-scale landforms. The contents lists of major geomorphological journals, such as *Geomorphology*, reveal that the recent emphasis in geomorphological research remains on process-response studies; landslide-oriented process-response studies include Gabet et al. (2004); Gabet and Mudd (2006), and Korup (2004). This type of research can be accomplished through observations made in the field or in the laboratory, or by numeric processing of measurements (Chorley, 1966).

2.4 Geomorphometry: the Definition of Land *Form*

Geomorphometry is the process of determining parameters that describe topographic variations (Evans, 1972). Topographic attributes directly control the effect of gravity on materials within the slope system, including internal variables such as surface and subsurface hydrology, and mass movement. In addition, geomorphic processes and slope-forming materials are affected by external variables such as insolation, and the strength and direction of both wind and precipitation.

Quantitative determination of morphology across a terrain surface is usually accomplished though processing DEMs, which has been a rich vein of research activity since Evans (1972). Reviews of the geomorphometric literature are given in Wood (1996), Evans (1981; 1998), Pike (1993, 1995, 2000), Shary (1995) and Shary et al. (2002). Most of the literature discusses the issue of parameterisation of the Earth's surface and its effect on specific landforms, hydrology and soils.

Zevenbergen and Thorne (1987) describe the quantitative assessment of terrain shape, including measures of curvature, using more generalised variants of the quadratic equations used by Evans (1972, 1975, 1979, 1980). Geomorphometric parameters are derived from the matrix of elevation values surrounding and including

the central point. Dikau (1989) subdivides the Earth's surface into a hierarchical subdivision of component landforms based on a combination of plan and profile curvature and radius of curvature. Irvin et al. (1997) investigate the validity of automated identification of the component hillside landforms for the purpose of soil classification, using continuous and unsupervised classification methods and attributes of elevation, gradient, profile and tangent curvature, and indexes of wetness and solar radiation. They conclude that the automated methods generate results similar to manual methods, but as they were based on a 10m DEM grid, the results are more detailed than manual soil mapping.

Subdivision of the terrain into units containing generally uniform soil development processes within hillsides is also likely to identify units with similar propensity to slope failure (landslide) due to the dominant influence of hillside hydrology on both geomorphic processes. Terrain classification based on hydrologic criteria is well-developed, with many GIS software packages able to divide the ground surface according to slope gradient, aspect, and plan and profile curvature. To provide two examples, the topographic parameters derived by Wood (1996) can be processed as formulae kernels within ER Mapper. Secondly, in the Arc/Info GIS package, internal and external software modules are available to define topographic parameters and complex hydrological attributes such as catchment contributing area, and distance from watershed. The grid version of the Tapes software (Terrain Analysis Programs for the Environmental Sciences; Moore et al., 1991) has been scripted as the TapesG-ArcGIS module to run inside ARC-GIS version 9 (TapesG-ArcGIS, 2005).

Pike (1988) uses DEMs to quantify the landforms characteristically prone to landslides, while Wood (1996) evaluates the reliability of a DEM generated by digital image processing, but uses visual inspection of the calculated elevation surface and its derivatives. Both authors note that uncertainty is usually characterised by local, high spatial-frequency variation. Li (1994) uses a statistical comparison of DTMs derived from contours, contours with break points and lines, grid DEMs, and DEMs with break lines. He found that the use of additional feature-specific elevation data reduces the standard deviation by 40 to 60%.

Ventura and Irvin (2000) and Wilson and Gallant (2000) describe various methods of simple and complex landform classification that use DEMs processed within the ANUDEM (Hutchinson and Gallant, 1999; 2000) and TOPMODEL packages (Beven, 1977; 1997). Meentemeyer and Moody (2000) demonstrate the identification and regional extrapolation of structural geological features, in this case bedding planes, using high resolution (10m) DEMs. Koike et al. (1995, 1998) assess methods of combining DEM-generated surfaces with geological lineaments identified in satellite-derived images. Dip orientation of the larger planes can be resolved from lineaments identified with reference to variations in position and orientation with altitude. Both these techniques generate parameters that describe geological structures in a form suitable for inclusion within a GIS database for use in slope stability assessment.

2.4.1 Morphometric Parameters

Gradient and aspect are parameters widely used in landscape studies (e.g., Hutchinson and Gallant, 1999, 2000; Wilson and Gallant, 2000). Gradient has a major control on the velocity of runoff, and together with soil type, also affects the rate of infiltration into the ground and soil throughflow. The thickness of both the soil (in both the agricultural and engineering senses) and regolith tends to decrease on steeper slopes due to the increased rate of transportational processes over weathering relative to low gradient slopes. Aspect is an indirect influence on soil thickness and soil moisture, through the combined effect of insolation affecting evaporation and evapotranspiration, and prevailing winds controlling precipitation.

Shary et al., (2002) summarises the formulae for deriving a wide range of curvatures, including several that he devised earlier (Shary, 1995). The set of curvatures include several variations that are predominantly oriented along a slope profile, or across the profile, as shown in Figure 2.6. The differences lie in the exact orientation of the axes, specifically whether the Z axis lies vertically, or in some orientation to the matrix of points being measured.

Evans's (1972) procedure is included as an appendix in Pennock et al. (1987), and is the result of collaboration between Young (1978) and Evans (1979). This method determines curvature values for each point in a regular array by deriving the second-

order polynomial for the points in a 3x3 kernel containing elevation values. Elevation values in the top row of the kernel are labelled, from left to right, z_1, z_2 and z_3; the middle row is z_4, z_5 and z_6, and the bottom row is z_7, z_8 and z_9. The spacing between points is w in both the horizontal and vertical directions. The formula for the polynomial is:

$$z = rx^2/2 + sxy + ty^2/2 + px + qy + z_0 \quad \text{Eqn. 2.1}$$

where the polynomial coefficients are partial derivatives of the surface z = z(x,y), and where:

$$p = \delta z/\delta x = (z_3 + z_6 + z_9 - z_1 - z_4 - z_7) / 6w \quad \text{Eqn. 2.2}$$

$$q = \delta z/\delta y = (z_1 + z_2 + z_3 - z_7 - z_8 - z_9 / 6w \quad \text{Eqn. 2.3}$$

$$r = \delta^2 z/\delta x^2 = [z_1 + z_3 + z_4 + z_6 + z_7 + z_9 - 2(z_2 + z_5 + z_8)] / 3w^2 \quad \text{Eqn. 2.4}$$

$$s = \delta^2 z/\delta x \delta y = (-z_1 + z_3 - z_7 + z_9)/4w^2 \quad \text{Eqn. 2.5}$$

$$t = \delta z/\delta y^2 = [z_1 + z_2 + z_3 + z_7 + z_8 + z_9 - 2(z_4 + z_5 + z_6)] / 3w^2 \quad \text{Eqn. 2.6}$$

These partial derivatives are used in the formulae summarised by Shary et al. (2002) to define eighteen forms of curvature plus solar insolation.

Evans-Young's method gives good results for maps based on first derivatives, i.e. slope gradient and aspect. However, the results for curvatures, which are second derivatives, tend to emphasise grid directions (Shary et al., 2002). This can be seen in results of synthetic surface experiments described in Chapter 5 of this dissertation.

Florinsky (1998; Florinsky et al., 2002) considers that Gauss's (1827) mean curvature is a more representative topographic attribute for use in landform studies than horizontal and vertical curvatures, as this curvature provides a significant control on soil moisture and vegetation. Vertical and horizontal curvatures (Figure 2.6) are local factors that determine the dynamics of overland and intra-soil water flow as they influence soil moisture, pH, thickness of soil horizons, soil organic matter and vegetation. Florinsky (1996) reports that horizontal curvature is a good indicator of strike-slip faulting, while vertical curvature works better at identifying dip-slip and reverse (thrust) faults.

Shary et al. (2002) include modifications to extend application of the procedure to a plane with the same elevation at the central point but not necessarily with a gravity-oriented Z axis. This revised procedure also allows smoothing by modification of

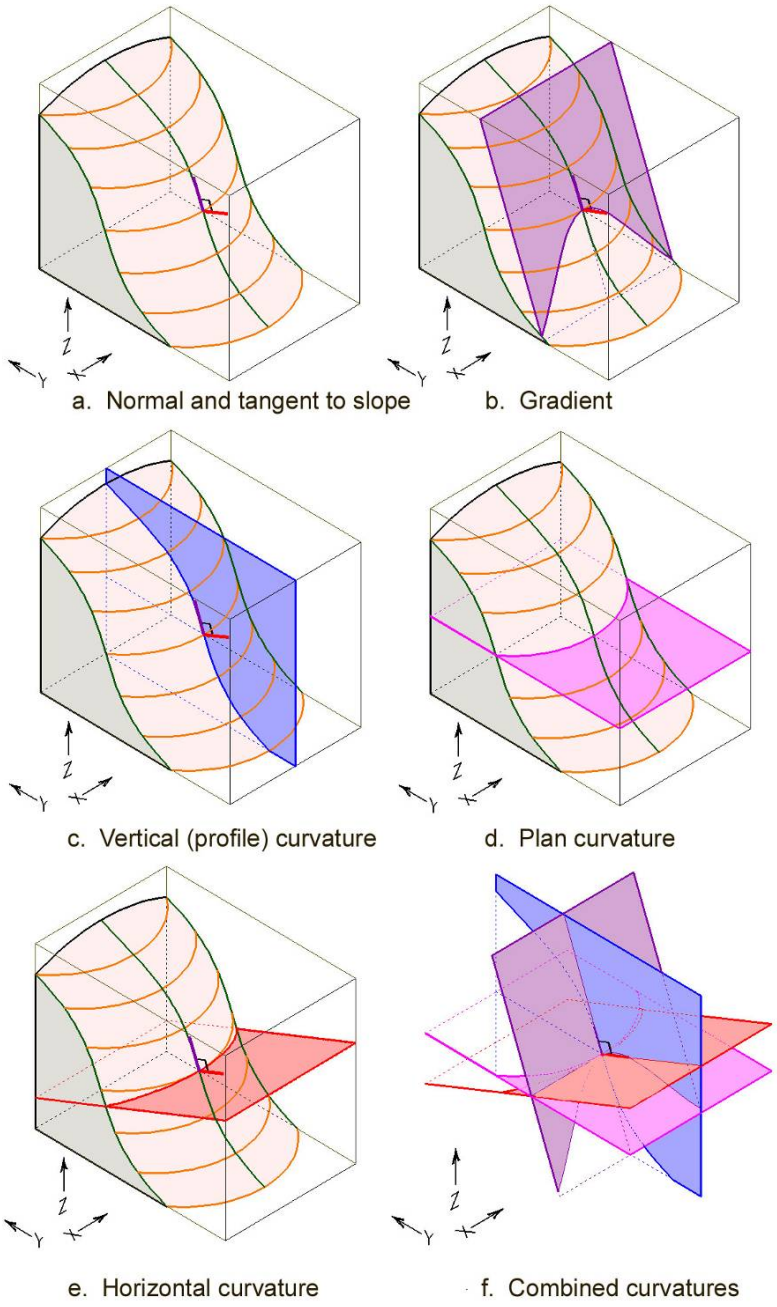

Figure 2.6 Relationship among curvatures

the central Z value, when needed. Weak smoothing is implemented within a 5x5 kernel around the nine internal points of the kernel being processed and uses three criteria: parts of plane surfaces are transformed into a plane; the smoothing filter is isotropic; and the filter weights decrease linearly with distance from the centre of the kernel. The authors state that, from empirical results, and using a suitable value for their modified parameter *s* of 0.2, '*weak smoothing gives good results of curvature for practically any terrain*'.

2.4.2 Change of Gradient with Kernel Size

Shary et al. (2002) describe an experiment in which slope gradients were determined across seven landscape surfaces plus an artificial surface consisting of pseudo-random noise. For every surface, the average slope gradient decreases when kernels of increasing size are used, confirming Evans's (1975) findings. This has a parallel in the automated image correlation function of digital photogrammetry, where kernels are used to compare patterns within images to identify the best fit between two images (Chapter 3).

2.4.3 Incorporating Vertical and Profile Curvature

Slope morphology needs to be defined in both profile and plan, as curvature in each direction has significantly different effects on geomorphologic and hydrologic processes. Plan concavity controls water flow, with plan concave slopes increasing flow concentration while flow diverges on plan convex slopes. The effect of gravity decreases downslope on profile concave slopes, while it increases downslope on plan convex features. Combining the three fundamental curvature configurations of

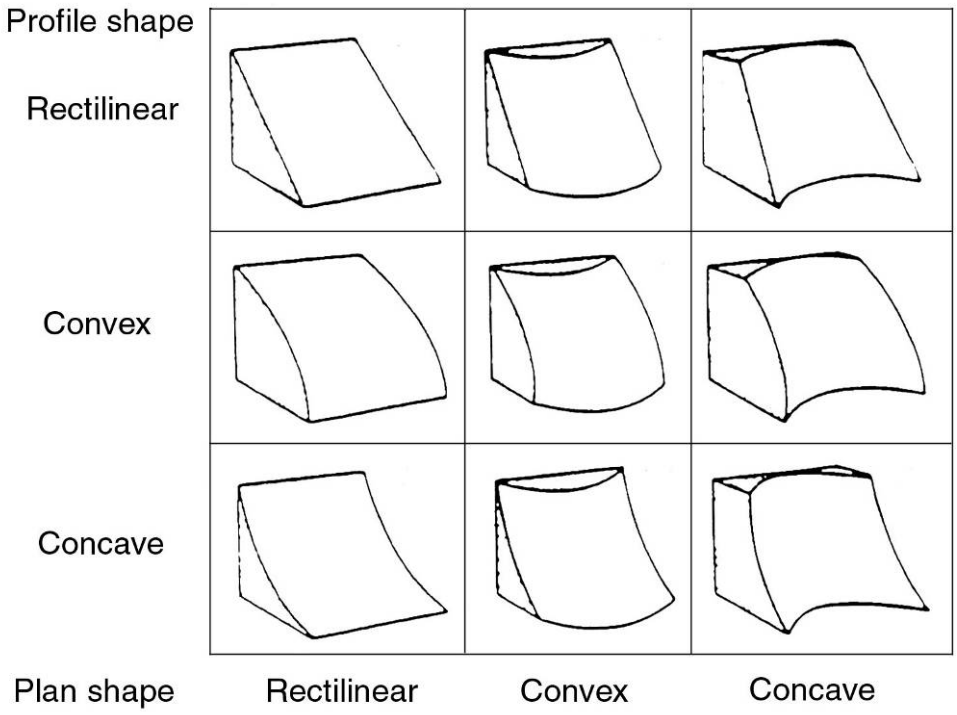

Figure 2.7 Range of landforms resulting from a combination of plan and profile curvatures (after Ruhe, 1975)

concave, rectilinear and convex in each of plan and profile gives nine separate combinations (Ruhe, 1975), as shown in Figure 2.7. These can be distinguished during curvature processing by reference to the signs of the profile and plan curvature values, while allowing a threshold curvature value on either side of zero to allow for the rectilinear class. Care must be taken when considering the effects of aspect, to ensure that profiles facing in opposite horizontal directions, e.g., east and west, give correct signs for concave or convex curvature.

2.5 Application of Landform Models in Landslide Hazard Studies

Selby (1982) recognises three types of landform model: analogue, slope evolution, and mathematical, which include analytical and simulation models. Representing a landform component in an analogue model allows other features such as materials

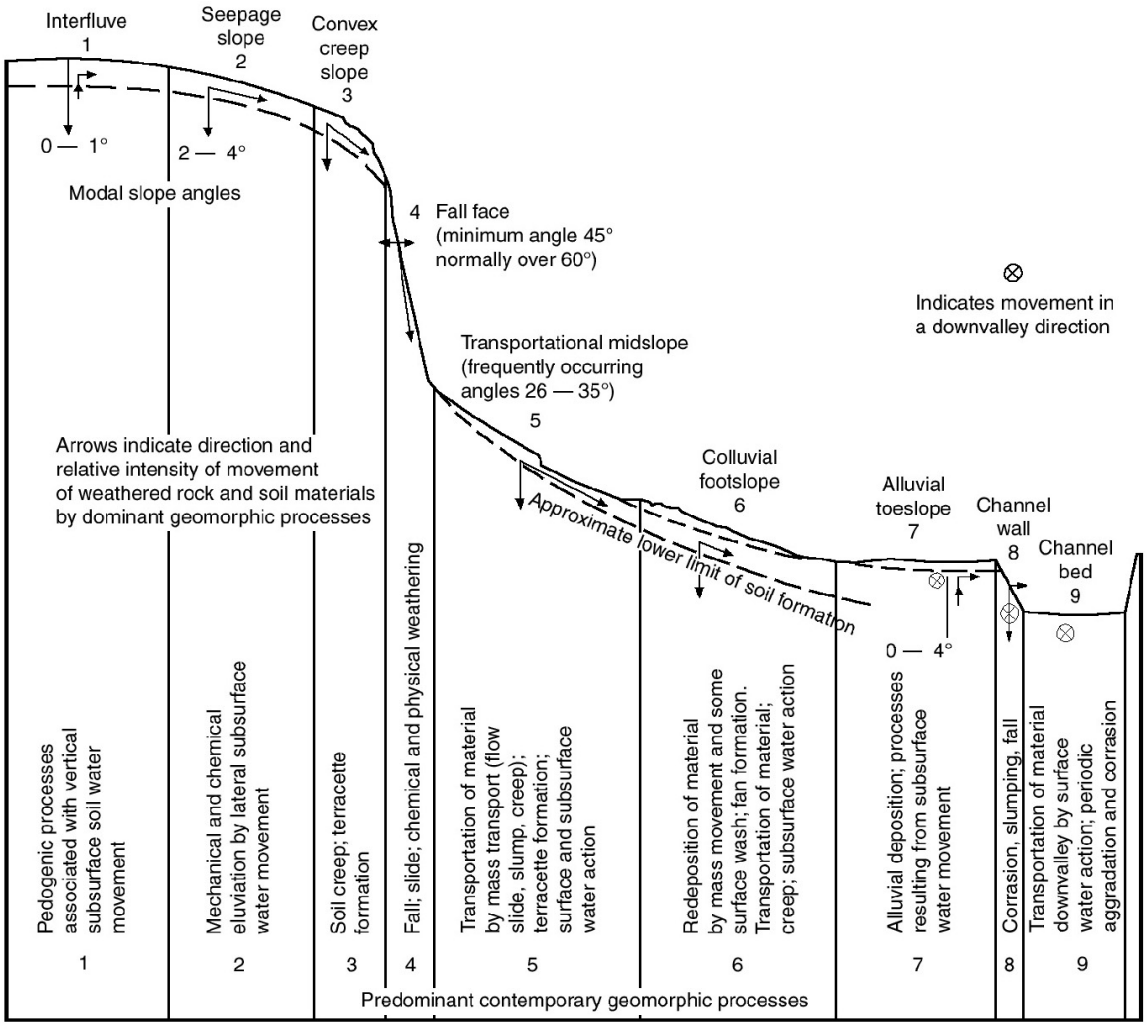

Figure 2.8 Nine-unit land surface model (from Dalymple, et al., 1968)

and processes to be associated with it. Before an analogue model can be prepared, the most significant landform units must be identified. These can be distinguished on plan and profile curvature, and on the process or processes acting on each unit. The nine-unit land surface model developed by Dalrymple et al. (1968) effectively summaries the interactions between form and the dominant processes acting on each slope unit (Figure 2.8). The arrows located near the top of each unit indicate the relative intensity and direction of movement of weathered rock and soil materials in response to the action of dominant geomorphic processes.

Evolutionary models generally follow the ergodic hypothesis (Chorley and Kennedy, 1971) which suggests that, under certain circumstances, sampling in space can be substituted for sampling in time. Categorisation of a landform into discrete units allows relationships to be developed for the constituent materials and causative processes that can be rationalised into a mathematical model. These are based on the continuity equation (e.g., Kirkby, 1971), whereby the difference between input and output in a section of slope results in erosion or deposition.

Throughout the range of geomorphological observations, there remains the need to disseminate the findings of geomorphological analysis both to other Earth scientists and to external parties who may not be as proficient in the underlying concepts, particularly in the fields of land use planning, environmental investigations and engineering. It is within the realm of applied geomorphology that the value of a visual model is of greatest benefit. Anderson and Burt (1981) consider that the field of applied geomorphology lies within the concept of a control system (Chorley and Kennedy, 1971); socio-economic decision-making is a complex process in which intervention in the physical process-response system is only one element. In geomorphological systems where thresholds are critical, such as that of slope stability, ensuring that decision-makers adequately understand the consequences of changes to the physical process-response system that can result from external factors can be seen as critical. While purists may argue that landform models are over-simplifications of reality, simplification may be justified as being necessary to convey meaning and understanding to the decision-makers; without understanding, the decision-makers will not act on the results, which will significantly reduce the value of the work.

The benefits of compiling conceptual landform models as 3D block diagrams to visualise the results from slope stability investigations can be demonstrated using two examples. In the first example, Brunsden et al. (1975) describe three case studies that demonstrate how geomorphological mapping played a central role in highway alignment projects across unstable terrain; their first case study was for the proposed alignment of the Dharan-Dhankuta Highway in Nepal's Himalayan foothills. The original alignment made three ascents/descents of >1000m across steep slopes and a deeply incised river gorge, and traversed long sections of sideslope where numerous landslides were identified. As a result of geomorphological mapping along the proposed alignment and adjacent slopes, a revised alignment was proposed where much of the route was relocated to run along the ridgelines upslope of the failures and active gully systems; while expensive slope-stabilisation works were concentrated on a few key ascents and descents, the revised alignment presented a total cost saving over the whole project. Figure 2.9 shows the block diagram from Brunsden et al. (1975) in which the dominant landform elements are depicted in simplified, topological form together with the initial alignment (labelled 'trace') and the alternative alignment. This block diagram clearly visualises the benefits of the alternative alignment compared with the terrain problems that would need to be overcome by the initial alignment.

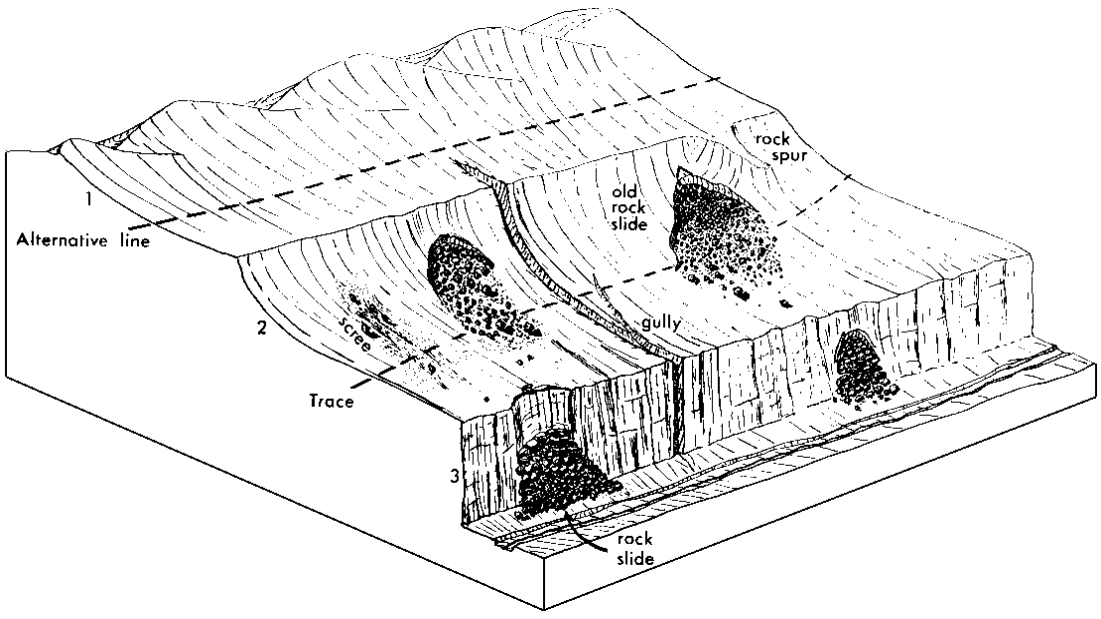

Figure 2.9 Block diagram demonstrating the landform elements in Eastern Nepal (from Brunsden et al., 1975)

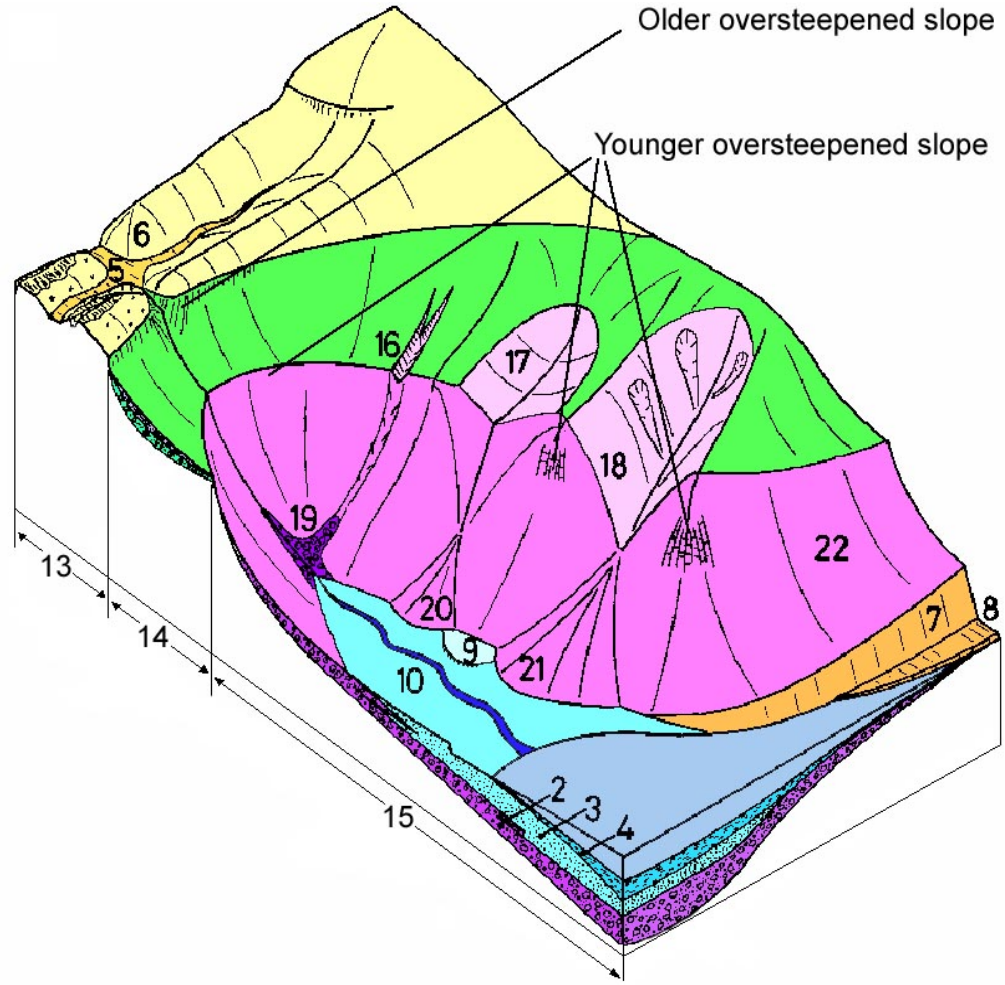

Legend:

Materials

1 Old colluvium
2 Young colluvium
3 Alluvium
4 Marine deposits

Landforms

5 Upland valley
6 Deeply weathered cliffs
7 Coastal Cliffs
8 Wave cut platform
9 Alluvial terrace
10 Floodplain
11 Submarine buried valley
12 Ridgecrest gully erosion
13 Relict landforms on uplands
14 Older landform assemblage
15 Younger landform assemblage
16 Stream incising into superficial deposits
17 Initial incision has widened to valley
18 Deep, bowl-shaped valley between spurs subject to instability on sides
19 Boulders in stream channel
20 Small colluvial fan
21 Large colluvial fan
22 Coastal slope (thin soils)

Figure 2.10 Block diagram illustrating landform elements in Hong Kong (after Hansen, 1984b)

The second example (Hansen, 1984b) uses two block diagrams to illustrate an evolutionary model of Hong Kong's terrain. The main elements of the landform sequence are depicted in Figure 2.10. These are used to explain the effect of

accelerated river downcutting in the lower reaches of a near-coastal valley due to the effects of global sea level fall during the Pleistocene glacial maximum, creating an oversteepened slope that has subsequently migrated higher upslope. Terrain dynamics will be different above and below the two waves of aggression (a laterally-extensive slope steepened by increased rates of erosion; Bjerrum, 1967) marked by the crests of two generations of oversteepened slope.

The model was devised to explain the presence of deeply weathered colluvial deposits on the tops of mid-slope benches that are much older than unweathered colluvial deposits in the valley floors. The terrain model explains the distribution of variable engineering properties for each of the materials present in the landscape, in a similar way to the nine-unit land surface model (Dalrymple et al., 1968 and Figure 2.10); for example, upslope of the younger oversteepened slope, the bedrock within units 13 and 14, the 'relict uplands' and the 'older landform assemblage', exhibit Tertiary deep weathering (Ruxton and Berry, 1957) that is not present in the lower 'younger landform assemblage', unit 15. The ergodic principle (substituting space for time; Chorley and Kennedy, 1971) is demonstrated by comparing the sequence of valley development into the upper landform assemblage from the narrow stream incising into superficial deposits (unit 16), through the narrow valley (unit 17) to the older, deep, bowl-shaped valley of unit 18 (Figure 2.10).

Figure 2.11 shows the relationship between four types of slope failure and the landform elements on the sideslopes of the Hong Kong terrain model. The two landform models contain a wide range of geomorphological features, including those with a dominant morphological element, such as the oversteepened slope between the younger and older landform assemblages, and the characteristic features of the landslide scars, debris trails and incised river valleys.

Griffiths (2001) contains a set of invited papers reviewing developments in various aspects of engineering geological and engineering geomorphological surveys. Section 3: Case Studies of Griffiths (2001) contains 24 papers; 13 of these use engineering geomorphological mapping, and 23 papers use 2D maps or profiles to portray Earth science observations; seven papers use annotated block diagrams to create 3D visualisations of the surface and subsurface terrain conditions. Lee and Moore's (2001) contribution is of particular note, as only a single 3D, annotated

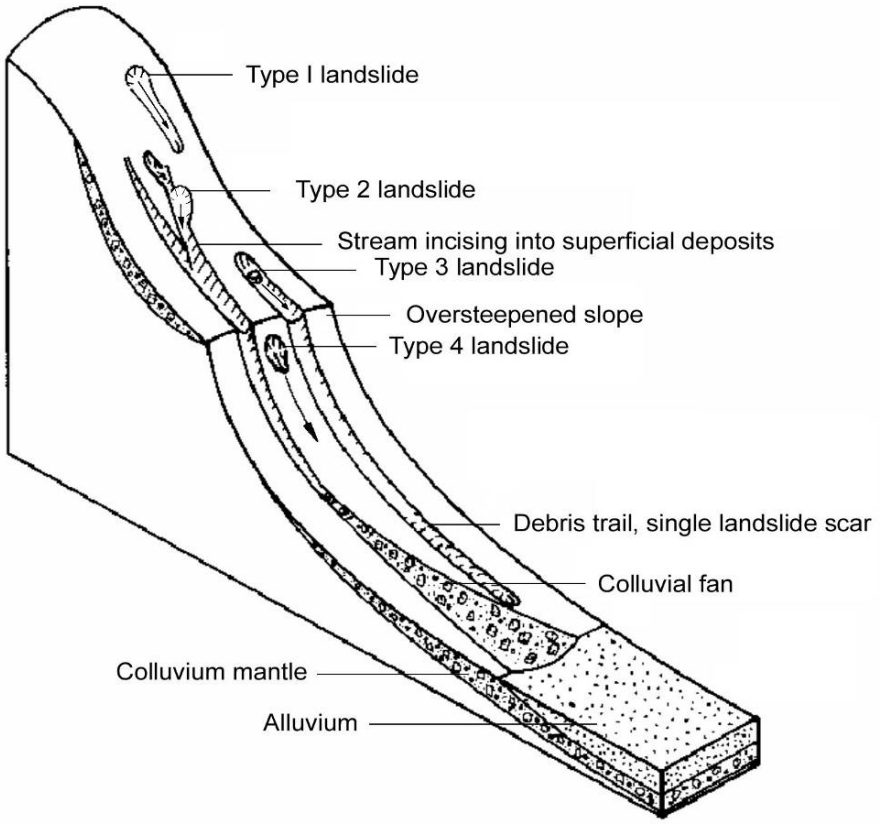

Figure 2.11 Location and types of landslide in relation to the Hong Kong terrain model (after Hansen, 1984b)

block diagram is considered necessary to describe the sequence of landforms controlling and affected by ground movement in the Ventnor Undercliff on the Isle of Wight. This block diagram was extracted from a consulting engineering report to the South Wight Borough Council, thus demonstrating the value of simple visualisations to convey complex terrain concepts to non-specialists (Rendel Geotechnics, 1995).

2.6 Landslide Hazard and Susceptibility Studies

Landslide hazard assessment methodologies developed significantly in the 1970s, building on earlier geotechnically-oriented case studies of individual or small groups of landslides (e.g., Anon, 1972, 1982). The range of landslide hazard assessment techniques in use by the early 1980s was the subject of wide-ranging reviews prepared by Cotecchia (1978); Bosi (1978), Hansen (1984a), Varnes (1984), Hartlén and Viberg (1988), and more recently by Dearman (1991), Leroi (1996), and Aleotti and Chowdury (1999). A detailed suite of landslide hazard studies have been carried

out in San Mateo County, California, which are summarised in Brabb (1995) and Brabb and Harrod (1989).

The primary subdivision of the mapping methodologies is between direct and indirect mapping (Table 13.2 in Hansen, 1984a), with an additional category for non-mapping, or geotechnical methods. Direct mapping requires the locations of landslides to be identified, while indirect mapping techniques use a range of terrain attributes to predict susceptibility to future slope failures and are very suitable for manipulation within a GIS (Aleotti and Chowdury, 1999). Van Westen (1993) classifies geomorphological methods as qualitative hazard assessment, further subdividing indirect methods into statistical and deterministic hazard analysis, and landslide frequency analysis. This demonstrates the increased range of processing options available when considering manipulation of parameters within a GIS.

2.6.1 Direct Mapping

Direct mapping methods include landslide inventory maps and geomorphological maps. For both categories, the mass movement landforms are shown as points, or if the scale is sufficient, by a feature boundary or associated series of symbols (Wieczorek, 1984). The distribution of mass movement landforms is usually collected by interpretation of imagery from satellite or aircraft, with supplementary ground survey and, if available, a search of historical archives and newspapers (e.g., the AVI Project, described in Guzzetti et al., 1994; Guzzetti and Tonelli, 2004).

The comprehensiveness of the inventory depends on temporal availability and scale of the imagery and ground surveys. For example, many small and old landslides may not be identified if the only available aerial photographs are small scale and taken many years after the landslide's occurrence. Unless the inventory is able to access a series of photographs taken at various dates, the sequence of landslides, or changes within a single landslide scar, may not be identifiable. Chandler and Brunsden (1995) give examples of landslide activity maps based on the interpretation of historical sequences of aerial photographs. The Hong Kong Government continues to update its Natural Terrain Landslide Inventory (Evans et al., 1998, 1999; King, 1999; Ng et al., 2000), although before 2004 this was limited to using high altitude (>3000m) aerial photographs, more recently low altitude photography has been incorporated.

Data contained within a geomorphological map may be used for landslide hazard determinations, either as a direct assessment, or as part of a wider consideration of terrain hazards. Keinholz (1977, 1978) developed a methodology for the mountainous Grindelwald area of the Swiss Alps, where 'stumme zeugen' (translated as 'silent witnesses' – landforming processes and the landforms produced by them) were identified. Extensive fieldwork was required to compile the 1:10,000 scale maps, but most features are shown true to scale. For the second stage of the Grindelwald project, a combined hazards map was produced, with the degree of hazard determined for approximately 4000 geomorphological units with the aid of checklists. Although the use of checklists creates 'decision rules' (van Westen, 1993) that reduce the subjectivity involved, the final hazard assessment was determined by geomorphological interpretation of landforms and other terrain features. This makes the assessment partly direct and partly indirect.

Characteristic landforms forming landslides are widely described in the literature, e.g., the review by Soeters and van Westen (1996). Some of the visual features to be mapped in a landslide-oriented, detailed geomorphological map are shown in Figure 2.12a (from Varnes, 1978). The salient features are the sharply convex break in slope at the crown (upslope end) and sides of the landslide, the concave exposed failure surface (depending on the extent to which the failed mass has been removed from the scar by movement and subsequent erosion), and the debris extending downslope. For rapid moving debris flows, the debris trail may become very extended and even be removed from the hillside if the debris is extremely wet or becomes mixed with sufficient overland water flow, as within a valley-side channel or large, concave hillside. Debris flow trails frequently deposit levées (elevated deposits) along the side of the eviscerated channel. McAlpin (1984; reproduced at Figure 2.12b to d, and Wieczorek (1984) (reproduced in Keaton and de Graff, 1996), illustrate how the detailed landforms of a landslide can become severely degraded through time. For example, at failure, the majority of landslide crowns contain sharply convex changes in slope, i.e., the radius of curvature is small in relation to the height of the scarp. If the slope-forming materials are very resistant to erosion, this sharp convexity may remain visible for many years; if the materials are relatively soft, and especially if they possess low cohesion, this sharp convexity will become more rounded as the radius of curvature increases, and the characteristic edges of the

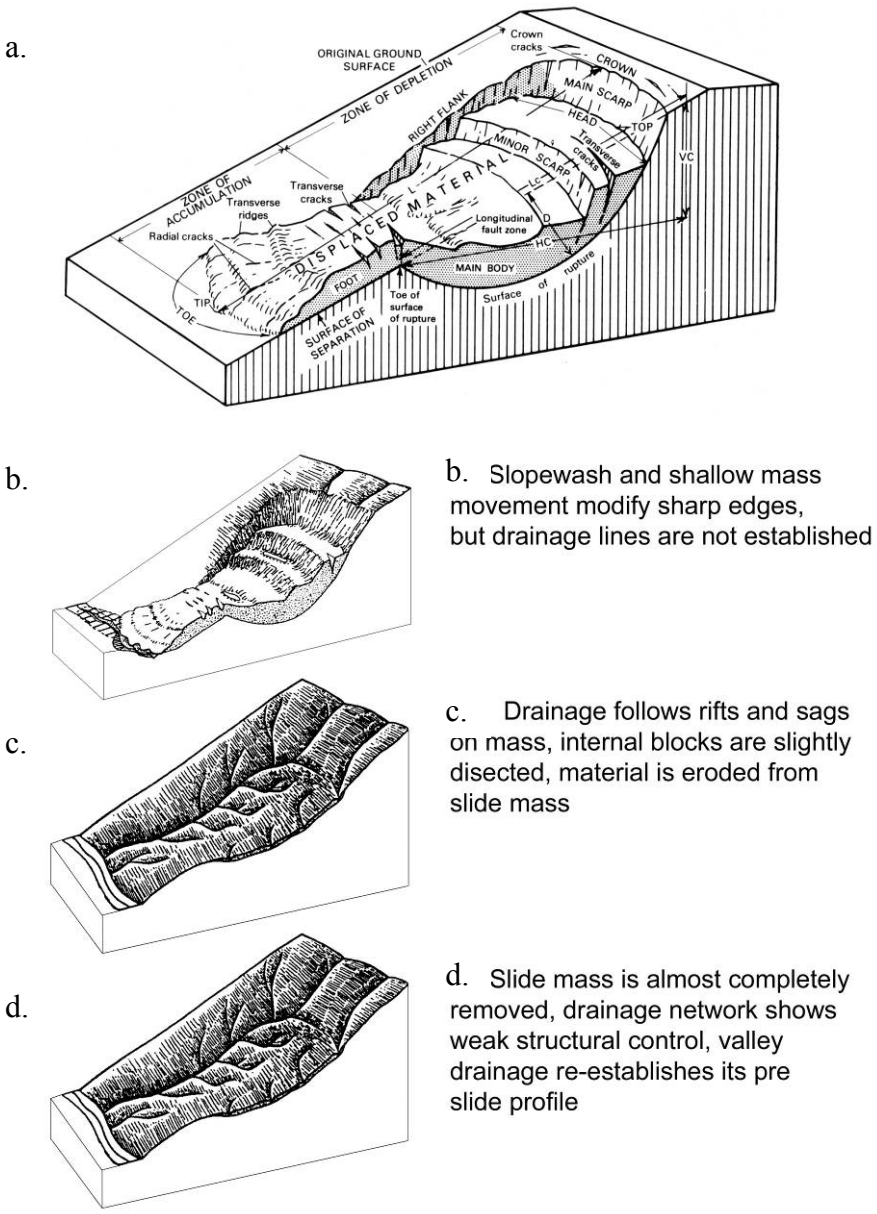

Figure 2.12 Landslide features and degradation through time
(a. from Varnes, 1978; b., c., d. from McAlpin, 1984)

depression in the slope surface become more difficult to identify. While this landform may be less clearly distinguished by its representation on a DEM, an Earth scientist experienced in terrain mapping and landslide identification may be able to recognise this degraded landform as evidence of past slope failure (e.g., Hansen 1984a; Dikau et al., 1996; Soeters and van Westen, 1996).

Ardizzone et al. (2002) demonstrate that landsliding processes produce a wide variety of landforms that may be difficult to interpret, even by experienced geomorphologists. When three teams of geomorphologists produced landslide maps of the same 300km^2 of the Staffora Basin in Italy, using different sets of aerial photography, the disagreement between areas identified as underlain by landslides approaches 68%, and the mismatch between the three data sets increases to 80%. This disagreement represents the total error and uncertainty due to landslide identification and classification and the transfer of locations from aerial photograph to maps.

2.6.2 Indirect Mapping

Indirect mapping methods extrapolate slope stability assessments beyond landslide boundaries by comparison of selected parameters (Hansen, 1984a). One of the simplest indirect methods is to compile an isopleth of landslide densities; the number or area of landslides occurring within a counting shape (usually a circle or square) are recorded as the shape is moved in a grid pattern across the map. The data are then contoured. While early applications of this method were manual (e.g., Wright and Nilsen, 1974), the preparation of density maps within a digital GIS follows a similar procedure.

Many multi-parametric area studies of landslide hazard use simple attributes of terrain shape derived from topographic data obtained from published contour maps, often at small scales. Early studies used physical map overlay techniques (e.g., Brabb, et al., 1972), although digital data comparisons within a GIS are facilitated by vectorising cartographic contours if raw digital data are not available (e.g., van Westen, 1993). Some studies have defined landslide susceptibility units based on slope gradient, bedrock and landslide distribution information for over 30 years (e.g. Brabb et al., 1972; Drennon and Schleining, 1975). More recently, slope curvature has also been identified as a significant parameter affecting hillside hydrology and consequently, slope stability (Gao, 1992; 1993; 1997).

Multivariate statistical techniques are commonly used to generate landslide susceptibility maps (Hansen, 1984a; Varnes, 1984; Soeters and van Westen, 1996)). Because of the limited resolution of the topographic source data, multivariate studies

of larger areas have used generalised topographic information, most commonly slope gradient. This is normally combined with geology in an attribute overlay operation to form geology/slope units that are then ranked by the occurrence of landslides within each unit (Brabb, 1995, et al., 1972; van Westen, 1993; Soeters and van Westen, 1996). During the late 1980s and increasingly up to the present (2007), GISs have been used to manipulate the variety of terrain and environmental attributes relevant to slope stability (van Westen, 1993; Carrara et al., 1995; Hansen et al., 1995)). Gao (1992, 1993, 1997) identified concave sideslopes as a topographic setting susceptible to landsliding using a DEM. Duran and Grant (2000) have extended earlier work (Ward et al., 1978; 1982) on using probability analysis to estimate parameters values, and incorporate it within a GIS through the use of Monte Carlo simulation to model multiple landslide events.

For both manual and digital processing, multi-parametric assessments of landslide hazard require the terrain and other environmental attributes to be categorised into areas. These can be rasters, TINs, or the terrain can be divided into geohomogeneous polygon units where the portion of the land surface contains a set of ground conditions that differ from adjacent units across definable boundaries (Hansen, 1984a). In the context of terrain morphology, homogeneous units should reflect differences in slope gradient and or plan and profile curvature. Both regular sampling units and homogeneous units can be manipulated within a GIS, either by raster methods or polygon overlay (Burrough and McDonnell, 1998). Polygon overlay techniques were favoured by early researchers, particularly those performing correlation and map overlay by hand (e.g., Brabb et al., 1972). Continuing increases in computing power has allowed grid-based methods using increasingly smaller cell sizes to be amenable to raster-based GIS processing and the use of regularly-spaced DEMs (e.g., ER Mapper). Smaller grid cells are more likely to contain consistent parameter values and yield results closer to the correct values (Li, 1994), thereby decreasing spatial inaccuracies, assuming the accuracy of the source data is consistent with the grid spacing used.

2.6.3 Non-mapping (Geotechnical) Methods

Slope stability at specific sites can be assessed by deterministic methods often involving detailed ground investigation and slope stability modelling, with the results

provided as specific values for a slope without analysis of the spatial distribution or variability of parameters. Limiting equilibrium methods compare the disturbing and resisting moments present within a hillside or embankment. Reviews of these engineering-oriented methods have been prepared by Lambe and Whitman (1979), Chowdhury (1978), Hoek and Bray (1981), Anderson and Richards (1987) and Bromhead (2000).

Values for the parameters can be obtained from materials sampling and testing, or through back-analysis of the failure, assuming values for the water level in the ground watertable or perched watertables. However, soil properties can be extremely variable both vertically within a profile, and laterally, which can reduce the reliability of deterministic methods, especially when the results need to be applied across large sites. For broad area studies, the cost of obtaining detailed ground investigation data can become prohibitive.

2.7 Processes and Constraints of DEM Generation and Use within a GIS

Measurement of terrain shape requires the continuous data of the real world to be sampled at an interval sufficiently small to be able to adequately represent the relevant component geometrical primitives, while limiting the data set to a manageable size and cost. In addition, errors in measurement must be identified and limited to an extent sufficiently small as not to degrade the captured data. The following discussion of issues includes some examples derived from the background study of the landslides forming detailed case studies in Chapters 6 and 7.

2.7.1 Problems of Using Existing Data

When existing source data are obtained as hard copy (e.g., printed or hand-drawn maps and photographs of source documents), these may not contain information as to the specifications for the data collection (metadata). When these data are used at more detailed scales than the initial capture, unwarranted accuracy may be inferred. In the context of digital terrain modelling, some imprecision may arise from the use of source data from existing contour maps where the digitized data can be enlarged to significantly higher resolutions than the original (McCullagh, 1998; Wise, 1998, 2000).

2.7.2 Contour Data

For economic reasons, most landslide hazard assessment work carried out over large areas has used existing published topographic information from national and regional surveys. The quality of DEMs based on contours has been studied in terms of the hydrological continuity of drainage networks (Wise, 2000).

In the present study, published 1:20,000, 1:5000 and 1:1000 scale digital topographic data were compared for a small but clearly visible, revegetated landslide scar (Figure 2.13). The landslide scar can be identified by curvature in ten 2m interval contours on the 1:1000 scale data (black lines in Figure 2.13), but only one 10m interval contour at 1:5000 scale (green lines). The 1:20,000 scale contours (purple lines) do not reveal the landslide scar or the concave and convex hillsides adjacent to the landslide scar. Contours at 2m vertical interval on the existing 1:1000 scale maps appear adequate for locating the landslide, which can be distinguished from the concave valley to the east by the presence of the 4m high, near-vertical slope at the northern (upslope) end of the concave depression. At 1:5000 scale, interpretation of

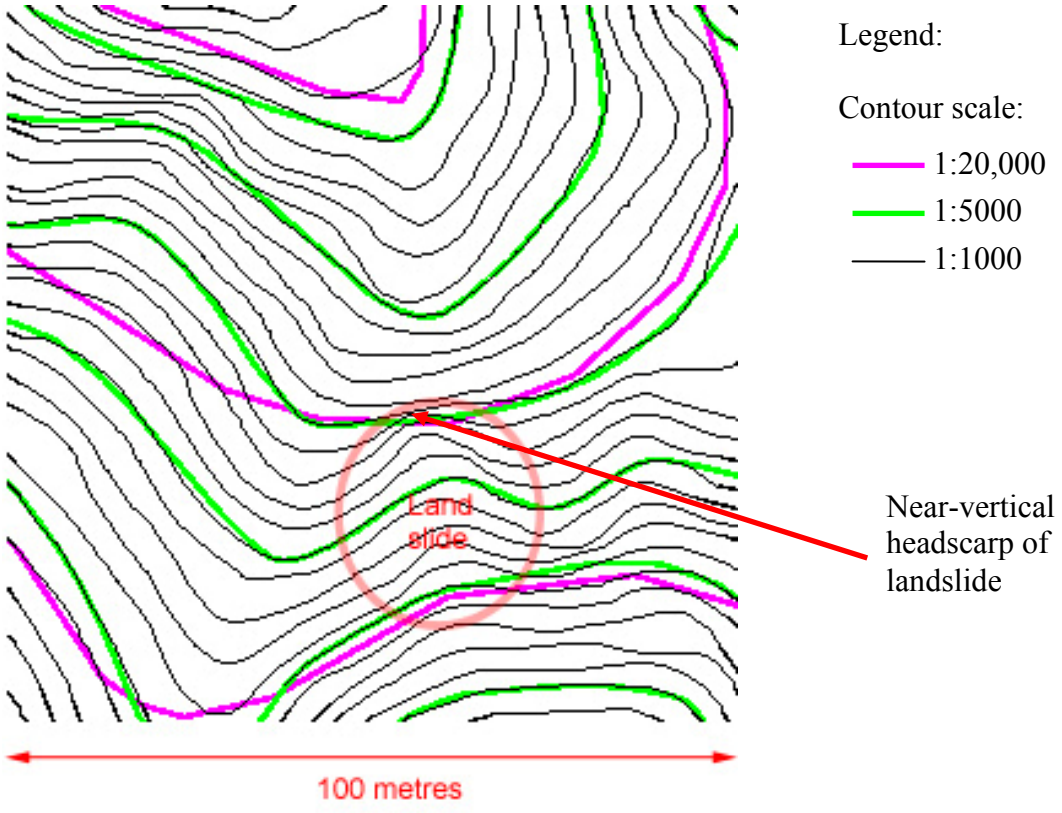

Figure 2.13 Comparison of 1:20,000, 1:5000 and 1:1000 scale contours around the One Rise More landslide scar, Hong Kong

the terrain from the 10m interval contours fails to distinguish between the landslide and the adjacent concave hillside, because the near-vertical slope is too small to be identified.

2.7.3 Features and Landmarks: Precision and Accuracy

While the types of error present in measurement is a core element in surveying and photogrammetry (Cooper, 1998), Lane et al. (1998) note that error analysis is not routinely considered by geomorphologists, although the trend is improving. Error analysis is particularly important if the measurements are being used for process studies based on rates of change of landform over a specified time (Cooper, 1998). Cooper (1998) notes there are three types of error:

(a) **Random error**: the normal variation in measurement due to errors within the measurement system, i.e. the repeatability of an individual measurement – this is measurement *precision*;

(b) **Systematic error**: inexact mathematical models used to relate measurements, i.e. how closely does the [landform] model fit the true shape and location – this is the *accuracy* of measurement;

(c) **Blunders**: avoidable mistakes made during measurement, i.e. the wrong feature is measured, typographical errors in recording data.

Figure 2.14 shows a section of an orthophoto prepared to aid field mapping of the One Rise More landslide in Hong Kong. This was compiled by draping a rectified (i.e., distortion-removed) aerial photograph (frame 9647) over a DTM derived from the digital 1:1000 scale topographic data supplied by the Lands Department, Government of Hong Kong SAR. Features visible on both the aerial photograph and topographic basemap were used as control points to georeference the image. Note that the mapped footpath (shown as a dotted line) appears mis-aligned by distances of between 1 and 2m from the footpath visible on the rectified image. The footpath at this location has been cut into the hillside, and small changes in location due to variation in vegetation are unlikely, i.e. the location of the footpath is stable over time, in contrast to a footpath on an open hillside. The *precision* of individual point measurement is dependent on the resolution of the image and the measuring system (See Chapter 3); in this case, the calibrated lens resolution (at ground scale) gives a measurement precision varying from approximately 0.11m at the centre of the

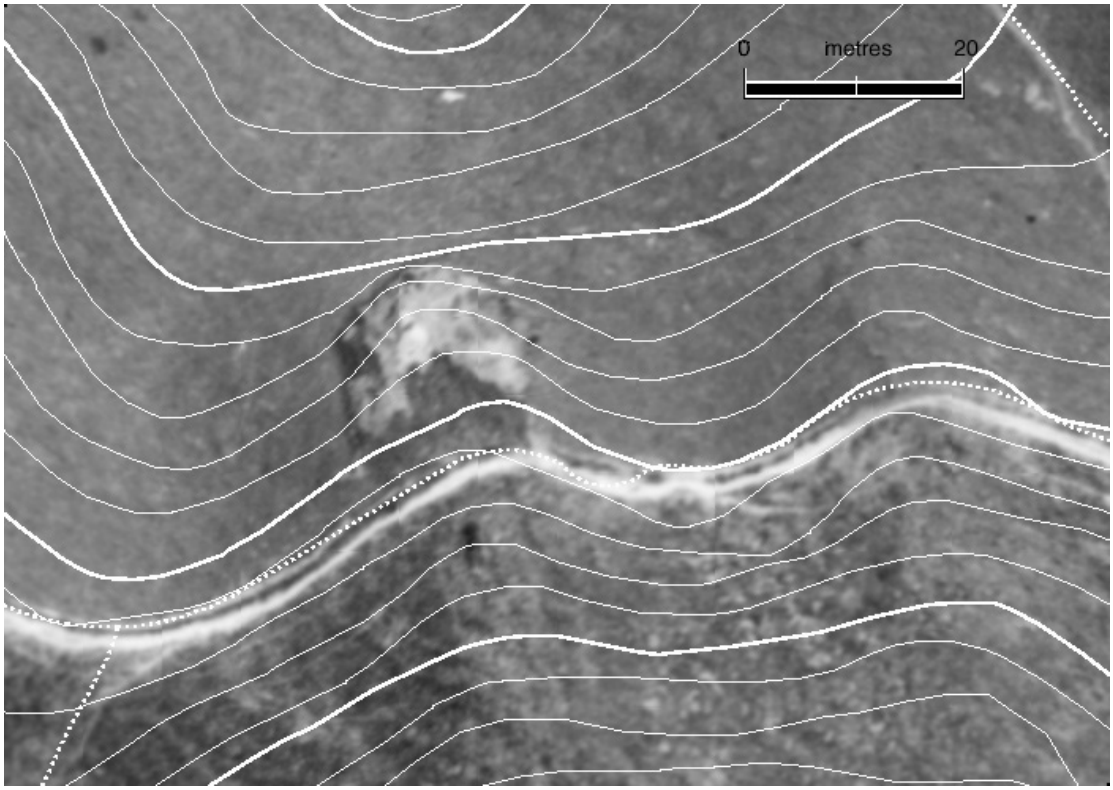

Figure 2.14 1:500 scale orthophoto of the One Rise More landslide, Hong Kong aerial photograph frame 9647, © Government of Hong Kong SAR

photograph to 0.18m near the edges. Although the standard deviations of the errors of the control points used to build the photogrammetric model (see Chapters 3 and 6) are 0.52m, 0.58m and 0.73, respectively for X, Y and Z values, the maximum residuals are 0.87, 1.28 and 3.1m respectively. This is an indication of identification *accuracy* for a combination of natural and man-made features on moderately-developed, hilly terrain, with 1:1000 scale topographic mapping. In terrain with few or no man-made features, only less-accurate features such as stream intersections and spot heights are available for use (as in the One Rise More case studies, Chapters 7 and 8), the resulting accuracy can be lower. Chapter 3 includes the relationship between precision and accuracy as part of the discussion on photogrammetric methods.

2.7.4 DEMs and DTMs: TIN and Raster

Closer inspection of the nodes forming the contours in the DTM of the terrain around the One Rise More landslide reveals other problems that come to light when the

'contours' are used to generate a TIN. Figure 2.15a contains the results of an uncontrolled Delaunay triangulation used to create a TIN model of the 1:1000 scale digital topographic data for the One Rise More landslide, and Figure 2.15b shows the resulting shaded relief model, illuminated from the top of the figure. The red arrow labelled '13.6m'on the shaded relief image indicates a narrow depression that does not appear on the model represented by the contours. This has been generated as a result of a wide spacing between two adjacent nodes along the original 500m elevation contour. Nodes on the adjacent contours are closer than the adjacent nodes along the contour, resulting in a triangle edge being placed almost perpendicular to the contour. This removes the control of the location of the sharply convex crest of the landslide scar clearly visible in Figure 2.14, with consequent errors in slope gradient, aspect and particularly curvature.

Incorrect placement of triangle edges has occurred elsewhere in the model (red arrows in Figure 2.15a and b); however, due to the gradual changes in slope gradient and aspect (that control the shading), these 'errors' are less visible.

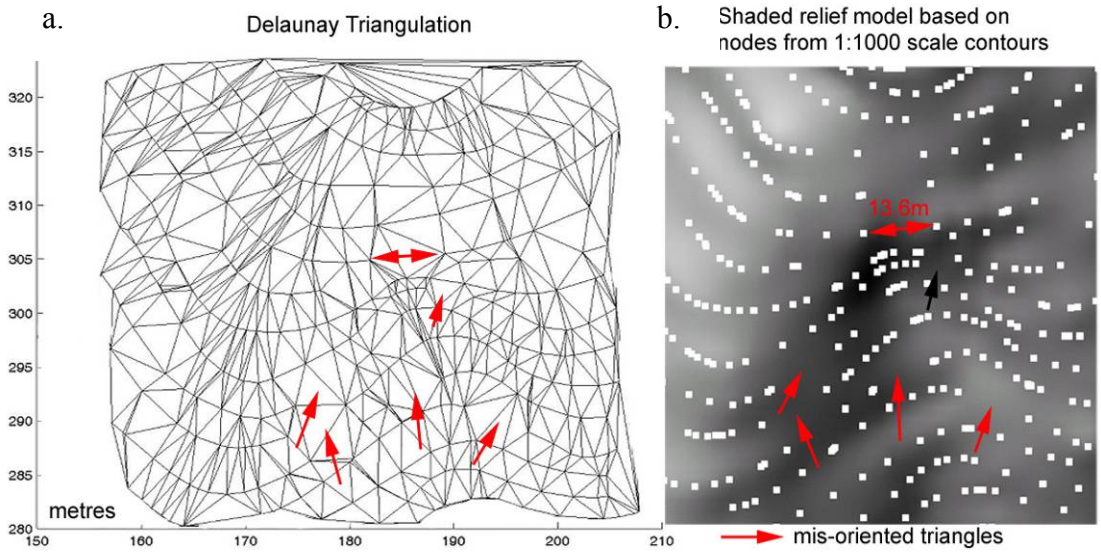

Figure 2.15 Contour nodes and TIN derived from the existing 1:1000 digital topographic data, One Rise More, Hong Kong

2.7.5 Spatial Location of the 3D Model

The major factors affecting the accuracy of a DEM generated photogrammetrically from vertical aerial photography include the accuracy of the ground control points

used, the photo-texture of the images being measured, and the properties of the image correlation window being used to capture each point (see Chapter 3 and Kraus, 1997, 2000). This is particularly important in the case of automated image matching as used to capture large numbers of height values across an area. From a geomorphometric perspective, the error in orientation of the photogrammetric model has two factors, firstly the rotation of the model relative to the coordinate axes of the object space (i.e., displacement of a point on the ground relative to the perspective centre of the image), and secondly, its relative position (i.e., errors in absolute position in terms of X, Y and Z).

Rotation is important as the Z axis is dominated by gravity and the X and Y axes affect environmental properties, including insolation and the dominant wind direction. If orientation of the model is performed with control points widely spaced across the area of stereoscopic coverage of the photographic model as is normal in photogrammetric measurement (Kraus, 2000; Wolf and Dewitt, 2000), the magnitude of the error in rotation orientation will depend on the flying height and the residuals of the X, Y and Z values at the control points. For example, with the 1:5000 scale imagery used for the One Rise More case study in Chapter 7, stereo pair 9648 and 9647 were oriented using 14 XY and 33 Z control points spaced over an area approximately 1063 m across the flight direction and 786 m along the fight direction. The standard deviations of the X and Y control points were given in Chapter 2.7.3; the flying height above ground was calculated by resection to be approximately 736m. Equation 2.7 gives the rotation error based on the mean error in X and Y rotated about the distance to the perspective centre of the image as less than 0.1º. This is negligible for practical purposes in most geomorphological investigations.

$$RotationError = \arctan\left(\frac{\sqrt{0.52^2 + 0.58^2}}{736}\right) = 0.06^{\circ} \qquad \text{Eqn. 2.7}$$

Secondly, there is the error in location. This is particularly important when data from multiple sources are used in a multi-parametric study. Errors in correlation may occur if the error in locating any point specific information is greater than the resolution of the data, which is particularly important in raster databases (Heuvelink, 1998).

Photo-texture is a measure of the variability in reflectivity across the terrain, which can change as a result of minor changes in reflectance with direction, through time and the repeatability of the sampling interval. For example, small scale changes in reflectance values may occur between exposures in adjacent images along an aerial photograph run due to changes in wind strength or the angle of many sub-parallel stems in a grassy slope; these changes may be random in pattern and result in variations in the texture and thickness of any vegetation cover. Vegetation in particular has been shown to affect the ability of automated image matching algorithms implemented within softcopy systems to match image points on adjacent aerial photographs (Gooch et al., 1999).

2.8 Processing DEMs to Generate Geomorphological Maps

Data capture procedures are discussed in Chapter 3 as part of the application of photogrammetry to geomorphology. This section contains a discussion on the resolution of data captured to generate the DEM, and its subsequent processing to obtain morphological and geomorphological attributes.

2.8.1 Defining Data Capture Resolution

Morphological and geomorphological mapping can be carried out at a wide range of scales. The examples used in this dissertation range from rock slopes over 23m high, to steep, mountainous catchments with areas over 10km^2. The choice of imagery used to capture the raw elevation data for the DTM depends on the needs of the project (Read and Graham, 2002; Wolf and Dewitt, 2000) and the resolution of the imagery relative to the size of the landforms to be identified and mapped. Major slope failures disturb the ground surface, exposing bare soil and rock, which often appears as a paler tone than the surrounding weathered rock or vegetated slopes (Lillesand and Kiefer, 1979). The visibility of these features depends on the time elapsed between the date of failure and capture of the imagery (longer elapsed time allowing greater revegetation growth), and the severity of the ground disruption.

The minimum size of a feature identified within a stereo image will depend on the number of pixels occupied. Rengers et al. (1992) introduce the concept of the Ground Resolution Cell (GRC), which is analogous to pixels for remotely-sensed digital imagery. Film-based images demonstrate a higher resolution due to the

mixture of different sizes of silver crystals in the emulsion (Thomson, 2004); Nathani (1990) reports that the effective GRC of a film image is 0.4 of the size of the equivalent digital image at the same flying height and scale; issues of digital image resolution in relation detector response characteristics are examined in Chapter 3. Soeters and van Westen (1996) note that while only 20 to 30 GRCs may be required for identification of high contrast objects, this number may increase to over 1000 for low contrast objects against a similar-toned background. Increasing the number of pixels required to identify and measure an object has an important effect on automated image correlation, which is further discussed in Chapter 3; use of larger correlation windows improves the consistency of correlation, but will also result in an averaging of the height of the included pixels due to loss of the high spatial frequency variations.

Landslides consist of a number of component features (e.g., Figure 2.12a), and successful identification requires recognition of sufficient components to interpret the landform as being due to slope movement processes. Fookes et al. (1991) note that high levels of skill, experience and local knowledge improve the ability of an interpreter to identify slope failures. Methods highlighting specific landform elements e.g., convex landslide crowns, or allowing integration of mapping with 3D visualisation, will improve the quality of interpretations.

The error train created by photogrammetric processing is well-defined (e.g., Wolf and Dewitt, 2000; Atkinson, 1996), and will be evaluated in Chapter 3 in the context of the precision and accuracy (Cooper, 1998) of DEM posts required for terrain modelling applications. The first stage in planning an image capture programme is to determine the imagery necessary to generate a DEM of sufficiently high resolution to generate terrain parameters with suitable resolution for terrain mapping. Carter (1992) and Gao (1997, 1998) have studied the effect of decreasing resolution on the accuracy of terrain attributes derived from a source contour map. Gao's conclusions are also relevant for DEMs generated directly by digital photogrammetry. Both Carter and Gao find that the accuracy of terrain representation increases with decreasing DEM resolution, because the approximation of a continuous surface is better with a smaller grid size, and a finer resolution samples more elevations, thereby better capturing terrain shape. Through studies of soil and fluvial erosion

processes, DEM resolution is shown to have a significant effect on the outcome of model simulations (e.g., Rees, 2000; Schoorl et al., 2000).

The practical use of small grid cells for terrain shape attribute storage and manipulation favours the direct acquisition of elevation data from the terrain as compared to indirect interpolation from contour data. The most obvious source of high-resolution elevation data is from aerial or terrestrial photogrammetry, as ground surveys at the same density would be prohibitively expensive. Hunter and Goodchild (1997) recognise error patterns in DEMs generated by digital photogrammetry, including distinct steps between the boundaries of image patches and rounding errors due to quantisation of the elevation data to integer values. Describing the application of a spatially autoregressive error model to a test DEM to determine the effects of uncertainty in DEM elevation on slope and aspect calculations, they conclude that a worst case consideration of the errors is a useful measure of the reliability of the source DEM, in addition to the normally quoted standard deviation.

In addition to DEM elevations, a further potential source of error is the algorithm used to generate morphometry from adjacent DEM sample posts. Skidmore (1989) reports that, starting from the same DEM, different algorithms for calculating slope and aspect produce results which differ by up to 5º in gradient and 70º in aspect. Using contour map source data interpolated to generate a DEM with 30m grid spacing, Skidmore (1989) notes differences in accuracy between six methods of determining gradient and aspect. He concludes that general linear regression or third-order finite difference methods appear to be optimal for calculating gradient and aspect from a gridded DEM.

Felicísimo (1994) studies the errors in slope attributes derived by a Monte Carlo simulation of errors in a DEM. He concludes that the error affecting the DEMs – expressed as the root mean square error (RMSE) – also affects models derived from the DEM, including gradient, so as to underestimate terrain slopes. The error appears to diminish with increasing relief and consequently gradient. Felicísimo stresses that the minimum quality of the derivative attributes and the consequent allowable error in the source DEM needs to be established.

Li (1992) suggests that the addition of breaklines to a regular grid can reduce the density of measurements, and also gives (Li, 1993a; 1993b) formulae for evaluating three additional precision parameters: average shape, average wavelength around the DEM cell, and the sampling density. Filin and Doytsher (1998) extend the summation of variances to provide a mathematical derivation of error sources.

2.8.2 Processing the DEM

After capture and editing to remove blunders (see Chapter 2.7.3) and holes, the DEM needs to be processed to extract the morphological and where possible, geomorphological entities. McCullagh (1998) notes the usefulness of visualisations of the data for identifying blunders; for example contours with the wrong height attributed will be revealed by a shaded relief visualisation in which they appear as parallel-sided grooves or ridges, and the spikes or holes of wrongly-heighted points. Processing is performed in four stages:

(a) Calculate morphological attributes;
(b) Use morphological attributes to identify feature boundaries;
(c) Convert boundaries to 3D lines and edges;
(d) Add morphological and geomorphological symbology.

The first part of this processing sequence is used to generate parameters in multi-parameter statistical assessments of landslide hazard, (e.g., Carrara et al., 1995). This dissertation discusses the use of particular morphological attributes to identify terrain features that can be used as boundaries of landforms for the purpose of compiling morphological and geomorphological maps.

2.8.3 Feature Extraction

The adequacy of the DEM for extracting morphologic landform components depends on the number of points forming the feature, which in turn depends on the grid spacing as compared to the size of the feature, and the variation in altitude between the points (Tribe, 1991). Different algorithms are required to identify geometric primitives such as planar features and curving landform components (Zhou and Li, 2001). Surfaces are differentiated by the identification of edges between

morphological units (Wood, 1996). Feature extraction algorithms are tested using the simulation model of the landslide in Chapter 5.

2.9 Value of Integrating Photogrammetry into Geomorphology

The value of interpretive landform models such as Figures 2.9 to 2.11 is demonstrated by van Westen et al. (1999), who compare geomorphological mapping and hazard assessments of the same mountainous area prepared by three independent expert teams. The authors found that two teams prepared very similar maps (75% agreement on landslide distribution, approximately 150 landslides); the third team identified only 20 landslides although these features were generally larger than those identified by the other two. A large part of the variation was considered to be due to differing interpretations of the geomorphological evolution of the area. Van Westen's team produced a 3D visualisation of the terrain, with geomorphic interpretation and hazard assessments superimposed. While noting that landslide occurrence maps contain a large subjective element (Fookes, et al., 1991; Cararra et al., 1992), these authors also note some differences of opinion could not be resolved in the short time available during a field visit at the end of the project.

Fieldwork is intensely time consuming, with access and visibility restrictions being common in steeply sloping terrain subject to landslides. Under these constraints, viewing digital versions of product geomorphological and hazard maps within a full stereo model before and after fieldwork would allow an intensive discussion on the nature of the geomorphological evolution of the area in a shorter time, thus making fieldwork more efficient. The studies described in this dissertation examine the potential benefits of this visualisation, coupled with the potential for automating components of the geomorphological mapping process.

The literature reviewed in this chapter demonstrates that the algorithms for morphometric analysis are arguably well-developed, and readily available within raster GIS systems, e.g., ER Mapper, which accesses curvature algorithms described by Wood (1996). The first task in automating geomorphological mapping is to define the shape and boundaries of the landforms. The major landforms associated with landslides have been described (e.g., Figure 2.12a, from Varnes, 1978), which include a prominent convex slope around the crest and sides of a bowl-shaped

hollow, which may or may not remain partly filled with the failed mass of soil and rock. Once the morphological entities have been identified, these landforms need to be defined in terms of the components of geomorphology relevant to the problem, for example, the landslide hazard. The complexities of geomorphological mapping have been reviewed, and these aspects are investigated in relation to a simulated landslide in Chapter 4 and landslides on hillsides in Hong Kong in Chapters 7 and 8.

For use in semi-automated morphological and geomorphological mapping, procedures need to be identified to allow the results of the raster-based morphometric processing to be incorporated into the stereo image processing systems of the photogrammetric systems. This is investigated in Chapter 7.

2.10 Chapter Summary: Automating Geomorphological Mapping

The literature review in this chapter considers the information content and processes required to create morphological and geomorphological maps. These include an initial stage of topographical definition, be it from contours or morphological mapping, followed by an interpretation of landforms based on the shape of the feature and the evidence of geomorphologic processes and materials that can be identified. Automated processing of DTM and DEM data is able to generate raster or polygon maps of topographic attributes, first derivative attributes of gradient and aspect, and second derivative attributes of curvature. Algorithms have been developed that calculate complex terrain attributes based on hydrological continuity and catchment properties; some of these have been used for soil mapping, hydrological and environmental studies. Slope stability is strongly correlated to ground and surface water levels and pore water pressure, the strength properties of soils and weathered rock, and the presence and orientation of discontinuities, and use of these parameters in addition to slope gradient and lithology for landslide hazard assessment is warranted. Enhancement of the geomorphological mapping process can operate though automating components of the manual process, through automated derivation of morphological attributes, and enhanced methods of symbolic mapping. Methods of performing these procedures are tested in Chapters 5 to 9.

Automated and semi-automated geomorphological mapping entails procedures to capture the raw topographic data, process that into a uniform raster dataset of

elevation data, and convert the raw elevation values into 2D and 3D representations of the boundaries between morphological features. The boundaries, forming breaklines in the landscape, need to be symbolised to create simple morphological maps or complex geomorphological maps. The vectors can be draped over a stereo pair of images, and the results viewed in 3D in common with the stereo pair of images. 3D point and line placement is a standard feature of many photogrammetric software packages, and point and line symbolisation is a feature of CAD software. Chapter 3 reviews the increasing use of photogrammetric measurement techniques in geomorphology, initially through analogue methods and with increasing adoption of the more adaptable technologies provided by computer-based analytical photogrammetry (often called softcopy photogrammetry). The combination of CAD packages into softcopy photogrammetry presents a further enhancement that allows stereo viewing of geomorphological maps and to combine the process of 3D point and line placement with geomorphological interpretation.

Chapter 3

SOFTCOPY PHOTOGRAMMETRY FOR GEOMORPHOLOGICAL MEASUREMENT AND MAPPING

Photogrammetry is a remote sensing technique for estimating geometry via 3D point coordinates measured on images instead of direct measurement. Developments in photogrammetry have taken this mature technology beyond topographic surveying and into the realms of 3D modelling and object recognition. This Chapter reviews the main elements of the technology with specific reference to its application to geomorphological measurement and mapping for slope stability purposes.

3.1 The Application of Photogrammetry to Geomorphology

This Chapter begins with a summary of the main elements of analogue and analytical photogrammetry, highlighting the similarities and differences between stereo and multi-image techniques applied to both vertical aerial and close range photography. After a review of photogrammetric applications to geomorphological measurement, the Chapter reviews and investigates the factors affecting the photogrammetric measurement process with particular emphasis on the use of low-cost digital cameras and scanners, subdivided into data sources and photogrammetric processing techniques. While the main landform mapping case studies are described in Chapters 6 through 9, the studies described in this Chapter were carried out to investigate particular effects including calibration of digital and film camera systems and the use of photogrammetric and desktop scanners. Chapter 4 describes studies into some of the properties of area-based automated coordinate measurement routines.

3.2 Aerial and Close Range Photogrammetry: Stereo and Multi-image Models

Cooper and Robson (1996) note that the term *close-range photogrammetry* is used to describe the technique of measurement using photographs taken from distances of less than about 100m, from many different directions, where the camera axis may not be parallel, and with a variety of cameras; camera quality can range from a precisely-quantified *metric camera* with stable internal geometry to *semi-metric*, and *non-*

metric cameras for which there is minimal geometric information available. This differentiates it from *aerial photogrammetry*, in which measurements are made using stereo pairs of photographs exposed with the central axis of a metric camera oriented to approximately vertical and obtained at constant intervals along a flight line (Figure 3.1a). Other characteristics of close range photogrammetry (Cooper and Robson, 1996) include the use of camera positions around and possibly inside an object, where the camera axes can be highly convergent (Figure 3.1c) or irregular (possibly highly variable camera-to-object distances, camera orientations and target centres; Figure 3.1d).

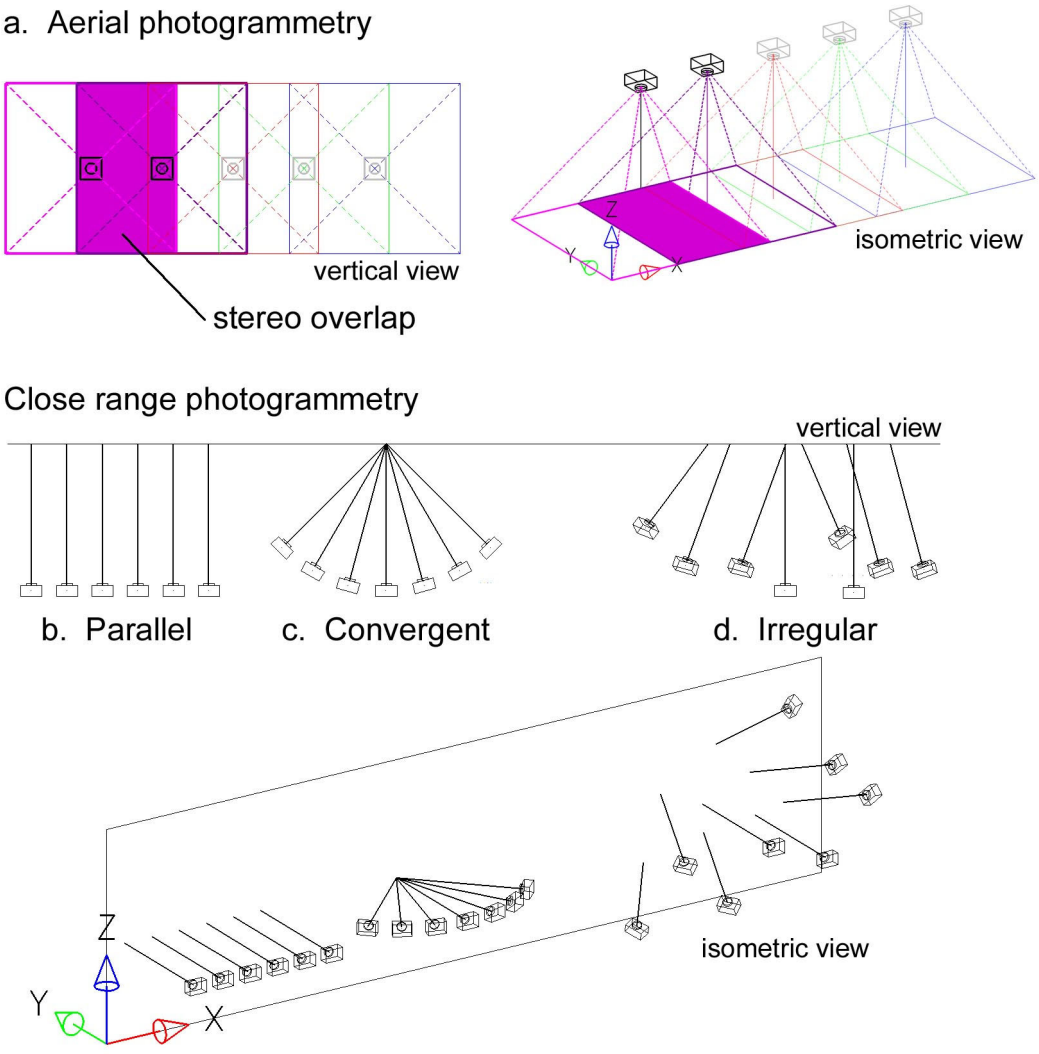

Figure 3.1 Range of camera configurations for stereo and close-image photography

Analogue photogrammetry obtains measurements by duplicating the photographic geometry for a stereopair of images; this ranges from the use of simple parallax bars on paper prints (with an image measurement error of approximately ±0.05mm) to high precision analogue plotters (with an image measurement error in the order of ±0.005mm) which were used primarily for topographic mapping (Slama, 1980; McGlone, 2004). In the latter, the stereo model is created mechanically by orienting two images (usually as film diapositives) mounted on independently-adjustable photo carriers to match the relative orientation of the camera(s) at the time of exposure of the two images. Restitution is limited by the available adjustment in the carriers, usually a few degrees in the omega (X) and phi (Y) axes. Scaling transformations are applied mechanically, with individual point measurement achieved by visually matching two 'floating marks' projected separately onto the surface of each image.

Analytical photogrammetry also uses the relative camera geometries but uses a mathematical model to estimate the ground coordinates of measured points. Consequently, it is more flexible and able to be adapted for a wider range of imagery, including multi-station, non-parallel images. The mathematical model also enables photogrammetric distortions to be applied to other sources of vector 3D data, allowing co-viewing by superimposition within the stereo model.

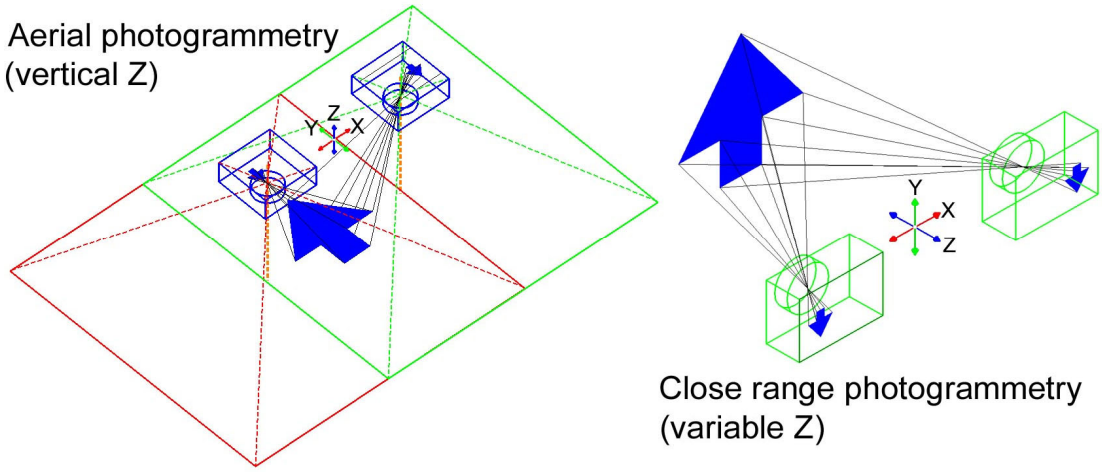

Figure 3.2 Rotation of Z axis for application of stereo image matching in close range photogrammetry

Photogrammetric software systems developed for topographic mapping use a Z axis aligned vertically (e.g., SocetSet, VirtuoZo and uSMART). To enable stereo-assisted automated point measurement for comparison with multi-image photogrammetry, either the conventional near-vertical camera axis constraint used in aerial photogrammetry has to be relaxed, or rotation applied to the coordinate system (e.g., Chandler, 1999). Consequently, within this dissertation, the term *stereo photogrammetry* is used to refer to both conventional vertical, stereo aerial photogrammetry and the quasi-vertical case where measurements are made using stereo observation with the Z axis of the photogrammetric model rotated to approximate the near-parallel lens axes of the two images (Figure 3.2). The dominant factor controlling the application of automated image matching is the similarity of perspective view of the objects, as measurement is achieved by comparison of small patches of each image. *Multi-image photogrammetry* is used here to refer to models generated from co-measurement on three or more images, instead of the conventional 'close range'; automated stereo image matching is not possible due to extreme perspective changes.

The case studies described in this dissertation use photographs taken from <5m to >1000m, which is generally larger than is usual for close range photogrammetry (Cooper and Robson, 1996), and use both stereo and multi-image photogrammetry.

3.3 Operational Comparison of Stereo and Multi-image Photogrammetry for Geological and Geomorphological Applications

The main application for softcopy stereo photogrammetry has been topographic mapping with multiple overlapping models built from stereo pairs; source imagery consists of parallel runs of consecutive, near-equally spaced, near-vertical aerial photographs. When applied to landform mapping, similar opportunities and constraints apply as for topographic mapping (Lane et al., 1993); achievable measurement accuracies depend on the quality of the available imagery (including the camera and lens system, scale and dimensional stability of the image) and ground control. Major differences between the application of photogrammetry for engineering and aerial survey purposes are summarised in Table 3.1 (after Granshaw, 1980, adjusted with consideration of digital photogrammetry).

Table 3.1 Some differences between engineering photogrammetry and aerial survey (extended, after Granshaw, 1980)

Engineering photogrammetry	Aerial (topographic) survey
• Object may have truly spatial characteristics (i.e., Z ≈ X,Y; multi-perspective 3D) • Required accuracy in X = Y = Z • Restricted format likely; possible use of small and medium format, metric, semi-metric and non-metric cameras • Highly 3D shape of object requires imagery with varying position and orientation • Point information dominates • Sub-pixel, automated centring of geometric targets may be possible for all points that require coordination • Small number of images • Site restrictions frequently encountered • Use of glass plates rather than film Note: digital images likely to dominate in future • May be possible to determine some camera parameters with considerable accuracy (e.g., survey of camera station and or camera orientation) • Flexible approach required due to differences between projects	• Relief small in comparison with flying height • Accuracy in Z < X, Y (Note, the increasing use of DEMs for determination of terrain attributes increases the need for similarly accurate Z values) • Entire format usable; high precision, large format, film or digital cameras • Vertical format employed almost exclusively • Images used for plotting as well as point determination • Excluding cadastral surveys, targets may only be used for control, if at all • Large block may consist of several thousand images • Few restrictions other than air traffic regulations • Auxiliary data have limited accuracy, although with onboard GPS systems, this is changing • Standardised approach adopted to reduce processing costs

Most modern softcopy stereo photogrammetry for topographic mapping uses high resolution, high geometric stability scans obtained from large format negatives or diapositives, using standard procedures described in aerial photogrammetry textbooks, e.g., Kraus (1997; 2000), Read and Graham (2002), Schenk (1999), Mikhail and others (2001), Kasser and Egels (2002), and Wolf and Dewitt (2000).

Warner et al. (1996) discuss the use of small format cameras for aerial photogrammetry, and Graham and Koh (2002) extend the discussion to focus on the

growing field of digital photogrammetry. The latter two groups of authors note that the major constraint on the use of small and medium format film and digital imagery for topographic mapping of large areas is the areal coverage of each frame; the need to process large numbers of images may limit the cost-effectiveness of using lower-cost camera equipment. While this constraint may hold true for regional geomorphological mapping, measurement of smaller-sized landforms or analogue (physical) geomorphological models would not be so constrained.

The constraints listed in Table 3.1 are more readily handled by mathematical models within analytical photogrammetry (Ghosh, 1988) than the physically-based analogue technology. Engineering photogrammetry has developed from the need to measure discrete, 3D objects to a very high accuracy with images obtained from a wide range of camera stations and orientations (Cooper and Robson, 1996), issues that are reflected in many geomorphological measurement problems.

Petrie (1990) identifies three significant developments in photogrammetric technology:

(a) Integration of graphics workstations with graphics-superimposition and stereo-superimposition;
(b) Enlarged photo stages to handle 25x50cm Large Format Camera images;
(c) Addition of *correlators* providing digital image matching for automated height measurement.

Petrie (1990) notes that stereo-superimposition of the plotted detail onto the stereo model allows visual checking of the measurement process (e.g., Beerenwinkel et al., 1986). This requires plotted detail to be reprojected onto each image, incorporating all distortions due to the optical system and terrain elevation, and must be performed in real-time to allow parallax-free stereo viewing. While Petrie (1990) reports that this development was incorporated in only the high-end workstations as of 1988, by 2004 this feature was available also in several mid-range softcopy systems (e.g., uSMART; VirtuoZo) as well as a standard feature in high-end systems (e.g., Z/I and SocetSet). Stereo-superimposition has great potential for visually-interactive applications such as geomorphological interpretation and mapping (Table 3.2), and is investigated further in the case studies of this dissertation (Chapters 6 to 9).

Table 3.2 Comparison of types of photogrammetry for geomorphological purposes

	Stereo photogrammetry	Multi-image photogrammetry
Automation of point measurement	*Advantages:* • Increases rate of DEM measurement • Use of adjacent DEM post to aid identification of point. • Sub-pixel measurement of fiducials and correlated ground features. *Limitations:* • Possible incorrect height measurement for steep terrain due to size of correlation patch. • Larger numbers of false matches if correlation threshold is set too low.	*Advantages:* • Once images have been oriented, epipolar lines can be superimposed to aid identification of corresponding feature. • Auto drive to feature after image orientation and measurement of point on two photos (including hidden points). • Sub-pixel measurement of fiducial and ground pre-marks. *Limitations:* • Full feature matching not implemented due to extreme changes in feature geometry.
Measurement viewing perspective	*Advantages:* • Stereo view - allows visual perception of landform during measurement. • Stereo-superimposition of results within 3D model. *Limitations:* • Areas of 'dead ground' without stereo coverage, obscured on one or both images.	*Advantages:* • Images from a wide range of perspectives can be incorporated. *Limitations:* • No automated stereo view - visual perception of landform depends on shape-from-shading (Limited stereo viewing can be achieved by manual window adjustment).
CAD output / export	• Available; CAD manipulation within softcopy routine, including stereo placement of symbolically-enhanced points and lines.	• Available export formats: DXF, 3D modelling and visualisation.
3D Modelling	*Advantages:* • Warping of 2D + Z = 0 vector files to DEM. • Stereo visualisation of vector mapping overlaid on stereo photo model. *Limitations:* • No on-the-fly warping of raster images	*Advantages:* • Surface texture mapping and visualisation. *Limitations:* • Limited stereo viewing of vectors (anaglyph of 3D model).

In addition to stereo-superimposition, Table 3.2 lists other developments and features of stereo and multi-image softcopy systems that present opportunities for application to geomorphological problems; these are automated point measurement, CAD output and 3D modelling. Opportunities and limitations of these component technologies have been investigated during the application of photogrammetric technologies to the problem of geomorphological measurement and mapping in steep terrain in the case studies presented in this dissertation.

The main contrasts between stereo and multi-image softcopy systems relate to the visual perception of the terrain model and the related feature of automated image correlation. Alternative methods have been implemented within both technologies to assist initial orientation of the images into a photogrammetric model and automated driving of the cursor (i.e., point of reference) to pre-defined coordinates; these facilities will enhance the ease of use of photogrammetric software products and bring them into further use by the geomorphological community and others.

3.4 Examples of the Application of Photogrammetric Techniques to Geology and Geomorphology

API (see Chapter 2.1.1) and photogeology are widely used in geology and geomorphology. These techniques are often used for terrain assessment in slope stability investigations, as the synoptic view provided by vertical or oblique stereo photographs allows assimilation of the inter-relationships between groups of landforms that may be difficult to observe on the ground (e.g., Norman, et al. 1975). While API is normally used for geomorphological mapping (Chapter 2.1.1), the results are often produced as annotated sketch maps based on the visual transfer of observed details onto either topographic base plans, aerial photographs, and aerial photographs rectified to produce orthophotos. Figure 3.3, after Kalaugher et al. (1987; Grainger and Kalaugher, 1987) is an example of a geomorphological sketch map for landsliding along coastal cliffs generated by API of vertical and oblique aerial photographs taken between 1928 and 1986. The transition from qualitative observations such as API to quantitative process modelling requires landform measurement, and it is important to recognise the accuracy limitations of the measurement techniques. Fryer et al. (1994) warn that errors in source height data can be propagated through to landform process models which may render them

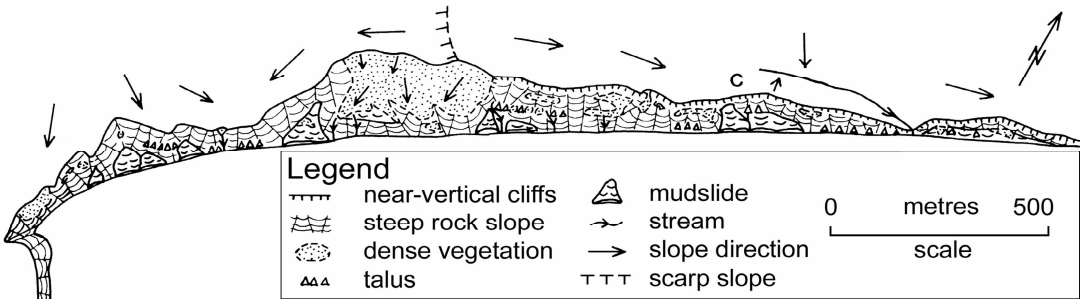

Figure 3.3 Geomorphological sketch map compiled by API (after Kalaugher et al., 1987)

inaccurate. Using a simulated example of a mapping project, the authors demonstrate how the variances of photogrammetric measurement are propagated through least squares estimation to allow an examination of the accuracy of elevation results; this is examined in greater detail in Chapter 4.

There are many examples of the use of analogue and analytical photogrammetry applied to geological and geomorphological problems (e.g., Chandler and Moore, 1989; Lane et al., 1993; 1998; Lane and Chandler, 2003). Investigations of geomorphological processes include analysis of the rates at which they act; where the action of a single or combination of processes result in changes of landform shape over time, the quantification of those changes can provide a significant contribution to the analysis. Photographs provide a permanent record of the terrain, and methods to extract and compare shape information from a variety of historical photographs is of immense value. Chandler (1989; Chandler and Cooper, 1989) notes that the satisfactory use of historical photographs requires solution to four problems:

(a) Obtaining adequate coverage of the features both spatially and temporally (which is likely to be improved if oblique and close range photography are available);
(b) Absence of conventional ground control;
(c) Unknown internal geometry of the camera;
(d) Definition of a common datum for all the epochs represented by the photography.

Review of the historical development of photogrammetric applications in geology and geomorphology demonstrates that these issues have been overcome to varying

levels of accuracy, and that the solutions have allowed advances in geomorphological measurement and analysis. Photogrammetric measurements consist of 3D point and line data that can be further processed to generate derivative products, including (extended after Chandler and Cooper, 1989):

(a) Contour plans;
(b) DTM of Difference (contours or grid determinations of volume change);
(c) Vertical derivative (gradient maps);
(d) Horizontal derivative (aspect maps);
(e) Systems analysis (Chorley and Kennedy, 1971; input and output analysis; volumetric sediment budget);
(f) Quantitative evolutionary models (e.g., Chapter 2.5);
(g) Movement vectors.

DTM/DEM processing options are examined in Chapter 3.7 after a review of existing Earth science photogrammetric applications and the fundamentals of analogue and analytical photogrammetry based on geological examples.

3.4.1 Analogue Photogrammetry

Terrestrial, oblique and vertical aerial photographs have long been used to obtain qualitative and quantitative estimates of landform shape and position, especially in hazardous and extreme environments. As early as 1897, Finsterwalder (quoted in Chandler and Moore, 1989) used photogrammetric techniques to study glacial movement and these techniques continue to be of use in such a difficult environment for field measurement (e.g., Stirling, 1982; Jania, Lipert and Mechlinski, 1984, Collin and Chisholm,1991). Mark and Seltzer (2005) compare a 30m DEM of the surface of the Queshque glaciers in the Andean Cordillera Blanca generated from vertical aerial photographs taken in 1962 and processed using a Wild B8 analogue plotter (Brecher, 1986; Brecher and Thompson, 1993), with a recent DEM generated from differentially-corrected GPS measurements at approximately 100m spacing.

As an example of the application of simple photogrammetric techniques in a similar glacial environment, Goodrich (1982) uses photographs taken of the toe of a glacier with a calibrated single lens reflex (SLR) 35mm film camera to demonstrate that the design accuracy of 0.3m from a range of 30m could be achieved under difficult field

conditions using low cost equipment, including measurements on paper enlargements made using a parallax bar. He concludes that accuracy limitations achieved during this project were largely due to small mis-orientations of the camera during the initial set up phase, as the measurements were processed assuming parallel camera axes.

In an investigation of the erosion of 25 stream banks over a two-year period, Collins and Moon (1979) compare measurements obtained using film stereo pairs taken with a Zeiss SMK 120 stereometric camera, where the camera axis was located sub-horizontally and approximately perpendicular to the steeply-sloping landforms under study. Parallax measurements were obtained by digitising landmarks and ground surface features on a manual stereo-digitiser with a precision of 0.018mm; the quoted worst-case error in object-space point measurement at a range of 18m was 18.2mm, but the overall accuracy was estimated as 2mm at a range of 5m to 12mm at a range of 20m. Measurement of the oriented stereo pairs is reported to be similar to contouring on conventional topographic photogrammetry, in relation to distance from the camera. The authors stress the benefits of the measurements being made by a geomorphologist, who was able to interpret the stereo model to identify ground features for measurement relevant to the nature of the erosion study.

Kirby (1991) describes the measurement of ground surface textures using stereo pairs of vertical photographs taken from an altitude of 1.5m using a pair of Hasselblad MK70 cameras mounted on a horizontal gantry between two surveying tripods. Ground control was obtained by theodolite survey of six nails fixed within the stereo coverage; height control was provided by an aluminium block and levelling to a precision of 0.01mm. The resulting plots show the dimensions and ground disposition of gravel and boulders. Lo and Wong (1973) and Welsh and Jordan (1983) also used vertical camera arrangements for measuring gully and stream bank erosion.

Within the field of slope stability investigations, Lo (1978) describes the preparation of a geomorphological map of the Po Shan Road landslide in Hong Kong using a CP1 analogue plotter. Resulting in 67 fatalities, the failure on 18th June 1972 was about 260m long and 60m wide, with an altitude difference between the crown and toe of about 155m. Mapping was performed at 1:1000 scale using a diapositive vertical stereo pair of vertical aerial photographs taken with a Wild RC10 large

format camera at an altitude of 610m, giving a nominal photo scale of 1:4000. The extreme elevation differences within the stereo model were close to the limits of the mechanical measuring system. While reporting that the standard error in heighting achieved was ±1.21m or 1.98‰ of the flying height, with a similar planimetric accuracy (1.81mm at 1:1000 scale), Lo notes that this was less accurate than a value of 0.2‰ of the flying height quoted elsewhere for the CP1 plotter (Thompson, 1972) for small scale models (1:20,000) with lower relief. The CP1 was used to plot the boundaries of landslide, terrain, roads and building features, including the distribution of vegetation, bare soil, wet soil, boulders, streams, parts of a fallen building, and road, wall and slope structures. Lo also demonstrates the application of simple 3D modelling based on a DTM to visualise the shape of the failure scar and debris.

McConchie (1986) used an analogue stereoplotter and vertical aerial photographs to monitor earthflows in New Zealand, although Chandler and Moore (1989) comment that these methods '*lack the flexibility and rigorous accuracy obtainable with analytical photogrammetry*'.

Engineering surveys commonly require highly accurate point information for use in numerical design or volume measurement, and early examples of the application of terrestrial photogrammetry to geological and geomorphological studies concentrate on these aspects. For example, Wicken and Barton (1971) determined the orientation of planes of weakness (i.e., cleavage, joint sets, shear zones and fault surfaces) in an open pit slope, with measurements taken using a Wild P30 phototheodolite; the camera was aligned to the horizontal and vertical and the film plane oriented parallel to the rock face. Camera stations were positioned to give base:distance ratios between 1:1 and 1:5; at least three measured points were dispersed across each identified plane to allow well-conditioned triangles to be defined; use of four or more points allowed residuals to be estimated. Although, with a photo scale of 1:400, the worst case residuals of 0.12m in X and Y, and 0.06m in Z were attributed to movement of the targets due to frost heave, the authors report this was within the required accuracy for slope stability analysis.

To investigate a physical model involving rock slope failure, Barton (1971; Wicken and Barton, 1971) used a stereo-comparator to measure deformations in the order of

2 to 3mm on a 2.4m long by 1.2m high model of a rock slope to an accuracy of ±0.15mm; in this case, the single camera station was fixed 2.4m from the model, and movement was detected by measuring the parallax between corresponding points in photographs taken at different times during the experiment. A stable glass grid at the front of the model and rock features that had not moved appeared without parallax in the 3D visualisation.

With respect to the use of analogue photogrammetry in geomorphology, Chandler and Moore (1989) and Lane et al. (1993) note the limitations of rigid camera perspective geometry, as demonstrated by the examples described above. These would be more easily overcome if the same photographs and image data were processed within an analytical softcopy system where the individual camera station coordinates and rotations are calculated by space intersection, and mathematical models of systematic distortions can be included.

3.4.2 Analytical Photogrammetry

Dixon et al. (1998) and Lane et al., (1993) identify the principle advantages of analytical photogrammetry over analogue technology as:

(a) Non-destructive and non-invasive. Measurements can be replicated without contact except for ground control, and even this may be obtainable by remote methods;
(b) Photographic record is preserved, allowing further measurement;
(c) Same points can be revisited automatically (with adequate ground control), allowing monitoring of changes through time;
(d) Relationships between height and non-morphological attributes can be observed and assessed;
(e) 3D measurement, allowing for constraints imposed by image quality, perspective and ground control;
(f) Incorporation of different image formats and compensation for distortion that would not be possible under analogue conditions.
(g) Data captured in digital form for rapid transfer into a GIS and other computer analysis packages.

While items (a), (b) and (e) also apply to analogue photogrammetry, the majority of these characteristics also apply to analogue photogrammetry.

Fraser (1983) quantifies the accuracy attainable in analytical photogrammetry with reference to a simulated low-level vertical aerial photogrammetric survey of the summit of Turtle Mountain in Canada, carried out to determine if such a survey could meet the precise requirements for monitoring differential movement across a remote mountain summit with a history of large scale slope failure. The results of his sensitivity analysis demonstrate that analytical restitution of low level (e.g., an image scale of 1:2100) vertical aerial photography could provide a measurement precision within the 1cm allowable error required by the specifications; Fraser and Stoliker (1983) and Fraser and Gruendig (1985) present results from the subsequent successful photogrammetric monitoring exercise constructed using 24 survey points which demonstrate that the specified monitoring accuracies could be achieved..

In an example of a long-term erosion study, Oka (1998) compares the results from aerial photogrammetry on vertical stereo pairs at scales from 1:25,000 to 1:10,000, compiled using an analytical stereoplotter, to estimate ground elevations over a 19-year period with direct measurements made at erosion pins fixed into the ground. The terrain consisted of deeply weathered granite slopes with gradients up to 45° and subject to rainfall-induced instability, gully erosion and deposition. With measurements were made at 20m grid intervals and between the epochs 1969, 1978, 1983 and 1988, elevation changes ranging from +10m to -10m were measured with an estimated accuracy of 0.5m.

Chandler et al. (1987; Chandler and Moore, 1989) describe an investigation of actively eroding road cuttings using photographs taken with Jenoptik Jena UMK 10/1318 and Wild P32 metric cameras, and analytically restituted using purpose-written software. Point measurements made from the images using a stereo digitiser yielded ground coordinates with a precision of 0.05m, which were used to generate slope profiles and contours. A comparison of ground positions between the two measurement epochs, May 1985 and May 1986, revealed displacement of 2.2m vertical and 3.0m horizontal in the upper part of one of the debris slides.

Klingmann and Blackwell (2003) use the PC-based DVP analytical photogrammetry softcopy system (Gagnon et al., 1990) to measure the location and orientation of rock surfaces on open pit walls. The authors note that the use of photogrammetry for measuring rock slope orientations in open pit mines is preferred over hand measurements, because the cameras can be mounted away from the potentially unstable rock face, more measurements can usually be made within a given time than structural mapping by hand, and thirdly, the photographs provide a permanent record that can be accessed for additional information if required. However, the point is made that the stereo image from small sized photographs may be so poor that the pointing precision for a specific target may be low, resulting in loss of accuracy.

3.4.3 Automated and Semi-Automated Photogrammetry

As noted in Chapter 2, process models continue to form a strong research direction in geomorphology. Amongst others, Lane (e.g., Lane, 1994; Lane et al., 2005; Butler et al., 1998; 2002) has been instrumental in extending the application of close range photogrammetric techniques to the quantification of fluvial erosion and transport processes in stream channels. These include studies at field sites and on sediment models in laboratory flumes. In a reflection on his work on the enigmatic problem of roughness (affecting water flow over stream beds and soil surfaces), Lane (2005) argues that high precision surface models, such as those determined by close range photogrammetry, will allow the development of new concepts such as numerical porosity (Lane et al., 2004) that present an emerging solution to an older geomorphological and hydrological problem. The capture of high resolution, high precision surface models requires automated or semi-automated methods of point capture due to the large number of points needed to effectively model the form of complex surfaces. While the new technologies of airborne and terrestrial laser scanning present opportunities for capturing very large clouds of 3D point data (e.g., French, 2003), there will continue to be situations where the use of photogrammetry, particularly analytical photogrammetry of digital images, will provide cost and or availability benefits over the use of lasers. One example is in the incorporation of historical photography into a model, as laser scan clouds cannot be generated retrospectively (Dixon, 1998).

Following a comparison of point measurement techniques within analytical photogrammetry applied to landform measurement, Bailey et al. (2003) conclude that automated methods can generate data with similar quality to traditional manual photogrammetric techniques provided that standards of adequate ground control and sensor calibration are met. The tests were carried out using 1:4000 scale vertical aerial photographs taken with an aerial camera fitted with a 152mm lens, of Maiden Castle in Dorset, UK; the first test compares a DEM prepared from manual height measurements by an experienced operator using a Kern DSR 14 and AP32 and Kork software, with check points obtained by differential GPS. When the analytical stereodigitiser was automatically driven to a set of 400 GPS points, the mean error was 0.33m with a standard deviation of 0.78m. A second measurement exercise involving the operator manually measuring over 42,000 points to produce a representative DTM, generated a mean error of 0.49m and a standard deviation of 1.10m; maximum errors were +2.9m above and -3.2m below ground. The authors note that the landform includes large horizontal areas of grassland and steep embankments, making the whole landform difficult to measure photogrammetrically. A second test performed using stereo correlation of image pairs was performed using the LH Systems Socet Set software and five strategies for image correlation, 'automatic', 'steep', 'steep plus', 'flat' and 'adaptive', which selects the most appropriate strategy according to the nature of the elevations being recorded. All strategies produced a small number of large errors, but the standard error was small. The authors note that editing of the data set would normally be carried out in a production or research environment to identify and eliminate the largest errors. Both manual analytical and automated measurement generate similar results for DTMs generated from a small number of measurement points, however, the automated technique has considerable speed advantages for the collection of high density DTMs.

The results of the studies carried out by Bailey et al. (2003) demonstrate the importance of quality control on both manually and in particular on automatically-generated DEM points. This is supported by studies carried out as part of this dissertation (Chapters 4, 7 and 9). One of the significant advantages of softcopy systems is that measured points and vectors can be draped dynamically across the stereo image, which greatly enhances an operator's ability to rapidly identify

erroneous points, which appear as spikes or pits when the triangulation is displayed in 3D.

Automated DEM extraction techniques include both fully automated systems where ground elevations are measured on a pre-defined grid, and semi-automated systems where the points are selected manually, but with the cursor maintained at the ground surface by image matching, forming a terrain-following cursor. While stereo observation can limit the number of grossly mis-measured points in semi-automated systems, no such visual control exists during the measurement phase of fully automated point measurement, although techniques including post-processing stereo observation and shaded relief models can be used to identify potentially erroneous points for editing. Gooch and Chandler (2001; Gooch et al., 1999) have proposed a Failure Warning Model to assist the identification of gross errors; multiple, independent, overlapping DEMs are compared, with small variations in elevations being averaged, but points with variations exceeding a specified threshold are rejected. Fox and Gooch (2001) have demonstrated this approach for partially glaciated terrain in Antarctica, allowing the various terrain elements to be divided into areas of "high accuracy" and "low accuracy", with areas of highly variable elevations being regarded with suspicion and highlighted for manual checking.

Lane et al., (2000) have examined some of the influences of various parameters used to control image correlation by stereo-matching (Dissart and James, 1995) for the measurement of DEMs for complex landforms. Parametric influence is important, as various algorithms are used to determine the goodness of fit of two dissimilar patches extracted from the stereo imagery; the algorithms do not have the benefit of human perception as used in manual stereo point placement with the consequent possibility of false correlations. Feature-based image matching uses edges to enhance the probability of correct matching between the image patches; (Kang et al., 1994) note that while this procedure is very effective in measurement of regular buildings with structural features marked by high contrast, linear edges, it is less effective in undeveloped terrain where image boundaries tend to be predominantly diffuse and irregular in shape. Under conditions without clear edges, including open hillsides common in the mapping of landslides on natural terrain, the success of the image correlation will depend on the availability of adequate, repeatable image texture.

The measurement of rock slopes is more likely to generate better image correlations than open hillsides, particularly where linear edges are present. Lane et al. (2000) conclude (p. 818) that '*for rough natural topography, further research is required to improve understanding of how area-based correlators work, notably in the vicinity of breaks of slope*'. The effects of image texture on area-based stereo-matching is investigated further in Chapter 7.

3.4.4 Multi-image Photogrammetry

The major difference between conventional topographic mapping and terrestrial applications is in the range of orientations of the target surfaces relative to the camera positions. For example, if the vertical sides and roof of a building need to be surveyed for architectural or engineering purposes, all the required surfaces may not be visible in either a stereo pair or set of photographs taken along a single, straight photographic run; similar problems of visibility apply to geomorphological applications, for example where the terrain may include steep rock faces, narrow gullies or landslide scars.

Multi-image photogrammetry has been widely used for architectural surveys (Dallas, 1996; Grussenmeyer et al., 2002) and when coupled with fully-automated target identification (e.g., Fraser and Edmunson, 2000; Hattori et al., 2002), it has been used for construction of 3D models of objects such as cars and aircraft, where the flexibility of imaging geometry needs to be greater than for wide area topographic mapping. Corresponding points identified on at least three photographs are processed in a bundle adjustment to estimate object coordinates (Granshaw, 1980). These techniques offer potential benefits to geomorphological applications where the object being measured consists of surfaces with a wide range of orientations, and have been employed in the case studies described in Chapters 5, 6 and 7. These can include discrete objects ranging in size from gravel to boulders, and to irregularly-shaped landforms including landslide scars, rock slopes and cave systems. Heritage et al. (1998) used this technique to estimate the morphology of four gravel bars ranging in size from $10m^2$ to $100m^2$ in two braided river beds. Between 30 and 50, 15x15cm, high contrast, flat targets marked with a quartered-diamond pattern, were distributed across the surface of each gravel bar and six photographs taken with a 35mm film SLR camera. Processing with the RolleiMetric close range digital

workstation (Rollei, 2005) yielded a mean error of ±0.015m, when compared with a tacheometric survey.

Fraser (1998) describes the use of automated image measurement in industrial situations ranging from the measurement of helicopters to pies and pastries, and broadly classifies 3D photogrammetric modelling systems into two applications domains. These are (i) high accuracy dimensional measurement in industrial manufacturing and large scale engineering, and (ii) low to medium accuracy architectural, archaeological and general visualisation applications. The use of multi-image photogrammetry for 3D visualisation of landslides as described in Chapter 8, as well as the majority of field and laboratory-based geomorphological applications, would fall into the second category; however, there will be situations where high precision would be required in measurement of some geomorphological processes, where the more precise photogrammetric configurations would be more appropriate.

3.5 Photogrammetric Operating Principles

Textbooks devoted to close range photogrammetry often also cover topics related to machine vision (e.g. Atkinson, 1996; Castleman, 1996), with extensive discussion of signal processing in addition to the geometric constraints of the imaging systems. The principles of stereo and multi-image photogrammetry are discussed in Chapter 3.5.1 with regard to the characteristics identified in Table 3.1.

3.5.1 Common Principles

Photogrammetric measurement uses the geometric relationship between the 3D object space coordinate system and 2D image space coordinate system. These are described in many photogrammetry textbooks (see Chapter 3.3); the fundamentals are also described in the geomorphology literature (e.g., Chandler and Moore, 1989).

The spatial relationship between the camera stations and object points is determined by the *relative orientation*. For *absolute orientation*, the coordinates of *ground control points* are applied to the geometric model. These two stages can be applied separately or as a combined process, as in the *bundle adjustment* technique described

by Granshaw (1980), in which the camera parameters are derived from the observed coordinates using the unified method of least squares (Mikhail, 1976).

In image space, the perspective centre of the model lies at the near nodal point of the camera lens, and the Z axis is perpendicular to the image plane. Points in object space (*X, Y, Z*) are projected in a straight line through the perspective centre (X_0, Y_0, Z_0) to form a homologous point in the image space (*x, y, -c*), where *c* is the focal length of the camera. This projective transformation, defined by two collinearity equations (Equations 3.1 and 3.2), forms the basis for the geometry, with the spatial displacements of each of the X, Y and Z axis multiplied by the nine elements of the rotation matrix that defines the relative orientation of the two coordinate systems.

$$x = \frac{- c[r_{11}(X - X_0) + r_{21}(Y - Y_0) + r_{31}(Z - Z_0)]}{[r_{13}(X - X_0) + r_{23}(Y - Y_0) + r_{33}(Z - Z_0)]} \qquad \text{Eqn. 3.1}$$

$$y = \frac{- c[r_{12}(X - X_0) + r_{22}(Y - Y_0) + r_{32}(Z - Z_0)]}{[r_{13}(X - X_0) + r_{23}(Y - Y_0) + r_{33}(Z - Z_0)]} \qquad \text{Eqn. 3.2}$$

Measurement of an object's location on two images is required to form a unique solution for the ground coordinates to be determined. In addition to the *X* and *Y* coordinates of the object point on each of the two images, the three elements of the rotation matrix and the perspective centre for each image are required for computation of the 3D coordinates; these factors form the camera parameters and determination of these constitutes the *external orientation* of the image.

The orientation of the camera in object space can be defined in several alternative conventions, two common forms being Tilt, Swing, Azimuth and Omega, Phi, Kappa (ω φ κ). Tilt is the angle between the optic axis of the lens, the exposure (camera) position, and the vertical and which forms the Principal Plane; swing is the angle in the image plane between the Principal Plane and the image coordinate system, and azimuth is the rotation of the Principal Plane relative to the ground coordinate system. Rotations in the Omega, Phi, Kappa convention refer to rotations about the *X*, *Y* and *Z* axes respectively. If these rotations M_ω, M_φ, and M_κ respectively, the 3 by 3 rotation matrix M is obtained by:

$$M = M_\omega M_\varphi M_\kappa \qquad \text{Eqn. 3.3}$$

where

$$M\omega = \begin{bmatrix} 1 & 0 & 0 \\ 0 & \cos\omega & \sin\omega \\ 0 & -\sin\omega & \cos\omega \end{bmatrix}, M\phi = \begin{bmatrix} \cos\varphi & 0 & -\sin\varphi \\ 0 & 1 & 0 \\ \sin\phi & 0 & \cos\phi \end{bmatrix}, M\kappa = \begin{bmatrix} \cos\kappa & \sin\kappa & 0 \\ -\sin\kappa & \cos\kappa & 0 \\ 0 & 0 & 1 \end{bmatrix}$$

Eqn. 3.4

The elements of the rotation matrix M are applied in the collinearity equations (Equations 3.1 and 3.2) in terms of $r_{(row,\ column)}$.

The geometric relationship between the image plane and the camera lens based on a central perspective projection is defined by the focal length of the lens and fixed positions on the image plane; together these constitute the *inner orientation*. Discrepancies between the ideal central perspective projection and a real imaging system form systematic errors that can be modeller and corrected through the process of *camera calibration* (see for example, Fryer, 1996, Wolf and Dewitt, 2000).

In a film camera, the fixed positions of the camera body are transferred onto the image either by fiducial marks projected onto the image, or by extrapolation of the edges of the image frame. No specific fiducial marks are needed in a digital camera, as the imaging array is located in a fixed position in relation to the camera body, and the corners of the array serve as the fiducial marks where these are required by the photogrammetric software; the stability of the charge-coupled device (CCD) array in the camera body should always be checked, as Fraser et al. (1995) report an estimated 0.3mm movement of the CCD in a Kodak DCS460 digital camera when rotating the camera upside down, while in other tests (e.g., Shortis et al., 2001), although no discernable CCD movement is noted. No CCD movement was identified during calibration of the four small format digital cameras used in the studies carried out for this dissertation.

An additional parameter that is commonly included in the calibration is the position of the optic axis relative to the centre of the camera lens system; this is termed the Principal Point of Autocollimation (PPA; usually x_p, y_p or x_0, y_0; also called the Principal Point of Symmetry, PPS). The fiducial centre is called the Indicated Principal Point, often abbreviated to Principal Point.

In addition to the focal length of the lens, there is an angular variation in the angle of incidence of the incoming light rays which is due to radial lens distortion δr (Cooper

and Robson, 1996) and is often expressed as a polynomial function (Equation 3.5) of the radial distance *r* from the point of symmetry of the lens.

$$\delta r = K_1 r^3 + K_2 r^5 + K_3 r^7 \qquad \text{Eqn. 3.5}$$

where K_1, K_2 and K_3 are the three polynomial coefficients.

While the amount of radial distortion in large format metric cameras built around 40 years ago is less than 6μm up to a radial distance of 135mm from the principal point (e.g., Wild RC10 camera serial number 15Ag141 with 151.96mm lens; Hunting Surveys, 1964), this has reduced to less than 2μm up to a radial distance of 148mm for the RC30 camera of the 1990s (Wild RC30 serial number 15/4 UAG-S 13221 with 152.79mm lens). Read and Graham (2002) note that radial distortion can be considerably larger for small format cameras; this is particularly significant, as the size of either the film frame or digital sensor array is very much smaller than the image size captured in large format metric cameras. Chandler et al. (2005) report radial distortion curves for a Nikon Coolpix 3100 reaching 165.7μm at a radial distance of 3.5mm, where the sensor dimensions are 5.27 x 3.96mm (DPReview, 2004); this can be restated as a maximum distortion near the edges of the image of approximately 64 pixels in the X and Y axes. In the present study, the radial distortion results for a Canon D10 camera fitted with a 28-70mm zoom lens and set at the 28mm focal length are given in Figure 3.4; the maximum distortion near the image edges is 710μm at a radial distance of 13.66mm, approximately 95 pixels on each of the X and Y axes.

Other parameters include decentring distortion caused by slight mis-alignment of the lens elements, as well as scale variation between the X and Y spacing of the pixel centres and non-orthogonality in the X and Y axes of CCD array (Fryer, 1996; Fraser and Edmunson, 2000). Total decentring distortion is given by:

$$P(r) = (P_1^2 + P_2^2)^{\frac{1}{2}} r^2 \qquad \text{Eqn. 3.6}$$

where P1 and P2 are the radial and tangential components of decentring distortion. This is commonly an order of magnitude less than the size of the radial distortion.

While close range photogrammetric software typically is able to accommodate complex camera models, the amount of camera calibration information that can be incorporated into stereo-based systems may be much less. This is because such

complex calibrations have been unnecessary due to the high quality of large format aerial mapping cameras; this aspect is being addressed by the software companies, sometimes in response to customer requests; for example, since 2005, the developers of the uSMART photogrammetric software used extensively in this study have incorporated a routine that allows use of camera calibration data in a format directly generated by the PhotoModeler package, also used extensively in this study.

Fraser (1997) notes that, although methods such as self-calibrating bundle adjustment have been developed for the recovery of complex interior orientation parameters, e.g., the ten parameter model implemented in Australis software (versions 5 and 6), and eight parameters in PhotoModeler (version 5), the factors limiting application of these models in analytical photogrammetry using low cost consumer and 'prosumer' grade non-metric cameras are (i) geometric stability of the camera and lens system, and (ii) unflatness of the CCD array.

Lichti and Chapman (1997) investigate an alternative method of camera calibration, using an area-based finite element method (FEM) to model systematic distortion at the film plane, concluding that this method is capable of defining the elements of interior orientation to a similar magnitude as polynomial-based methods; although SmartTech have included an area-based algorithm in their calibration routine for the uSMART system (SmartTech, 2007), this has not been used in this dissertation. While the area-based methods will assist in the systematic corrections due to the fixed variations due to CCD unflatness, they will be no more successful than self-calibrating bundle adjustment methods when faced with the problem of geometric instability due to relative movement between the camera body and the lens, and between elements within the lens. Temporary or permanent fixing of moveable lenses should be considered where practical, and single focus lenses are preferred over zoom lenses.

3.5.2 Variations in Calibrated Focal Length

Three camera calibrations were performed on a Canon EOS D10 camera fitted with a 28-70mm zoom lens in the indoor camera calibration facility at Curtin University of Technology. Australis software (version 6.0; Fraser and Edmunson, 2000) was used to perform the calibration in all three cases. These calibrations were carried out with

the camera focus set to (i) 5m, (ii) infinity (both with the autofocus disabled), and (iii) autofocus at a range of approx 3m. These gave different values for the focal length of 28.841mm, 28.949mm and 28.739mm respectively, indicating the variable focal length of the zoom lens. In addition, a field camera calibration was performed at Boya Quarry (Chapter 6) also using Australis software, on the control points marked on 58 images captured along one straight and one curved run to check the laboratory calibrations. This gave a focal length of 29.049mm for a focal distance of 42m, with similar radial distortions to the indoor calibrations (Figure 3.4a and c).

The indoor calibration autofocus results produced a higher radial distortion than either of the other two indoor calibrations with pre-set focal lengths, and for the field calibration (Figure 3.4a and c). When used in autofocus mode, especially for planar surfaces oriented at highly oblique directions to a camera lens axis as used for the calibration photography, the autofocus may set the focus to either close or distant parts of the target. With the case of the indoor calibration wall, this could vary from 3 to 6m. This highly variable focal distance is undesirable for camera calibration.

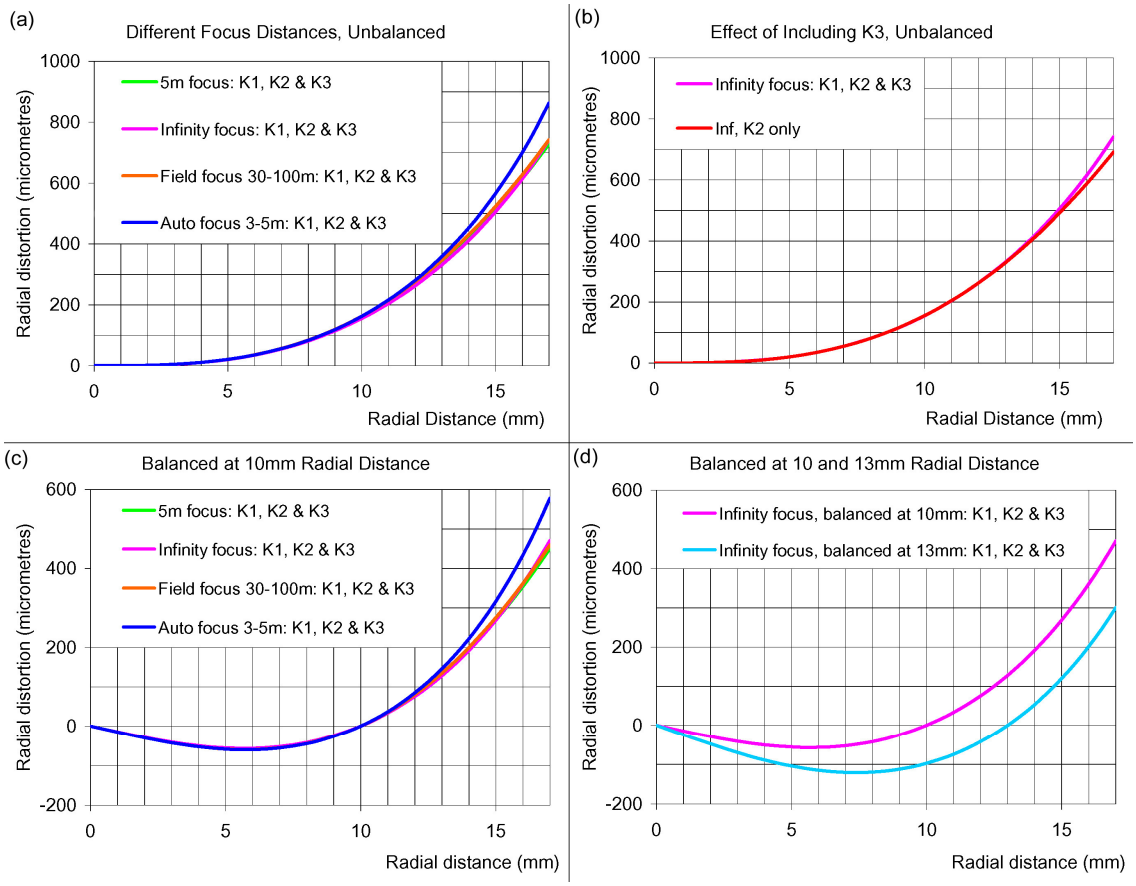

Figure 3.4 Radial distortion charts for Canon EOS D10 camera with 28-70mm zoom lens; 28mm focal length setting

3.5.3 Data Sources: Digital Arrays – Cameras and Scanners

Both cameras and scanners use CCD arrays to capture a scene and convert it to a digital file. The process is simplest when using a digital camera – the scene is projected onto the CCD array through the lens, and the optical distortions can be modelled and removed using conventional camera calibration processes. If paper prints or film (as diapositives or negatives) are scanned, the systematic distortions are more complex, including the original camera and lens, film distortion in processing and storage, printing, subsequent distortion during storage, and finally scanning, due to CCD unflatness, scale variations and non-orthogonality of the moving CCD array (Baltsavias, 1994; Robinson, et al., 1995; Fraser, 1997; Weir, 2000).

Photogrammetry for topographic mapping normally uses high quality imagery obtained with specialist large format aerial survey cameras. When converting film images to digital format, the high resolution negatives (or more rarely transparencies) are scanned on high precision scanners. In low-cost applications, the aerial photographs may be obtained as paper prints that need to be scanned using desk-top scanners. While A3-size scanners are preferred because they allow the paper print to be held flat against the glass surface, this size of scanner with greater than 700dpi (dots per inch; 275 dots per mm, or 36.3µm pixels) is relatively expensive. A4/US Letter-sized scanners are more readily available, but at 216mm (±4mm, depending on manufacturer), the width of the glass platen is less than the 230mm of the image on a normal "ten inch" (254mm) paper print.

Careful cropping of the paper print to fit within the raised sides of an A4/US Letter scanner will allow the corner fiducial marks of the Wild series (RC8, RC10, RC20, RC30) aerial cameras to be included within the digital image, but the margin for error is only about 4mm on either side of the centres of the corner fiducial marks. The centres of the fiducial marks on a RMK Top series large format camera are ±113mm from the principal point; consequently, the whole corner fiducial marks may not fit inside the width of the CCD array within the A4/Letter sized scanner head.

Table 3.3 gives a comparison between the size of a pixel on the ground, due to scanning of film negatives limited only by the resolution of the lens, and the scanning of paper prints at the commonly available desktop scanner resolution of

1200dpi. The comparison is based on aerial photographs commonly used in Hong Kong for terrain mapping, obtained at three altitudes in 1963 and 1964 by Hunting Surveys Ltd. with an RC10 aerial survey camera.

Table 3.3 Flying height, resolution and minimum ground feature sizes

Large Format Aerial Camera, lens focal length = 152mm			
Flying height	1189m, 3900ft	2134m, 7000ft	3810m, 12,500ft
Negative: central image resolution pixel size (37 $lp.mm^{-1}$: 0.0135 mm)	0.11 m	0.19 m	0.34 m
Negative: near-edge image resolution pixel size (22 $lp.mm^{-1}$: 0.0227 mm)	0.18 m	0.32 m	0.57 m
Paper prints: diameter of smallest natural object (approximately 3 pixels)	0.43 m	0.76 m	1.36 m
Paper prints: minimum object size for scanning at 1200 dpi (0.02117 mm)	0.5 m	0.9 m	1.5 m

Figure 3.5 shows three enlargements of the One Rise More landslide investigated in Chapter 6 of this study, taken from frame number 9467 at an altitude of 1167m

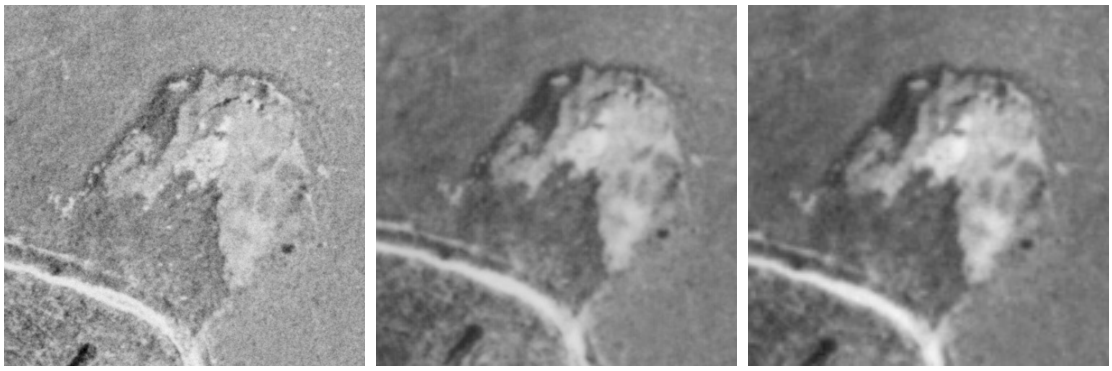

a. b. c.

a. 12.5µm (2032 dpi) photogrammetric quality scanning from the negative film,
b. 21.17 µm (1200dpi) desktop scanning of paper print, and
c. 36.3µm (700 dpi) desktop scanning of paper print.
(© Government of Hong Kong SAR, reproduced with permission)

Figure 3.5 Section of 1963 vertical aerial photograph 9647 showing the One Rise More landslide, scanned at three different resolutions.

above sea level and 676m above the landslide. Figure 3.5a shows the results of photogrammetric quality scanning at 12.5µm (2032 dpi) resolution obtained directly from the original aerial film negatives, compared to two desktop scans, at 21.17µm (1200dpi; Figure 3.5b) and 36.3µm resolution (700 dpi; Figure 3.5c) of a paper print of the same image. Although the high resolution photogrammetric quality scan contains significantly more fine detail, which would be invaluable for geomorphological interpretation purposes, stereo image-matching algorithms do not interpret the detail; indeed, where the highest frequency variations are not reproducible between the images on a stereo pair, such detail may constitute noise that results in lower correlations.

Warner et al. (1996) caution that the low image base:height ratio of 35mm format images (i.e., 24mm:36mm = 2:3; and of digital cameras with a similar ratio CCD array) may limit the overlap of successive images taken from fixed camera installations on moving platforms. This will apply particularly where the camera's shorter array Y axis is aligned in the direction of motion, when the photobase will be small and the cycle time between images may become critical, depending on the velocity of the moving platform. The investigation described in Chapter 4.1.6 has shown that small photobases result in a non-linear reduction in the accuracy of area-based image correlation (see Figures 4.15 and 4.16). This small photobase restriction may not apply to terrestrial or non-fixed cameras in photogrammetric applications that are able to use imagery obtained with convergent camera orientations as depicted in Figure 3.1c.

The final aspect of CCD construction that affects photogrammetric measurement is the arrangement of the light-capturing cells. A single pixel in the digital image contains red, green and blue values, but the Bayer pattern array used in many CCDs (Figure 3.6a) contains either red (25%), green (50%) or and blue (25%) pixels at each photosite (Castleman, 1996). Two-thirds of the pixel values in the final image are interpolated, and the effective resolution relative to the capturing pixels is twice the image pixel resolution. The Canon EOS10D camera is also fitted with a low pass filter in front of the CCD which also slightly reduces the effective resolution (Canon, 2004); the effect of this filter is unspecified. An alternative CCD design introduced by the Fuji Photo Film Co Ltd, (2001) uses photosites arranged in a diamond pattern, (Figure 3.6b) with the result that the number of photosites on the array is half that of

a. Bayer pattern

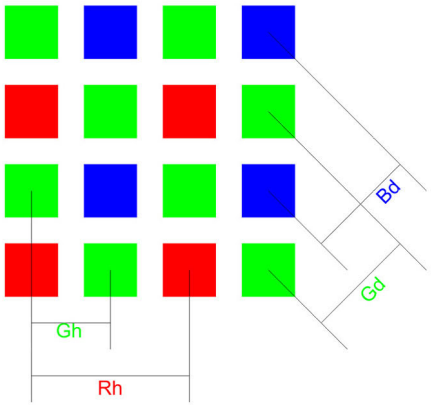

b. Super CCD

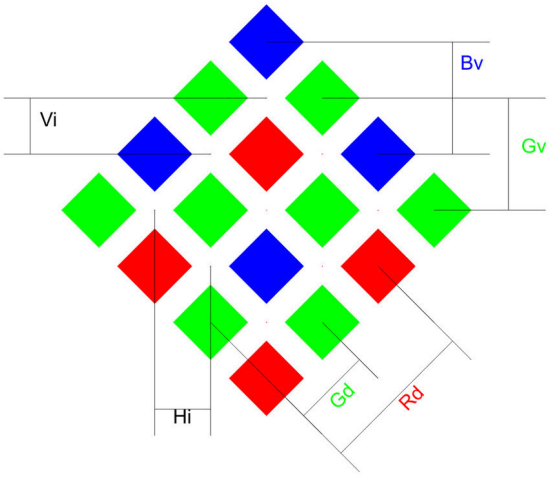

Legend:

Gh, Rh	horizontal resolution	Gv, Bv	Vertical resolution
Gd, Bd	Diagonal resolution	Hi	Horizontal interval
		Vi	Vertical interval

Figure 3.6 Comparison of the distribution of raw pixels in a Bayer pattern CCD and 'Super CCD'

the Bayer pattern CCD. This was found to adversely affect the recognition of small objects, for example, in the multi-image photogrammetry at the One Rise More landslide investigated in Chapter 8.1.2; where 6mm and 8mm diameter, high contrast yellow adhesive disks were used as targets, the target boundaries appeared more blurred than was anticipated in relation to the pixel size quoted for the Leica and Fujifilm cameras (Table 8.1).

3.6 Chapter Summary: Softcopy Photogrammetry and Geomorphology

Where the literature review in Chapter 2 focused on geomorphological mapping, Chapter 3 reviews the main elements of photogrammetric systems that are of relevance to geomorphological measurement and mapping of slopes, together with past applications of photogrammetry to geomorphological applications.

Both photogrammetric topographic mapping and geological/geomorphological API have traditionally used stereo viewing of vertical aerial photography. Stereo photogrammetric systems are readily adapted to small and medium-scale (regional) geomorphological mapping and detailed studies in low or gently undulating terrain. Multi-image (close range) photogrammetry has developed from engineering

applications where a more flexible approach to image perspectives has been required; photogrammetric measurement of steep hillsides and rock faces may also present similar perspective problems that are not adequately handled by vertical aerial photography. Stereo photogrammetry can be applied to non-vertical photography provided that coordinate axes are rotated so that the view direction approximates the normal to the plane of the photographs. Stereo image matching allows automation of the measurement process, although the resulting data need to be edited to remove or adjust points with incorrect 'object distance' values resulting from false correlations; object distance in an oblique or terrestrial imagery is equivalent to height in a vertical stereo pair.

For both stereo and multi-image photogrammetry, choice of camera and lens equipment is critical. For large format aerial photography, the only parameter critical to measurement adequate for the majority of geomorphological applications is the focal length, which is normally recorded on the frame of the image. If small and medium format cameras are used, camera calibration becomes critical due to the considerably larger systematic distortions present; however, recovery of the interior orientation parameters such as by using self-calibrating bundle adjustment or area-based methods will greatly increase measurement accuracy.

Lane et al.'s comments, reported earlier, that *'for rough natural topography, further research is required to understand how area-based correlators work, notably in the vicinity of breaks of slope'*. Chapter 4 describes a laboratory-scale investigation of perspective effects on area-based stereo image-matching that impact on the quality of measurements and hence the integrity of any derivative geomorphological interpretation based on the DEM. Stereo image matching is used in field studies to compile high resolution DEMs from terrestrial small format photographs in Chapter 6, vertical large format aerial photographs in Chapter 7 and on helicopter-borne small format photographs in Chapter 9.

Multi-image photogrammetry has the advantage of being able to handle images with a wider range of scale and view perspectives, because the systems currently do not use patch-matching algorithms; this is investigated in Chapters 6 and 8.

Chapter 4

USE OF AREA-BASED IMAGE CORRELATION FOR GENERATING DEMS

3D visualisation and measurement form a central thread to the investigations carried out for this dissertation; many of the algorithms use area-based image correlation to automate the measurement process. This can take the form of a terrain-following cursor, or automated DEMs generated across pre-defined regions, usually in a grid pattern. CCD arrays allow digital scanners to convert film negatives and prints, and low cost digital cameras to obtain directly, high resolution digital images. The reduced size of the area of ground covered by each image pixel implies that the resolution of derivative DEMs can also be increased.

Developments in analytical photogrammetry allow the accuracy of point measurement in object space to be defined in terms of the accuracy of point measurement on the component imagery. For analogue (mechanical) photogrammetric digitisers, the accuracy of measurement is controlled by the stability and precision of the measuring system; for digital photogrammetric systems, the equivalent measure is the size of the pixels in the image, and whether the algorithms record measurement values in terms of whole pixels or if interpolation to a sub-pixel scale can be applied.

The investigations described in this Chapter were initially carried out between March 2004 and April 2005 using version 8_14_2 of the uSMART softcopy system, and expanded from February to May 2007 using versions 9_07_B (released 2 April 2007), where similar results were obtained. The studies carried out in this Chapter have identified a phase-wrapped quantisation effect that limits the measurement precision of a softcopy photogrammetric system when operating in single pixel accuracy mode; this effect is not fully removed when image correlation operations are applied at sub-pixel mode, suggesting that some single-pixel bias remains within the sub-pixel algorithm. The effects have not been checked against other softcopy systems but corresponding patterns have been identified on other published imagery (Chandler, et. al., 2005), and a similar effect has been noted by other authors (e.g., Stojic et. al., 1998, Chandler, et. al., 2003), as described in Chapter 4.1.2 below.

4.1 Photogrammetric Data Processing

While stereo and multi-image photogrammetric processing use variations of the collinearity equations to derive 3D spatial coordinates, the extent to which these processes can be automated varies (Chapter 3). Extreme perspective and scale distortions in highly convergent multi-image photogrammetry have limited automated point recognition to centroiding of high contrast targets, e.g., Australis (Fraser and Edmunson, 2000) and PhotoModeler (EOS, 2003) photogrammetric software. Although feature-based image correlation algorithms may be able to overcome this problem, these were not available in the photogrammetric software used for this investigation and are not considered further. Networks of highly convergent imagery have been shown to contribute a greater precision in the recovery of elements of interior and exterior orientation (Fraser and Edmunson, 2000; Kenefick et al., 1972; Granshaw, 1980; Chandler, et al. 1989). Part of the present investigation compares the use of automated image extraction methods on conventional parallel camera axis sets of imagery with convergent configurations.

The quality of the results is dependent on the integrity of the input data and the semi-automated data extraction algorithms. The studies carried out in this chapter investigate the effects of the automated image correlation routines on the accuracy of measurement data in relation to:

(a) Single pixel and subpixel measurement modes;
(b) Correlation window size (pixels);
(c) Variations in separations between camera stations (photobase) and between the camera stations and the target (object distance);
(d) Variation in camera orientation;
(e) Focal length of the lens;
(f) Resolution (pixel size) of the images;
(g) Image compression.

4.1.1 Methodology

While the effectiveness of photogrammetric processing on natural terrain is investigated in detail in later Chapters, an initial small study was carried out in a laboratory environment with a target chosen to remove terrain-related effects such as

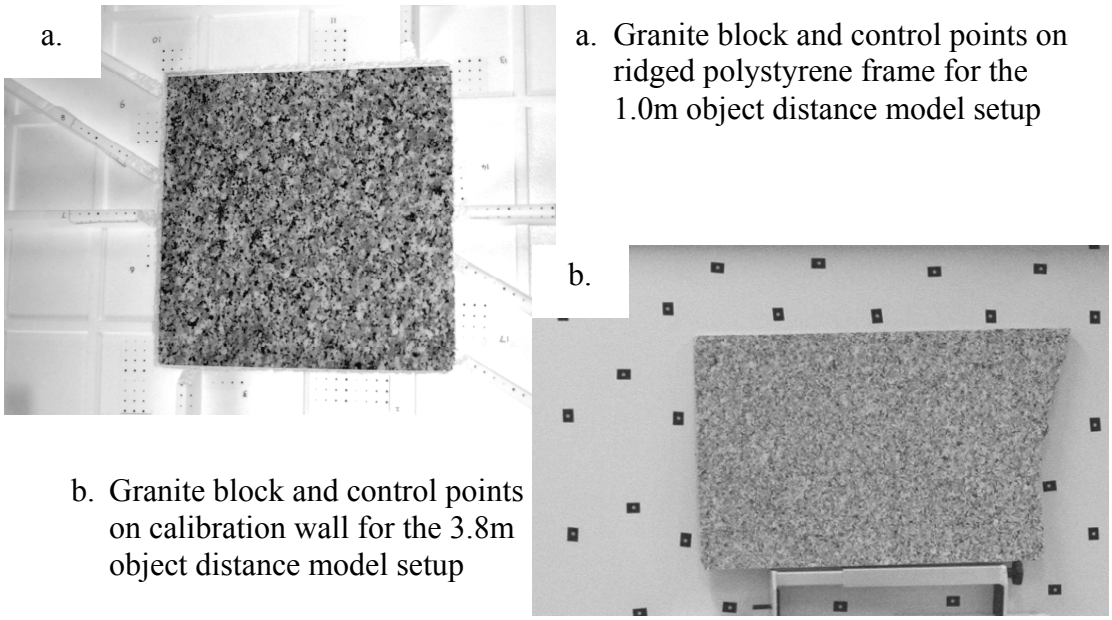

a. Granite block and control points on ridged polystyrene frame for the 1.0m object distance model setup

b. Granite block and control points on calibration wall for the 3.8m object distance model setup

Figure 4.1 Granite block with the 1.0m and 3.8m model setups

topographic and land cover variations. The study involved photographing a smooth-surfaced block of machine-polished granite (700mm long by 436mm wide), with sets of approximately equally-spaced images taken along straight lines with the camera lens axis approximately perpendicular to the long axis of the granite, the parallel runs, and around arcs at a fixed distance from the centre of the granite target, the convergent runs.

DEMs of the surface of the granite were generated using the automated grid DEM measurement routine of the uSMART software, under conditions of varying camera direction, camera separation, correlation window size and lens focal length. Some of the stereo models were used for further testing where the parameters of the measurement algorithms were changed, and with varying image pixel size and image quality. The experimental set-ups are shown in Figure 4.1a and b. The camera body used was a Canon EOS D10 digital camera fitted with a 50mm lens, and a 28-70mm zoom lens fixed at the 28mm and 70mm settings.

Two model setups were used; the 50mm lens, and 28mm and 70mm settings of the zoom lens with the granite block mounted in front of a camera calibration wall with an object distance of approximately 3.8m. A second set of parallel and convergent images were taken with the 28mm setting at an object distance of approximately

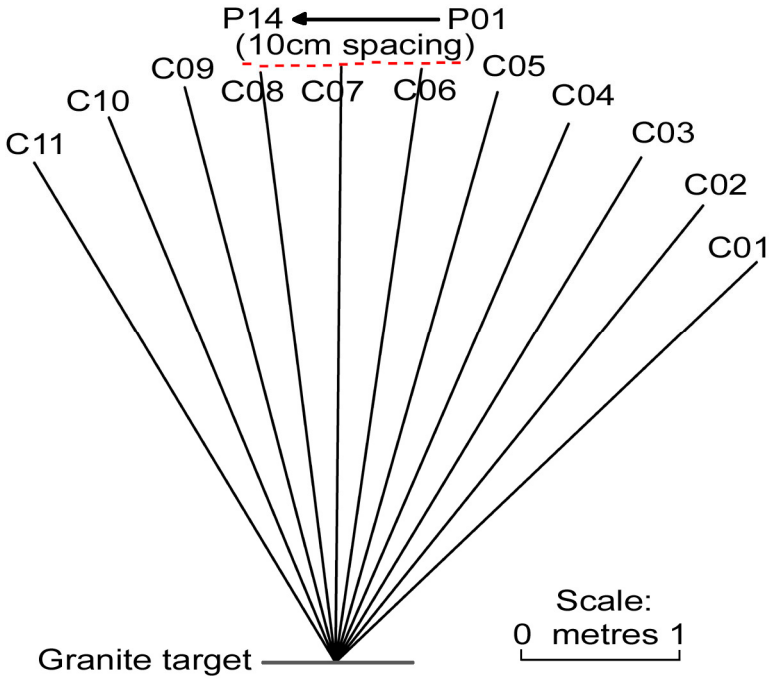

Figure 4.2 Locations of camera stations and target centres for 50mm lens

1.0m. In both cases, additional sets of photographs were taken to allow camera lens calibrations to be determined for the specific object distance of the setup; in the case of the 1.0m setup, additional points on adhesive paper were placed across the face of the granite only for the calibration images. For all runs, the image numbering is sequential and is prefixed by 'P' for parallel view direction runs and 'C' for concentric runs.

The granite block was chosen because it contains a wide range of high-contrast grain sizes while presenting no features that would result in stereoscopic dead ground. As the polished granite has a specular reflection, photography for the 1m setup was carried out outdoors under cloudy shade to reduce the possibility of direction-specific, high intensity light reflections that might have a negative effect on image correlations. The 3.8m setup was carried out in the laboratory, under conditions of bright daylight and fluorescent illumination; a tripod was used to reduce camera movement during exposure. Figure 4.2 shows the camera orientations and separations used to build the set of stereo pairs.

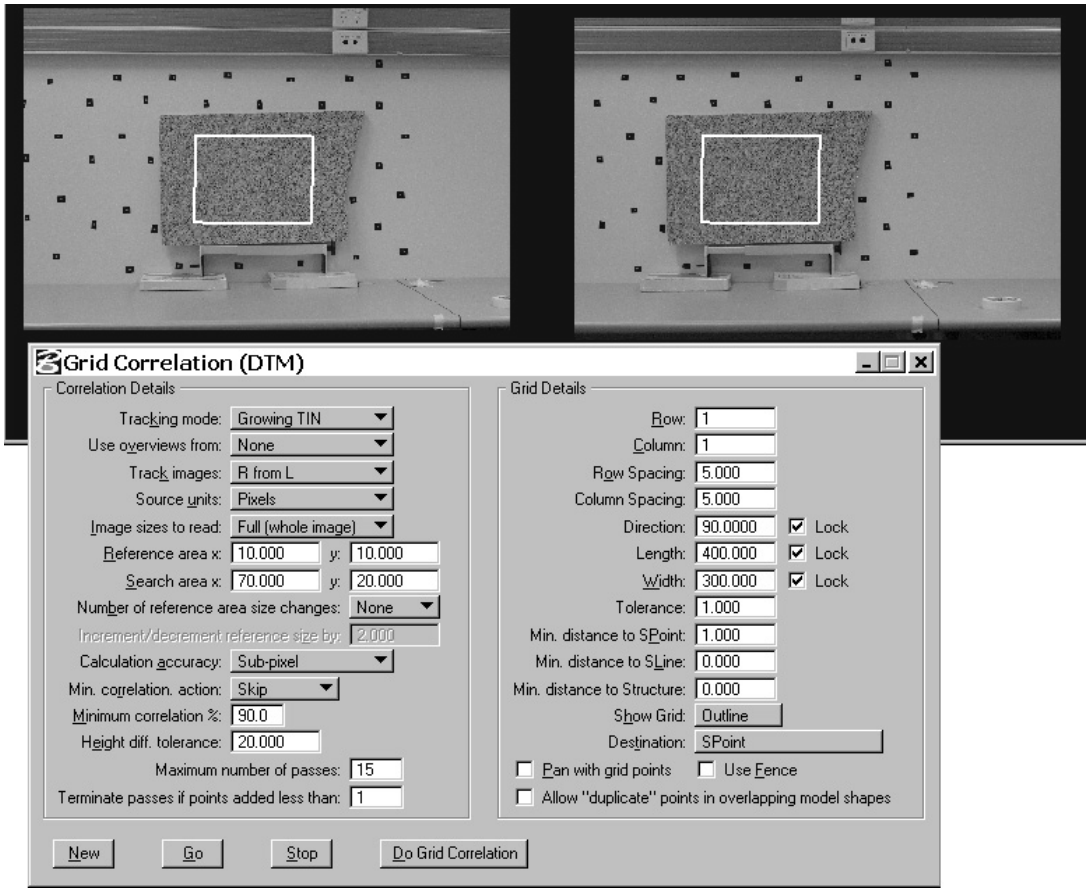

Figure 4.3 Grid correlation control window with stereopair P07-10, 50mm lens

DEMs were generated using uSMART's Grid Correlation routine; the screen capture shown in Figure 4.3 shows the stereopair of images P07 and P10 taken with the 50mm lens, with the measurement area superimposed. The autocorrelation parameters tested in this study were the size of the Reference area, size of the Y dimension of the search area relative to that of the Reference area (both dimensions are in pixels), and the Tolerance, which is the maximum distance that the measured point is allowed to deviate from the centre of each point in the DEM grid (dimensions in object space units, in this case mm). The DEMs measured were 400 by 300mm with a nominal grid spacing of 5mm. Each DEM was created with an initial pass using the minimum acceptable correlation of 90% to ensure the best fit with the target plane, with subsequent passes decreasing at 10% intervals to 50%. The height difference tolerance was kept at a comparatively large value, normally ±20mm, to try to limit false correlations. The 'Growing TIN' mode for DEM generation allows the measurement routine to make sequential passes across the DEM, updating the TIN stored in memory until no additional points are added; the

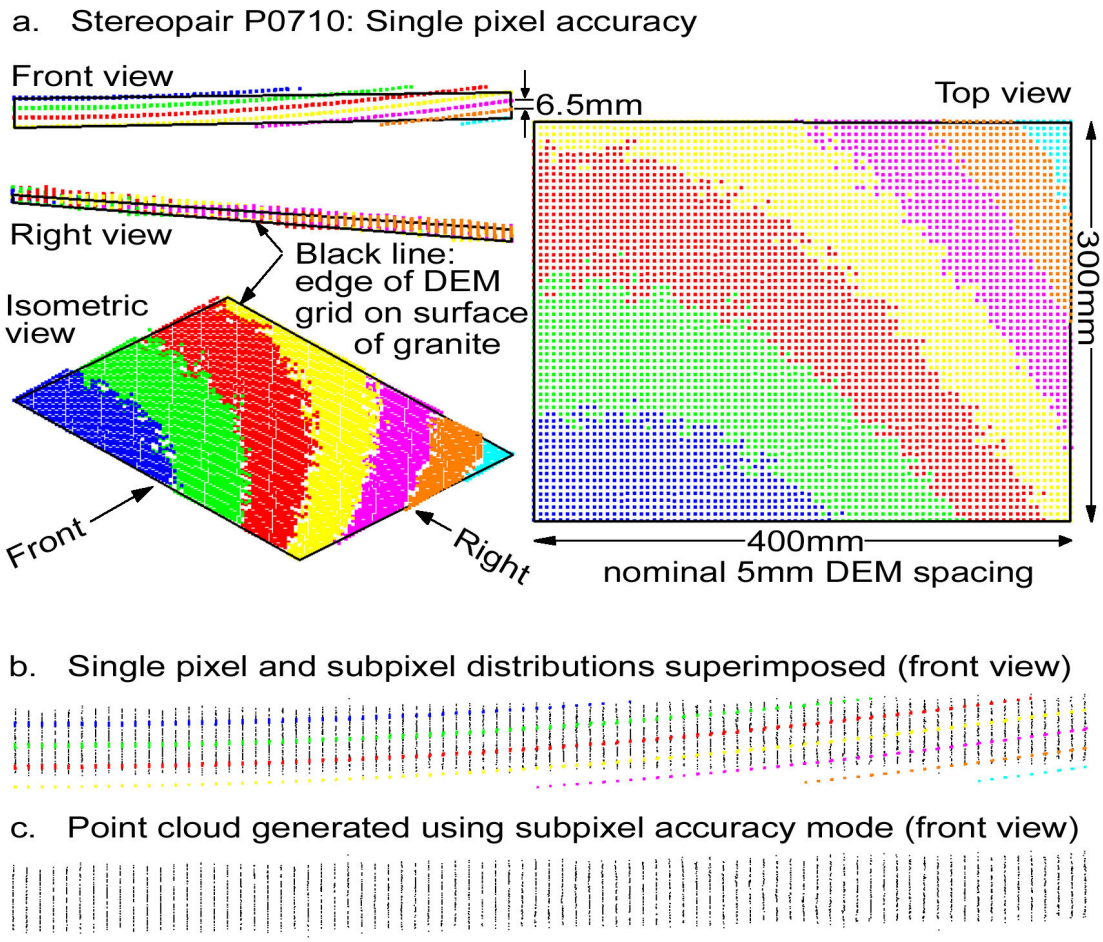

Figure 4.4 Layers generated by single pixel mode for stereopair P07-10 and comparison with subpixel mode. Note: b and c show a sloping plane.

TIN is used to initiate the search for each new DEM point. A TIN created between the four corners of the granite block was attached as a reference file to ensure the initial search coincided with the surface of the granite block.

The DEMs were processed through a MatLab routine (LSP; see Chapters 5.5.2 and 5.6) to determine the best-fit plane through the point cloud, with the aim of extracting the residual distances from the measured point to the best-fit plane. The residuals from the best fit plane were used to remove any bias due to the orientation of the granite surface. In the 3.8m setup, the plane was oriented with a dip of approximately 4.4° from the XY axis in a direction of 352° relative to the Y axis, using x = horizontal and y = vertical coordinates of the calibration wall targets, i.e., tipping back at the top of the granite target. In the 1.0m setup, the plane was oriented with a dip of approximately 0.1° from the XY axis of the control points; with such a

small inclination, the dip direction as determined by the best fit plane varied around 38°, ±4°, although in a few instances the dip direction was rotated 180°.

Each of the point clouds of residuals was processed to determine the means and standard deviations of the correlation coefficients and the residuals, plus the maximum range of the residuals. In most cases, each stereo pair was generated twice, once using the single pixel accuracy mode and a second time using the subpixel accuracy mode. The LSP routine (Chapter 4) generates a graphic plot of the residuals with the points located above the best fit plane coloured blue and those below the plane coloured green. Where distinct layers were identified in some of the plots, a second visualisation was prepared where the surfaces were recoloured. Figures 4.4 and 4.5 show the DEMs generated for stereopair P07-10 from the 50mm lens images, using the single pixel and subpixel accuracy modes of DEM measurement. In Figure 4.4a, the single pixel mode point cloud has been coloured to distinguish the layers. To enhance visualisation, the plots were further processed to simplify the graphics to opaque blue circles and green squares (Figure 4.5).

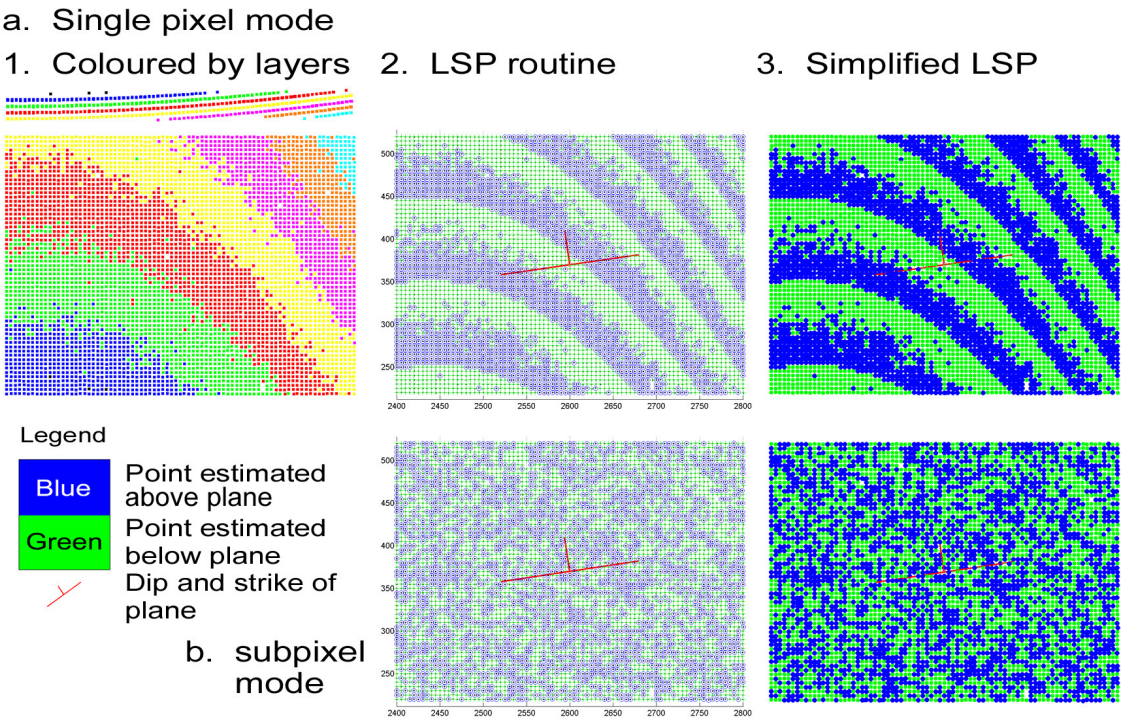

Note: The normal LSP output (Chapter 5.5.6) in a2 and b2 above are simplified in a3 and b3 to show only whether the residual is above or below the plane

Figure 4.5 Processing sequence for stereo pair P07-10

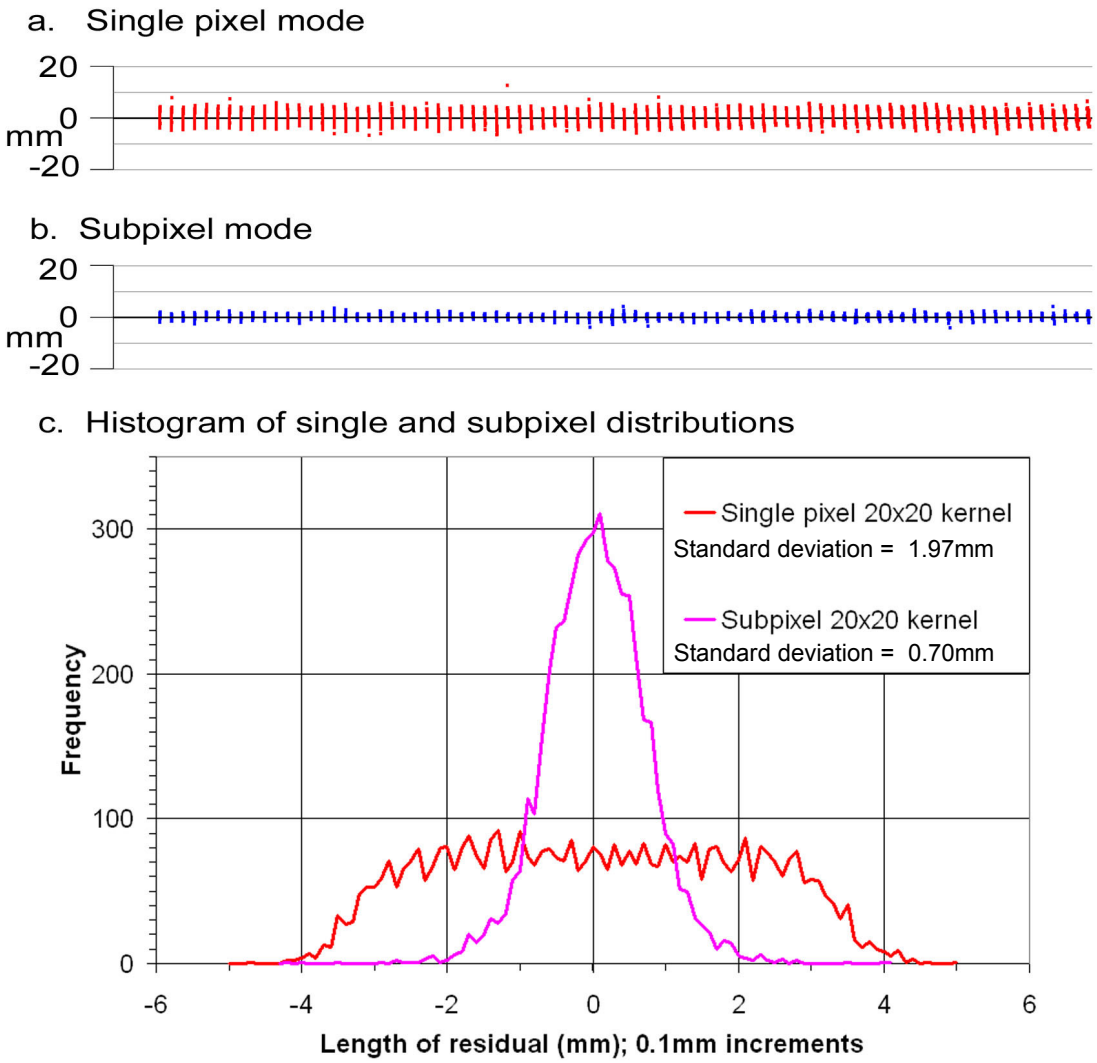

Figure 4.6 Comparison of the distribution of residuals for single and subpixel modes for stereo pair P07-10

The most striking feature of the resulting point cloud is that it is divided into seven separate layers; in this case, each layer is separated by a perpendicular distance of approximately 6.5mm. Note that, as demonstrated by the side and front views of the plane in Figure 4.4a, the number of layers present has been increased by the sloping target surface. The point cloud shown in Figure 4.4c demonstrates that the same layering effect does not occur to the same extent as for the single pixel mode.

Figures 4.5 and 4.6 show the results of the extracting the residuals to each DEM point from the best fit plane using both the single and subpixel accuracy modes using the LSP routine. The main features to note about the distribution of points shown by the two display formats are:

(a) For the single pixel mode:

(i) Points are placed in distinct phase-wrapped layers with a small variation within each layer;

(ii) Isolated points can be located beyond the main mass of each layer, which form the maximum and minimum limits to the envelope;

(b) While the subpixel mode distribution is Gaussian, the single pixel mode is nearly uniform, with Gaussian distributions at each end due to sporadic limits to the layers;

(c) Close visual comparison of the distribution of points in the subpixel mode (item b3 in Figure 4.5) reveals that the phase-wrapped layering pattern visible in the single pixel distribution remains slightly discernable within the otherwise apparently random distribution.

There appears to be a significant difference in the way the automated image correlation routine performs when operating in single pixel and subpixel accuracy modes, as implemented within the uSMART software package. As with many commercial software packages, uSMART's source code is not available for analysis, however, the *'image correlation routines are based on the mathematical descriptions given from pages 354 on in Kraus (2000)'* (Allen, 2004, 2007). Discontinuous surfaces identified by other authors are described in the next section and investigated in greater detail in Chapter 4.2.

4.1.2 Discontinuities Created by DEM Generation: Other Case Studies

The presence of discontinuities within DEM data has been noted by Chandler (et. al., 2003) and investigated as part of a laboratory-scale study of sediment dynamics in a model flume, 2.9m wide by 11.5m long as described in Stojic et. al. (1998). These authors identified a step-wise source of error in automatically-generated DEMs created using the ERDAS IMAGINE OrthoMAX software package. The images used in this study were digitised at 12.5μm resolution from film negatives taken with a medium format non-metric camera fitted with a 55mm focal length lens. The errors in overlapping DEMs were found to be over 15mm near the edges of two adjacent photogrammetric models, and that a visible step-wise pattern was present. These authors' solution was to use only the sections of DEM away from areas where these artefacts were found. The authors concluded that changes to the camera model parameters and a lack of precision of the fiducial locations on the film negatives

could not account for this systematic error; they further suggested that the systematic errors are attributable to the over-simplification of the camera calibration, film deformation or small errors in the adaptive method of interior orientation which would be difficult to resolve.

Figure 6 in Chandler et. al. (2005) shows four images of a flat board model used to test the performance of low cost digital cameras when used to capture images as input into automated DEM generation using the OrthoBASE Pro software package; this package uses a 'hierarchical, feature-based matching algorithm' (Chandler, et. al., 2005) for image correlation. All four images captured by different cameras contain similar ellipsoidal patterns although the centres and XY scaling of the patterns vary slightly. Although the colouration of these patterns is not explained, they all show a gradation from green (low points) to red (high points) with a highly irregular and abrupt transition back to green. This pattern is identical to that identified in Figures 4.4 and 4.5 above, except that in Chandler et. al. (2005) the patterns are concentric, whereas that of Figures 4.4 and 4.5 form only a small lateral section of the ellipsoidal pattern.

Chandler et al, (2005) and Stojic et al., (1998) refer to these patterns as '*domed structures*', although they are concave upwards, and note that a theoretical proof is given in Fryer and Mitchell (1987) which explains them as being due to '*uncorrected radial distortion which introduces x parallax into the stereo model in the form of a cubic surface centred on the photobase*'.

4.1.3 Variations in Controlling Parameters in Single Pixel DEM Generation

Three parameters that have significant effect on the process of generating single pixel mode DEMs are:

(a) Variance in DEM post location;
(b) Size of the reference window; and
(c) Size of the search window relative to the reference window.

Repeated patterns of pixel intensities may be present in some images, e.g., rows of crops, trees or urban areas. The granite rock mass might present some pattern with regard to grain sizes within the rock mass, no such pattern was visually obvious

within the surface of the target used in this study; although there is a small chance that this may affect the results of the present study, this is considered unlikely as similar phase-wrapped surfaces can be identified in images of a structurally different target in Chandler et al. (2005; Chapter 4.1.2 above).

Variance, as used in uSMART, is the variation of DEM position allowed during the search for the maximum value for image correlation within the search window. If this value is set at zero or a very small value, the DEM post is forced to be located at the grid intersection defined by the DEM spacing; this is rarely necessary and some variation should be defined to allow the search routine to identify the most well-defined feature within the proximity of the specified DEM post. The maximum value should be no more than half the grid spacing, otherwise the same target location may be identified from starting points at adjacent DEM posts; uSMART reduces this possibility by also including the option of a constraint on the minimum allowable distance between measured points or pre-existing points and lines.

Figure 4.7 shows the effect of changing the values for variance on the single pixel

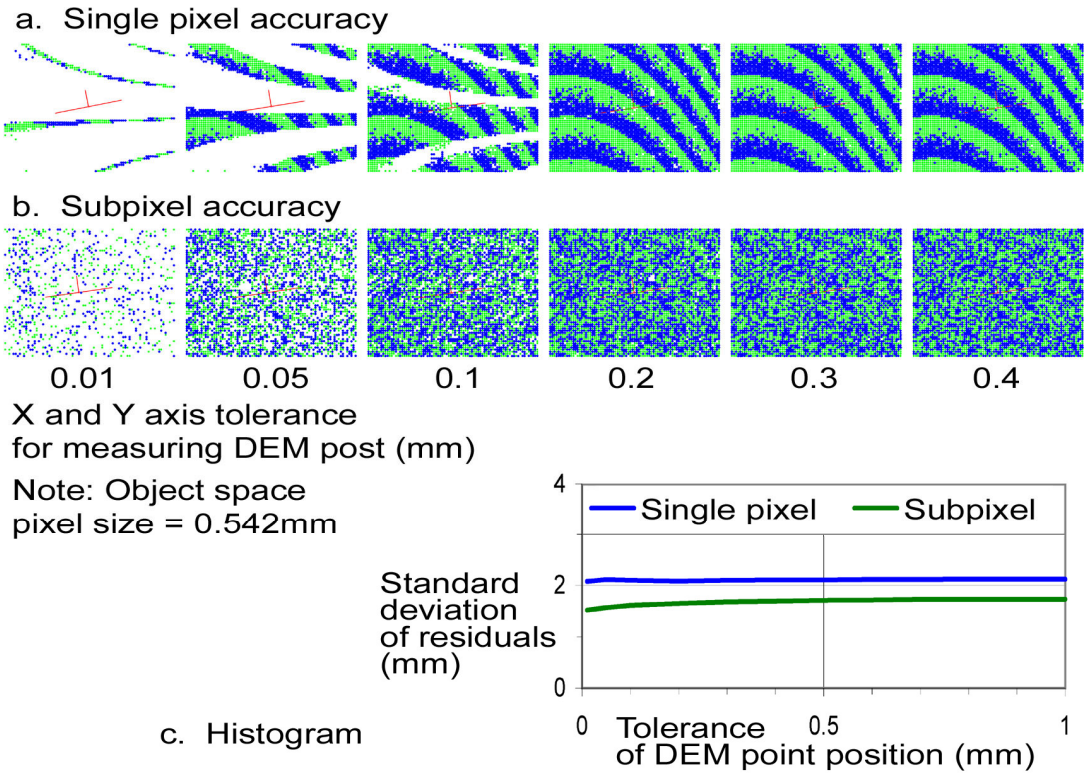

Figure 4.7 Effect of changing variance for stereo pair P07-10 using a 10pixel reference kernel

and subpixel modes for stereo pair P07-10. For the single pixel mode, very small values of tolerance results in correlation failures for large areas of the image; although regular, the pattern appears to be independent of the dominant pattern of phase-wrapped layers (although there may be some effect induced by a secondary phase-wrapped pattern discussed in Chapter 4.2.2 below). For the subpixel mode, the effect is not as clearly defined as there is no clear pattern, however smaller values of tolerance also results in larger numbers of correlation failures; the numbers of points successfully correlated is similar between single and subpixel modes. The graph in Figure 4.7c shows that there is very little change in the standard deviation of residuals as the tolerance is increased.

Figure 4.8 shows the results of changing the size of the reference kernel, from very small values of four pixels width up to an extreme value of 100 pixels. For the single pixel mode, the numbers of outlier points separated from the main part of the surface

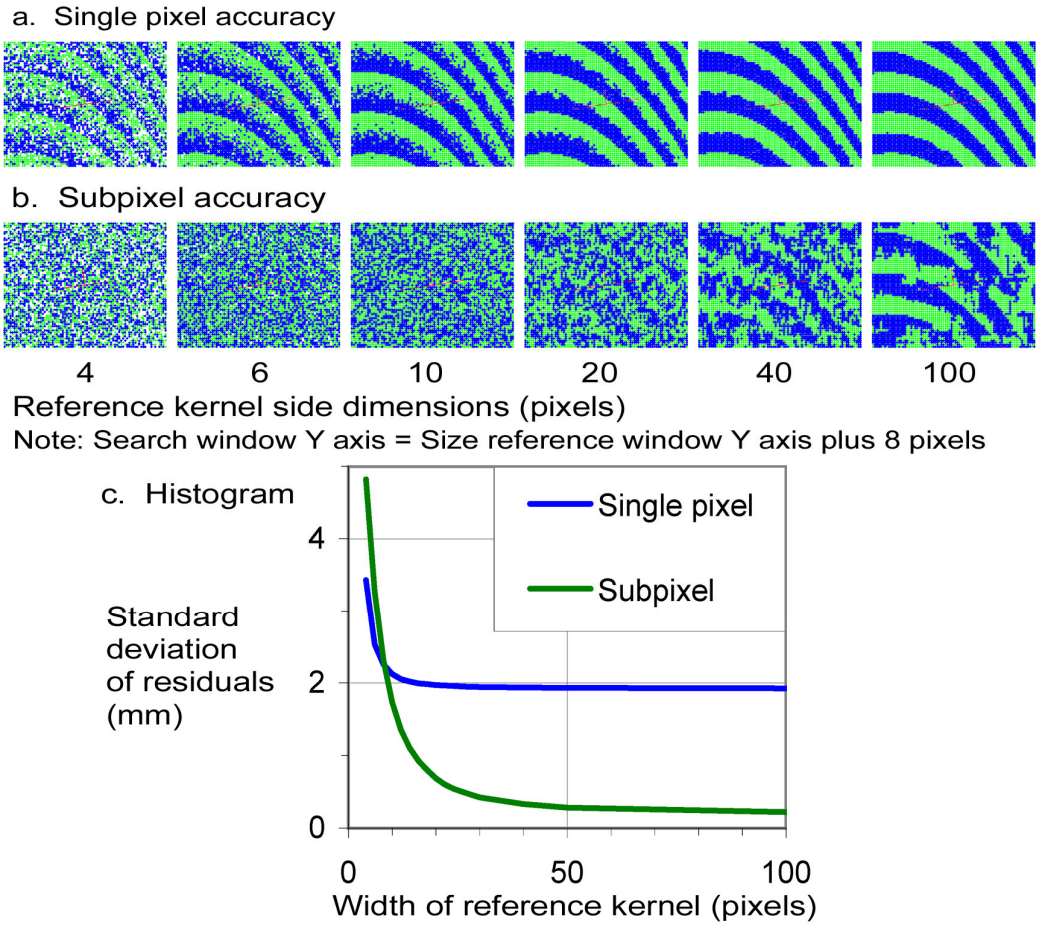

Figure 4.8 Effect of changing the size of the reference kernel for stereopair P07-10

decreases with increasing reference kernel size; correlation failures are also more common with smaller kernel sizes below ten pixels. Of greater significance is the re-emergence of the phase-wrapping effect with increasing reference kernel size when operating in subpixel mode; this effect is noticeable even when the reference kernel is only ten pixels wide. For reference kernels 20 pixels wide and greater, the single pixel phase-wrapping effect is clearly distinguishable. The graph in Figure 4.8c shows that the standard deviation of residuals increases rapidly for kernels smaller than 20 pixels, therefore the optimum size for the reference kernel is generally between ten and 20 pixels.

Figure 4.9 shows the effect of changing the size of the Y dimension of the search window relative to the Y dimension of the reference window, when using a reference kernel 24 pixels wide. The results show that there is no distinguishable difference when operating under single pixel mode. However, there is an important effect when operating under subpixel mode where the search window is between one and three pixels larger than the reference window as the routine is effectively operating in

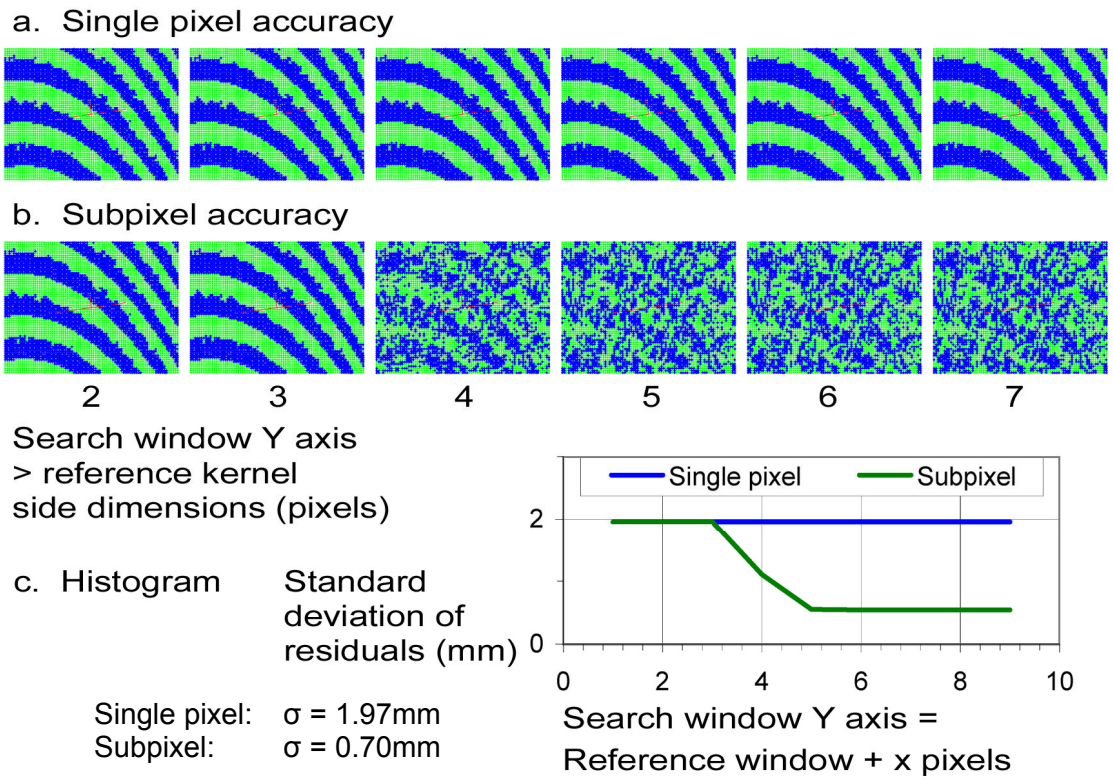

Figure 4.9 Effect of changing the Y dimension of the search window relative to that of the reference kernel for stereo pair P07-10; note that the width of the reference kernel in this case was 24 pixels.

single pixel mode. When the search window is four pixels wider, the phase-wrapping remains noticeably stronger than for larger values and the standard deviation of residuals lies between those recorded for the single pixel mode and for larger values for the difference. For five pixels and above, the phase wrapping effect remains at the same level as that shown to be due to the size of the reference kernel in Figure 4.8b and the standard deviation of the residuals remains at the stable minimum level.

These three effects are important because they fall within commonly applied practice and unfortunately, were only identified after the case studies carried out for most of this dissertation, including this Chapter, had been substantially completed. The search for a corresponding image patch is normally constrained to the epipolar line which forms the intersection of the image plane with a plane formed by the two camera stations and the required DEM point; where the image distortions have already been largely removed by the interior orientation, the search should not need to use a large Y axis search dimension, and values of two to four pixels were normally applied during the case studies in this dissertation. The patterns visible in Figure 4.7 show that the tolerance should always be set to a minimum of half the size of a pixel in object space, i.e., on the target (ground). If large areas of correlation failure are noticed during operation of the automatic DEM generation, values of the tolerance should be inspected to determine if this is the cause of the failure, and the values increased. Thirdly, use of a reference kernel between ten and 20 pixels is recommended because 'the "height averaging" problem typical of auto-correlation is virtually eliminated' (SmartTech, 2005); if the use of smaller reference kernels is required, additional editing of DEM results may be required because of the greater variation in the standard deviation of residuals between the measured and true positions.

4.1.4 Comparison between Measured and Estimated Vertical Accuracy

The accuracy of measurements in the X and Y axes of a horizontal object within an image are dependant on the scale of the image, where:

$$\text{Scale} = \frac{\text{Focal length of the lens}}{\text{Flying height above the terrain}} \qquad \text{Eqn. 4.1}$$

In the context of the present investigation, the unit of horizontal precision is the width of a single pixel in image space, which in the case of the Canon EOS D10 camera body is 0.0074mm. Errors in the measurement of the corresponding vertical coordinates (along the Z axis) can be determined using the standard solution (Moffitt and Mikhail, 1980; Mikhail et. al, 2001; Förstner, et. al, 2004; Hussain and Bethel, 2004):

$$\sigma_h = \sigma_p \frac{H'}{f} \frac{H'}{B} \qquad \text{Eqn. 4.2}$$

where σ_h = height precision

σ_p = planimetric precision

H' = flying height above the terrain

f = focal length of the lens, and

B = photobase at ground scale (equivalent to airbase for vertical aerial photography)

Thus the standard deviation of height measurement is inversely proportional to the ratio of photobase to object distance.

The results of the measurement of the variations of standards deviations of the residuals between the measured points and the least squares plane through the point cloud for the set of images taken with the 50mm lens and with parallel camera axes

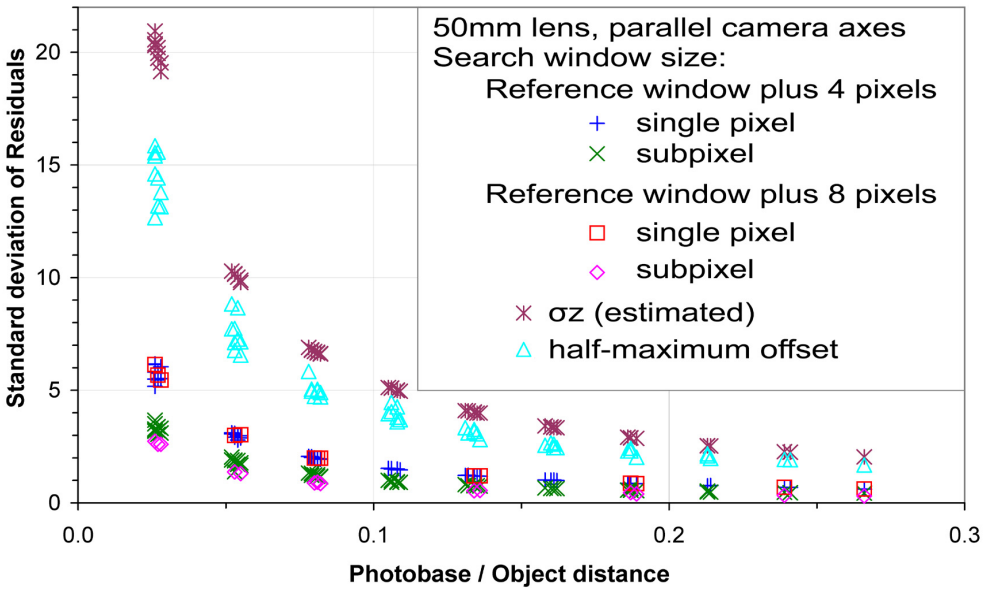

Figure 4.10 Distributions of the standard deviations of the residuals from the measured points to the least squares plane for single and subpixel mode stereo models built using images obtained with the 50mm lens and parallel camera axes.

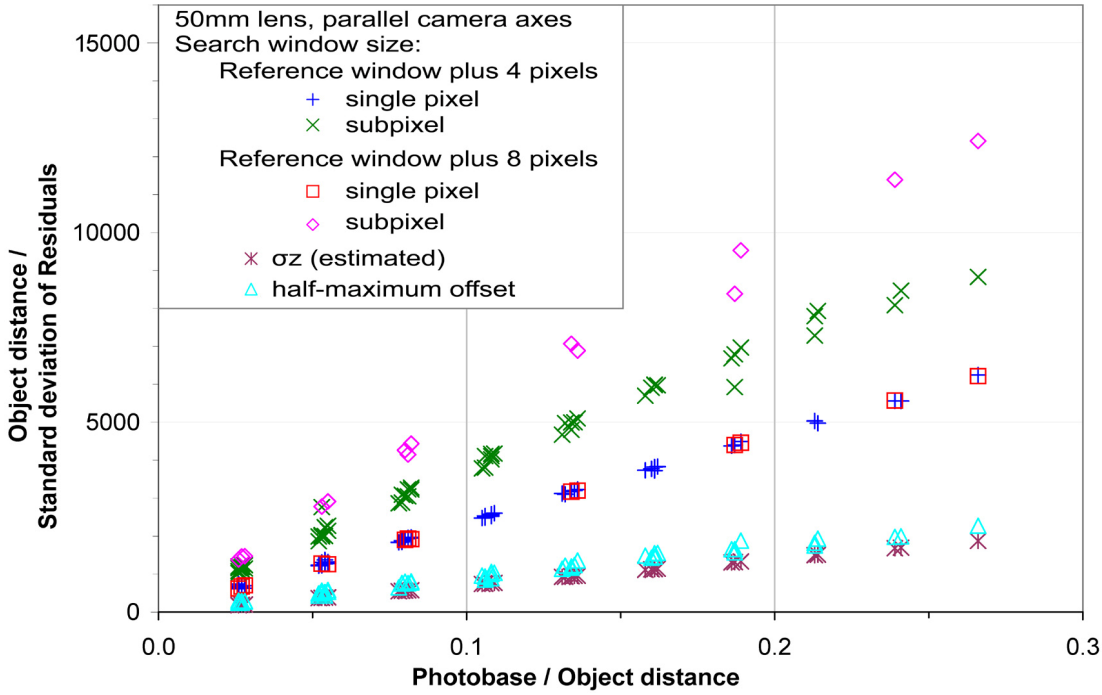

Figure 4.11 Data from Figure 4.10 normalised by using the object distance multiplied by the reciprocal of the standard deviations of the residuals against the photobase / object distance ratio.

are shown in Figure 4.10. For comparison, the estimates obtained using the width of the image pixel as the horizontal precision are also shown, together with half the measured maximum offset of points from the least squares plane.

In the context of vertical aerial photogrammetry, the vertical measurement precision is often stated in terms of parts per ten thousand of the units of measurement for the flying height. The standard deviations of the residuals can be converted into this format by dividing the object distance (distance from the camera to the target) by the standard deviation of the residuals, as shown in Figure 4.11. This graph clearly shows that the envelope defined by the limits of the phase-wrapped layers ("half maximum offset") corresponds closely to the estimated precision obtained from using the horizontal precision as the image pixel size. The consequences of the measurement error artefact induced by changing the size of the search window relative to the reference window is also shown; while there is no change to the results for the single pixel mode measurements, the subpixel results are greatly improved by the use of the larger search window Y axis (eight pixels instead of four). Vertical

aerial photography normally follows this configuration, with the camera axis varying from vertical by a small angle, commonly <4°.

4.1.5 Effects of Variations in Camera Focal Length

Estimates of the maximum unbalanced radial distortions of the three lens settings obtained through calibration were found to be similar to published values (Fryer, 1986; Fryer and Brown, 1986); For this study, these were (i) 28mm: 420µm, (ii) 70mm: -13 µm (iii) 50mm: 93µm.

The three lens settings were used in a simple comparison of the results of single pixel and subpixel mode measurements, and the results are shown in Figure 4.12. These measurements were carried out using the sub-optimal parameters of the Y axis of the search window being only four pixels larger than the reference window; consequently, although the results for the single pixel mode are correct, the subpixel mode residuals are larger than could be achieved with more optimised parameters.

Note that, although the gradient of the 28mm lens is lower than that for the 50 and 70mm lenses, the increased extremes of the photobase/object distance ratio due to the

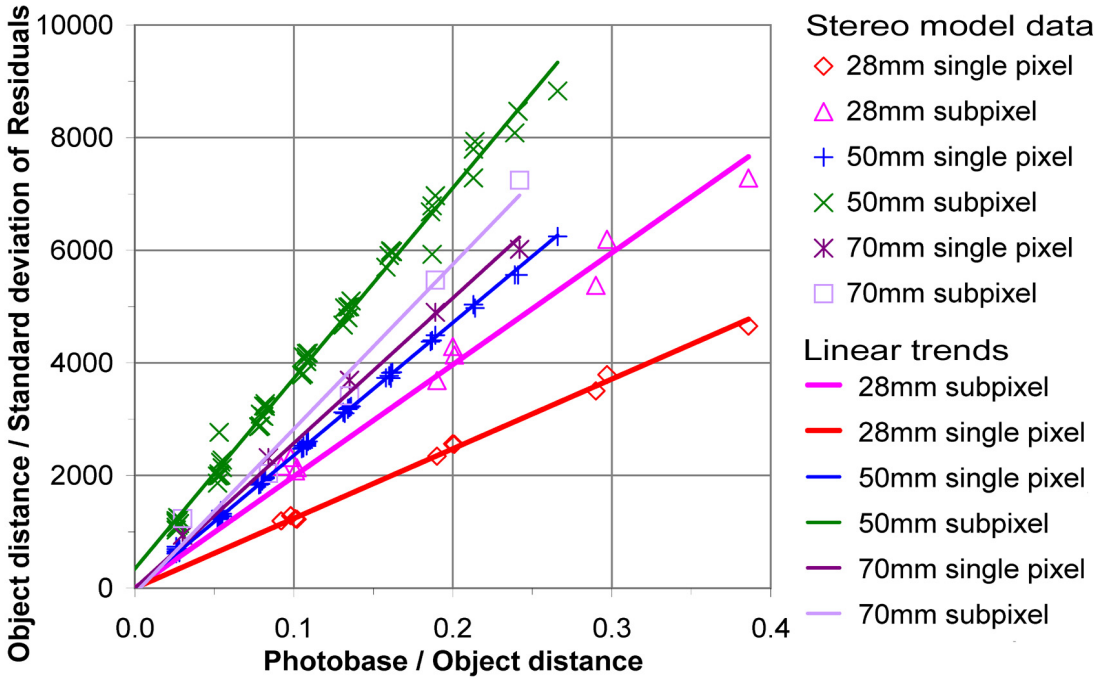

Figure 4.12 Comparison of the results for 28mm, 50mm and 70mm focal lengths, parallel runs (sub-optimal parameters used for all lenses)

wider angular coverage allow the overall accuracy expressed in relation to the object distance to approach that achievable from the longer focal length lenses.

The trends shown by both the single pixel and subpixel mode measurements are strongly linear. However, in these tests, the photobase axis remains approximately parallel to the surface of the target, and no comparison is possible for variations in the orientation of the surface relative to the photobase; this is possible when using convergent imagery, where the lens axis is directed towards the centre of the target, as discussed in the next section.

4.1.6 Effects of Variations in Camera Orientation

Varying the camera orientation by traversing at an approximately fixed radius around the target creates a set of stereo pairs where the photobase:object distance ratio is changing over a wider range than is possible with parallel camera axes. In addition, the mean of the two lens directions will form an incident angle with the perpendicular to the target surface. This is important in the measurement of sloping terrain, both as steeply sloping ground in conventional vertical aerial photography

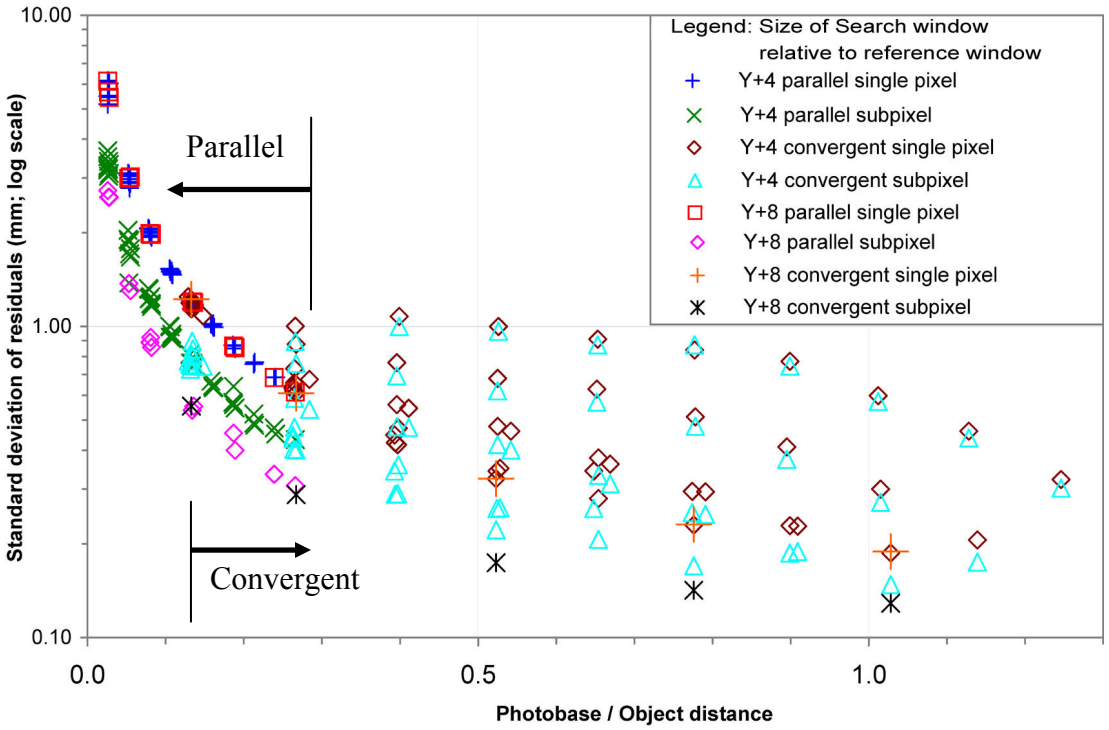

Figure 4.13 Standard deviation of residuals for 50mm lens, parallel and convergent camera axes

and varying rock faces in terrestrial and oblique aerial photography as may be obtained from helicopters (see Chapter 9).

Figure 4.13 shows the results from using convergent lens axes superimposed over the results for the parallel axis imagery. The results for the smallest tested values for the photobase:object distance ratio of 0.13 fall within the section of linear trends for the parallel lens axis imagery. While the bulk of the convergent data were obtained using the suboptimal parameters, five models were reprocessed with optimal parameters. Similar to the parallel axis results, there is minimal difference for the single pixel mode, but a significant increase in the subpixel mode, as shown by the black symbols. The results also diverge from straight linear trends in the reformatted data in Figure 4.14, which is the result of the orientation of the target plane relative to the mean lens axis. The results for the five optimal parameter models record the highest accuracies, peaking at of over one part in 28,000 where the photobase:object distance ratio is approximately unity. At the lower end of the range of accuracies, there are results showing one part in less than 4000. Also of note, the lower accuracy results show very little improvement between the single pixel and subpixel modes (denoted by the vertical separation between the two symbols).

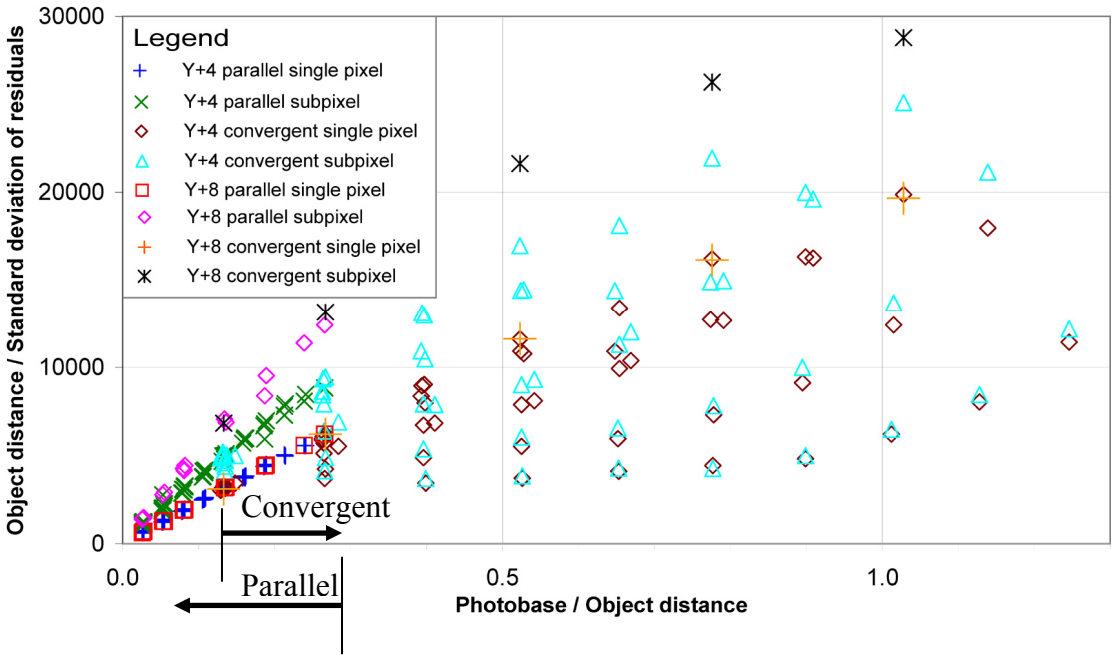

Figure 4.14 Reciprocal of the standard deviation of residuals multiplied by the object distance against the photobase:object distance ratio for 50mm lens, parallel and convergent camera axes

The effects of the mean incident angle and the angular separation of the two images for each stereopair are shown in Figure 4.15. Trend lines have also been added to highlight in black, the maximum accuracies obtained using the subpixel mode. The increase shown by a-b in Figure 4.15a shows the increase in accuracy between the single pixel and subpixel mode, for the sub-optimal parameters, and the increase a-c for the optimal parameters. The highest accuracies, and the highest increase in accuracy between single pixel and subpixel modes, are achieved when the mean

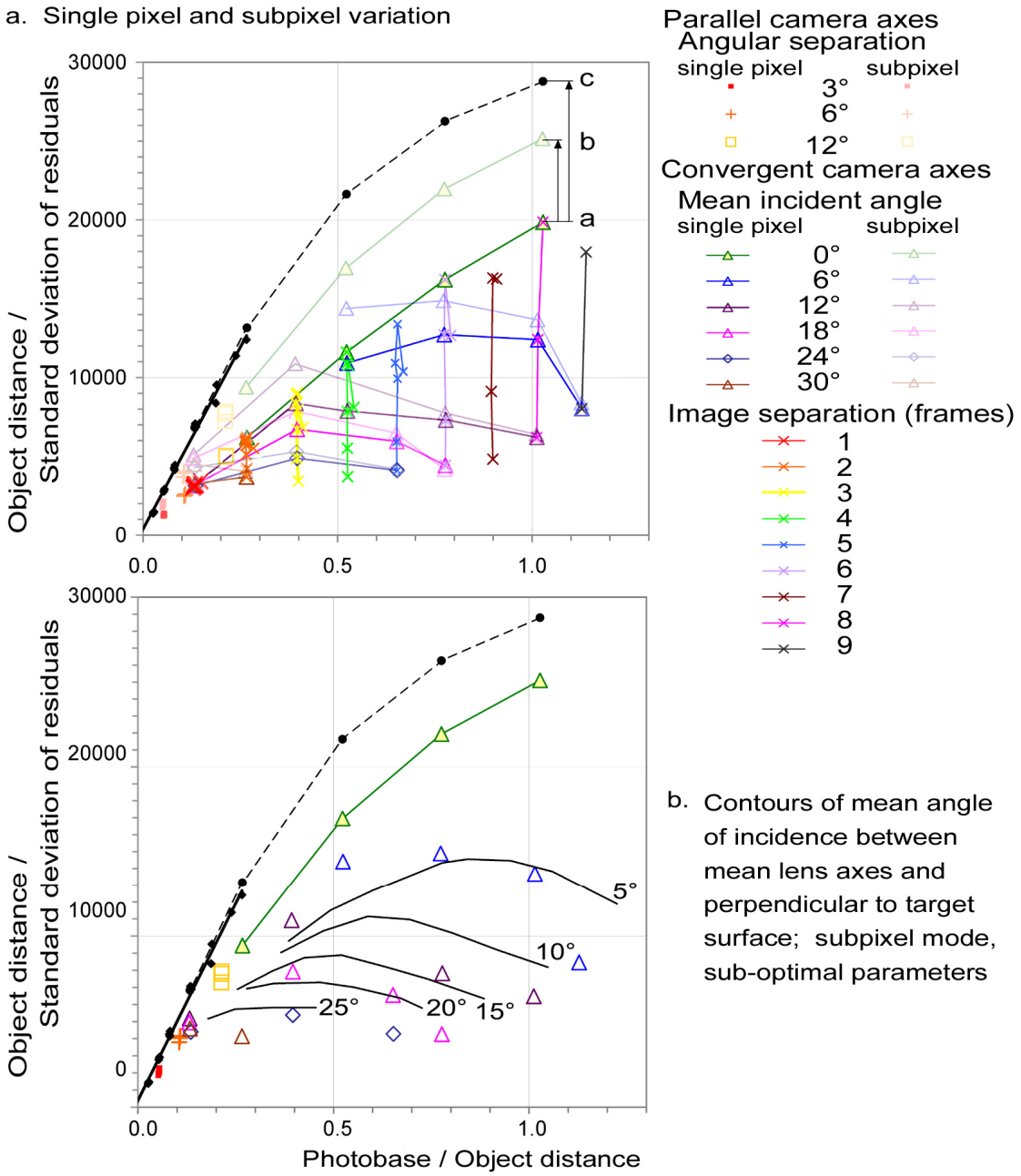

Figure 4.15 Data for parallel and convergent lens axes showing effect of mean angle of incidence and image separation (approximately equivalent to photobase) for 50mm lens, parallel and convergent camera axes

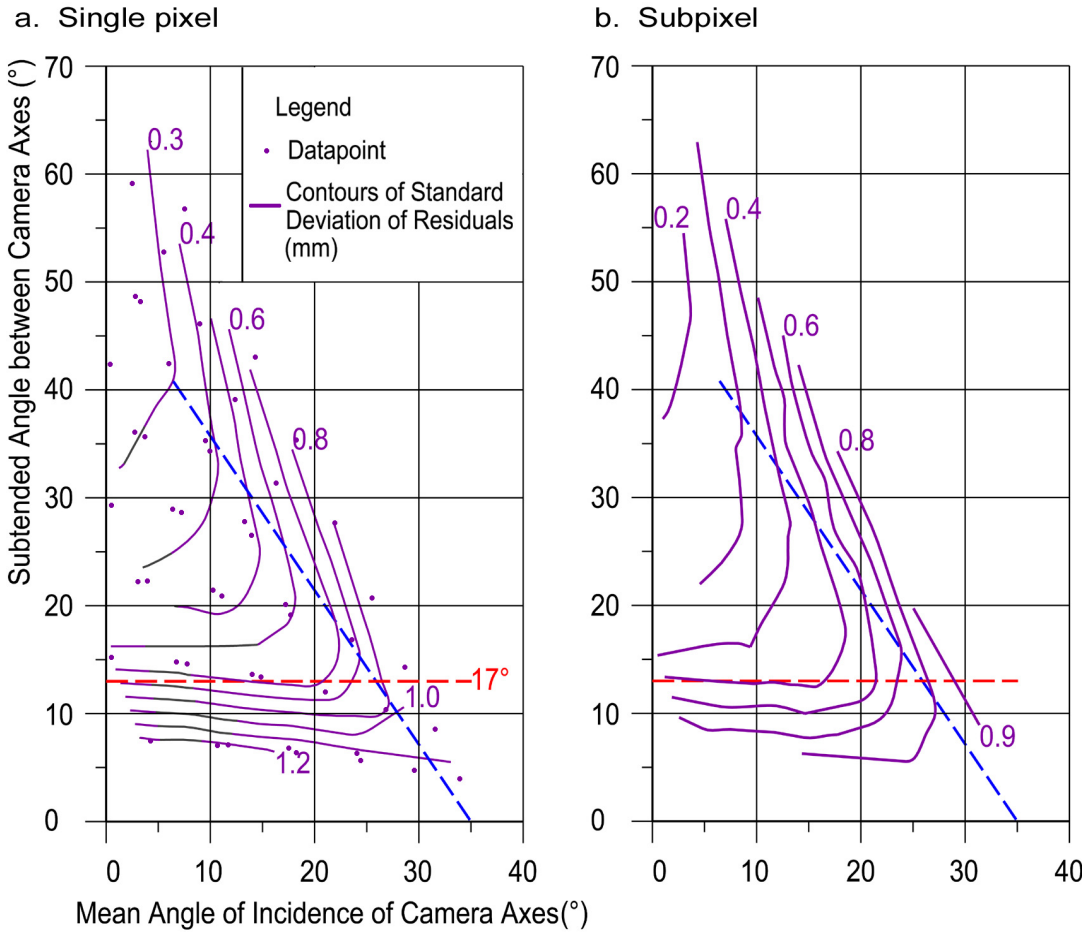

Figure 4.16 Contours of the variation of standard deviation of residual with changes in the angle subtended between the lens axes in convergent imagery, and the mean incidence angle between the lens axis and the normal to the measured surface

incident angle is close to zero, i.e., when the stereopair is symmetrical on either side of the target surface. Even a mean incident angle of 5° reduces the accuracy by between 30 and 40%.

Figure 4.16 has been compiled to illustrate the degradation in measurement accuracy with changes in the photobase (equivalent to the angle subtended by the two lens axes for convergent imagery) against the mean incident angle for measurements of the granite plane using convergent imagery obtained with the 50mm lens.

Comparison between Figures 4.16a for single pixel mode and Figure 4.16b for subpixel mode, demonstrates that the basic pattern is similar, but that the standard deviation of residuals is lower for the subpixel mode. In both cases, there is a central triangular zone with subtended angles greater than 17º, where the smallest standard deviations of residuals are found. In both cases, the accuracy of measurement of a

plane decreases rapidly, firstly with the increasing angle between the mean axis of the pair of lens orientations and the normal to the measured surface, and secondly, with subtended angles less than 17º, corresponding to a photobase:object ratio of 0.288.

The effect of using different focal length lenses has not yet been studied, but the results of this determination are of great relevance to studies of rock slope orientations such as was carried out in Chapter 6. However, it should be stressed that these tests were not comprehensive, using only a few variations in controlling parameters.

4.1.7 Effects of Variations in Camera Orientation: Discussion

With respect to the effect on image correlation for point measurement, consider the effects of the relative positions of a pair of images taken along either the curved or straight photo runs. To simplify the discussion, consider the effect of camera position and direction on a flat target oriented perpendicular to an initial camera position as illustrated in Figure 4.17a and b. The case with the camera axis remaining parallel (Figure 4.17a) is the normal case for vertical aerial photography. As the camera moves past the target, assuming that the systemic distortions have been adequately modelled, the width of the image subtended by the target remains constant (similar triangles) because the ratio of the focal length to object distance

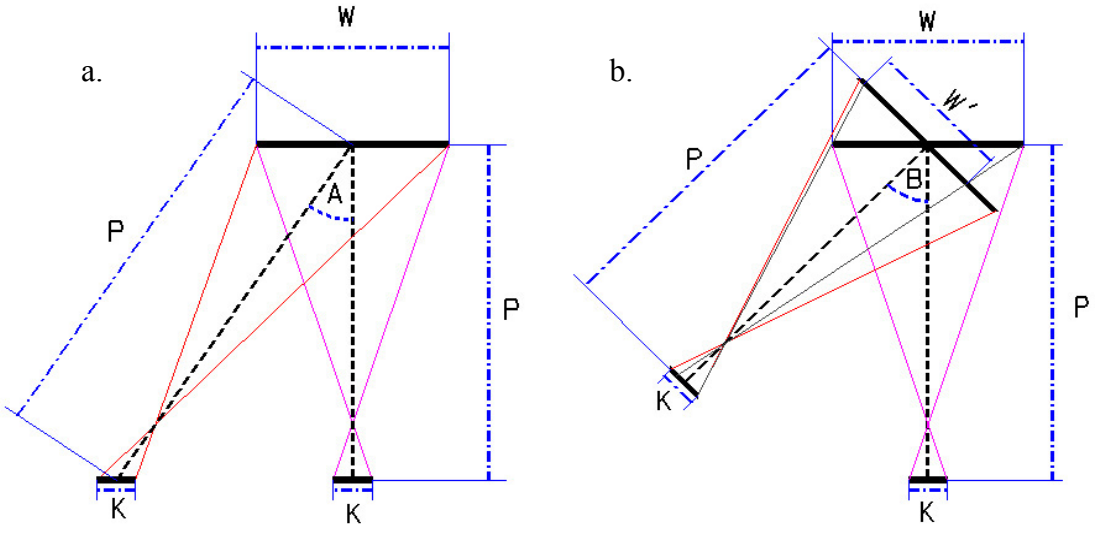

Figure 4.17 Geometric changes to correlation window due to relative lens axes

remains constant. Consequently, when parallel images are used for image matching, as is the normal case for aerial photogrammetry, the only changes in geometry between the reference kernel and the search window are related to parts of the target being visible or obscured because of the changing view direction.

When consumer grade non-metric cameras are used, the mechanics and optics of the systems are not as stable as for metric equipment, and the camera calibrations may not model the distortions as consistently as for metric cameras. To provide one example from studies carried out for this dissertation, although full camera calibration had been carried out in both the laboratory and in the field, this effect was noted when using the same 'prosumer' grade non-metric Canon camera in the Boya Quarry modelling (Chapter 6), when a significant Y parallax error was found when using stereo pairs with a very wide photo base and image overlaps of <50%.

Figure 4.17b illustrates the effect on imaging geometry when the camera is moved in an arc around the target. The width of the target (W) is foreshortened in the imaging array (W') as the angle between the camera directions (B) increases. Considering a flat target, the scale is shortened by the sine of the angle between the two images. The effect on the image correlation coefficient *r* will be greater than for the case when the camera axis remains parallel by a factor of the sine of the subtended angle (B). The consequence of the scale change is that, at pixel to pixel correspondence, the reference kernel and search window will not be comparing the same coverage of the target.

Kraus (2000) observes that the image correlation coefficient *r* responds favourably to edges. When a single high contrast edge is present in an otherwise uniform surface, the effect of reference to search window scale changes is not likely to be significant as the change in image densities will be identifiable, even if the specific area coverage of the target is not the same. However, if more than one high contrast edge is present within the reference kernel, the correlation coefficient *r* will decrease with angle-induced scale changes and consequent degradation of image matches.

4.2 Investigations of the Phase-wrapped Surfaces

Some initial investigations into the nature of the phase-wrapped surfaces are described in this section, which reveal a few characteristics that may need to be studied further; however, these investigations have not been exhaustive. The possibility of phase-wrapping effects should be considered when noting the error sources of DEMs produced by area-based automated image correlation. It should be noted that this phase-wrapping behaviour was also observed when tracking across the granite target using the terrain-following cursor function as implemented within the uSMART package. Consequently, this effect may have increased the measurement error for the mapping results obtained in the application of the uSMART package in other studies carried out in this dissertation, particularly Chapters 6, 7 and 9, as these studies were performed using values for the 'DEM position variance' and 'Y axis of the search area relative to the reference window' within the critical zones identified in Chapter 4.1.3. The possibility remains that the phase-wrapped surfaces are due to some quantisation limitation within the image measurement or processing system, including inadequate camera calibration, but this has not been identified.

4.2.1 Effects of Variations in Photobase

Variations in the pattern of phase-wrapped surfaces with changing photobase are shown for the parallel lens axis run using the 50mm lens in Figure 4.18 for single pixel mode; only the 10cm photobase stereopair P04-05 contains the central part of the concentric phase-wrapped structures. As the photobase increases, the surfaces increase in gradient and the number present within the same measured DEM; in this case, 400mm by 300mm at a spacing of 5mm. As demonstrated in Figure 4.4, the number of surfaces present may have increased as a result of the target surface dipping at 4º towards the top of each model. The patterns also show the side of the concentric pattern, which appears to be due to slight rotations of the lens of ±2º due to misalignment of the tripod when moving across the measured baseline. The phase-wrapped surfaces in Figure 4.18 have been sequentially coloured to highlight the number of surfaces present in each stereopair.

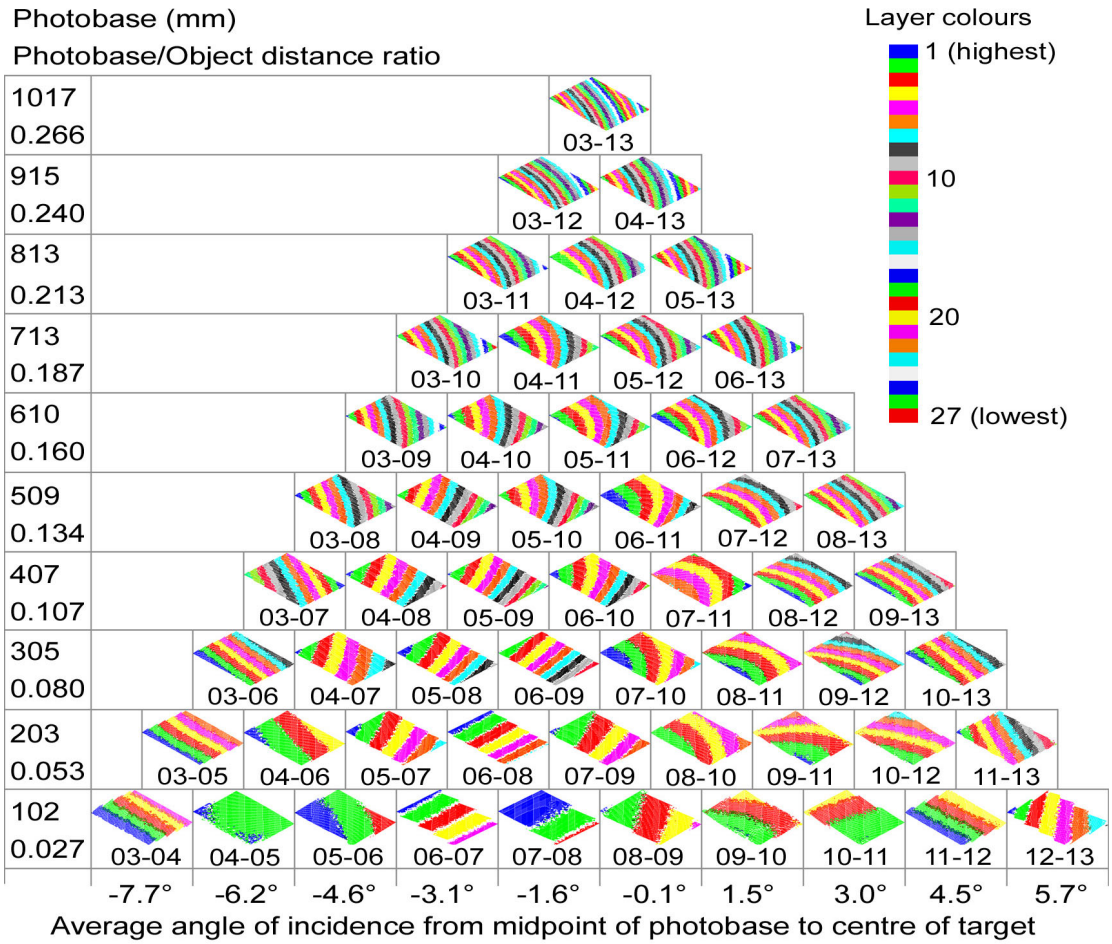

Figure 4.18 Patterns of phase-wrapped layers resulting from increases in photobase; single pixel mode: 50mm lens, parallel lens axes

4.2.2 Nature of the Phase-wrapped Surfaces

The surfaces in two of the stereo models have been investigated in more detail. Model P04-05 was chosen because this is dominated by a single surface with only a small region of a higher layer. Model P07-10 was also chosen as this has a larger photobase:object distance ratio than model P04-05, and the two images were taken from approximately symmetric positions on either side of the centre of the target (Figure 4.18).

Individual point clouds of XYZ coordinates were extracted from both models. Each point cloud was input into 3D data modelling routines available for public use at James R. Phillips' website, ZunZun (2007).

Figure 4.19 and Table 4.1 show the results of processing the most extensive layer visible in P04-05 (green layer in model 04-05, Figure 4.18) through the "User-selectable polynomial" routine at ZunZun.com, using various polynomials with the

highest maximum power of X and Y between one and four. Although there is no obviously better pattern to the distribution of residuals shown in Figure 4.19, the lowest standard deviation for the length of the residuals is 0.039mm obtained when using a polynomial of maximum power x^3 and y^2.

Table 4.1 Goodness of fit for various polynomials for Layer 2 in Model P04-05

Residual (mm)	Maximum powers of X and Y used in polynomial									
	X1 Y1	X2 Y1	X1 Y2	X2 Y2	**X3 Y2**	X2 Y3	X3 Y3	X4 Y3	X3 Y4	X4 Y4
Min.	-3.982	-0.396	-3.772	-0.444	**-0.379**	-1.122	-0.856	-0.392	-1.236	-0.525
Max.	2.565	1.152	1.767	0.173	**0.116**	0.312	0.214	0.186	0.315	0.287
Range	6.547	1.548	5.539	0.617	**0.496**	1.434	1.070	0.578	1.551	0.812
Mean	0.000	0.000	0.000	0.000	**0.000**	0.000	0.000	0.000	0.000	0.000
Std. dev.	1.498	0.311	1.417	0.054	**0.039**	0.126	0.086	0.049	0.151	0.077

The variation in distance between Layers 1 and 2 in model P04-05 as determined by multiplying the vertical distance between each layer by the cosine of the gradient of Layer 2, ranged from a minimum of 19.700mm to a maximum of 20.011mm; this constitutes about one part in 1900 of the object distance (3.808m).

Model P07-10 has a greater photobase:object distance ratio (0.080) than Model P04-05 (0.026) and contains seven layers within the same measurement area. The layers were separated and passed through the polynomial fitting routine at ZunZun.com to obtain the coefficients of the cubic polynomial surface. An attempt was made to

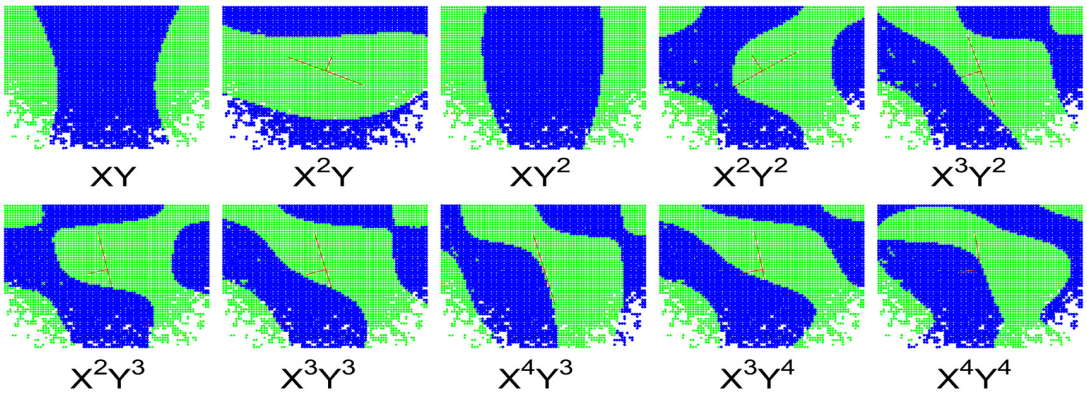

Figure 4.19 Positive and negative residuals after removal of various polynomial surfaces from plane L2 on Model P04-05

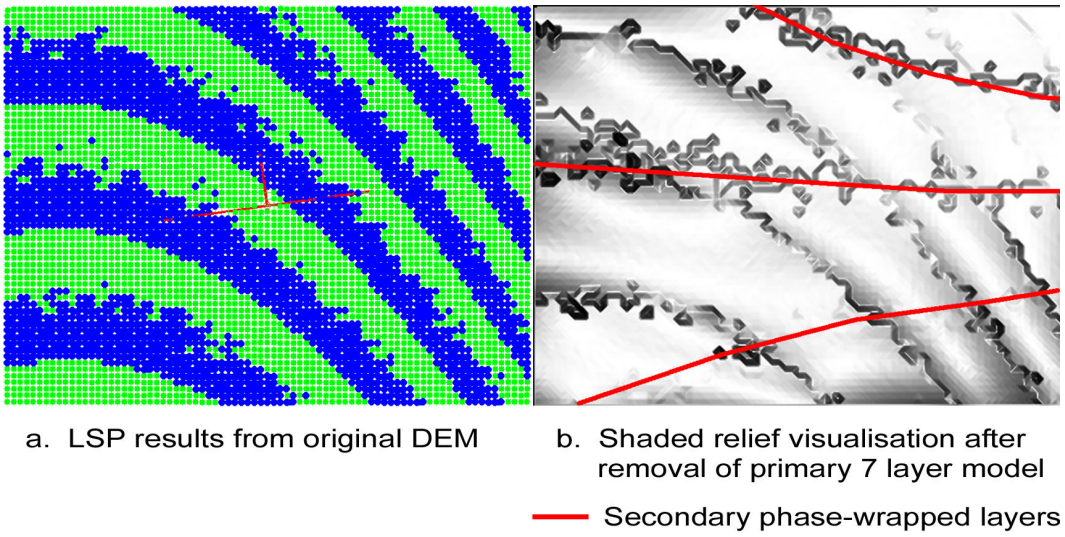

Figure 4.20 Primary and secondary phase-wrapped surfaces in Model P07-10

remove the effect of the phase-wrapping by testing each point in the original model against each of the layers and selecting the minimum absolute value for the corrected residual.

The resulting surface is shown as a shaded relief model in Figure 4.20b, as compared to the original LSP visualisation in Figure 4.20a. The interesting point to note here is that the primary phase-wrapping has not been completely removed, and that a secondary set of phase-wrapped surfaces is now apparent. It appears that the variations caused by the secondary phase-wrapping have limited the effectiveness of determinations of the surface coefficients for the primary set of surfaces. These secondary surfaces have been identified also in some of the other models where surface removal was attempted.

Comparison of the patterns of points successfully correlated when using the very small values for the variance in DEM position shown in Figure 4.7a shows that this appears to be very similar to that of the secondary phase-wrapped surfaces, as both results have used the same model, P07-10.

4.2.3 Phase-wrapped Surfaces Generated with the 28mm Lens

Figure 4.21 shows the patterns of phase-wrapped surfaces that are produced when using the single pixel mode on concentric imagery obtained using the 28mm lens.

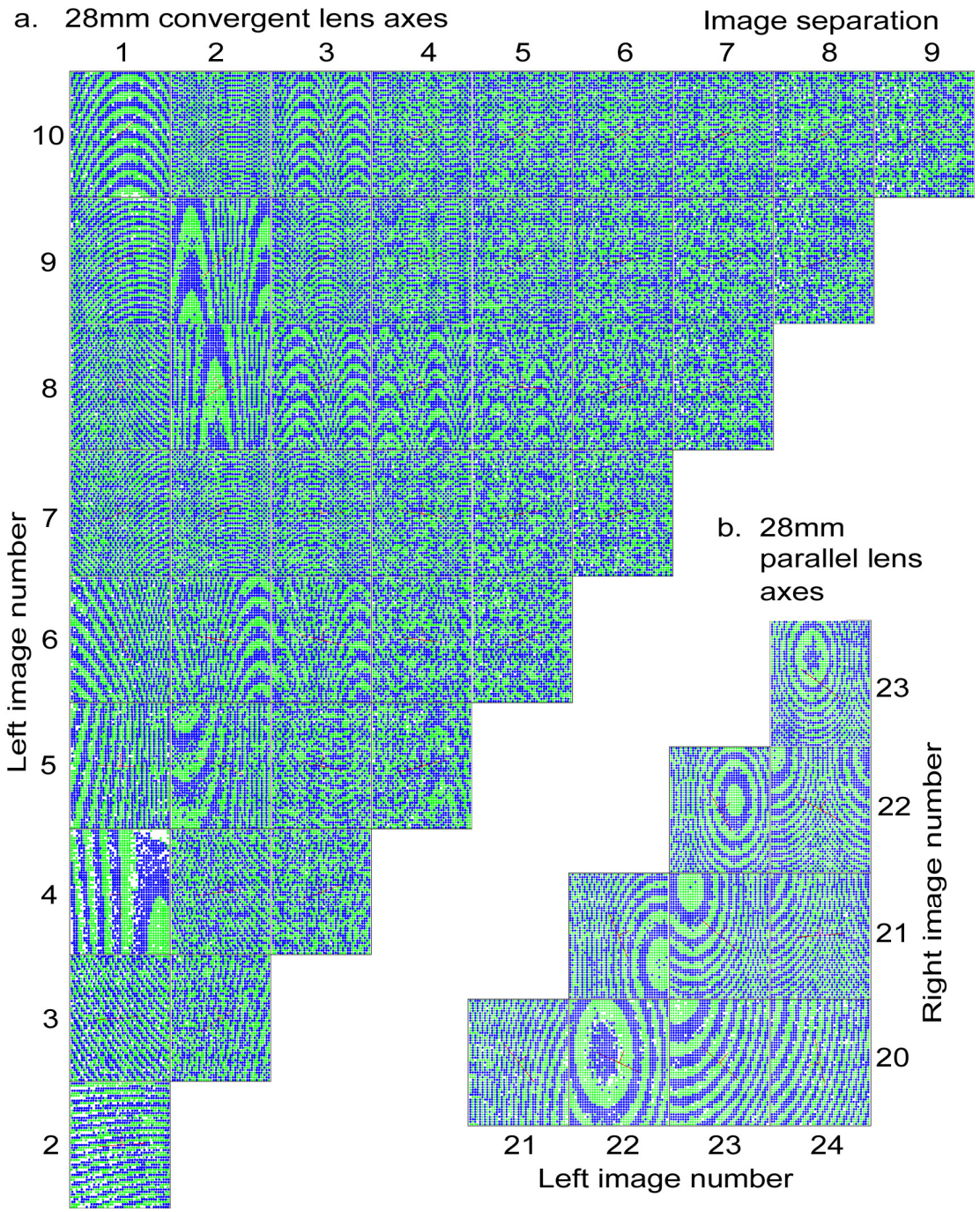

Figure 4.21 Pattern of phase-wrapped surfaces obtained from DEMs of parallel and concentric imagery taken with the 28mm lens

In the case of the 28mm lens set up, the target was kept closer to perpendicular to the lens during the parallel runs, consequently, the centres of the ellipsoidal patterns occur in several of the model results. The patterns for parallel run models 24-22 and 24-23 in Figure 4.21 clearly show two overlapping sets of phase-wrapped layers. For the concentric imagery in Figure 4.21a, only half of the possible set of stereopairs

has been included for clarity; Image 01 lies at an incident angle of 36º, while image10 has an incident angle of 0.2º; the patterns become generally more complex for the concentric lens axes shown in Figure 4.21a. The ellipsoidal concentric patterns tend to be narrower in the x axis than for the parallel imagery, and for many of the stereo pairs, the patterns appear to be affected by aliasing where the separation of the layers is close to or less than the DEM sampling interval. Apparent simplicity in the pattern is not limited to those models with very small mean incident angles; model 0403 (left image 4 with image separation of 1) shows only five layers despite a mean incident angle of 29º.

4.2.4 Discussion

The origin of these patterns was considered initially to be due to quantisation effects derived from uncorrected Y parallax the single pixel sampling interval; while this is possibly true, the complexity of the structure suggests an alternative origin as the resultant surfaces are the result of interference or interaction between two concentric patterns centred on each of the two images in the stereopair.

Read and Graham (2002) commend using small format (35mm) single lens reflex (SLR) cameras for many applications including remote sensing and oblique aerial photography, because of low equipment costs and wide range of lenses available. They advise that zoom lenses may have inferior resolution and caution that automatic focus may limit image quality by causing uncontrolled changes in focal length.

4.3 Effect of Variations in Image Resampling

Digital image files contain large volumes of data and the storage and transmission of these files can present problems, both within the camera and during processing. This problem is not limited to photogrammetry, and standards have been developed to define formats where the size of the image files can be reduced. There are two forms of image compression, lossless and lossy, depending on whether the original data can be replicated by reversing the compression process. The effects of this can be significant to the accuracy of feature identification - including ways that may not be apparent on initial inspection of the images, especially where high levels of detail are being measured.

Image size is a significant factor in the use of digital cameras, due to the cost of the storage medium and the transfer rate for the processed image onto the storage medium inside the camera. The latter is particularly significant when taking photographs under time-limited circumstances, such as when movement limits the time available to capture the multiple photographs necessary to adequately measure the target. This can occur either on the part of the camera as in a helicopter taking oblique or vertical aerial photographs, or when photographing a moving target such as a debris flow or flood. Consumer-grade digital cameras have smaller internal memory buffers than 'professional' or the intermediate 'prosumer' grade equipment, and commonly require the image to be processed to a compressed format for transfer onto the removable storage medium.

'Prosumer' and professional grade digital cameras may possess the option to store images in 'raw' formats; while these remain proprietary for each manufacturer, the aim is to store the image in an unprocessed form, allowing greater flexibility in signal processing once the image is downloaded to a computer. Raw images may contain a wider dynamic range than the normal 256 by three layers (for colour images) of TIFF or JPEG formats, allowing detail to be extracted from over exposed or under-exposed portions of the image. This is probably useful especially in aerial photography, when time limitations and rapidly-changing sun and cloud conditions may render parts of an image under or over exposed in relation to most of the image.

Although not directly related to image compression, experience with a consumer-grade Leica digital camera, and a closely-related FujiFilm digital camera, revealed examples where the visible resolution of the stored image was lower than would be expected from the numbers of pixels forming the width and height dimensions of the image file. This was attributed to the conversion between the camera CCD array in which the measuring cells are arranged in an octagonal pattern (Fuji Photo Film Co. Ltd., 2001). Although this has the apparent colour-rendering advantage of allowing red, green and blue photodiodes on each line of the array, the total number of photo-detectors is only half the final rectangular grid of image pixels. Image pixel values are alternately measured directly at a photodiode, and interpolated from the adjacent photodiodes, resulting in a small but apparently significant amount of low pass filtering of the image detail.

The optical resolution of film (negative and diapositive) scanners has improved significantly over the past few years, and sub-11μm pixel scans can be obtained from 35mm and 120mm (medium format) film. Many high-end consumer and mid price-range 'prosumer' digital cameras have arrays with more than five million pixels, allowing capture and rapid transfer of high resolution digital images into computers for further processing, removing the need for film scanners. Camera memory capacity (also known as 'digital film') costs are decreasing per megabyte, providing a cost-effective opportunity to capture large numbers of images within a short period of time.

Compressed images, particularly if stored in-camera using the 'raw' (i.e., native array) format allow high image storage capacity. For example, the Canon EOS 10D used in the case studies in this Chapter and Chapters 6 and 9, can store approximately 76 raw format colour images at 3072 by 2048 pixel resolution on a 512Mb Compact Flash card, with each 7Mb raw image expanding to 18.5Mb in TIFF format. Use of the raw format allows data extraction across a greater dynamic range (10 bits per pixel, i.e. 1024 quantum levels, both within shadows and very bright regions) than in-camera conversion to the eight bit TIFF or JPEG; the latter may also result in file compression-losses. For example, this can be significant in imagery of rock slopes where overhangs can create shadows that may partly obscure prominent rock surfaces, while upward-facing surfaces may be brightly illuminated.

The effect of data loss that results from image compression from the use of JPEG has been investigated with regard to photogrammetry by Lam et al. (2001; Li et al, 2002), and in the case of medical diagnostic imagery by Smith et al. (2000) and Siragusa and McDonnell (2002), who found that diagnostic interpretation was restricted by loss of edge detail in JPEG images compressed to a size greater than six times smaller than the equivalent TIFF file. Lam et al. (2001; Li et al, 2002) demonstrated that the use of JPEG-compressed images up to a compression ratio of approximately ten presents no significant loss of measurement quality; above this value, the loss of accuracy increases approximately linearly with compression ratio. Two visible image artefacts are generated by high levels of JPEG compression (i) typically a 'blocky' appearance due to gross variations between each 8x8 pixel compression block, and (ii) a loss of detail within each 8x8 pixel block due to

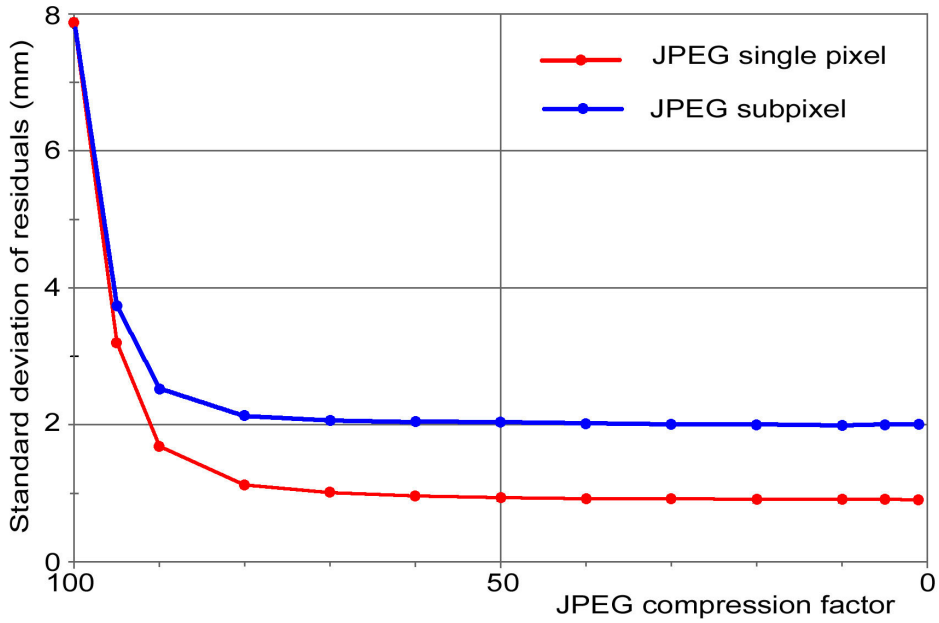

Figure 4.22 Effect of changes in the JPEG compression factor on the standard deviation of residuals for model P07-10, 50mm lens, single and subpixel modes; 20x12 pixel correlation kernel.

smoothing (Paola and Schowengerdt, 1995). The consequences of image compression using JPEG 2000 has been studied by Shih and Liu (2005), who note that, while an increase in image compression also leads to lower elevation accuracy, the results are generally more favourable than for compression using JPEG. As a general conclusion, all the above authors have noted that some loss of measurement resolution is inevitable under higher compressions, especially for high contrast edges where these effects are most apparent, and where the image has a rich texture.

Figure 4.22 shows the effects of JPEG compression on the standard deviation of residuals obtained during stereo matching for the granite slab using stereo pair P07-10, with the 50mm lens; as the compression factor decreases (increasing file size and image quality), the standard deviation of residuals declines, but the standard deviation of residuals remains stable for large compression factors up to about 70. The correlation kernel used in this test was 20 pixels in the X axis, by 12 pixels in the Y axis, considerably larger than the eight by eight pixels of the JPEG compression pattern. Smaller correlation kernels have not yet been tested but are likely to yield poorer results as the JPEG sampling box may create edge artefacts within the correlation kernel. These effects are likely to be less prominent in imagery compressed using wavelets such as with ER Mapper's ECW or JPEG2000.

Table 4.2 Variations in standard deviations of residuals with resampled imagery

Image Pixel size (μm)	Resampling method	Correlation kernel size (pixels)	Correlation Mode (pixels)	Standard deviation of Residuals (mm)
14.8	Bicubic	10x6	Single	2.954
	Bicubic	20x12	Single	1.998
	Bicubic	40x24	Single	0.906
7.4	Original	20x12	Single	1.991
			Sub	0.889
3.7	Bilinear	20x12	Single	1.454
	Bicubic	20x12	Single	1.443
1.85	Bilinear	20x12	Single	2.944
	Bicubic	20x12	Single	2.914
	Bicubic	20x12	Single	2.914
	Bicubic	40x24	Single	1.215
	Bicubic	80x48	Single	0.496

As a final test, the original imagery was resampled to change the effective pixel size, and the results are shown in Table 4.2, which should be read in conjunction with Figure 4.8. As expected, the error increases with increasing kernel size for each variation of the sampled image. This is an important consideration, because resampling the image will change the area of the target sampled in the correlation kernel unless the latter is modified accordingly. The most significant result of the Table 4.2 is that it is possible to reduce the standard deviation of residuals by resampling to reduce the effective pixel size whilst increasing the size of the correlation kernel by a corresponding amount; e.g., halving the pixel size from 7.4μm to 3.7μm while increasing the correlation reference kernel from 20x12 to 40x24 pixels, reduces the standard deviation of residuals by 27%. Resampling the image to 1.85μm pixels and increasing the correlation window to 80x48 pixels reduces the standard deviation of residuals by 75%, to a value lower than the results for the subpixel mode. The disadvantage of this is the large file sizes, but even with resampling to 25% original pixel size, the size of images from a consumer or prosumer grade digital camera should remain smaller than a full size vertical aerial photograph which the proprietary photogrammetric products are generally designed to handle.

Ahmed and Chandler (1999) compare the precisions and accuracies of three Kodak digital cameras, models DC40, DCS420 and DCS460. They found that precisions increase linearly with the resolution of the CCD array, as the pixel size in each camera is similar, at 9μm, from 1:8500 for the DC40 with 756 pixels in the X axis, to 1:36,100 for the DCS460 with 3060 pixels in the X axis. Although the configurations of the cameras are different in this case, the results are broadly support the findings of the current study.

4.4 Chapter Summary: Area-based Image Correlation

The preparation of high density DEMs for a smooth planar surface was originally intended to investigate the behaviour and quantify errors due to the automated image matching algorithm, independent of variations due to errors in ground survey and undulating terrain. The phase-wrapped layering effect that was found to dominate DEMs created when the procedure is operated in single pixel mode, and under some parameter settings when operated under subpixel mode, was not anticipated. Although the consequences of this effect are significant and relevant to the application of terrain assessment and mapping when carried out using 3D visualisation and measurement techniques, the origin of the effect has not been identified.

The use of the granite slab target has demonstrated that smooth, highly textured targets can be extremely valuable in testing image correlation algorithms and controlling parameters as well as the scale of systematic measurement errors due to the camera and lens systems. Effects due to single-pixel precision within the controlling algorithm may partially remain even if subpixel accuracy measurement algorithms are implemented, especially with sub-optimal variations in some of the controlling parameters. The phase-wrapping effect appears to consist of two overlapping ellipsoidal sets of surfaces each possibly related to the lens axis and which may be of significantly different magnitudes. The possibility remains that the phase-wrapped surfaces are due to some quantisation limitation within the image measurement or processing system or incomplete modelling of the lens distortion.

Parameters found to be critical to the optimum application of the area-based image correlation algorithm include:

(a) Within object space, the location of the DEM posts should be allowed to vary by at least half a pixel along both the X and Y axes;

(b) Within image space, the Y dimension of the Search window should be at least 6 pixels wider than that of the reference kernel; larger search windows have no detrimental effect although search times for each DEM post will be greater due to larger processing overheads;

(c) Reference kernels should be kept small; the range 10 to 16 pixels was found to produce stable results. Smaller kernels resulted in larger standard deviations of residuals while larger kernels reduce the ability to identify local variations in topography.

At about 39μm, the standard deviation of the residuals of the distance between the DEM posts and the least squares best-fit plane obtained after removal of the phase-wrapped effects suggests that this effect could have some potential for the measurement of very small deformations in planar targets. This will be particularly valuable if the mechanism behind this effect can be identified and quantified. While the accuracy of subpixel measurements approached one part in 29,000 for convergent imagery using the 50mm lens with a photobase:object distance ratio of unity, accuracies of 0.039mm over an object distance of 3.759m gives an accuracy of one part in 96,000.

Under normal operating conditions, the uSMART software as applied to the projects in this dissertation has proved capable of measuring adequately textured terrain with an accuracy of between one part in 1500 for small photobase:object distance ratios of around 0.1, up to one part in 8000 for larger photobase:object distance ratios, especially where some convergence of the camera orientations is possible. Consequently, careful design of the imaging network is paramount. Unfortunately, the maximum accuracies achievable as determined by the present study have been compromised by operational constraints identified within the automated image correlation parameters; some limited testing has been able to demonstrate that results between 20 and 40% better in terms of reduction in the standard deviation of residuals could be achieved if the optimum correlation parameters had been used.

Tests using imagery obtained with the camera axes aligned parallel and in a convergent arc around the smooth, highly textured granite target have demonstrated

that area-based image correlation is able to generate successful correlations over a wide range of orientations, from perpendicular to over 35º from the normal to the target plane. Systematic errors as quantified by the reduced standard deviation of residuals become less pronounced at photobase:object distance ratios smaller than 0.288, and as the mean angle of incidence between the lens axes of the stereopair and the normal to the target plane increases; where the imagery is approximately symmetrical about this normal, adequate correlations can be achieved with highly convergent imagery. The limiting factor appears to be scale and perspective distortion between the two images.

Chapter 5 discusses the development of photogrammetric methods to extract morphology from non-planar surfaces as a precursor to adding interpretive elements for the creation of 3D geomorphological maps and models.

Chapter 5

EXTRACTING MORPHOLOGY FROM DEMS

5.1 Integrating Photogrammetry and GIS

Morphologically, hilly terrain is often a complex association of landform units with concave, convex and rectilinear curvatures in both plan and profile (Figure 2.7; Ruhe 1975). Automating the identification of terrain morphology for inclusion within a geomorphological map requires either the identification of a single terrain parameter, or an overlapping set of scale-dependent morphometric attributes. However, the constraints of existing softcopy technology require linear cartographic elements to be stored as 3D vectors if they are to be superimposed as an overlay onto images with known camera location, orientation and geometric calibration; the vector overlay is generated separately for each image by applying to each vector the parallactic distortions modelled by the camera calibration and orientation. Scale-correction is also applied to ensure the visual elements retain a constant width. Stereo systems use dynamic display of two images to create the visual illusion of a 3D model; with tracking and zooming being performed in real time, the vectors are converted to a raster for superimposition at a scale suitable for the visual display and need to be continually updated as the image zooms and pans. Multi-image systems may generate vector overlays for all the open images (e.g., PhotoModeler); stereo-visualisation may be limited to a single pair of images but may need to accommodate vector updates during panning across the stereo view.

GIS systems are less restrictive and can allow superimposition of multiple rasters and vectors (e.g., ER Mapper), which is facilitated by creating the 3D visualisation by draping one or more 2D rasters over an existing DEM; the vectors are rasterised prior to overlay. Remotely-sensed imagery is rectified using similar camera/sensor calibration and orientation models to generate orthophotos prior to inclusion in any 3D visualisation.

Within the past few years, there has been an increasing overlap between GIS and photogrammetric software with basic photogrammetric functionality being added to GIS systems and visa versa, especially to high-cost systems. This trend will continue

in the future because of converging usage of both technologies in applications such as this study.

Comparisons of geometric parameters for the purpose of defining morphological boundaries are readily achieved using a raster data model. Before using extraction methods on samples of landslide-prone terrain, a numerical model of synthetic terrain was developed to test effects of extraction strategies on models with various amounts of data degradation, and to develop visualisation techniques to review the quality of the measurement data.

5.2 Measuring Surfaces by Direct Contact or Remote Methods

Landforms consist of groups of geometric primitives for which causative geomorphological and hydrological processes can be inferred (Chapter 2). The success of the interpretive phase of the identification procedure depends on the scale of the landforming process and its rate and longevity, particularly for large magnitude episodic events such as slope failures. Overlapping geomorphological processes may complicate landform interpretation due to the masking effect of subsequent processes where an initial landform is substantially modified over time. For example, a newly-formed landslide scar may contain a sharp convexity with a radius of a few centimetres or decimetres around the upper part of the scar, see Figure 2.12a (termed the ‘crown’; Crozier 1973; Varnes 1978; Hutchinson, 1988; IAEG Commission on Landslides, 1990; Cruden and Varnes, 1996). After a few years, this sharp convexity may become partly obscured by vegetation and partly rounded by the normal processes of soil erosion and transportation across a hill slope (soil creep, rain splash, sheet wash, rill erosion), as depicted in Figure 2.12b to d.

Consideration of the features visible in Figure 2.12a demonstrates that landslides can be morphologically complex landforms. However, some elements are more significant in terms of providing clues as to either the long-term degradation of slope stability, or the short-term triggers that initiate slope failure. These include landforms associated with planar or gently curving surfaces forming zones of weakness or changes in hydraulic permeability within the rock or soil mass that give rise to sliding surfaces across which the bulk of the material is transported (Wieczorek, 1996). These surfaces may be more or less identifiable within the

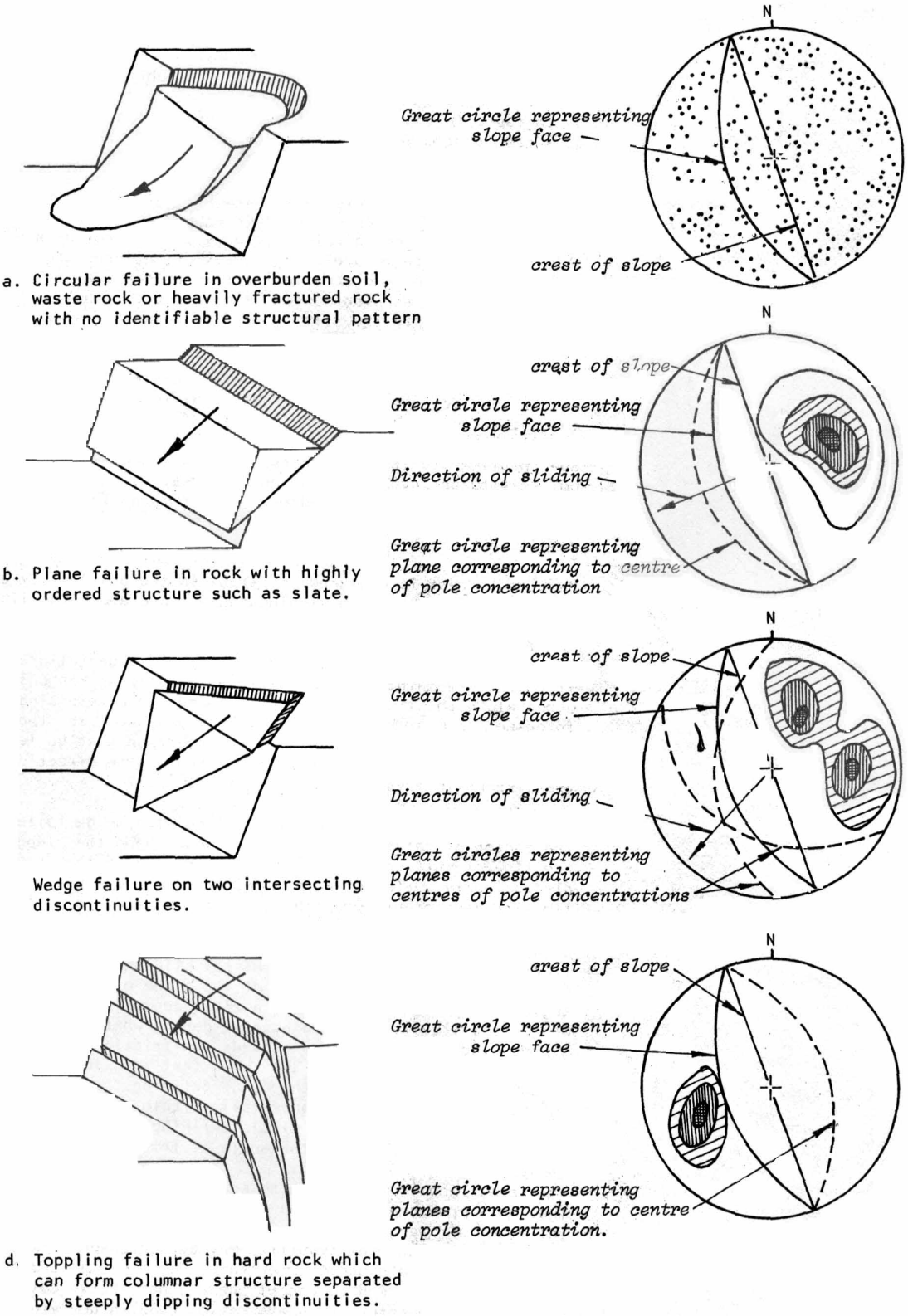

Figure 5.1 Modes of failure and their diagrammatic representation by density plots of surface normals (from Hoek and Bray, 1981)

landslide scar, depending on the amount of surface exposure and erosion that has occurred during and after the failure. Some of the larger planes of weakness within a soil or rock mass can also extend to form topographic features outside the failure scar or be visible on hillsides and rock outcrops prior to failure.

Correct measurement of the size and orientation of these features can be vital for the consideration of geomorphic processes and landform origin, and subsequent assessments of landslide susceptibility and hazard. For example, together with knowledge of joint roughness, measurement of the orientation of rock surfaces is vital to any kinematic assessment of a rock face prone to wedge or toppling failures, as depicted in Figure 5.1 (Hoek and Bray, 1981). Errors in the correct measurement of joint orientation will depend on the methods used. Measurement accuracy for rock surfaces obtained directly on-site using a clinometer and compass laid directly onto the rock plane can result in joint surface orientation measurements that may lie within ± two to five degrees of the real value (Chapter 6.4.2). Hoek and Bray (1981) describe a technique to measure the planar orientation of a rough rock surface with a circular plate to average the local undulations due to roughness. Repeated measurements of a single surface may yield slightly differing results, depending both on measurement error and consequences of local undulations in the surface, as the measurements are taken across a small section of the rock surface.

A plane may be defined using a direction (which needs two XY coordinate pairs) and a gradient (which needs three Z values), a total of seven observations. Within a cloud of points each defined within Cartesian geometry by a triplet containing an X, Y and Z value, the orientation of a plane can be determined from any three points. The resulting orientation will be well-conditioned, provided the three points are not colinear, in which case the orientation will be poorly constrained in any axis perpendicular to the line. As the three triplets contain nine observations, a least-squares estimation can be carried out to yield residual values for the variance of the direction of the plane, but no redundancy exists for the dip as defined by the three elevation values. Adding a fourth triplet point allows redundancy in both dip and dip direction, which has the advantage of identifying possible gross errors in the measurement, and of giving an estimate of the error in the orientation result.

Orientation can be determined remotely without contact measurement when this is determined with respect to the locations of a set of points; the application of photogrammetry is an obvious demonstration of this approach. The accuracy by which the surface's orientation can be determined will depend on the number and geometry of the points, the precision of measurement at each point, and the orientation of the images used in the measurement. Although these precisions would normally be determined with respect to the coordinate axes used to define the measurement space, for terrain applications the precisions should be determined also in relation to the geological context of the surface, i.e., the dip (angle between XY plane and the surface) and strike (direction of the intersection of the surface with the XY plane), and the perpendicular offset from the plane which is an indication of the surface roughness at scales within the resolution of the measurement separation.

Within any DEM being used to identify rock surfaces, the important issues are defining boundaries of the surfaces and measurement precision for individual points within or on that surface. All measurements contain errors and it is important to understand the effects of cumulative errors on the accuracy of determination of landform morphology. Use of a geometrically simple, synthetic numerical landform model allows the morphology extraction techniques to be evaluated in terms of data quantity and quality.

5.3 Synthetic Landslide Model

Natural landforms, especially those associated with slope instability, tend to consist of geometrically-complex shapes. A geometrically-simple model of a landslide similar to those found in the Hong Kong case study area, has been developed to investigate data extraction methods, and the effect of errors on data quality.

5.3.1 Aims of Model Development and Testing

The aim of the model is to generate synthetic point clouds to test extraction methodologies that may then be applied to photogrammetrically-generated point clouds of terrain containing landslides. The initial terrain model consists of a synthetic 'landslide scar' given simplified representation by part of the lower surface of an ellipsoid (see Figure 2.12a, from Varnes, 1978) intersecting a sloping plane representing the ground surface. This simple model was further refined by including

either one or two additional sloping planes exposed within the concave partial ellipsoid of the landslide scar. Figure 5.2 depicts the model, with the ellipsoid intersecting a steep plane representing the pre-failure ground surface; an additional two planes within the concavity represent planar features such as rock surfaces. The model is formed on a grid with 128 cells along each of the X and Y axes, with unit vertical exaggeration applied to the Z axis.

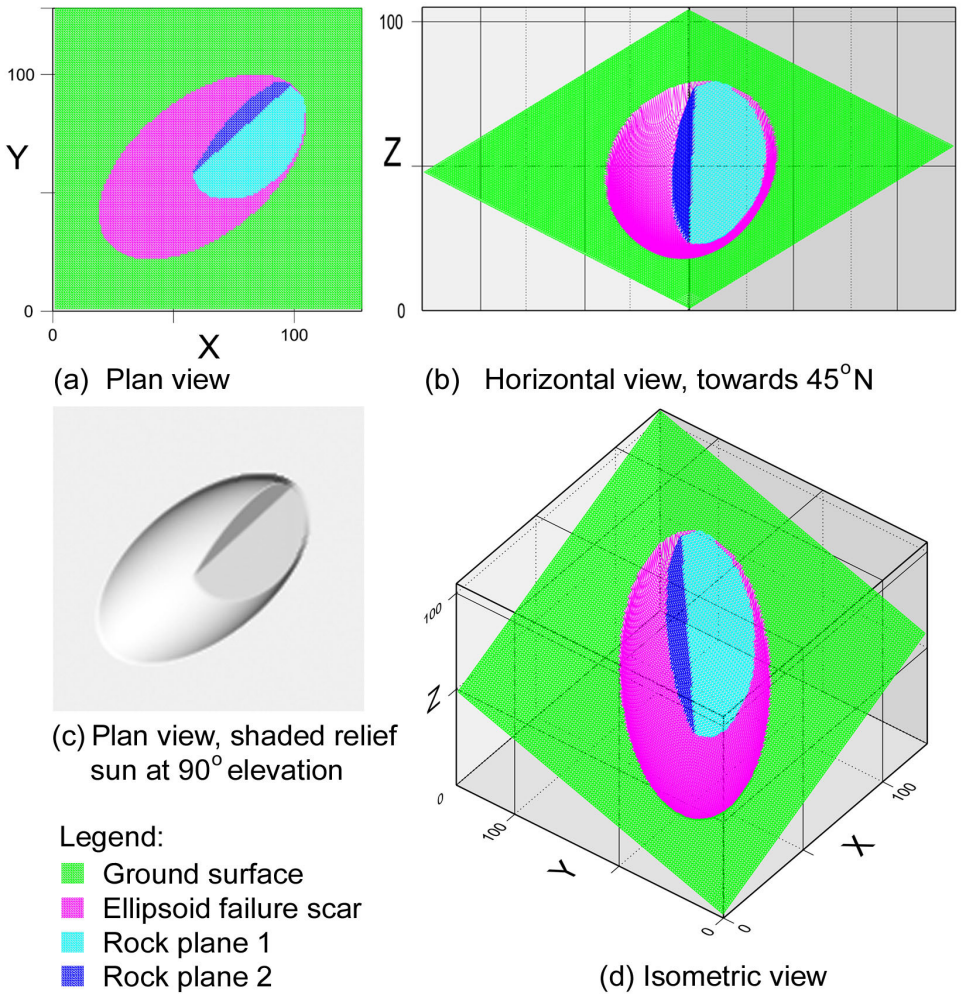

Ellipsoid Parameters:	a = 60; b = 30; c = 35
Centre of Ellipsoid:	x = 64; y = 64; z = 50
Orientation of Semi-major axis:	Dip = -30º, Direction = 230ºN

Plane:	Dip	Dip Direction
Ground	30º	230ºN
Rock Surface 1	45º	240ºN
Rock Surface 2	65º	290ºN

Figure 5.2 Parameters used in the synthetic landslide model

The synthetic numerical model allows:

(a) Visualisation of simple geometric primitives that can be found within natural landslide scars;

(b) Testing of visualisation methods for data used to define the landform;

(c) Assessment of the data requirements to successfully identify different types of geometric primitives; and

(d) Assessment of the effects of data degradation by errors in measurement of point data on the identification and extraction of geometric primitives.

5.3.2 Calibrating the Synthetic Model

The synthetic numerical landform model has been generated using MatLab script and consists of a grid containing 128 lines by 128 points. To calibrate the model against one particular landslide, the failure scar at One Rise More in Hong Kong, measured photogrammetrically in Chapter 7 (Figures 3.5a and 7.1), is approximately 14.4m wide and forms an image across 190 pixels of the 0.0125mm pixel resolution scanned aerial photograph number 9647, resulting in a ground pixel size of approximately 0.055m. In these images, the high-resolution photogrammetric scanning slightly exceeds the resolution of the original film, reported on the camera calibration certificate (Hunting Surveys Ltd., 1964) to be between 37 $lpmm^{-1}$ (line pairs per mm) at the centre of the image and 20 $lpmm^{-1}$ at the edges, giving ground image resolutions of approximately 0.06 to 0.11m respectively. Consequently, the smallest identifiable object is approximately 0.2m wide (Chapter 2.8.1). The maximum width of the ellipsoid is 57 model units; scaling this to the 10.7m width of the One Rise More landslide gives a model scale of approximately 0.19m per cell, similar to the smallest identifiable object.

While Equation 4.1 and 4.2 could be used to determine the accuracy of photogrammetric coordinate measurement, an alternative formulation derived by Moffitt and Mikhail (1980) gives:

$$\sigma_x = \sigma_y = \frac{\sqrt{2}H\sigma_i}{f} \qquad \text{Eqn. 5.1}$$

$$\sigma_z = \sigma_x \frac{H'}{B} \qquad \text{Eqn. 5.2}$$

Where:

σ_x, σ_y = standard deviations of horizontal measurement accuracy,

σ_z = standard deviation of vertical measurement accuracy,

σ_i = standard deviation of point measurement precision,

H' = flying height above target,

B = airbase (distance between perspective centres),

f = focal length of the lens.

The difference is that the horizontal accuracy is considered to result from the combination of the measurement accuracies for the X and Y axes.

For the One Rise More landslide, measurement on the 1963 aerial photograph stereo pair frames 9647 and 9648 gives:

σ_i = 1 image pixel = 0.0125 mm

H' = 675m B = 373m f = 0.15196m

Therefore:

$\sigma_x = \sigma_y = (1.414 * 675 * 373) / 0.15196 = 0.079$m

$\sigma_z = 0.079 * (675/373) = 0.142$m

The vertical measurement accuracy σ_v for the photogrammetric model of the One Rise More landslide above is approximately 0.75 of one unit cell.

5.3.3 Noise-free Model

The initial model was developed to include a steeply-sloping plane representing the ground surface. The orientation of the plane is easily adjusted, but the direction of maximum dip was chosen to be oblique to both the X and Y axes to reduce the effects of aliasing in the data. An ellipsoid was chosen as the landform most closely resembling a simple landslide scar, to limit the computational complexity and to allow ease of comparison of the extracted landforms to the original. Terzaghi and Peck (1967) note that the curved sliding surface within cohesive materials often resembles the arc of an ellipse. Hovland (1977) identified an ellipsoid as being more representative of non-planar failure surfaces than circular slip surfaces used in other rigorous slope stability computations (e.g. Fellenius, 1927; Bishop, 1955). The IAEG Commission on Landslides (1990) also uses an ellipsoid when defining suitable landslide dimensions for field measurement.

In addition to being able to adequately represent a curved surface, the model also needs to include multiple small, planar surfaces, representing rock joints and bedding planes exposed within the failure scar. In this case, this was achieved by defining two planes at elevations that intersect the ellipsoidal landslide failure surface, as shown in Figure 5.2. The larger plane dips at a gradient 15º steeper than the ground surface, and with a direction of maximum dip close to that of the ground surface. A second plane truncates part of the first rock surface, dipping steeply at 65º in a direction of 290º that is highly oblique to both the ground and the first rock slope, and was included to test measurement of an elongate but narrow feature, forming a prominent edge with the first rock surface. As can be seen from Figure 5.2, the rock planes intersect the ellipsoid at varying angles, and with varying exposure of the outer part of the ellipsoid above the rock surfaces. The numerical model takes no account of any increases in the radius of the convex edge between the ellipse, both rock surfaces and the original slope, as would be expected on a natural hillside with a layer of soil overlying the bedrock; as such, this may be more representative of a newly-failed slope than an older, partially eroded landslide scar.

5.3.4 Effects of Noise

The DEMs estimated for the smooth granite block in Chapter 4 demonstrate that some variation will occur in the measurement of point elevations due to small errors in the photogrammetric measurement process. When the coordinates of large numbers of points are estimated, the variations should generate a Gaussian

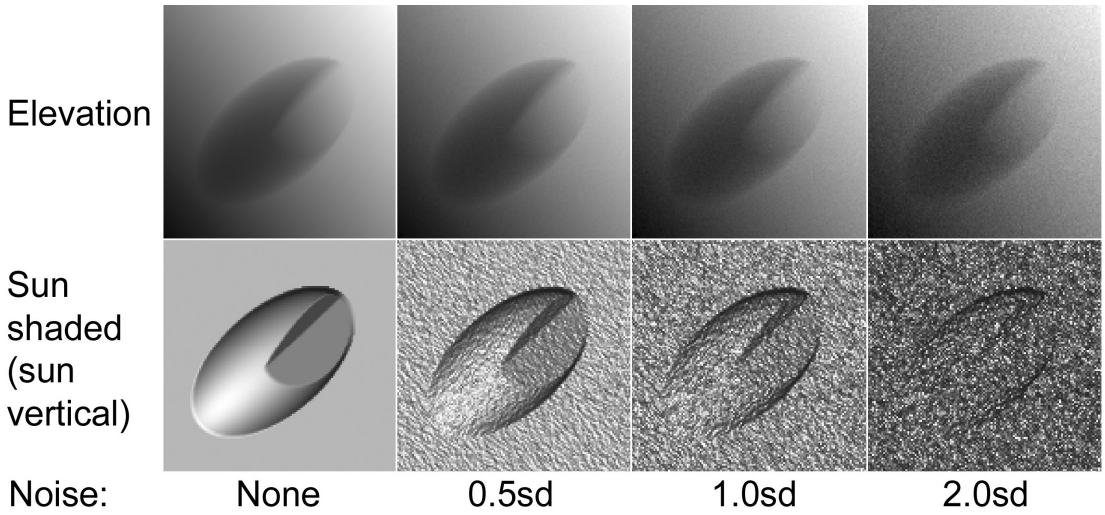

Figure 5.3 Elevation and shaded relief models degraded with up to 2 standard deviations of random noise

distribution of errors about the true surface; these variations will be identified as the length of the residual between the estimated point and the statistically-determined best-fit plane.

The noise model was added to the original synthetic surface to form composites with 0.5, 1.0 and 2.0 standard deviations of noise; the 0.5 and 1.0 multiples bracket the empirical vertical measurement precision determined in Chapter 5.3.2. The resulting three noisy synthetic models are shown Figure 5.3, together with the noise-free model. The sun-shaded images were generated using the standard routines in ER Mapper with a vertical sun elevation to minimise directional effects and enhance the lateral margins of the ellipsoid equally.

As might be expected, while increasing the magnitude of noise makes the elevation-shaded image visually only slightly less well-defined, the effects are considerably more apparent with the sun-shaded models. The sun shading is more photo-realistic, and with increasing amounts of noise, the four geometric elements become more difficult to visually identify, and the feature boundaries lack definition. With two standard deviations of noise, even the largest feature, the ellipsoid, is largely

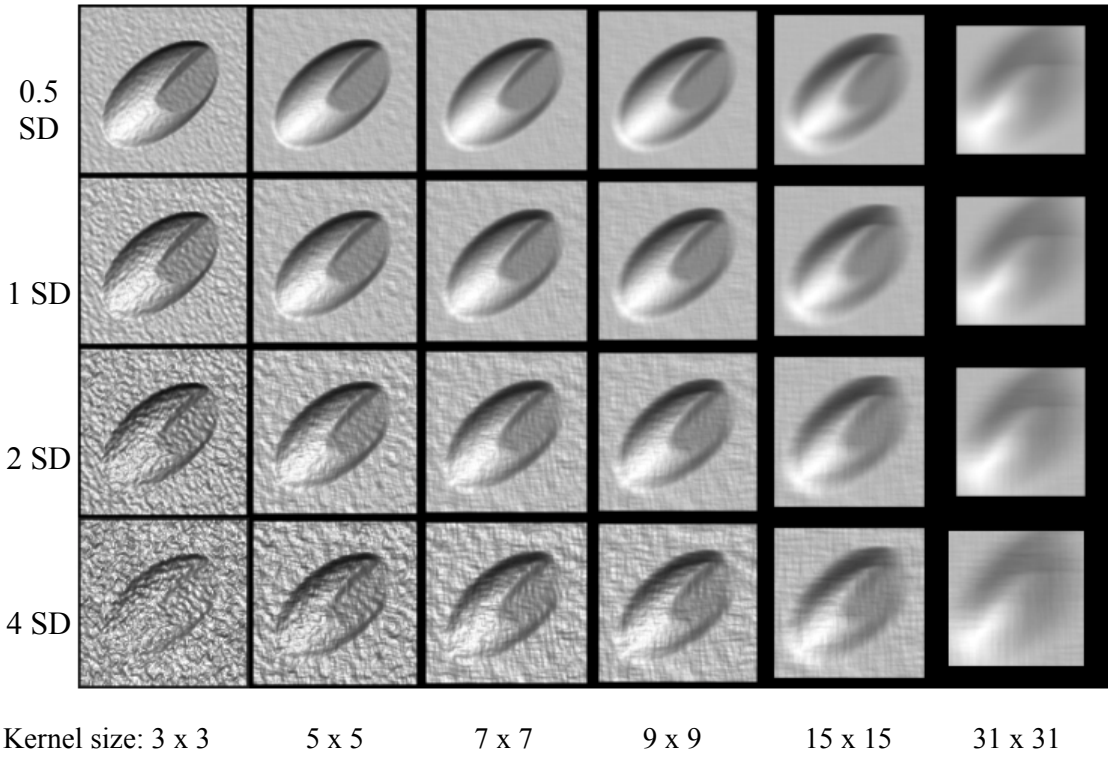

Figure 5.4 Use of smoothing as a simple noise reduction filter

obscured and the smaller planes are difficult to identify without prior knowledge of their presence. These results show that the addition of random noise has a strong effect in concealing the visibility of the landforms depicted in the model.

As the first stage in identifying suitable geometric elements for extraction as feature boundaries, the noisy models were convoluted with simple averaging kernels of varying square dimensions from 3x3 to 31x31 pixels using ER Mapper. The effects of this convolution are displayed in Figure 5.4.

The smoothed images clearly show that the visual recognition of component features improves significantly when the noisy data are convoluted with a low pass (simple averaging) filter. Where the addition of four standard deviations of noise almost completely masks the features visible without filtering, with the application of the smallest low pass filter (3x3 averaging), the four landform elements are rendered visible although the less prominent angular boundaries remain obscured. As expected, when the kernel dimensions approach and exceed the dimensions of the landform elements, the smaller elements merge into the adjacent features.

5.4 Edge Detection Algorithms

Delineation of different surface components depends on the successful identification of feature boundaries. The simplest surfaces to differentiate are planar or near-planar, as the junction between any two non-parallel surfaces will be a straight line with greater curvature perpendicular to the line than within either of the adjacent planes. Figure 5.5 shows the noise-free model processed within ER Mapper (version 6.1) by (i) enhancing the frequency distribution by clipping the histogram at 99%, and (ii) displaying the results on a 256 increment greyscale.

The left-hand side of Figure 5.5 shows the results when using each of the five parameters of the quadratic equation for the surface formed by the 9 points in the 3x3 kernel. The a and b parameters do not discriminate well on curves oriented parallel to the Y and X axes respectively; the c parameter discriminates poorly along both axes; all three parameters successfully discriminate edges oblique to the axes. The d and e parameters are intensity-shaded by surface, with variable intensity on the

curved surface. As expected, the slope gradient image is reversed to that of shaded relief with the sun elevation at 90º.

Of the curvature algorithms in Figure 5.5, plan convexity is a poor discriminator of the small change in direction between the ground surface and the largest internal plane, and profile convexity is also very weak at this location as well as at the base of the failure scar. The plan convexity produces a strong linear artefact along the axis of the ellipsoid where the change in curvature is very slight. Maximum convexity identifies most of the ellipsoid edge and the internal convexity between planes, but is very weak on the concave edges; minimum convexity is weak at slight convex edges, but very strong at the major concave edges.

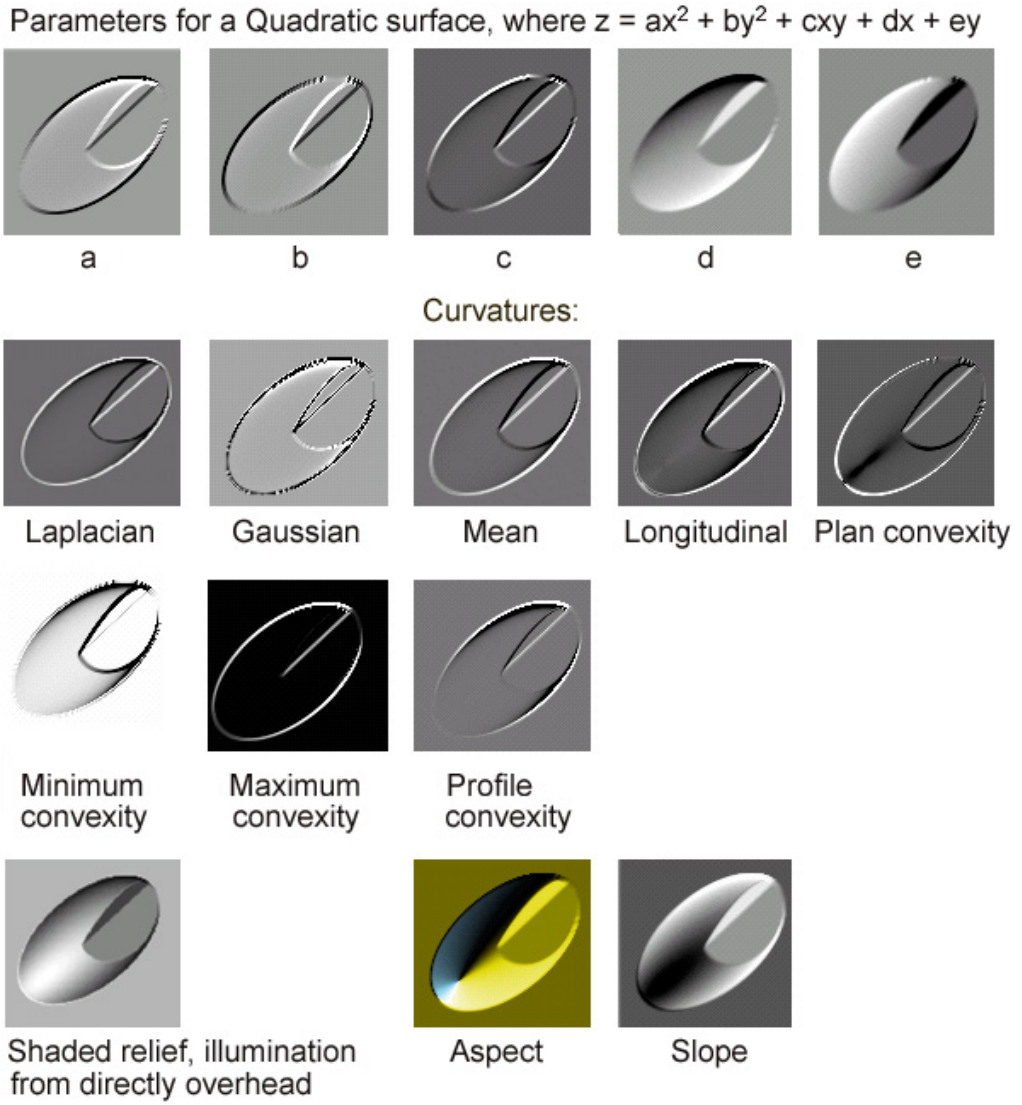

Figure 5.5 Feature discrimination by curvature in the noise-free synthetic model

The four visually most-successful edge detectors as seen in Figure 5.5 are the Gaussian, Laplacian, mean and longitudinal curvatures. Of these, the Gaussian curvature generates a triple-line result around much of the edge, including between the two internal planes; however, it is very weak at the shallow gradient-change boundary at the upper boundary of the ellipsoid. The mean, Laplacian and longitudinal curvature filters generate a consistent line around most of the ellipsoid and the two planes, but are weakest at the head and base of the ellipsoid where the change in curvature is the least. The longitudinal curvature kernel produces a double boundary at the base and crest of the ellipsoid, and along the concave edge of the internal planes.

5.4.1 Use of Simple Filters

The simplest low pass filter reduces high frequency noise by a moving average technique. The Laplacian and 3x3 average low pass filters are similar in structure, consisting of the kernels as shown in Figure 5.6. Wood (1996) provides routines for calculating the mean, maximum and minimum convexity, Gaussian, longitudinal, plan and profile curvatures that are available within the ER Mapper package (version 6.0 and above).

-1	-1	-1
-1	8	-1
-1	-1	-1

Laplacian filter

1/9	1/9	1/9
1/9	1/9	1/9
1/9	1/9	1/9

3x3 average filter

Figure 5.6 Kernels for Laplacian and 3x3 average filters: factors applied to each element in 3x3 kernel

Linear differentiation problems increase significantly when noise is added to the synthetic model as even small amounts greatly increase the variability of curvatures within the kernel, and between adjacent kernels. This effect is shown in Figure 5.7a, b and c, where three potential extraction strategies were applied using averaging to reduce noise prior to application of the Gaussian, Laplacian and mean curvatures.

The complex lines created by the Gaussian curvature filter remain mostly visible with convolution by a 3x3 filter, but are moderately degraded by 5x5 averaging.

This filter does not perform well when noise is added to the synthetic model, as shown by the lower two rows in Figure 4.8, where the edges of the model are almost completely obliterated. Even with application of the 5x5 averaging filter, and a comparatively small level of noise at 0.5 standard deviations, only a small part of the largest edge is visible. Of the filters evaluated, this one was the most sensitive to variation with clipping limits to the histogram within the ER Mapper processing sequence.

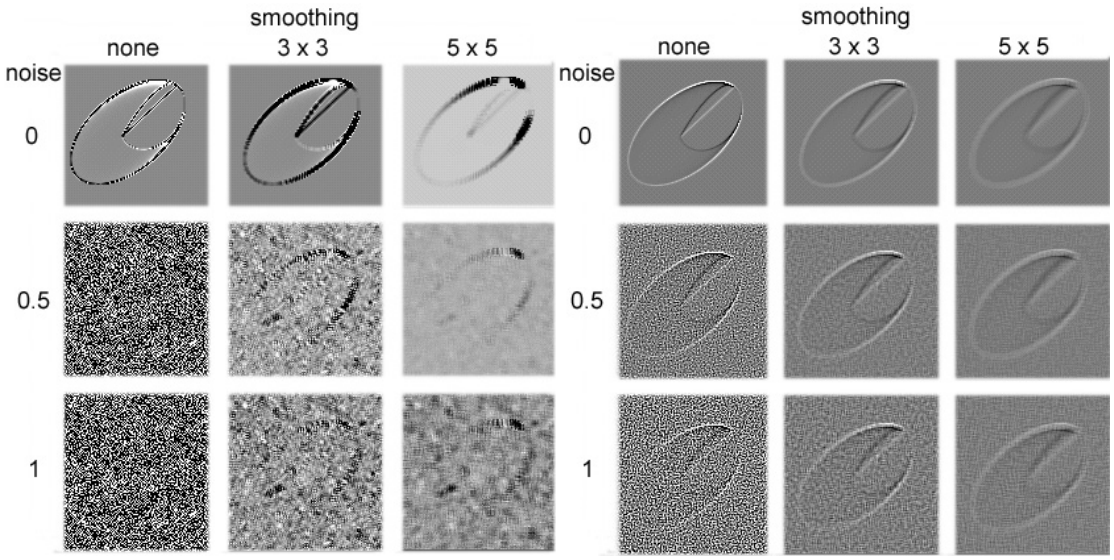

a. Gaussian curvature b. Laplacian Curvature

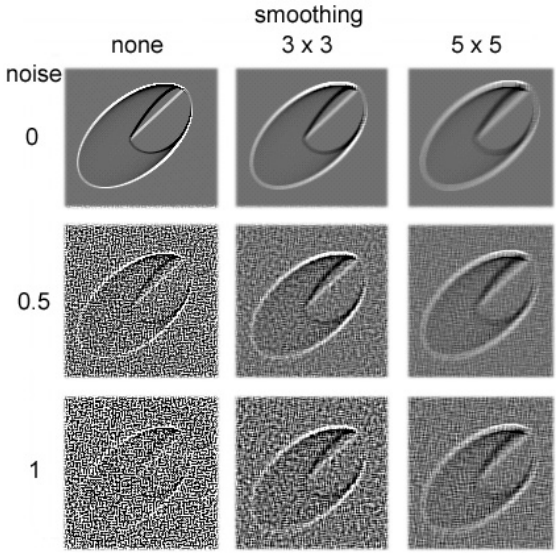

c. Mean curvature

Figure 5.7 Effect of noise and averaging: three curvatures

The Laplacian curvature filter seen in Figure 5.7b performs better than the Gaussian, with the edges of the model being just discernable when the one standard deviation of noise is added to the model. The edges are very narrow as the Laplacian filter is an efficient non-directional edge detector (Castleman, 1996). Figure 5.7c shows the results generated by use of the mean curvature filter. The edges are wider and of a slightly higher contrast than those generated by the Laplacian, and the overall appearance is very similar.

ER Mapper includes an additional filter, 'maximum curvature in any plane' which provides a simple means of utilising the highest curvature region as determined by comparison with the implemented range of curvature filters to identify terrain with local maximum convexities and, by using the minimum values for maximum convexity, local maximum concavities. While the Laplacian curvature filter was used for processing the synthetic model (Figure 5.10), the 'maximum curvature in any plane' filter has proved valuable in the complex morphology of deeply eroded hillsides such as examined in the case study at One Rise More in Hong Kong (Chapter 7).

5.4.2 From Measurement to Description: Planar Landforms

The edges identified in Figure 5.7c are extracted as point clouds using masks defined by regions of high curvature, as shown in Figures 5.8 and 5.9. These edges are then used as input into the morphological map, using the standard morphological mapping symbols. The procedure used is shown in Figure 5.10 and entails:

(a) Compile multi-layer data file containing the elevation data and the multiple attributes, each optimised to maximum discrimination along the edges;
(b) Apply 99% thresholds (may need to vary, depending on results) on the curvature layers to optimise discrimination of the boundary lines;
(c) Extract the boundary pixels to the thresholded regions of maximum convexity and concavity;
(d) Convert the region polygons to vectors to represent the linear boundaries;
(e) Add the relevant convex or concave morphology to the vectorised lines;
(f) If 3D visualisation is needed, warp the 2D lines to the TIN of the surface.

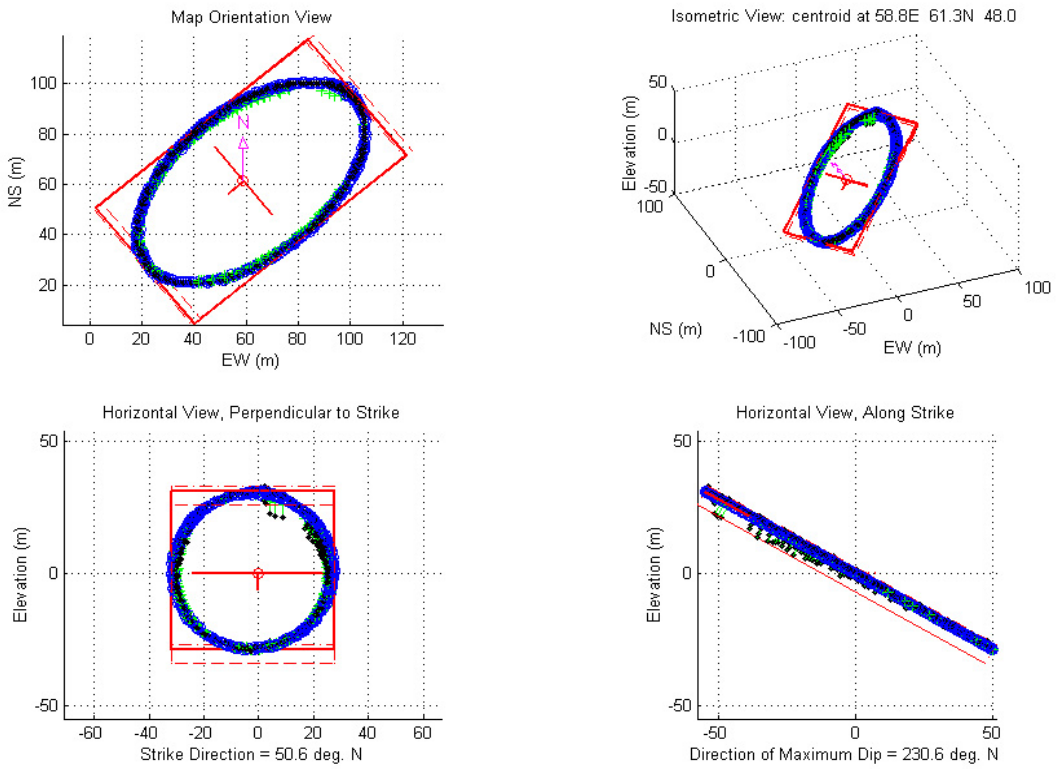

Figure 5.8 Boundary points extracted from the curvature region between ground surface and ellipsoid, 0.5 standard deviations of noise

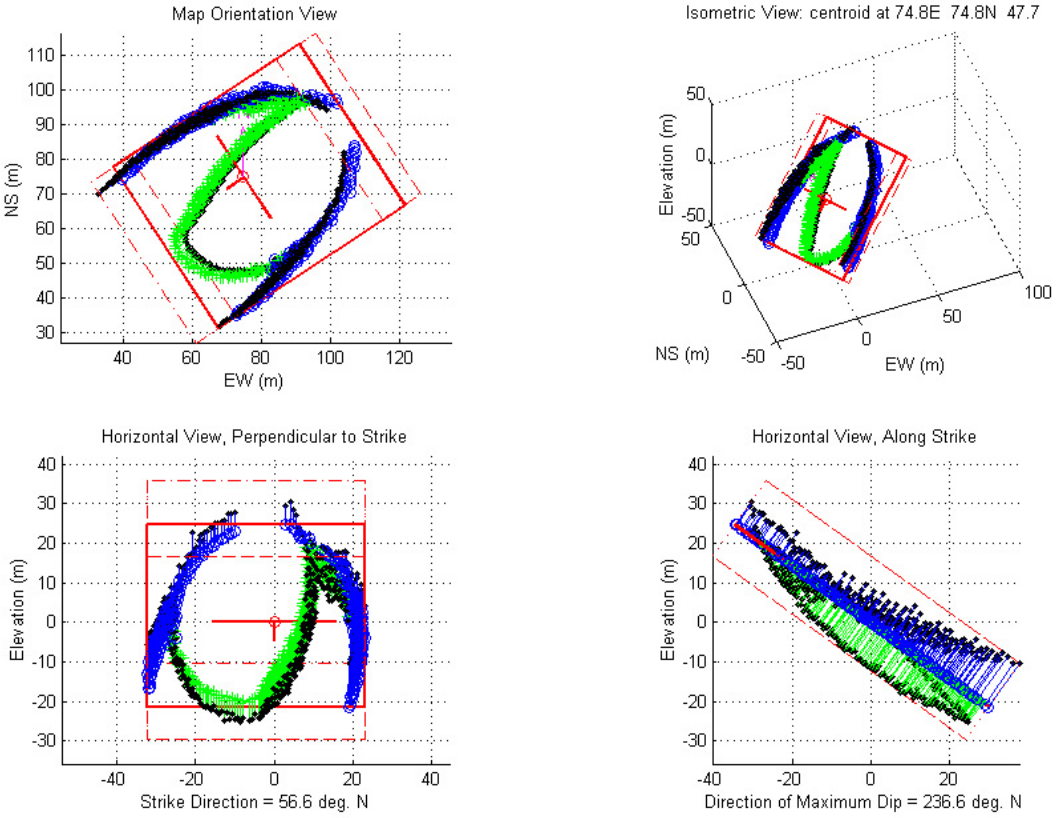

Figure 5.9 Boundary points extracted from the curvature region between ellipsoid and Plane 1

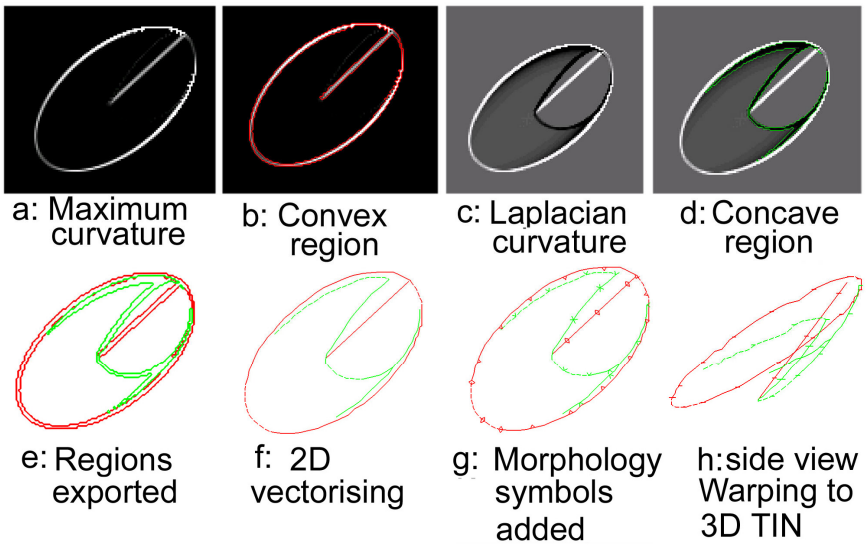

Figure 5.10 Edge and threshold processing sequence

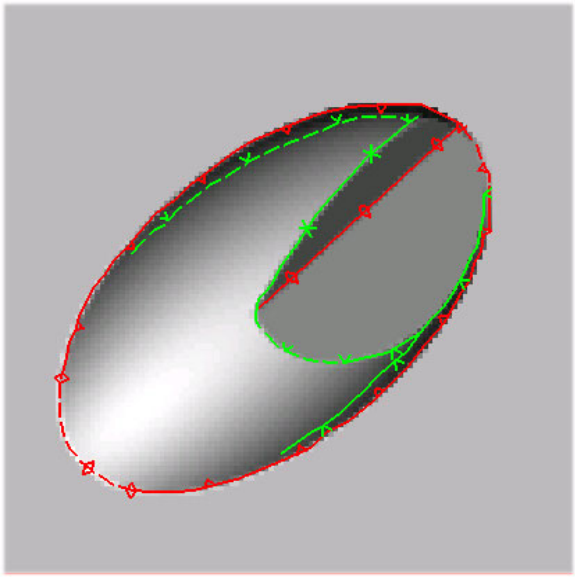

Figure 5.11 Sun-shaded synthetic landslide model with morphology

The resulting morphological map is shown overlaying the Laplacian curvature results in Figure 5.11. The morphology is a close fit to the shape of the landslide as depicted by the sunshading.

Feature boundaries were used to extract clouds of points for the two internal planes, plus three edges. The results for these planes are described after the description in Chapter 5.5, of the procedure used to determine the orientation of these planes.

5.5 Determining Orientation of Planes

5.5.1 Best-fit Plane Estimated by Least Squares

Gauss (1827) developed the method of least squares adjustment, where the most probable values for the adjusted quantities are determined by enforcing the condition that the sum of the weights of the measurements, times their corresponding residuals, is minimised (Elfick, et al., 1994). It may also determine the precision of the adjusted values and the presence of mistakes and large errors. Measurement weights derived by block bundle adjustment are included in results generated by the PhotoModeler for multi-image models.

5.5.2 Visual Determination of Goodness of Fit

Rock slopes are rarely smooth and planar, and the surface roughness can be a significant factor in the shear strength of the rock mass. In addition to generating the best-fit plane through the points, a graphical display of the residuals is useful in identifying gross errors, and to help visualise the roughness. A suite of MatLab code functions have been written to determine the best fit plane using least squares estimation, which are referred to in this dissertation as the LSP routine. The display options created include the following components:

(a) Raw data points (green crosses at points above the plane; blue circles for points below the plane);
(b) Extent of the plane, defined by the minimum and maximum extent of the measured points in the directions of strike and maximum dip;
(c) Residuals from the source points to their closest point on the plane (marked by a black dot);
(d) Bounding cube defined by the minimum and maximum residuals and (b);
(e) Dip and strike symbols at the centroid (centre of mass) of the points;
(f) North arrow (plotted horizontally).

The plane and points are visualised in four forms:

(a) Map view: plane with its map coordinates;
(b) Isometric view: plane translated to small coordinate values;

(c) Perpendicular view: View orthogonal to the plane with the direction of maximum dip translated to the negative Y axis, which shows the distribution of points around the plane;

(d) Strike section view: Perpendicular to (c), this is a horizontal view along the strike, which highlights the residuals and the thickness of the bounding cube.

An example of the plotted isometric view output is included at Figure 5.12, using the results for Plane 1 of the synthetic model.

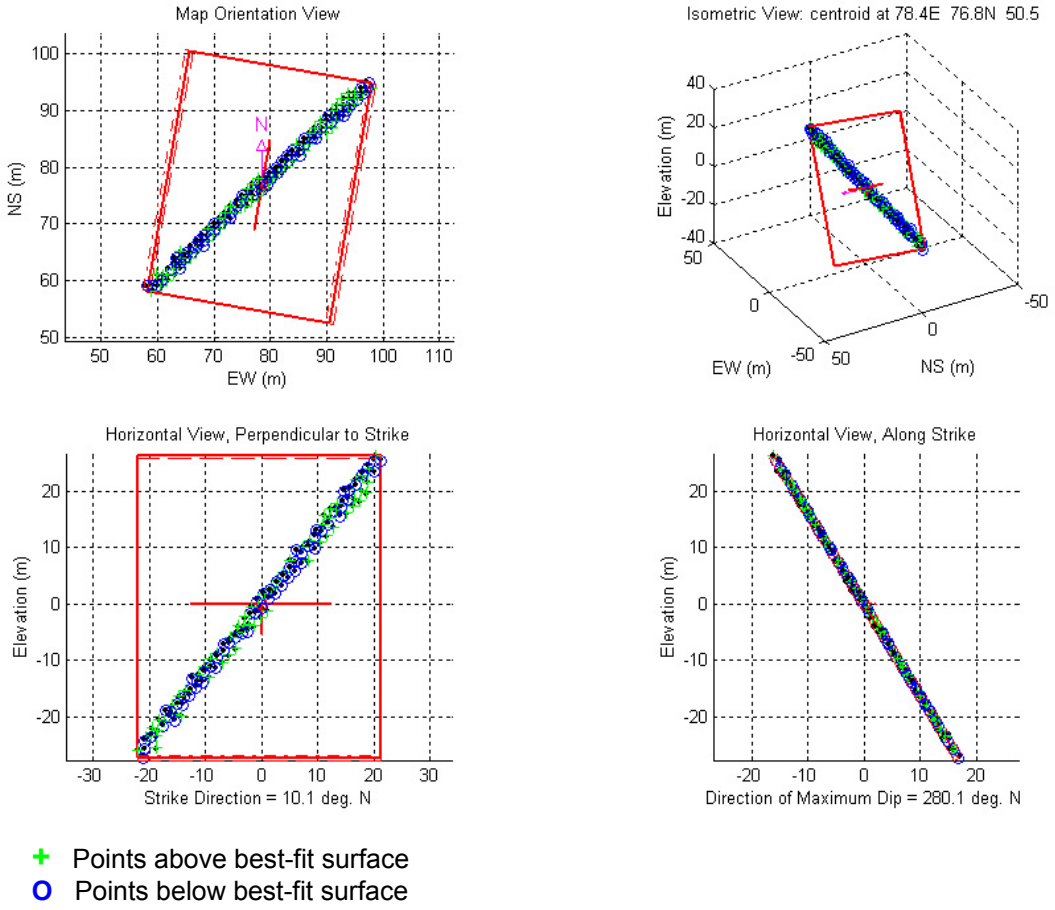

Figure 5.12 Graphical representation of the estimated orientation for Plane 1 of the synthetic model degraded with 0.5 standard deviations of noise

5.5.3 Differentiating Planar from Curved Surfaces

The perpendicular and strike section views of the LSP routine are useful in analysing the distribution of points. In addition, two graphical displays are generated showing

the variations of the length of the residuals against (i) bearing between the centroid and the measured point, and (ii) the distance between them. The routine also determines the coefficients of the second and third order polynomials which can be used if the visual display indicates that the surface is not planar, and the dimensions and orientation of the best fit line through the point cloud. This is useful to determine the orientation of linear boundaries between planes, for example, the linear edge between the two internal planes in the synthetic landslide model, as seen in Figure 5.13. The results for this edge, tabulated against the variation in orientation due to no noise, and four increasing levels of noise, are given in Table 5.1. Note that the orientation remains consistent, even when a large amount of random noise is present in the model; this is to be expected unless some bias is present in the noise.

Table 5.1 Orientation of the convex edge between Planes 1 and 2

Results for 3D line through edge between Planes 1 and 2	Length	Bearing (ºN)	Dip (º)
0.0 sd	5.31	4.70	4.42
0.5 sd	5.31	4.70	4.42
1.0 sd	5.31	4.70	4.43
2.0 sd	5.31	4.70	4.45
4.0 sd	5.31	4.70	4.52
Minimum	5.31	4.70	4.42
Maximum	5.31	4.70	4.52
Range	0.00	0.00	0.10

5.6 Least Squares Estimation Modified by Point Measurement Weights

Let $(x_1, y_1, z_1,)$, (x_2, y_2, z_2) … (x_n, y_n, z_n) be the points on the surface, and δ_1, δ_2 … δ_n be the weights of the point measurements. A weighting of 100 is applied to δ_{ave} to ensure the a, b and c coefficients produce direction cosines while retaining the ability to compensate for the errors. The initial values of a, b, c and d are calculated from the unique plane determined from the first three points. Values for a, b and c are converted to direction cosines. For a least squares adjustment solution using a, b and c defined as direction cosines:

$$
\begin{array}{ccccccccccc}
ax_1 & + & by_1 & + & cz_1 & + & d_1 & = & 0 & - & \vartheta_1 \\
ax_2 & + & by_2 & + & cz_2 & + & d_2 & = & 0 & - & \vartheta_2 \\
ax_3 & + & by_3 & + & cz_3 & + & d_3 & = & 0 & - & \vartheta_3 \\
\vdots & & \vdots & & \vdots & & \vdots & & \vdots & & \vdots \\
ax_n & + & by_n & + & cz_n & + & d_n & = & 0 & - & \vartheta_n \\
a^2 & + & b^2 & + & c^2 & - & 1 & = & 0 & - & \dfrac{\vartheta_{ave}^2}{100}
\end{array}
\qquad \text{Eqn. 5.3}
$$

Differentiating θ respect to a, b, c and d:

$$
\frac{\delta\vartheta}{\delta a} = \begin{pmatrix} x_1 \\ x_2 \\ x_3 \\ \vdots \\ x_n \\ 2a \end{pmatrix}, \quad
\frac{\delta\vartheta}{\delta b} = \begin{pmatrix} y_1 \\ y_2 \\ y_3 \\ \vdots \\ y_n \\ 2b \end{pmatrix}, \quad
\frac{\delta\vartheta}{\delta c} = \begin{pmatrix} z_1 \\ z_2 \\ z_3 \\ \vdots \\ z_n \\ 2c \end{pmatrix}, \quad
\frac{\delta\vartheta}{\delta d} = \begin{pmatrix} 1 \\ 1 \\ 1 \\ \vdots \\ 1 \\ 0 \end{pmatrix}
\qquad \text{Eqn. 5.4}
$$

5.6.1 Iterative Solution

In the iterative solution, the initial values for a^0, b^0, c^0 and d^0 are calculated, the least squares mis-closure solution is solved, and new values for a^1, b^1, c^1 and d^1 are generated and compared with the previous values. If the difference for all the values is less than a threshold, the revised a^n, b^n, c^n and d^n values are accepted as the least squares adjusted solution. If any one of the values is greater than the threshold, the iteration is repeated using the new values as the initial input, or until a set number of iterations is completed.

Solution = $\mathbf{-N^{-1}u}$, where $\mathbf{N = A^T P A}$ and $\mathbf{u = A^T P \omega}$

$$
\mathbf{A} = \begin{matrix} \\ \\ \\ \\ \\ n+1 \end{matrix}
\begin{bmatrix} x_1 & y_1 & z_1 & 1 \\ x_2 & y_2 & z_2 & 1 \\ x_3 & y_3 & z_3 & 1 \\ \vdots & \vdots & \vdots & \vdots \\ x_n & y_n & z_n & 1 \\ 2a^0 & 2b^0 & 2c^0 & 0 \end{bmatrix}^4, \qquad \text{Eqn. 5.5}
$$

$$\mathbf{A^T} = \begin{matrix}4\\ \\ \\ \end{matrix}\begin{bmatrix} x_1 & x_2 & x_3 & \cdots & x_n & 2a^0 \\ y_1 & y_2 & y_3 & \cdots & y_n & 2b^0 \\ z_1 & z_2 & z_3 & \cdots & z_n & 2c^0 \\ 1 & 1 & 1 & \cdots & 1 & 0 \end{bmatrix}^{n+1}, \qquad \text{Eqn. 5.6}$$

$$\mathbf{P} = \begin{matrix}n+1\\ \\ \\ \\ \\ \\ \end{matrix}\begin{bmatrix} \frac{1}{\sigma_1^2} & 0 & 0 & \cdots & 0 & 0 \\ 0 & \frac{1}{\sigma_2^2} & 0 & \cdots & 0 & 0 \\ 0 & 0 & \frac{1}{\sigma_3^2} & \cdots & 0 & 0 \\ \vdots & \vdots & \vdots & \ddots & 0 & 0 \\ 0 & 0 & 0 & 0 & \frac{1}{\sigma_n^2} & 0 \\ 0 & 0 & 0 & 0 & 0 & \frac{100^2}{\sigma_{ave}^2} \end{bmatrix}^{n+1}, \qquad \text{Eqn. 5.7}$$

$$\omega = \begin{matrix}n+1\\ \\ \\ \\ \\ \end{matrix}\begin{bmatrix} -v_1 \\ -v_2 \\ -v_3 \\ \vdots \\ -v_n \\ -v_{ave} \end{bmatrix}^{1} = \begin{matrix}n+1\\ \\ \\ \\ \\ \end{matrix}\begin{bmatrix} a^0x_1 & + & b^0y_1 & + & c^0z_1 & + & d^0 \\ a^0x_2 & + & b^0y_2 & + & c^0z_2 & + & d^0 \\ a^0x_3 & + & b^0y_3 & + & c^0z_3 & + & d^0 \\ \vdots & & \vdots & & \vdots & & \vdots \\ a^0x_n & + & b^0y_n & + & c^0z_n & + & d^0 \\ a^{0^2} & + & b^{0^2} & + & c^{0^2} & - & 1 \end{bmatrix}^{1} \qquad \text{Eqn. 5.8}$$

$$\mathbf{N} = \mathbf{A^T P A} =$$

$$\begin{matrix}4\\ \\ \\ \end{matrix}\begin{bmatrix} \frac{x_1}{\sigma_1^2} & \frac{x_2}{\sigma_2^2} & \frac{x_3}{\sigma_3^2} & \cdots & \frac{x_n}{\sigma_n^2} & \frac{2a^0}{100\sigma_{ave}^2} \\ \frac{y_1}{\sigma_1^2} & \frac{y_2}{\sigma_2^2} & \frac{y_3}{\sigma_3^2} & \cdots & \frac{y_n}{\sigma_n^2} & \frac{2b^0}{100\sigma_{ave}^2} \\ \frac{z_1}{\sigma_1^2} & \frac{z_2}{\sigma_2^2} & \frac{z_3}{\sigma_3^2} & \cdots & \frac{z_n}{\sigma_n^2} & \frac{2c^0}{100\sigma_{ave}^2} \\ \frac{1}{\sigma_1^2} & \frac{1}{\sigma_2^2} & \frac{1}{\sigma_3^2} & \cdots & \frac{1}{\sigma_n^2} & 0 \end{bmatrix}^{n+1} \begin{matrix}n+1\\ \\ \\ \\ \\ \end{matrix}\begin{bmatrix} x_1 & y_1 & z_1 & 1 \\ x_2 & y_2 & z_2 & 1 \\ x_3 & y_3 & z_3 & 1 \\ \vdots & \vdots & \vdots & \vdots \\ x_n & y_n & z_n & 1 \\ 2a^0 & 2b^0 & 2c^0 & 0 \end{bmatrix}^{4}$$

$$= {}_4\begin{bmatrix} \sum_{i=1}^{n}\frac{x_n^2}{\sigma_n^2}+\frac{4a^{0^2}}{100\sigma_{ave}^2} & \sum_{i=1}^{n}\frac{x_n y_n}{\sigma_n^2}+\frac{4a^0 b^0}{100\sigma_{ave}^2} & \sum_{i=1}^{n}\frac{x_n z_n}{\sigma_n^2}+\frac{4a^0 c^0}{100\sigma_{ave}^2} & \sum_{i=1}^{n}\frac{x_n}{\sigma_n^2} \\ \sum_{i=1}^{n}\frac{x_n y_n}{\sigma_n^2}+\frac{4a^0 b^0}{100\sigma_{ave}^2} & \sum_{i=1}^{n}\frac{y_n^2}{\sigma_n^2}+\frac{4b^{0^2}}{100\sigma_{ave}^2} & \sum_{i=1}^{n}\frac{y_n z_n}{\sigma_n^2}+\frac{4b^0 c^0}{100\sigma_{ave}^2} & \sum_{i=1}^{n}\frac{y_n}{\sigma_n^2} \\ \sum_{i=1}^{n}\frac{x_n z_n}{\sigma_n^2}+\frac{4a^0 c^0}{100\sigma_{ave}^2} & \sum_{i=1}^{n}\frac{y_n z_n}{\sigma_n^2}+\frac{4b^0 c^0}{100\sigma_{ave}^2} & \sum_{i=1}^{n}\frac{z_n^2}{\sigma_n^2}+\frac{4c^{0^2}}{100\sigma_{ave}^2} & \sum_{i=1}^{n}\frac{z_n}{\sigma_n^2} \\ \sum_{i=1}^{n}\frac{x_n}{\sigma_n^2} & \sum_{i=1}^{n}\frac{y_n}{\sigma_n^2} & \sum_{i=1}^{n}\frac{z_n}{\sigma_n^2} & \sum_{i=1}^{n}\frac{1}{\sigma_n^2} \end{bmatrix}^4 \qquad \text{Eqn. 5.9}$$

u = $\mathbf{A^T P \omega}$=

$$ {}_4\begin{bmatrix} \frac{x_1}{\sigma_1^2} & \frac{x_2}{\sigma_2^2} & \frac{x_3}{\sigma_3^2} & \cdots & \frac{x_n}{\sigma_n^2} & \frac{2a^0}{100^2\sigma_{ave}^2} \\ \frac{y_1}{\sigma_1^2} & \frac{y_2}{\sigma_2^2} & \frac{y_3}{\sigma_3^2} & \cdots & \frac{y_n}{\sigma_n^2} & \frac{2b^0}{100^2\sigma_{ave}^2} \\ \frac{z_1}{\sigma_1^2} & \frac{z_2}{\sigma_2^2} & \frac{z_3}{\sigma_3^2} & \cdots & \frac{z_n}{\sigma_n^2} & \frac{2c^0}{100^2\sigma_{ave}^2} \\ \frac{1}{\sigma_1^2} & \frac{1}{\sigma_2^2} & \frac{1}{\sigma_3^2} & \cdots & \frac{1}{\sigma_n^2} & 0 \end{bmatrix}^{n+1} {}_{n+1}\begin{bmatrix} a^0x_1 & + & b^0y_1 & + & c^0z_1 & + & d^0 \\ a^0x_2 & + & b^0y_2 & + & c^0z_1 & + & d^0 \\ a^0x_3 & + & b^0y_3 & + & c^0z_2 & + & d^0 \\ \vdots & & \vdots & & \vdots & & \vdots \\ a^0x_n & + & b^0y_n & + & c^0z_n & + & d^0 \\ a^{0^2} & + & b^{0^2} & + & c^{0^2} & - & 1 \end{bmatrix}^4$$

$$= {}_4\begin{bmatrix} a^0\sum_{i=1}^{n}\frac{x_n^2}{\sigma_n^2}+b^0\sum_{i=1}^{n}\frac{x_n y_n}{\sigma_n^2}+c^0\sum_{i=1}^{n}\frac{x_n z_n}{\sigma_n^2}+d^0\sum_{i=1}^{n}\frac{x_n}{\sigma_n^2}+\frac{2a^{0^3}}{100^2\sigma_{ave}^2} \\ a^0\sum_{i=1}^{n}\frac{x_n y_n}{\sigma_n^2}+b^0\sum_{i=1}^{n}\frac{y_n^2}{\sigma_n^2}+c^0\sum_{i=1}^{n}\frac{y_n z_n}{\sigma_n^2}+d^0\sum_{i=1}^{n}\frac{y_n}{\sigma_n^2}+\frac{2b^{0^3}}{100^2\sigma_{ave}^2} \\ a^0\sum_{i=1}^{n}\frac{x_n z_n}{\sigma_n^2}+b^0\sum_{i=1}^{n}\frac{y_n z_n}{\sigma_n^2}+c^0\sum_{i=1}^{n}\frac{z_n^2}{\sigma_n^2}+d^0\sum_{i=1}^{n}\frac{z_n}{\sigma_n^2}+\frac{2c^{0^3}}{100^2\sigma_{ave}^2} \\ a^0\sum_{i=1}^{n}\frac{x_n}{\sigma_n^2}+b^0\sum_{i=1}^{n}\frac{y_n}{\sigma_n^2}+c^0\sum_{i=1}^{n}\frac{z_n}{\sigma_n^2}+d^0\sum_{i=1}^{n}\frac{1}{\sigma_n^2} \end{bmatrix}^4 \qquad \text{Eqn. 5.10}$$

The solution presented here allows efficient use of weighting values for point clouds. For smaller data sets, including those derived by hand measurement of smaller, planar surfaces; the code can be implemented by directly setting up the **N** and **u** matrices and solving iteratively.

5.6.2 Application of Results

Once the least squares plane has been determined, either with or without individual point measurement weights, the results are converted to the geologically-relevant format of dip and strike. For Earth science purposes, where the gravity field controls most of the mechanical weathering and transport processes (Shary et al., 2002),

planar surfaces are described in terms of the dip of the rock surface and either the dip direction or its perpendicular strike direction.

Results generated by some photogrammetric software, e.g., PhotoModeler and Australis, include tables containing a number of parameters relating to the measurement and precision of the results. Precision is strongly controlled by the quality of the imagery as this affects the ability to identify individual points, the geometry of camera stations, and the camera calibration parameters. While the photogrammetric output contains X, Y and Z coordinates, plus precisions in the X, Y and Z axis directions, for measurement of geological planes it is better to define

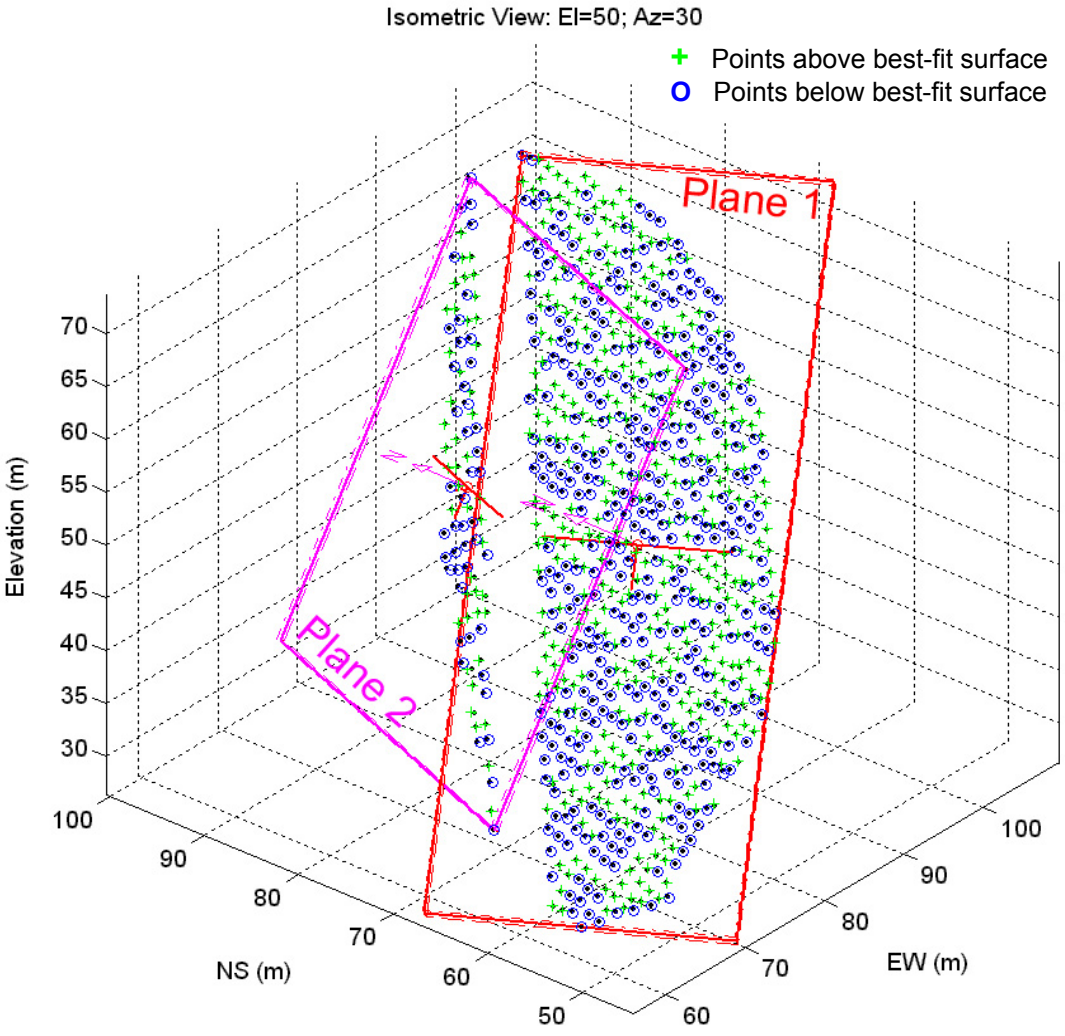

Figure 5.13 Graphical representation of the estimated orientations for Planes 1 and 2 of the synthetic model degraded with 0.5 standard deviation of noise

additional dimensions and precisions in terms of the dip and strike directions, plus the offset perpendicular to the orientation of the plane. These additional parameters can be obtained by first determining the dip and strike directions of the best fit plane, and then rotating the coordinate axes so that the direction of maximum dip lies parallel to the negative Y axis, the strike is parallel to the X axis, and the perpendicular offset of the residuals from the measured points to the plane are aligned parallel to the Z axis. The two rotations needed to accomplish this transformation are a rotation about the Z axis (Kappa, κ, where κ = Bearing (N) – (p/2) radians) to reduce the strike direction to the X axis, and a rotation about the X axis (Omega, ω, where ω = dip angle below horizontal in radians). Where transformations are required from the dip and strike coordinate system to map coordinates, the rotations are applied as negatives of the same angles, and in the opposite order, i.e. -ω then -κ.

The LSP routines convert the equation for the least squares plane into geological dip and direction of maximum dip, and display the residuals between the point measurements and the least squares plane. As geological dip is the angle between the line of maximum gradient on a plane and the horizontal, the value is the same as the angle between the normal to the plane and the Z axis. The direction of maximum dip is the same as the component of the normal vector reduced to the plane formed by the XY axes and stated as a clockwise bearing from North. The graphical output showing the locations of the measured points and the distribution of positive and negative residuals between the measured points and the best-fit plane is given at Figure 5.13, and the orientation results for Planes 1 and 2 are given in Tables 5.2 and 5.3 respectively.

Table 5.2 Orientation results for Plane 1

datafile	Dip (º)	Dip Direction (º)	Strike (º)
0sd noise plane1	45.00	240.00	60.00
0.5sd noise plane1	45.16	239.98	59.98
1.0sd noise plane1	44.83	240.16	60.16
2.0sd noise plane1	44.98	240.59	60.59

Table 5.3 Orientation results for Plane 2

datafile	Dip (º)	Dip Direction (º)	Strike (º)
0sd noise plane2	65.00	290.00	20.00
0.5sd noise plane2	65.57	290.94	20.94
1.0sd noise plane2	65.81	291.27	21.27
2.0sd noise plane2	67.95	294.19	24.19

5.6.3 Results for the Synthetic Landslide Model

Clouds of points were extracted for the two internal planes, the straight convex edge between Planes 1 and 2, the curving concave edge between each of Planes 1 and 2 and the ellipsoid, and the convex edge between the ellipsoid and the ground surface. The orientation results for the two internal planes are given in Tables 5.3 and 5.4, and for the edge between the two planes is in Table 5.1 above.

For Plane 1, the dip and dip direction remain within a small 0.2º range, with up to 1.0 standard deviations (equivalent to 0.38m on the One Rise More landslide) of random noise. A larger error of 0.59º in dip direction is present for Plane 1 with 2.0 standard deviations of noise. The results for Plane 2 are more variable, increasing to almost 3º error in the dip with two standard deviations of noise. These results are expected, because Plane 2 is an elongate feature as seen in Figure 5.15, although the bounding box shown in Figure 5.13 shows that the measurements are extensive in both the dip and strike directions. Within the context of Earth science and slope stability applications, these errors are small, and mostly within the expected precision of manual measurements under field conditions of ±2º.

5.7 Discussion

Using random noise to degrade the synthetic DEM represents an extreme case, as there is a high degree of autocorrelation between adjacent points in the DEM. Evans (1972) notes that smoothing before analysis will make the statistical properties of a DEM more stable, and this is particularly true when using curvatures; as second derivatives (Chapter 2.4.1), curvatures are more sensitive to noise in the elevation data that the first derivatives of gradient and aspect (Guth, 1995; Shary et al., 2002).

All geomorphometric parameters are sensitive to the sampling interval and the scale of the landforms (Evans, 1980).

The application of uncorrelated or weakly-correlated noise may be closer to the situation when using multi-image close range photogrammetry, where statistical image matching algorithms are not generally available and corresponding features are identified by visual inspection. Although this too implies a degree of autocorrelation due to the nature of visual perception through the interpretation of the differing appearance of objects when viewed from a range of directions, the autocorrelation is countered by increased random error in precise feature placement.

While the first derivatives of elevation, slope gradient and aspect, give uniform results for planar features, they provide poor discrimination with respect to defining feature boundaries, especially for non-planar elements where gradient and aspect can vary across the landform element. Of the second derivatives, those that are strongly correlated with slope gradient and aspect such as plan and profile curvature generate variable results with regard to boundary discrimination, depending on the orientation of the features on either side of the boundary relative to the gravitational field; both functioned better for planar features than curving features such as ellipses. The most consistent second derivatives were independent of the gravitational field, including Laplacian and Gaussian curvatures, and the composite mean curvature. While slope failures are predominantly driven by gravitational forces, the resulting landform boundaries can vary widely in their orientation relative to the gradient and direction of the local hillside; consequently, the most consistent algorithms for landform boundary discrimination are the Laplacian and Gaussian curvatures.

5.8 Chapter Summary: Synthetic Landslide Model

The synthetic landslide model has been used to investigate the effects of random noise on the ability of morphological filters to extract feature edges. Gaussian, Laplacian and mean curvature algorithms have been found to function well in an environment containing random digital noise provided that some smoothing filters are applied. In the case of the synthetic landslide model, a “maximum curvature in any plane” algorithm was used to extract the convex edges, and a Laplacian filter used to identify the concave edges, with a low pass filter used to reduce the effects of

noise. The extraction procedures will be tested in the following chapters in relation to landslide maps and rock outcrops.

A set of routines have been developed to visualise the orientation of planes and the points used to generate the surface. These routines were used in Chapter 4 to depict the distribution of residuals between the measured DEM posts and the target plane to demonstrate the presence of phase-wrapped surface artefacts within the DEM of an artificial planar target in a laboratory environment. They are used also in Chapter 6 where planes are measured in a field case study on a rock face using stereo and multi-image photogrammetry.

Chapter 6

DEVELOPING PHOTOGRAMMETRIC METHODS FOR LANDFORM MEASUREMENT

6.1 Measuring Land *Form*

6.1.1 Land Form as a Measurable Entity

Landform morphology can be measured as varying patterns of 3D shapes across the terrain, or as discrete geometrical units. The purpose of the measurement will determine the form that measurement will take. For area studies, the optimum form of data capture is likely to be through a DEM, although the scale used may vary widely. For example, interpretation of DEMs derived from stereo or multi-image photogrammetry can be used to measure gravel and stones in a laboratory flume (e.g., Chandler, et al., 2001), in a river bed (e.g., Lane, 1994; Chandler, et al., 2003), or on a broader scale to identify drainage lines and water sheds across a hill range (e.g., Miliarensis and Argialas, 1999; Miliarensis, 2001). Alternatively, the target landform may be a specific geometric form, for example a planar rock surface, and appropriate photogrammetric methods may be used to define the form and goodness of fit of the measured points.

This chapter examines the application to real terrains of the measurement techniques described for the synthetic landform model in Chapter 5. The emphasis is on how the photogrammetric techniques affect the precision of measurement, with the aim of improving the design of photogrammetric surveys towards geomorphological data capture. The first case study examines how both stereo and multi-image digital photogrammetry can be used to measure the orientation of surfaces within a near-vertical rock slope within a quarry; this represents a morphologically-simple case containing near-planar landforms with well-defined boundaries. The results are compared to measurements obtained by hand-held compass and clinometer and from a high-resolution terrestrial laser scanner (TLS). Measurement precision resulting from the use of multi-image photogrammetry is compared to semi- and fully automated stereo photogrammetry using image correlation routines for 3D point capture. Some measurement artefacts generated by the processing are discussed.

6.1.2 Feature Size, Orientation and Location

Geomorphological surveys can cover an extreme range of scales from particles to continents. Common to all these surveys, the critical property in the investigation is the size of the smallest geometric unit within the object (be it a particle or landform) relative to the number of pixels in the image. The number of pixels required within the image to define the feature will depend on the contrast of that feature relative to the surrounding terrain as well as its geometric complexity at the scale of the investigation. For example, a boulder exhibiting a high reflectance contrast may be identifiable with only one pixel during regional scale mapping although only an approximate size can be estimated; more specific dimensions can be determined if the same boulder occupies more than about 16 to 25 pixels. Low contrast objects may need 25 pixels or sometimes considerably more to allow unambiguous identification of the feature through either interpretation using stereoscopic observation or automated measurement of a DEM across the surrounding area (Soeters and van Western, 1996, Table 8-7).

In addition to choice of image resolution, image orientation relative to the feature being measured is critical. Multi-image photogrammetric measurement is only possible where the same feature is identifiable on two or more images; visual stereoscopic measurement also requires each image to contain similar-scaled features with a limited amount of perspective distortion. This Chapter examines the effect of image geometry on automated and semi-automated stereoscopic measurement in the context of landform measurement. Where softcopy photogrammetric techniques have been developed for use with vertical aerial photography, processing requires the view direction (i.e., the axis of the lens) to approximate the Z axis of the measurement coordinate system; for these to be used with terrestrial or oblique imagery, the object coordinate system may need to be rotated as shown in Figure 3.2.

6.1.3 Photogrammetric Constraints and Opportunities

The major photogrammetric constraints on feature measurement precision are related to the geometry of the camera and lens, and, if a softcopy system is being employed, the image scanning systems (Chapter 3.5.4).

Photogrammetry presents a significant opportunity when used for the capture of geomorphometric information within the context of slope stability investigations, because in many cases the potentially hazardous terrain is located on steep and or unstable slopes, and where access can be difficult. Some geological and geotechnical measurements require direct access to a landform, for example sampling for mineralogy or shear strength; other properties can be measured remotely, including the orientation of planes of weakness within and on the surface of rock masses. Geometric properties obtained by measuring or aggregating point values obtained over large areas can be as accurate as or possibly even more accurate than when normal hand measurements are taken at specific locations on a feature using a compass, tape and clinometer, especially where access is difficult or when the surface of the feature is undulating; surface roughness can also be measured for wavelengths up to twice the sampling interval, if sufficient measured points are available across the surface of the feature.

6.2 Terrestrial Photogrammetry Case Study: Mountain Quarry, Boya, Western Australia

6.2.1 Description of the Case Study

Small format aerial photography, coupled with digital (softcopy) photogrammetry is increasingly being used for topographic surveys purposes, particularly for small areas (e.g., Mills et al, 1996; Warner et al., 1996) and also for geomorphological and engineering geological purposes (e.g., Butler et al., 1998). Lane et al. (2000) have cautioned that, although automated extraction methods can generate DEMs of high accuracy for geomorphological investigations in areas of smooth terrain, further research is needed in areas of complex and rough topography and for different spatial scales. Many rock slopes fall into the 'complex and rough topography' category. While the softcopy systems present technological opportunities, the quality of the results also depends on the equipment used to capture the raw images, and the quality of orientation of the 3D model. The case study described in this Chapter investigates some of the practical factors affecting the use of softcopy methods for measurement of rock slope orientations.

The case study was carried out at Mountain Quarry, Boya, in the granite hills to the east of Perth, Western Australia, using multi-image and stereo photogrammetry and a terrestrial laser scanner (TLS) to measure clearly-exposed rock surfaces. This investigation was designed to compare the measurement precision of the two methods and highlight opportunities and constraints that applied to each, with specific reference to:

(a) precision of point measurement between multi-image and stereo photogrammetry;
(b) precision of point measurement using image correlation in stereo photogrammetry using varying photobases;
(c) effect of varying planar geometries on measurement precision using image correlation windows of varying sizes;
(d) comparison of planar orientations derived from multi-image and stereo photogrammetry, TLS and hand-held measurements; and
(e) adequacy of orientation for the 3D model using a hand held compass.

The measurement of planar surfaces forms an important component of slope stability investigations, as these often form discrete components of the total failure surface (Figure 5.1).

6.2.2 Data Capture

Source data obtained for this investigation consisted of:

(a) Stereo pair of vertical aerial photographs frames 4822063 and 4822064, obtained from the Department of Land Information (DLI), Government of Western Australia, supplied with the calibrated focal length and exterior orientation data (x, y, z, ω, φ and κ for the two perspective centres); scanned at 0.021mm pixels (1209 dpi) by DLI; 3330m (10,930ft) altitude; scale 1:21,137; within this stereo pair, the quarry forms an image approximately 350x300 pixels, with a ground resolution of 0.44m per pixel. An extract of DLI's 2004 SkyView orthophoto produced from aerial photograph 4822064 was also purchased for use in the detailed mapping (forming the base to Figure 6.1).

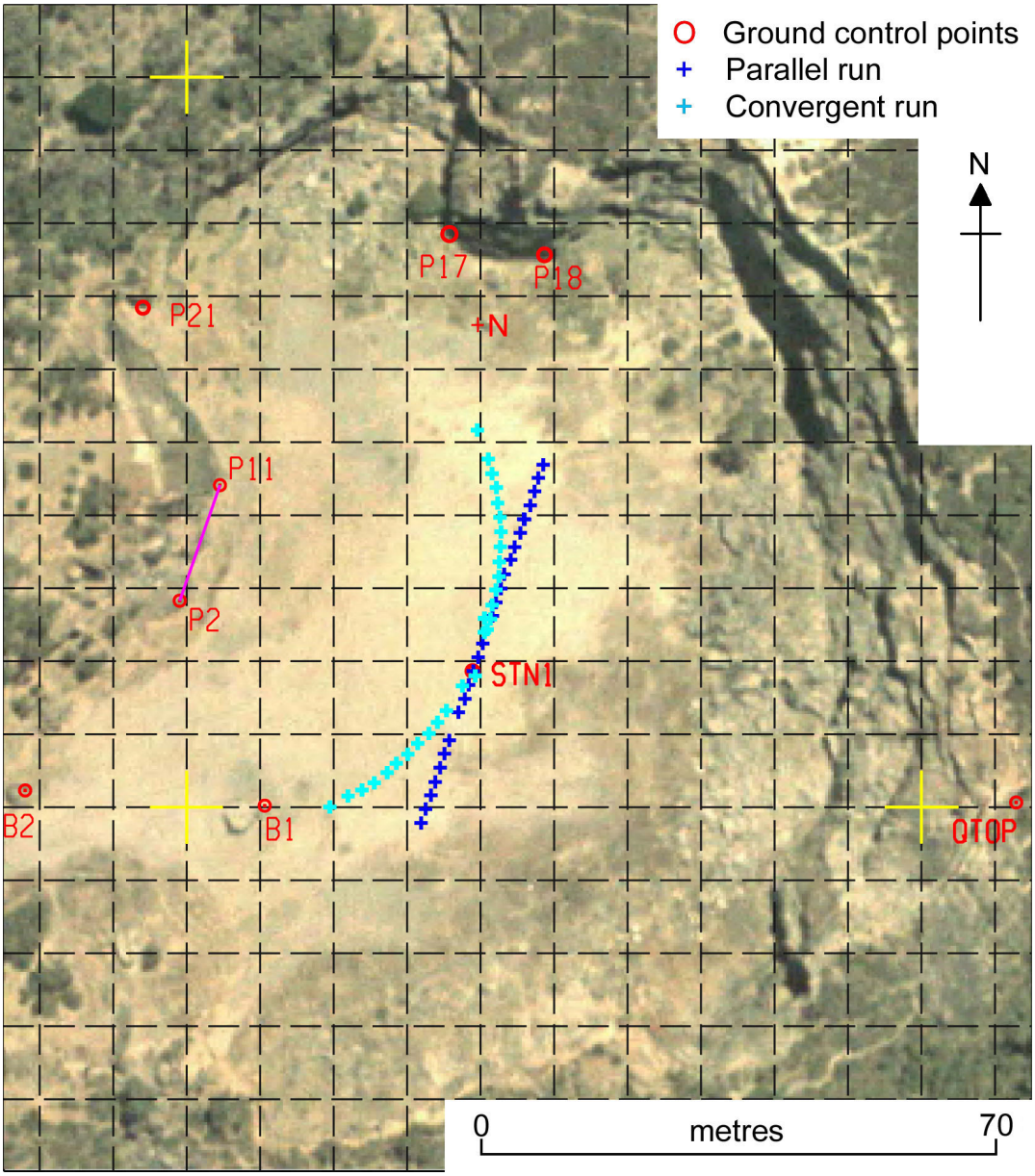

Figure 6.1 DLI SkyView orthophoto of Mountain Quarry from DLI aerial photograph 4822064

(b) three runs of images of the rock slope obtained using a Canon EOS 10D digital camera with a 28-70mm zoom lens set to 28mm focal length, consisting of:

(i) parallel images (Figure 6.1, dark blue crosses), obtained at a distance of 42m from the base of the rock slope by moving a tripod along two 30m tapes at approximately 2m centres, keeping the front two legs of the tripod aligned with the plastic tapes stretched along the ground; at a

project distance of 42m, the ground pixel size was 11.1mm when using the 28mm focal length setting on the camera;

(ii) convergent images (Figure 6.1, pale blue crosses), taken at approximately 2m centres around 90º of a 42m radius arc marked on the quarry floor using a surveyor's metal chain held at the centre of the base of the rock slope; each photograph was centred on the same point in the centre of the rock face;

(iii) convergent images centred on the rock face, taken from vantage points around the top of the eastern face of the quarry, opposite the rock face to be measured (includes QTOP marked on Figure 5.1)

(c) TLS point clouds of:

(i) west, north and eastern quarry faces, centred at STN1 in the centre of photo runs (i) and (ii) above (Figure 6.1); and

(ii) west rock face between points P2 and P21 shown in Figures 6.1 and 6.2.

The target rock face used for detailed study measured approximately 26m across the base (points labelled P2 to P11 in Figures 6.1 and 6.2) and 25m high. Sixteen 84mm

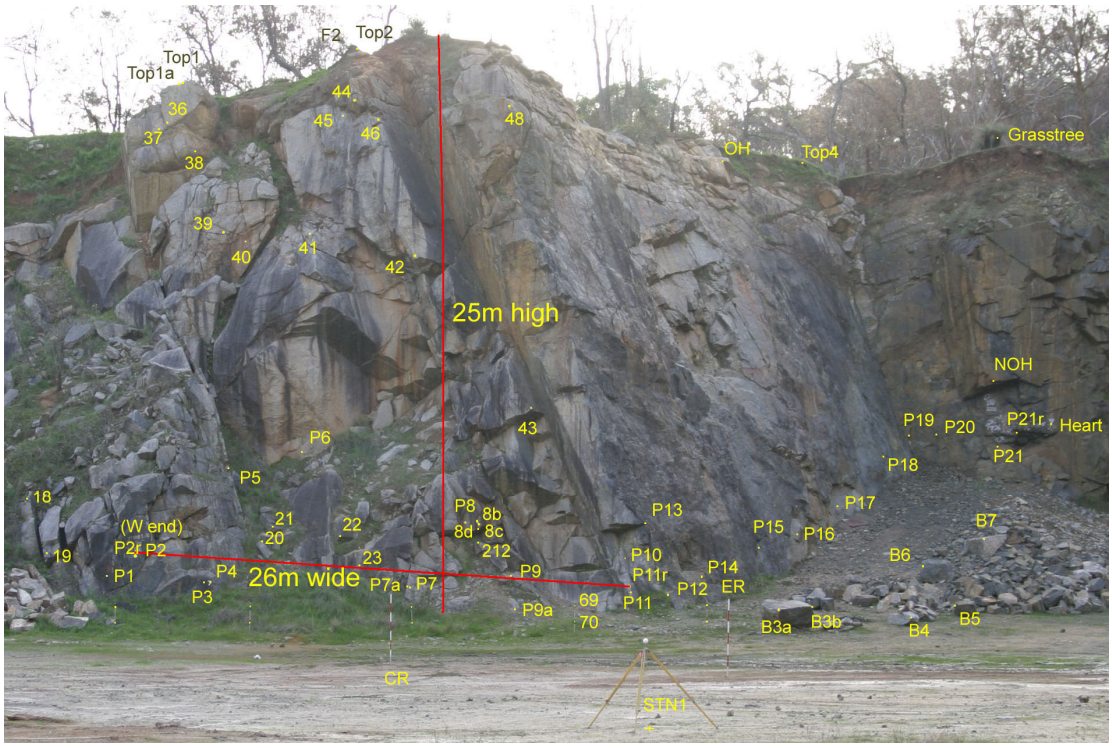

Figure 6.2 Western rock face at Mountain Quarry, with index to control points

diameter circular reflectors and twelve rectangular white 50mm wide adhesive tape targets were placed around the crest, base and rock face of the south west to north west quadrant of the quarry. An additional eleven 5cm-sided white-painted triangles and ten 19mm orange adhesive paper discs were also placed on low rock faces, five 60cm poles and four 2m ranging poles were also placed in the quarry floor as secondary targets to increase the number of control points for use in the field camera calibration. The targets in the centre of the rock face were placed by scaling the rock face with the aid of climbing ropes. The large number of targets was used to:

(a) ensure consistent co-registration of the many multi-image and close range stereo photogrammetric models built with images taken from a wide range of orientations; and
(b) to perform a field calibration of the camera lens.

The reflective targets were used to allow co-registration between the photogrammetric and TLS point clouds.

6.2.3 Defining the Object Space within the Quarry

The main aim of the study in the quarry was to compare the orientations and measurements of rock surfaces obtained from photogrammetric, TLS and manual methods. Consequently, the two most important orientation parameters defining the local object space were the North direction and the horizontal plane. Absolute ground coordinates were not directly relevant to the orientation study, but were used for bringing in the external coordinate system into the quarry and visualising the results by superimposition onto the oriented stereo pair of vertical aerial photographs and existing SkyView orthophoto (Figure 6.1). Two independent surveying methods were used to determine the orientation of the coordinate system within the quarry:

(a) Points were extracted from the vertical aerial photography stereo model oriented using an imported exterior orientation, and extended to the quarry object space using the TLS point cloud;
(b) A Total Station survey bringing in an external bearing to a known point on the hillside at the edge of the quarry.

A permanent survey station, STN1 (see Figures 6.1 and 6.2) was marked by drilling a hole into the surface of a large boulder protruding through the gravel in the centre of the quarry floor. An additional reflector and painted mark were sited on a large

boulder ("N" on Figure 6.1) estimated using a hand-held sighting compass to be due north (magnetic) of STN1 (precision estimated to be ±1º). STN1 was used as the centre of both the TLS and photographic surveys.

6.2.4 Object Space Defined by Aerial Photogrammetry and TLS

Two 1:20,000 scale digital aerial photographs together with the external image orientation data, purchased from the DLI, were loaded into the uSMART softcopy program (version 8.20.0). The aerial photographs had been photogrammetrically scanned at 21μm (1209 dpi), resulting in a ground resolution of approximately 0.44m. Assuming a measurement precision of 0.5 pixel, $\sigma_i = 1.05e^{-5}$m; $\sigma_x = \sigma_y =$ 0.31m and $\sigma_z = 0.53$m. Ground height at the location of STN1 at the centre of the quarry floor was measured from the vertical stereo pair to be 94.15m. As neither STN1 or N were visible on the aerial photography, the TLS was used to obtain coordinate estimates for STN1 and N based on a set of six points that were clearly visible in both the vertical aerial photographs and the post-modification quarry.

The iSiTE TLS system includes a Reigl LMS Z-210 scanner that offers a 336º horizontal field of view and 80º vertical field of view (Reigl, 2004; Lichti, et al., 2002a, 2002b). While the range accuracy is quoted at ±25mm, this is improved by the aggregation of repeated scans; 16 scans in high accuracy mode reduces the quoted accuracy to ±6mm (Lichti, et al., 2002b). The quoted beamwidth of 3mrad samples a circular spot 150mm in diameter at a range of 50m; in the fine resolution sampling mode, the sampling interval of 2mrad is approximately 100mm at the same range.

The TLS was set up over STN1, and two point clouds were collected. One point cloud (labelled "Quarry") was averaged over four scans for the maximum available horizontal sweep ±168º, with the scanner horizontal rotation initially centred towards the N mark. A second point cloud (labelled "Rockface") was collected over the north west quadrant of the quarry that included the rock face containing the planes to be measured; this was averaged over 25 scans and also oriented with respect to the "N" target. Six reflectors were visually identified within the Quarry point cloud at prominent rock features that could be identified on the aerial photographs (B1, B2, P2, P11, P17 and P18 on Figure 6.1), and an additional reflector (N) was located only

in the TLS point cloud. The iSiTE TLS viewing software was used to extract centroids of the reflectors from the point clouds; these were included within a rigid body transformation with two unknown points, STN1 and N; the results are given in Table 6.1. As the centre of the TLS point cloud, the coordinates for STN1 are the C and D parameters from the rigid body transformation, and the bearing from STN1 to the N reflector was estimated to be 357º 40’ 0”, with an estimated precision of 31’ 39”.

Table 6.1 Results of 2D rigid body transformation on control points

Reflector	Photo coordinates		TLS coordinates		Residuals	
	X (m)	Y (m)	X (m)	Y (m)	X (m)	Y (m)
B1	411310.453	6468600.488	-28.776	-17.178	0.104	-0.101
B2	411278.045	6468602.648	-61.388	-13.739	-0.399	0.091
P2	411298.559	6468628.558	-39.512	10.963	0.248	-0.237
P11	411303.999	6468644.061	-33.551	26.596	0.272	0.183
17	411338.074	6468676.650	1.790	57.542	0.685	-0.088
18	411349.022	6468675.163	11.038	55.990	-0.910	0.152

Transformed points				Transformation parameters (m)	
	X (m)	Y (m)	Z (m)		
B1	411310.557	6468600.387	94.436	A =	1.005598
B2	411277.646	6468602.739	93.859		
P2	411298.807	6468628.321	96.168	B =	-0.033929
P11	411304.271	6468644.244	95.766		
17	411338.759	6468676.562	96.329	C = (#)	411338.912
18	411348.112	6468675.315	96.968		
19*	411367.834	6468675.699		D = (#)	6468618.637
N*	411336.965	6468666.430	93.981		

* Transformed reflector coordinates for TLS data only

\# TLS origin at STN1 is 411338.912 mN, 6468618.637mE
Bearing to N reflector is 357º 40' 0"

6.2.5 Object Space Defined by Total Station Survey

In the second procedure defining the object space, a Trimble 5600 Reflectorless Total Station was used to bring the known bearing to a known feature into the quarry; in this case the bearing to the narrow supporting column of the Perth Airport Control Tower, 8.89km away. The Control Tower was sighted from a survey station

at the top of the quarry (QTOP on Figure 6.1) that was located at the northern edge of a rock platform clearly visible on the stereo vertical aerial photographs. Coordinates for QTOP were obtained from the oriented stereo vertical aerial photography. Table 6.2 gives the calculations for the positions of STN1 and N based on bearing and distance from QTOP. Using the external bearing from the Control Tower, the orientation from STN1 to N was calculated be 357° 57' 33".

Table 6.2 Calculation of bearing from STN1 to N obtained by Total Station survey

Coordinates of Airport Control Tower	403126mE	6465382mN
Coordinates for QTOP obtained from oriented aerial photography	411412.894mE	6468600.625mN
Bearing from QTOP to Control Tower	248º 46' 25"	
Distance from QTOP to Control Tower	8890m	
Bearing from QTOP to STN1	284º 01' 08"	
Horizontal distance from QTOP to STN1	75.046m	
Coordinates of STN1	411338.912mE	6468618.637mN
Bearing from QTOP to N	310º 35' 55"	
Horizontal distance from QTOP to N	100.971m	
Reduced coordinates for N	411336.965mE	6468666.430mN
Reduced bearing from STN1 to N	357º 57' 33"	

6.2.6 Comparison of Orientation Results

Geosciences Australia provides values for magnetic declination online at their website (http://www.ga.gov.au/oracle/geomag/agrfform.html); as of the date of the field survey, 30 June 2004, the magnetic declination for Boya was -1.279º. Coupled with the -0.496º variation for the MGA94 grid convergence at Boya Quarry (calculated using *redfearn.xls*, downloaded from the Geosciences Australia website), the variation between compass measurements and orientations derived from grid coordinates in June 2004, was estimated to be -1.775º. Variation from the hand-held compass orientation was approximately 0.55º for the vertical aerial photography oriented using the exterior orientation data provided by DLI, and 0.27º for the Total Station survey oriented with respect to the Airport Control Tower. This confirms that hand-held compass bearings are unlikely to be more accurate than about 1º, ±0.5º.

6.2.7 Artefacts Visible in the TLS Point Cloud

Once downloaded into the iSiTE software, the "Rockface" TLS point cloud was re-oriented using the ground coordinates of STN1, the measured height of the instrument and the coordinates of control points P2 and P11. The oriented point cloud was subsequently imported as a set of 3D points into the stereo photogrammetry softcopy model and visually compared to the features on the stereo image. Viewing the point cloud as stereoscopic points proved visually confusing as the regular distribution of points produced optical illusions due to visual mis-matching of point pairs. Consequently the point cloud and primary GCPs were rotated (κ = -70º, ω = -82º; following Chandler, 1999) so that the plane of the rock face approximated the XY plane of the softcopy coordinate system, and translated to a model space lying between zero and 1000m in X, Y and Z, to simplify subsequent measurement. This allowed the TLS point cloud to be treated as a conventional XY-based DEM in the uSMART softcopy package for TIN creation and grid-based auto DEM generation. The TIN model of the point cloud was viewed more easily as a stereo overlay in the photogrammetric models than the point cloud because the lines provided a more consistent visual reference than points.

Two measurement artefacts were easily observed within the TLS point cloud:

(a) TLS cloud points could be seen to lie at locations closer to the scanner when located within sharp concavities between two planes separated by five or fewer sampling increments, indicating these points would be unsuitable for use for orienting small planes bounded by concave edges, particularly within narrow recesses;

(b) Some TLS cloud points were seen to extend for one to two sampling increments beyond planes with sharp convex edges. This could be attributed to the compound effect of the beamwidth of approximately 0.15m at the target distance of 50m, and the scanning resolution of approximately 0.1m, where sufficient signal is returned from the outer part of the beam to record a point approximately continuous with the adjacent plane.

6.3 Multi-Image Photogrammetry

Plane measurement with error estimation using multi-image photogrammetry requires co-identification of points across at least three photographs. A multi-image photogrammetric model was built with PhotoModeler (version 5.0) covering most of the quarry floor and rock faces on the south west, north and eastern faces. This was oriented using the ground control points listed in Table 6.1, and used to estimate coordinates for the reflectors and painted triangles on the western rock face. The model included 379 points measured on a total of 50 photographs; 32 photographs formed the convergent run and 18 photographs were taken at higher elevations around the southern, eastern and northern crest of the quarry. The RMS error of all the estimated measured point coordinates was 23.8mm, which included 124 measured points on planes within the western rock face, as shown in Figure 6.3. The RMS error of the painted and reflective pre-marks was 9.2mm. Image coordinates for each of the measured points were exported from PhotoModeler and converted into a format suitable for input in a bundle adjustment carried out using Australis

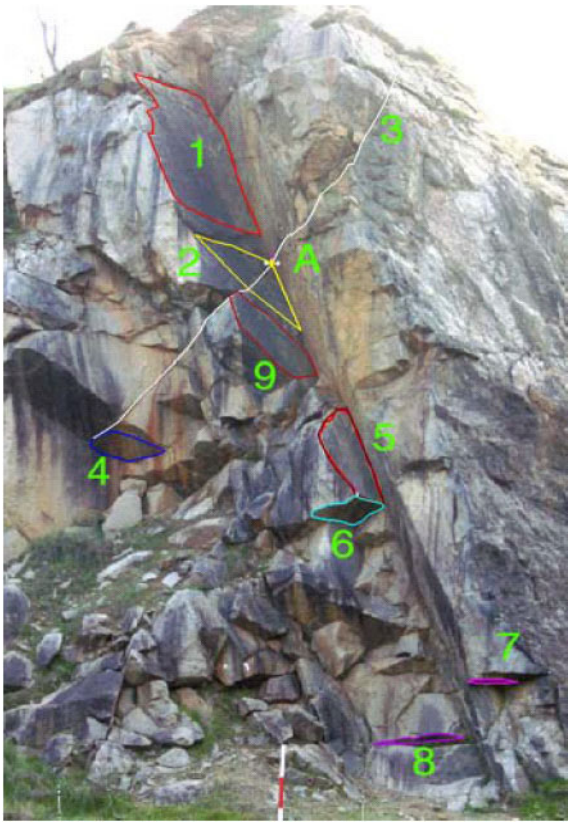

Figure 6.3 Index of target planes on the western rock face

software (version 6.0; Fraser and Edmunson, 2000), with a higher weighing given to the TLS-confirmed points. The adjusted coordinates were used as the control points in setting up the photogrammetric stereo models and to perform a field calibration of the camera.

A sub-set using image numbers 4, 8, 12, 16, 20, 22, 24 and 28 from the 32 images in the convergent run was used for the measurement of rock surfaces. Planes 1, 2, 4, 5, 6 and 9 as shown on Figure 6.3 were measured on six images over an arc of 43º, while Planes 3, 7 and 8 were measured on eight images over 62º of arc. The measured points and the outline of the planes are shown in Figure 6.3. Points were located on prominent features on the rock surface around the edges of the target planes and cross referenced to either six or eight images, depending on visibility. The RMS error of the natural features forming the boundaries around the target planes was 29.4mm.

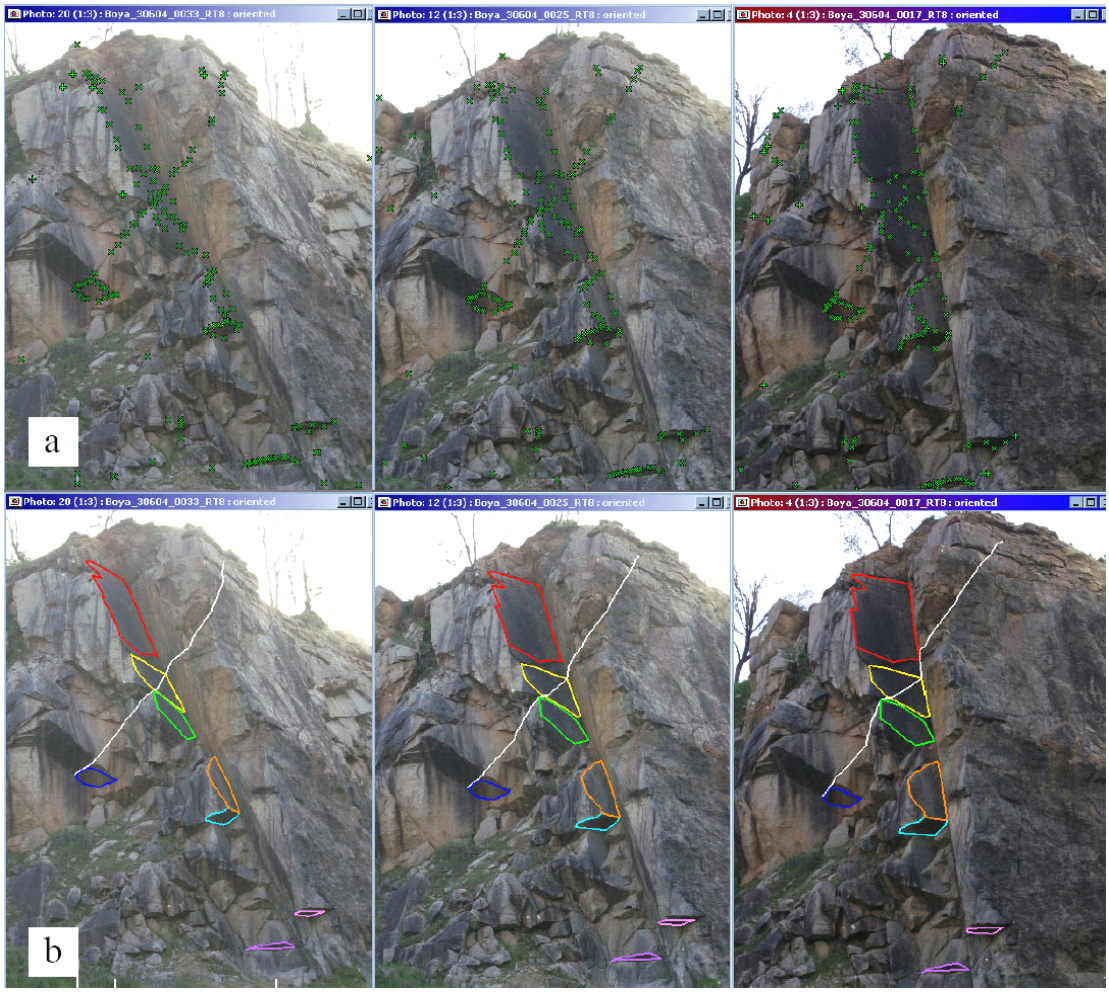

a: measured points b: outlines of planes

Figure 6.4 Three of the images used in PhotoModeler for plane measurement

Individual points were audited using two methods to eliminate gross errors. PhotoModeler software highlights the residual between the measured location on each photograph and the projected location as calculated from the 3D model. The point was moved only where this clearly indicated the wrong feature had been selected. Points were not moved where no visible improvement was identified based on the shape or colouration of the rock surface, as any remaining residual was likely to be due to uncertainty in location and systematic error through the camera calibration. Lines joining the identified points around the edges of the target features were colour-coded to aid 3D viewing. Once oriented, the model was observed during rotation in PhotoModeler's 3D Viewer which further aided identification of gross errors, due to differential parallax between good and adjacent potentially erroneous points. Figure 6.4 contains three of the images used showing the points co-identified and the relative perspective view of the edges of the planes.

Multi-image photogrammetry programs already include routines such as auto-drive and auto-centroiding to assist in point measurement. However, manual point selection techniques are time-intensive as the points need to be correctly identified on each image if quality control is to be maintained. True stereo viewing is not possible with PhotoModeler, although this was achievable by placing two image windows side-by-side, manually adjusting the scale, X and Y parallax, and viewing with a mirror screen-stereoscope. However, this did not allow true stereoscopic placement as corresponding points on each image need to be identified independently. This technique proved useful in identifying corresponding features on the rock face, as in some cases the appearance of the features changed significantly depending on the perspective. Perspective changes are investigated in greater detail in the following section on stereo photogrammetry, where large variations can limit the possibilities for automated point measurement.

6.4 Stereo Photogrammetry

One major difference between multi-image and stereo photogrammetry is in the number of independent models needed for measurement. While it is possible to include terrain with a wide range of orientations within one multi-image model, stereo photogrammetry captures measurements from independent stereo pairs. The conformity of adjacent stereo models depends on the ability of the system to

correctly measure the true ground coordinates, especially at edges of terrain units between models. Where there are system-induced errors, for example due to incorrect geometric camera calibration or displacement of the measured point, the same feature may be given different coordinates when mapped on different stereo models. The present investigation quantifies some of the limitations to be considered when using semi-automated measurement for complex terrain such as hillsides.

A set of photogrammetric models was built in the uSMART softcopy package using stereo pairs from the parallel run with an increasing photobase (ratio between the separation of the two perspective centres and the target distance) for each subsequent model. The photobase was increased by taking the next-outside image alternately at each side of the run, starting with the two frames identified as lying closest to the bisector of the two major rock surfaces forming the largest steeply-sloping wedge on the rock face (Figure 6.3). Overlap between the two images reduced to less than 50% when the photobase exceeded 16m; at this photobase, stereo viewing uses the opposite outer areas of each photograph and a significant problem was encountered with Y parallax that prevented accurate point measurement. This was attributed to systematic error remaining unmodeled within the camera calibration, coupled with unmodeled lens motion probably due to the use of a zoom lens (Chapter 3.5). Figure 6.5 shows the comparatively large radial distortion which approaches 0.4mm near the outer parts of the lens. With an array pixel size of 0.0074mm, this gives a distortion of 0.418mm at the maximum radial distance of 13.661mm, although the practical working limit is 10mm radial distance (Figure 6.5b) at which the radial distortion is

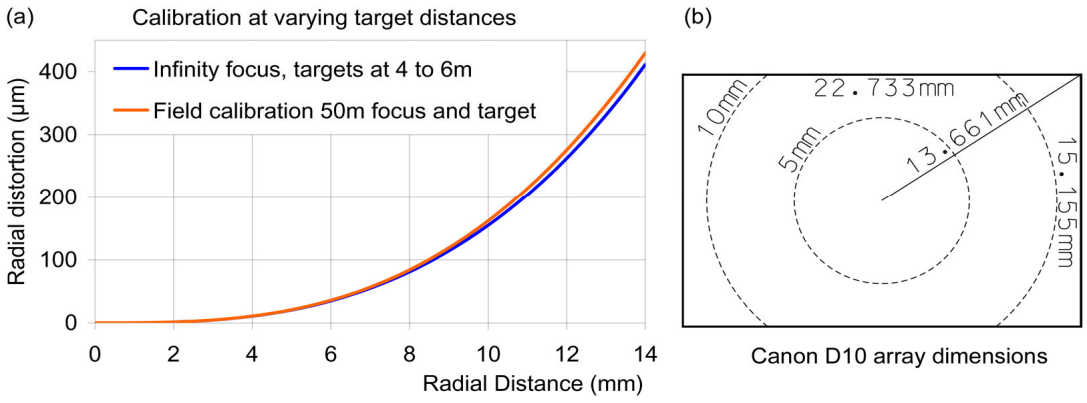

Figure 6.5 Distortion curves for the Canon EOS D10 fitted with a 28-70mm zoom lens, 28mm focal length setting

0.170mm (23.0 pixels on the axial directions). Small errors in the determination of the Principal Point and Asymmetrical Distortion components of the calibration are more likely to have significant effects when using widely-separated areas from different images, especially the outermost parts of the frames, an effect that is normally very small when using high precision metric cameras in aerial topographic surveys (Krauss, 2000; Mikhail et al., 2001).

To reduce the effect of unmodeled distortions in the camera calibration, a second set of photogrammetric models was built using similar increasing photobases but with images from the convergent run. Photobases as determined by spatial resection are listed in Table 6.3, together with the approximate photobase:object distance (equivalent to Base/Height ratio for vertical aerial photography, Chapter 3.4). Chandler et al. (2005) note that photobase:object distance ratios of 1:6 are common in scientific photography, which is approximately equivalent to that present in stereo model C16_20_8m (Table 6.3).

Table 6.3 Photobase variations for stereo models in the convergent run

Stereo model	Photobase (m)	Photobase:distance ratio (approximate target distance is 45m to centre of rock face)
C17-18_2m	1.972	0.044 (1:22.8)
C17-19_4m	3.782	0.084 (1:11.9)
C16-19_6m	5.723	0.127 (1:7.86
C16-20_8m	7.508	0.167 (1:5.99)
C15-20_10m	9.314	0.207 (1:4.83)
C15-21_12m	11.286	0.251 (1:3.99)
C14-21_14m	13.182	0.293 (1:3.41)
C14-22_16m	15.179	0.337 (1:2.96)
C13-22_18m	17.018	0.378 (1:2.64)
C13-23_20m	18.714	0.416 (1:2.40)

After orienting the stereo models to the rotated sub-horizontal ground control points (Table 6.1), clouds of 3D points to be used for the determination of plane orientation were measured by three methods:

(a) Manual boundary line placement (operator-control of X,Y and Z, stereoscopic determination of rotated Z value);

(b) Semi-automated boundary line placement with the feature boundary followed by the operator (the rotated X and Y axes) and allowing the image-matching algorithm (named dynamic correlation in uSMART; also known as a terrain-following cursor) to determine the rotated Z value. This matches the contents of the left and right images and is controlled through setting the correlation window size and the minimum correlation threshold (Chapter 3.4; Kraus, 2000);

(c) Automated DEM generation. The correlation settings are similar to dynamic correlation, but the routine attempts to place 3D points across a user-defined grid, with points added when the correlation exceeds a user-specified threshold. Minimum correlations of 90%, 80%, and 70% were used in this investigation.

A sample of nine planes were repeatedly measured using the three methods to assess the relative effects of photobase, point resolution and the local effects of adjacent non-parallel rock surfaces. Once captured, the point clouds were transformed back to the original orientation and then passed through the LSP program (Chapter 5.5) to determine the orientation of each plane. The effect of changes in the photobase on the image correlation routine were tested using stereo pairs consisting of frames taken at increasing distances from both sides of a central point on the set of convergent images. This gave image separations ranging from 1.972 to 18.714m (Table 6.3).

The nine sample planes represented three types of feature as shown in Figure 6.3:

(a) Planes with good visibility, i.e., upward-facing, brightly-illuminated Planes 1, 2, 5 and 9, and downward-facing, moderately illuminated Planes 4 and 6;

(b) Planes with poor visibility, i.e., Planes 7 and 8. Plane 7 faces steeply downward but is open underneath, whereas Plane 8 forms the upper plane of a narrow crevice with a second plane limiting illumination within the crevice;

(c) Plane 3 forms the daylighting trace of a joint surface within the rock mass, but doe not form any exposed planar surfaces.

6.5 Comparison of Results

Table 6.4 contains the results of the three methods used for the nine target planes; the lower pane of the table contains the variation between the dip and dip directions

Table 6.4 Comparison of photogrammetry and TLS results

	Dip length (m)	Strike length (m)	PMu		PMw		uSMART		Laser scanner	
			Dip (°)	DD (°)	Dip (°)	DD (°)	Dip (°)	DD (°)	Dip (°)	DD (°)
Plane 1	5.4	2.8	63.7	63.7	62.7	62.9	62.5	64.0	62.9	63.4
Plane 2	2.4	2.1	63.0	69.2	64.2	69.9	62.0	68.6	61.8	66.4
Plane 3	11.9	2.7	56.4	169.3	55.6	171.4	56.4	169.4	Δ	Δ
Plane 4	1.0	1.7	51.4	292.1	49.8	293.3	47.8	295.1	51.6	292.7
Plane 5	2.5	1.3	63.9	65.7	64.2	65.7	64.7	66.2	64.7	66.6
Plane 6	0.9	1.6	44.4	254.6	43.2	257.2	42.1	257.5	40.0	254.5
Plane 7	0.5	1.2	18.9	264.6	18.2	264.5	14.7	261.8	24.5	262.8
Plane 8	0.4	1.6	58.4	294.5	56.6	295.1	34.2	287.3	32.3	124.3
Plane 9	2.6	2.0	67.2	66.6	66.7	66.6	64.3	65.7	67.0	69.1
	PMw - PMu		PMu - uSMART		PMw - uSMART		PMw - Laser		uSMART - Laser	
	Dip (°)	DD (°)	Dip (°)	DD (°)	Dip (°)	DD (°)	Dip (°)	DD (°)	Dip (°)	DD (°)
Plane 1	-1.0	-0.8	1.2	-0.3	0.2	-1.1	0.8	0.3	-0.4	0.6
Plane 2	1.2	0.7	1.0	0.7	2.2	1.3	1.2	2.8	0.3	2.2
Plane 3	-0.8	2.0	-0.1	-0.1	-0.9	2.0	Δ	Δ	Δ	Δ
Plane 4	-1.6	1.2	3.7	-3.0	2.1	-1.8	-0.2	-0.6	-1.8	0.6
Plane 5	0.3	0.0	-0.9	-0.5	-0.5	-0.5	-0.9	-0.9	-0.5	-0.9
Plane 6	-1.2	2.5	2.3	-2.8	1.1	-0.3	4.4	0.1	3.2	2.6
Plane 7	-0.7	-0.1	4.2	2.8	3.5	2.7	-5.6	1.8	-6.3	1.7
Plane 8	-1.8	0.5	24.2	7.2	22.4	7.7	26.1#	170.2 #	24.3#	170.8 #
Plane 9	-0.4	0.1	2.8	0.8	2.4	0.9	0.2	-2.6	-0.2	-2.5
Abbreviations: PMw = PhotoModeler weighted; PMu = PhotoModeler unweighted; DD = Dip Direction										
Δ Note (1): No laser results produced for this feature										
# Note (2): Laser results are unreliable for this feature										

obtained for the four methods: multi-image photogrammetry without and with weighting, stereo photogrammetry, and the TLS.

Planes 1, 2 and 9 have the minimum dimensions along both the dip and strike axes of 2.0m; Plane 5 is smaller, with dimensions 2.5m down dip and 1.3m horizontally. For these planes, plus the daylighting Plane 3 that was only measured photogrammetrically, the dip and strike values estimated for each feature by the three alternative methods agree within 2.8º. Of the smaller features, the results for Plane 4 agree within 3.7º; this forms a clearly-visible feature oriented at close to orthogonal to the bisector of the camera axes. Plane 6 is a steep overhang where the lower, more recessed part of the feature is in shadow (Figure 6.3); while the results for the three photogrammetric methods agree within 2.8º, the variations with the laser scanner

increase slightly to a maximum of 4.4º. When viewed stereoscopically, the points in the TLS point cloud can be seen not to penetrate sufficiently deeply into the concave recess at the base of the feature. This latter problem is also apparent with Plane 7 and especially for Plane 8, where the multi-image photogrammetry also over-estimates the dip due to poor placement within dark shadow enhanced by the short down-dip dimension. Both Planes 7 and 8 form shallow gradient overhangs, dipping into the rock face at a small angle to the camera axis and forming a narrow recess.

The results for the weighted multi-image photogrammetry are slightly closer to those for the stereo photogrammetry than the unweighted estimates. Excluding Plane 8, RMSE (root mean square error) values averaged over both the dip and strike are 2.1º for the comparison between the unweighted multi-image and the stereo photogrammetry, and 1.7º for the weighted comparison. If the second problematic feature, Plane 7, is also removed, the RMSE values decrease to 1.8 and 1.4º respectively.

6.5.1 Comparison with Manual Measurement

Orientations of the planes were measured by hand using a Suunto compass with integral clinometer. Hand-measurement was difficult for all the planes except for Plane 8 (lowest), as they were taken while suspended on a climbing rope, belayed from the top of the rock face. Measurement of low gradient, overhanging planes was facilitated by use of a small plate to project the orientation of the plane beyond the rock face to where a measurement could be made (as recommended by Hoek and Bray, 1981). Table 6.5 compares the hand measurements of each feature with the stereo photogrammetry. Of the 16 differences noted in Table 6.5, half differ by less than 3º. Planes 7 and 8 are small, dark overhangs, where the measurements made by photogrammetry have low reliability; if these two planes are excluded, ten out of 12 measurements (83%) lie within 5º of dip and dip direction.

The variation is due to the difficulty of taking the hand measurements plus the effects of local curvature within the broadly planar surfaces. These undulations are apparent if the pattern of residuals from the measured points to the best-fit plane is considered; Figure 6.6 depicts the high density of measurement results from the TLS on Plane 1.

Table 6.5 Comparison between manual measurements of planes using compass and clinometer and stereo photogrammetry

	Hand Measurement		Stereo Photogrammetry		Difference	
	Dip (°)	Dip Direction (° N)	Dip (°)	Dip Direction (° N)	Dip (°)	Dip Direction (°)
Plane 1	66	66				
	62	71				
	67	68				
Minimum	62	66				
Maximum	67	71				
Mean	65	68.3	62.5	64	-2.5	-4.3
Range	5	5				
Plane 2	62	65				
	64	79				
	65	71				
Minimum	62	65				
Maximum	65	79				
Mean	63.7	71.7	62	68.6	-3	-10.4
Range	3	14				
Plane 4	45	291				
	47	293				
	48	289				
Minimum	45	289				
Maximum	48	293				
Mean	46.7	291.0	47.8	295.1	-0.2	2.1
Range	39	257				
Plane 5	64	71	64.7	66.2	0.7	-4.8
Plane 6	39	257	42.1	257.5	3.1	0.5
Plane 7	13	302	14.7	261.8	1.7	-40.2
Plane 8	53	301	34.2	287.3	-18.8	-13.7
Plane 9	64	71	64.3	65.7	0.3	-5.3
Plane 10	82	359	81.5	357.0	-0.5	-2.0

Undulations are visible across the width of the rock surface forming this plane, with an area of negative relief forming the central part of the feature as shown by the green + symbols, and the outer regions of mostly positive relief shown by the blue O symbols. The wavelength of the undulations is approximately 2 to 3m. The dimensions of the red bounding box in Figure 6.7 are 2.7m along strike, 4.8m down dip and the offset range (maximum combined length of positive and negative residuals) is 0.22m; note that the maximum negative residual was larger than the maximum positive, indicating that some points from within the adjacent plane were

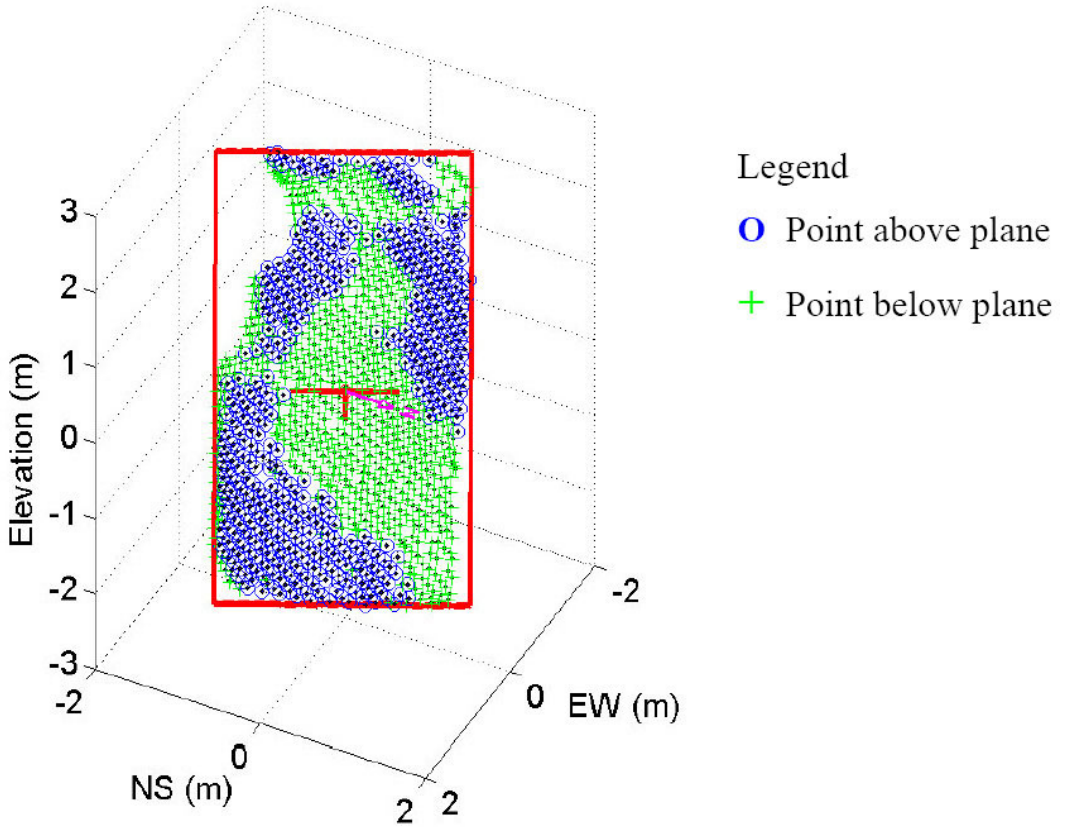

Figure 6.6 Isometric view of the distribution of residuals from the TLS point cloud to the best-fit plane for Plane 1

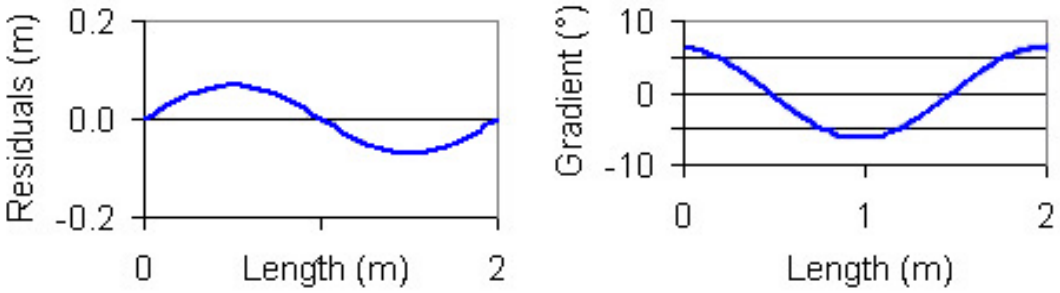

Figure 6.7 Graphs showing the variation of gradient for a 2m wavelength line with amplitude 0.07m

also included in the sample, as shown by the thin green line of + symbols along the southern edge in Figure 6.6. Some variability in individual gradient measurement is expected with an undulating surface, depending on the boundary selected relative to the wavelength of the undulations. Figure 6.7 graphically shows the variation in amplitude and gradient along a sine wave with amplitude 0.07m and wavelength of

2m, in which the maximum gradient is 6.25º. This indicates that the photogrammetrically-measured results fall within a similar range to the manual measurements as the North orientation bearing between survey stations STN1 and N (Chapter 6.2.6).

6.5.2 Semi-automated Mapping of Points and Lines

Semi-automated point capture is a potentially very valuable tool for the geomorphologist, who may be less experienced in precise stereoscopic point measurement than a photogrammetricist trained in topographic mapping, as it allows them to concentrate on feature delineation rather than maintaining accurate height determination. While morphological mapping is examined in greater detail in Chapter 7, it has been used here to aid visualisation of the results of the automated DEM generation. In semi-automated point and line capture, one of the cursors is driven to or along the feature to be digitised, while the software controls the position of the stereo cursor to maintain correlation with the surface in the image. In its simplest form, information enhancement of a line, symbology can be added to portray some characteristics of that line; in morphological mapping, the symbology

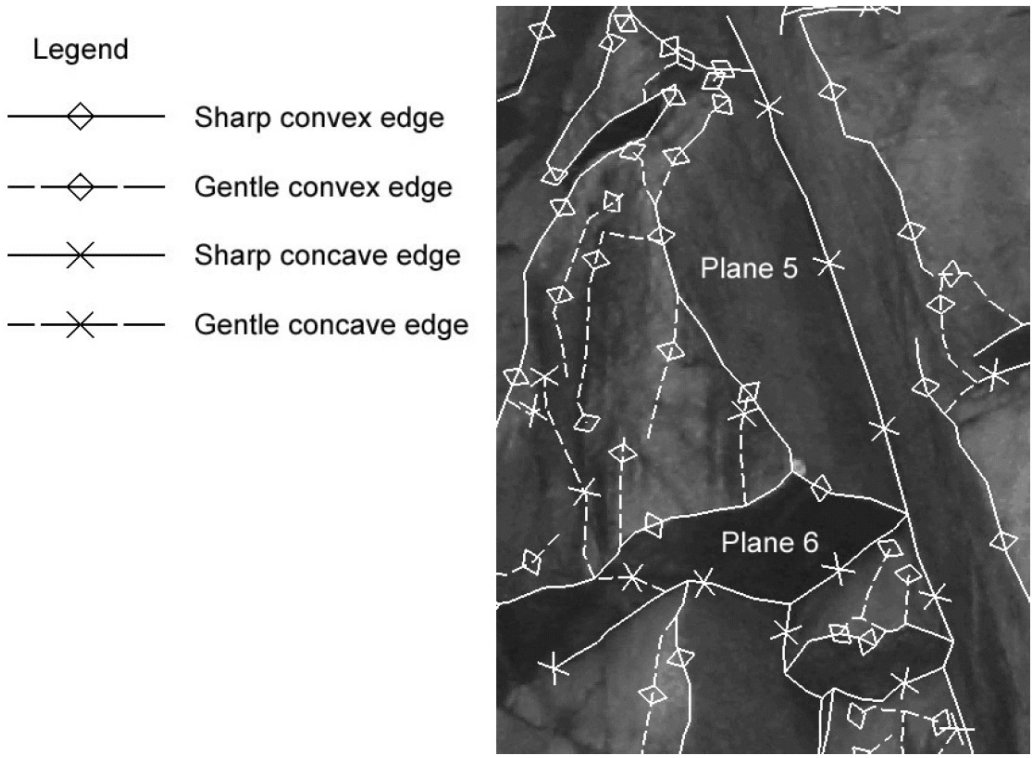

Figure 6.8 Morphology of the rock face around Planes 5 and 6

refers to whether the edge is convex or concave, and whether the boundary is sharp or gently curved. The principle is demonstrated in Figure 6.8, in which the morphological features of the rock slope around Planes 5 and 6 have been annotated.

The practical usefulness of semi-automated morphological mapping depends firstly, on the ability of the system to maintain digital image correlation, and secondly on the quality of that correlation. These aspects have been investigated in further detail below.

To test the effects of varying image correlation window size and photobase, the boundary of Plane 4 was measured with the stereo cursor driven manually (i.e. dynamic correlation routine disabled) for photobases ranging from 1.97 to 9.31m. These were compared with the results from semi-automated measurements (dynamic correlation routine enabled) using 4, 8 and 12 pixels wide square correlation window sizes, and with the same photobases. The results are given in Table 6.6 and as two graphical formats in Figure 6.9 and Figure 6.10. Figure 6.9 shows the results as lines plotted under semi-automated operator control using stereo photogrammetry, and

Table 6.6 Plane 4 image correlation results, rotated and unrotated models

Photo base (m)	Plane 4: Model coordinates				Range (°)	Plane 4: World coordinates				Range (°)
	Manual	Width of correlation				Manual	Width of correlation			
		4	8	12			4	8	12	
	Dip (°)					Dip (°)				
1.97	57.7	65.6	53.0	60.2	12.6	41.0	32.4	45.0	37.9	12.6
5.72	51.6	53.1	48.6	49.6	4.5	46.7	45.5	49.4	48.5	3.9
9.34	50.2	48.8	50.5	46.3	4.2	47.8	49.2	47.8	51.8	4.0
Range (°)	7.5	16.8	4.4	13.9		6.8	16.8	4.4	13.9	
Photo base (m)	Plane 4: Model coordinates				Range (°)	Plane 4: World coordinates				Range (°)
	Manual	Width of correlation window (pixels)				Manual	Width of correlation window (pixels)			
		4	8	12			4	8	12	
	Dip Direction (°)					Dip Direction (°)				
1.97	187.8	179.6	181.7	181.1	8.2	300.1	289.3	291.9	291.6	10.8
5.72	185.4	187.7	182.9	183.4	4.8	295.9	298.6	292.9	293.5	5.7
9.34	180.7	183.2	184.9	185.0	4.3	290.7	293.2	295.1	294.6	4.4
Range (°)	7.1	8.1	3.2	3.9		9.4	9.3	3.2	3.0	

Plane 4: (Independent of coordinate system)					
Photo base (m)	Manual	Width of correlation window (pixels)			Range (m)
		4	8	12	
	Offset Length (m)				
1.97	0.26	0.43	0.29	0.30	0.17
5.72	0.18	0.21	0.09	0.16	0.12
9.34	0.11	0.16	0.07	0.14	0.09
Range (m)	0.15	0.27	0.22	0.16	

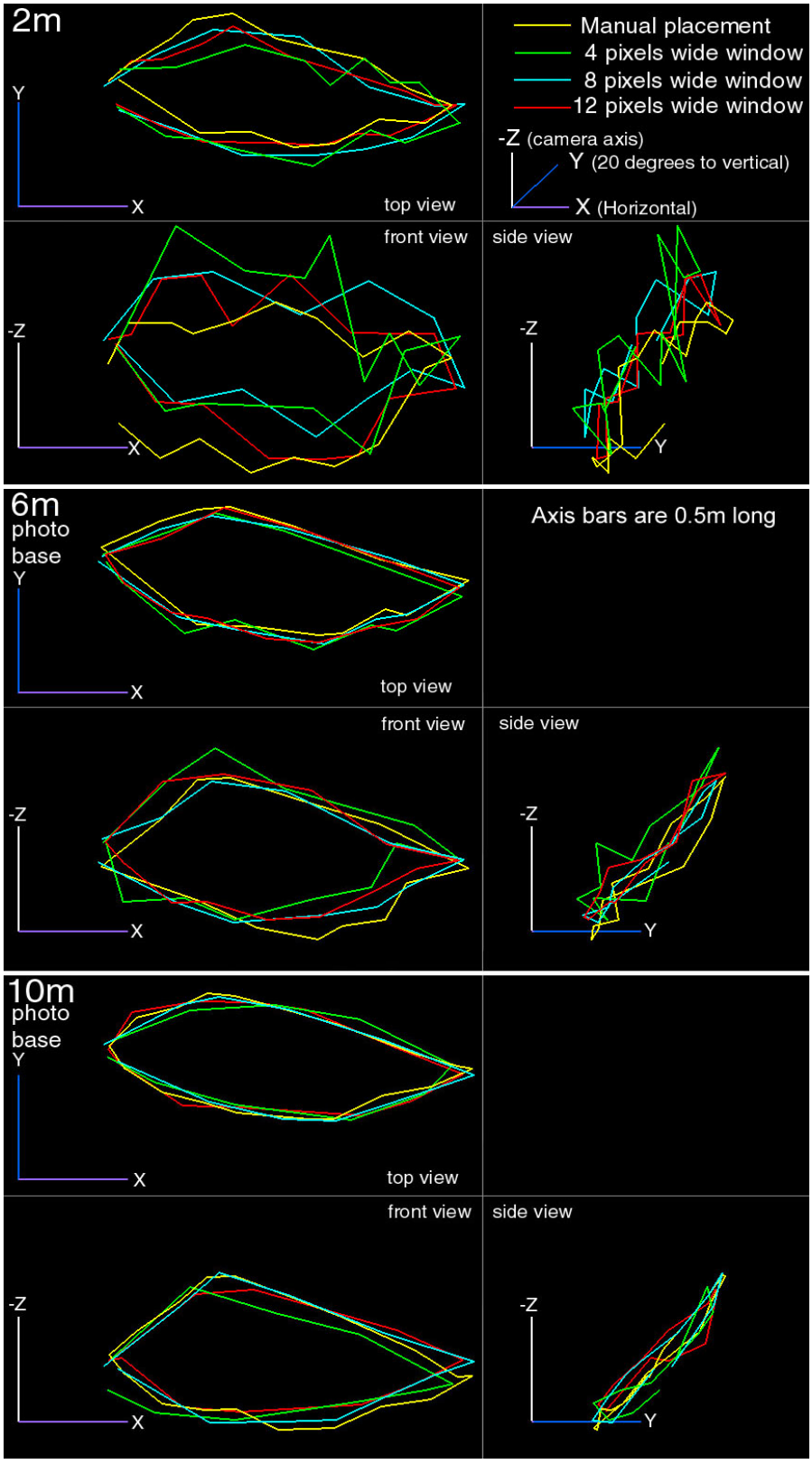

Figure 6.9 Plane 4 results measured with stereo photogrammetry

Figure 6.10 gives the results processed through the LSP program. For a narrow photobase, the individual points produce a wider scatter and slightly under-estimate

the dip, especially with small-sized correlation windows. Larger correlation windows are better able to match the quality of the visual mapping. For the wider photobase, the use of an 8 pixel wide correlation window results in a closely-followed surface that appears to deviate less from a planar surface than that produced manually by stereo-visual plotting.

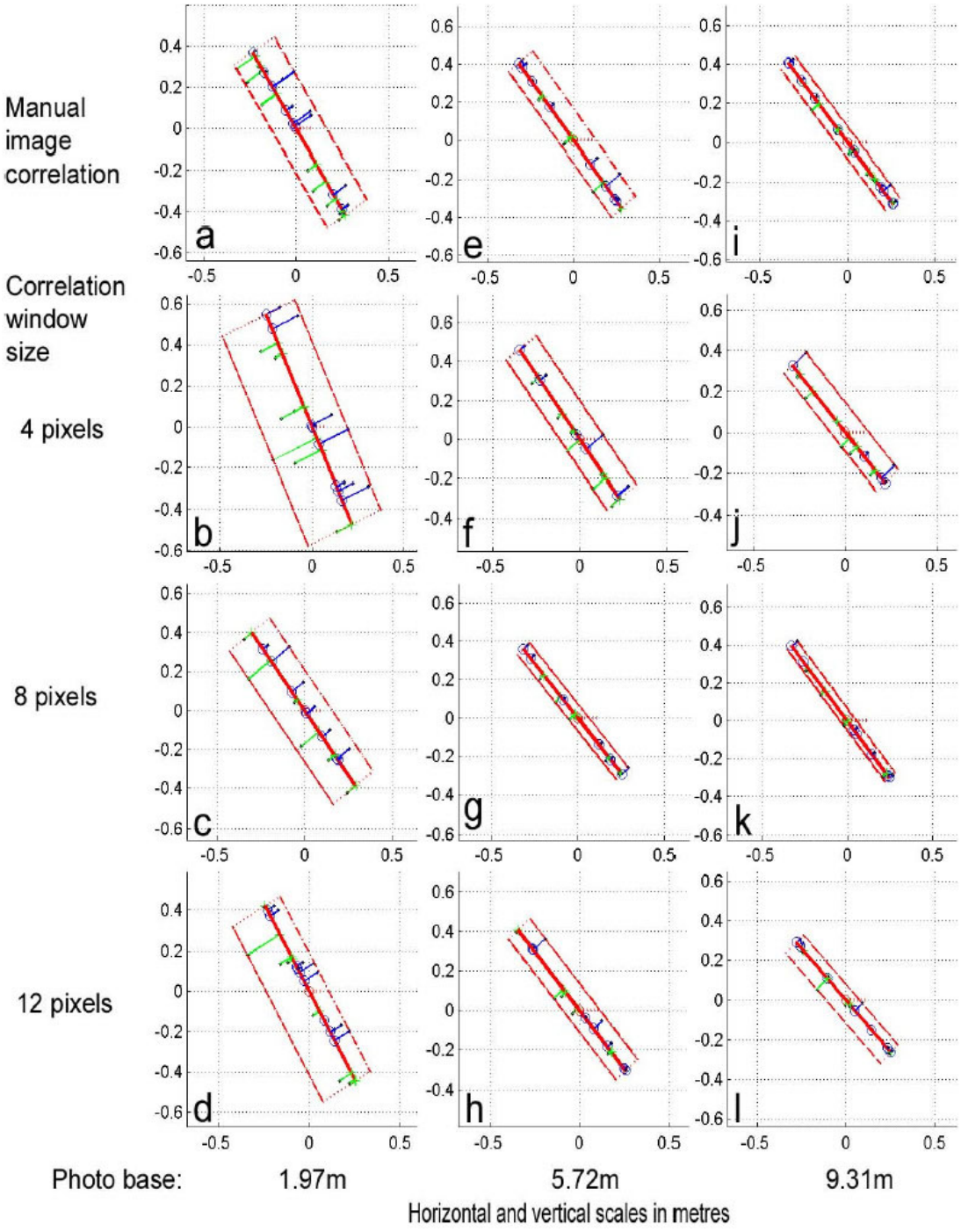

Figure 6.10 Variation in residuals from measured points to Plane 4 against correlation window size and photobase

6.5.3 Variations in Correlation Window Size

To investigate the effects of extreme changes in the size of the dynamic correlation window, the boundary of Plane 5 was plotted using increasing widths of the correlation windows, ranging from four to 56 pixels. Plane 5 occupies an area approximately 120 pixels wide on the images most perpendicular to the strike of the plane. The northern side (right hand side on Figure 6.4 and Figure 6.5) is bounded by the steep Plane 10 (Table 6.5) forming a sharp, 66º concavity with Plane 5, while the southern (left) and lower boundaries (with Plane 6) are sharp, convex edges. Figure 6.11 graphs the results, demonstrating that as the size of the correlation window increases, the orientation of the plane as derived by least squares estimation changes by over 10º. Although the variation produced by the raw photogrammetry affects both the dip and dip direction, it can be seen to be concentrated in the variation of dip direction once transformed to map coordinates.

This effect appears to be due to averaging of the elevations across the area covered by the correlation window; for concave angles the average elevation will be moved towards the camera, and for convex boundaries the average elevation will be moved away from the camera.

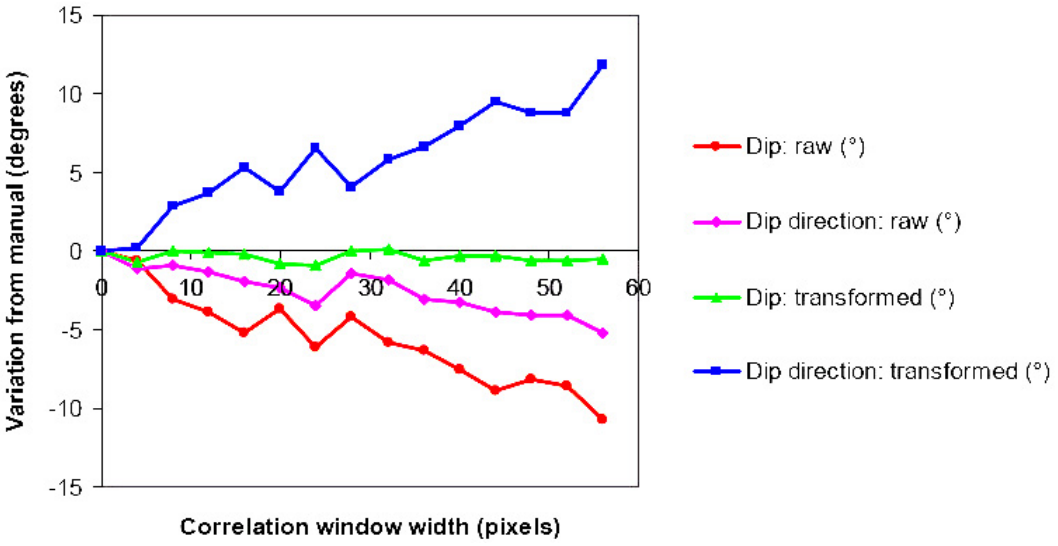

Figure 6.11 Effect of changes in size of the image correlation window

6.5.4 Effect of Increasing Photobase on Fully Automated DEM Generation

Dynamic image correlation in stereo photogrammetry uses the match between corresponding images to determine the best-fit cursor position and consequently 3D location. Factors that cause the geometric relationships between the patterns of light and shade to change between images are likely to affect the ability of the system to establish a true positive correlation, as compared to a false positive correlation that would generate an erroneous XYZ coordinate. In practical usage, small correlation windows (4 to 8 pixels wide) produced very erratic cursor movement responses while the cursor was being manually driven to follow the boundaries of a feature, with frequent correlation loss or false-positive matches. When correlation windows greater than 12 pixels wide were used, cursor tracking motion was smoother and the number of false positive correlations was generally reduced for any photobase. In the present study, the optimum window size for complex terrain was found to be ten to 12 pixels, as this allowed mostly smooth cursor movement while limiting the adverse effect of elevation averaging. For any given correlation window size, image correspondence is likely to decrease with increasing photobase due to perspective-induced changes in feature geometry; the negative effect will be amplified if the object contains smaller irregularities of shape such as depressions and ridges, especially if micro-topographic changes are mirrored in variations in texture and colouration, as is likely with the consequences of surface water flow and weathering.

When stereo photogrammetry is used in semi-automated mode to assist operator-directed feature mapping, the operator is able to see when the stereo cursor loses visual contact with the ground, and adjust the position until stereo lock is regained. When used for fully automated point measurement, this visual check is not possible until the data editing stage. Planes 5 and 6, which form a vertically-convex pair of surfaces, were measured using the grid correlation routine within uSMART to assess the effect of changing photobase on the resulting points. The grid correlation routine was set up to capture points at an X and Y spacing of 10cm across an area 3m wide by 4.5m high, surrounding the two planes (transformed coordinate space). The correlation window was set at 20 pixels, and the minimum acceptable correlation at 0.80 (80%); a large correlation window size was used to emphasis the potential effects of elevation averaging, while the correlation threshold was set at a high level to minimise the number of false positive correlations. With a ground pixel size of

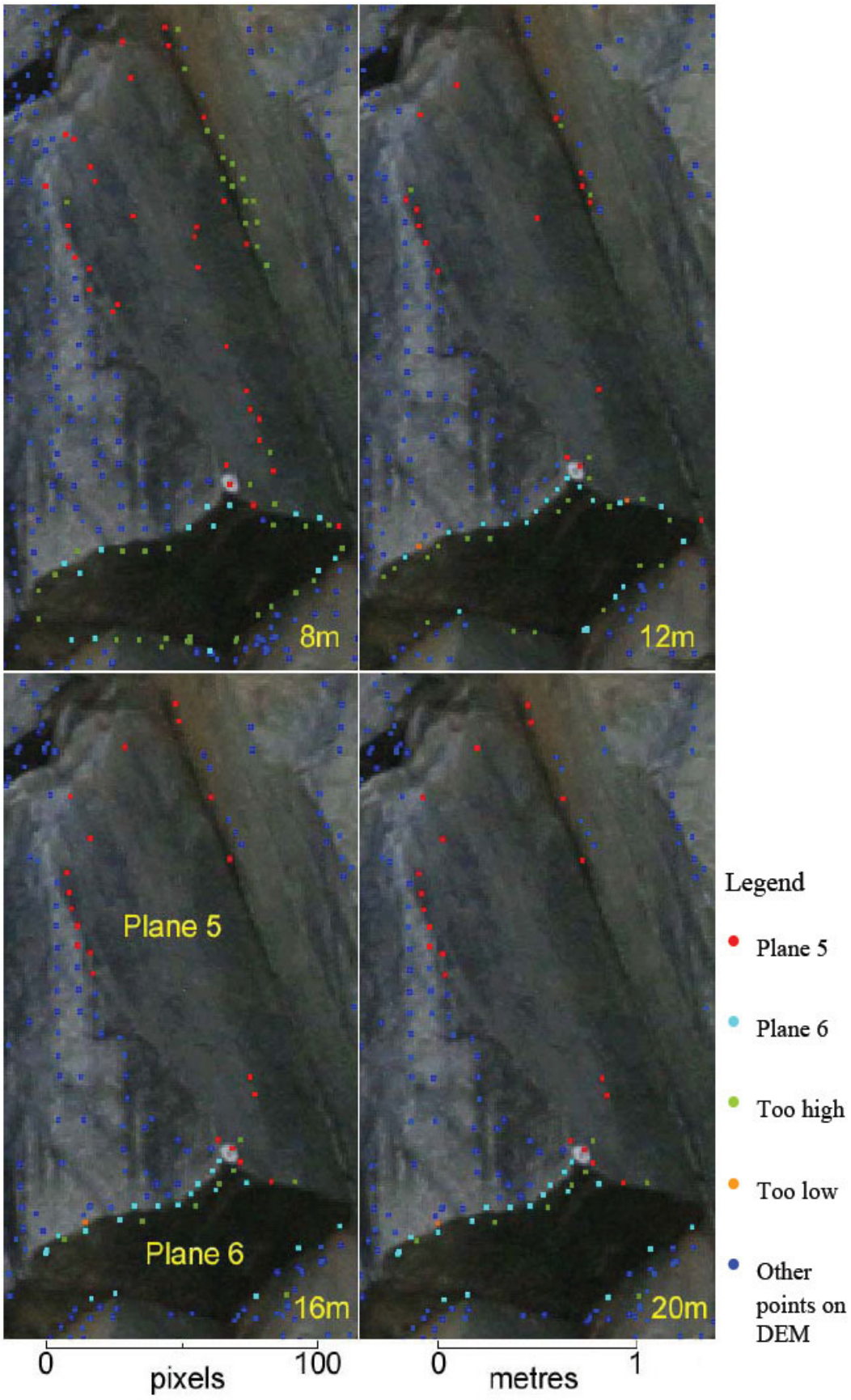

Figure 6.12 Planes 5 and 6, effect of changes in photobase, minimum image correlation threshold is 90%

approximately 11.1mm at an object distance of 42m, a 20 pixels wide correlation window included approximately 22cm width of ground when perpendicular to the camera axis. The results of the trial are shown in Figure 6.12, which includes four DEMs generated using photobases of 8, 12, 16 and 20m, draped over one of the pair of images used. The DEMs can be seen to contain points at widely varying spacings, with few points placed in areas of the image with low contrast and photo texture as compared to the higher textured regions.

The DEM for the 8m photobase contains many true positive correlations, especially across the highly-textured surface on the left of the image. DEM points are spread across most of the boundaries of Planes 5 and 6. The highly-textured surface to the left of Plane 5 has successful correlations for over 50% of the targeted locations. Within the low-textured surfaces of Planes 5 and 6, only 12 points were successfully correlated on the 8m photobase stereo pair, out of approximately 180 targeted points; this number reduces to only two points within the planes for the 12m photobase, and three for the 16m and 20m photobase stereo pairs. However, the planes were adequately bounded by successfully correlated points in all the stereo pairs.

Most false-positive points lie closer to the camera than the surfaces being measured, located along both convex and concave edges. For both Planes 5 and 6, and for both convex and concave edges, the number of false-positive correlations decreases with increasing photobase.

Figure 6.13 shows the effects on the estimated orientation of Planes 5 and 6, based on the automatically measured DEM points. Both planes show greater variability for photobases less than 7m, and consistent results for wider photobases.

The variation of over 2º for photobases less than 6m reduces and is consistent in the range 8 to 17m. The larger variability for Plane 6 was attributed to the smaller dip and strike dimensions as the larger Plane 5 will mask small variations in the measurement of bounding points (Table 6.4; Plane 5 has 2.5m dip length and 1.3m strike length). However, the dip orientation of Plane 6 changes by over 10º from the smallest photobase used (1.97m; Figure 6.6), which is probably due to the increased depth perception of wider photobases.

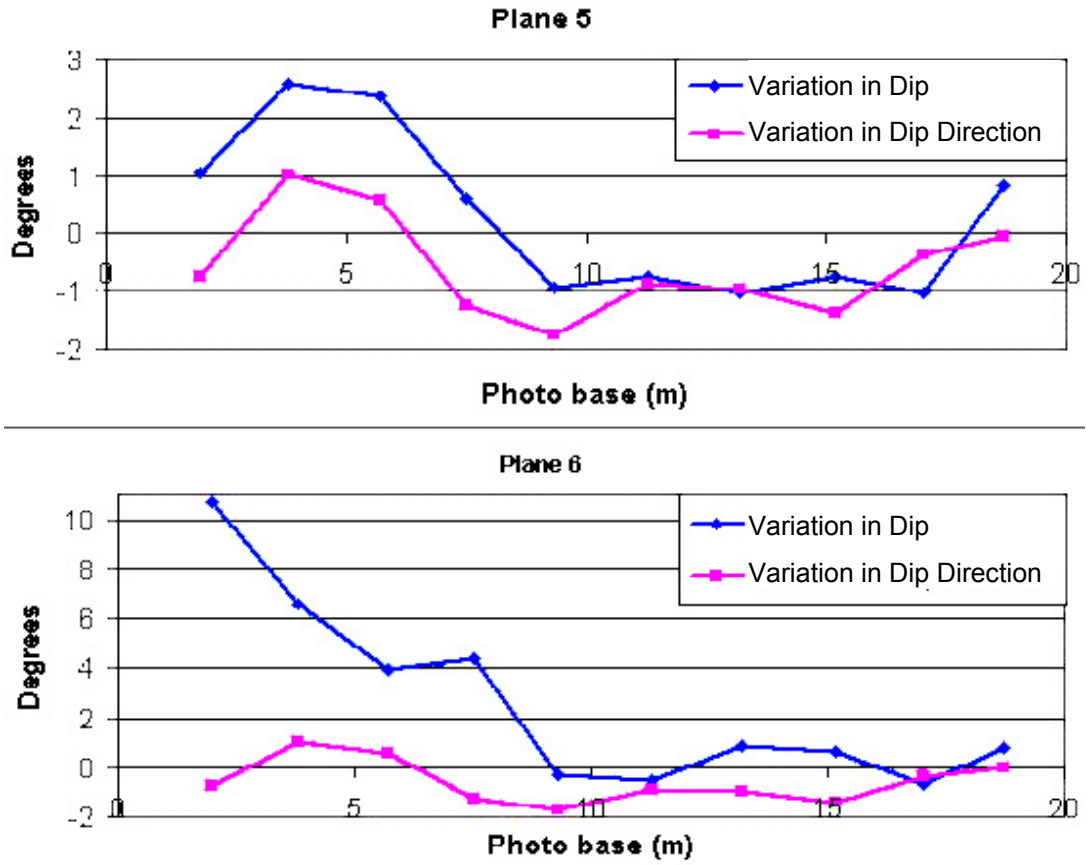

Figure 6.13 Results of changing photobase with concave and convex edges

6.5.5 Variation of Correlation with Photobase

Automated image correlation is widely used in proprietary stereo photogrammetry programs to collect DEM data for topographic mapping (see Chapter 3) where large reference and search windows, tightly constrained along epipolar lines, can generate good quality topographic data over large areas, although there is always the need to carry out post-processing review and editing to remove or correct erroneous matches. When applied to highly detailed DEMs, the significance of point editing is critical, as relatively few points may be used to calculate the shape of a landform.

To further investigate the effect of photobase on the quality of automated DEM production, the grid DEM generating exercise in Chapter 6.5.4 was repeated to include lower correlation thresholds. A smaller correlation window 12 pixels wide was also used with the aim of more closely following the 3D morphological lines shown in Figure 6.9.

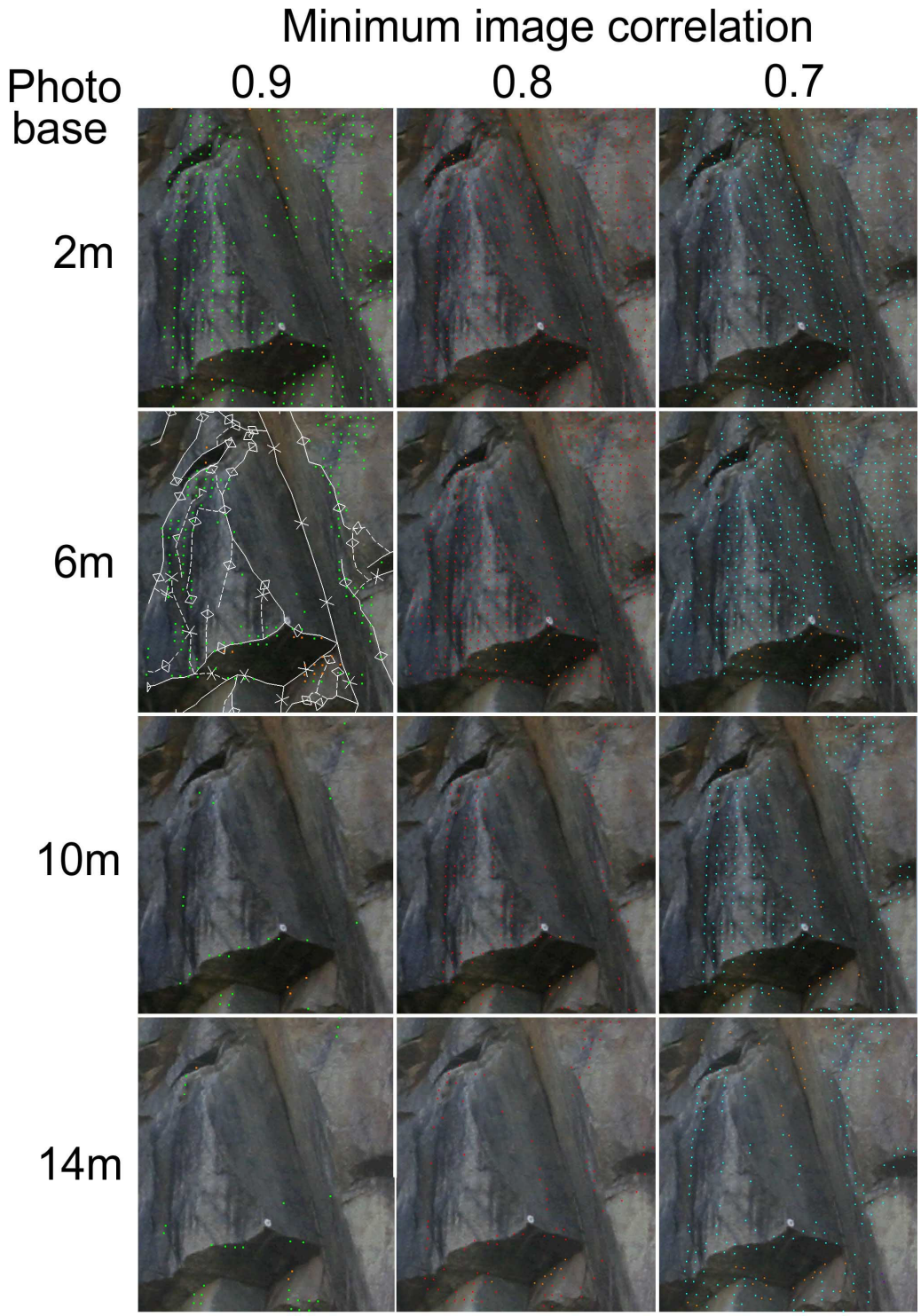

Figure 6.14 Variations in image correlation with correlation threshold and photobase

Figure 6.14 contains the results for image correlation on Planes 5 and 6, using thresholds of 0.9, 0.8 and 0.7, together with stereo pairs of photobases 2m, 6m, 10m

and 14m. The two most obvious observations are that the number of successful correlations increases both with decreasing correlation threshold and photobase. Not surprisingly, the number of true-positive correlations is highest in regions of the stereo pair where the photo is highly textured and lowest across the very uniformly-textured surfaces. A further observation is the rapid decrease in highly correlated (>0.8) true-positive image matches with increasing photobase which, at between ten and 14m, has occurred at a smaller photobase than with the 20 pixel correlation window results described in Chapter 6.5.4.

The brown dots visible in all the component images of Figure 6.15 highlight the false-positive correlations. The majority of these are in two topographic settings, the low-contrast region of shadow where Plane 6 overhangs, and along the narrow, sharply concave boundary between Planes 5 and 10, and at the toe of Plane 6.

6.5.6 Variations in Image Correlation with Kernel Size in Non-planar Surfaces

In Chapter 6.5.5, the observation was made that the number of successful true-positive image matches decreased with increasing photobase. Kraus (2000, p. 354; and Chapter 3.2) states that in the image correlation process, the search for the best location of the reference area proceeds by testing all positions of the reference kernel within the search window, and identifying the location with the highest correlation coefficient, *r*. The coefficient is based on the standard deviations and densities in both areas and the covariance between both areas. Kraus (2000, p. 357) also reports that positioning accuracy increases if the reference kernel contains '*jumps in density*' (edges), and that larger reference kernels will have higher accuracy because of the additional edges that are contained.

As an example of how the image correlation relationship changes with respect to reference kernel size in complex terrain, measurements of a rock joint-controlled feature were made using a single stereo pair and increasing the size of the square reference window. The smallest photobase, 1.97m, was used to ensure that the changes in correlation response were due to the complexity of the image enclosed by the reference kernel while minimising perspective changes in image geometry. The reference kernel was increased from 4 pixels to 50 pixels; at a project distance of 42m, this gave ground coverages of approximately four to 56cm respectively. Figure

Left image Right image

Camera separation: 1.97m

Object distance: 42m

Figure 6.15 Coverage of four pixel and 50 pixel reference kernels

6.15 shows the areas covered by the 4 pixel and 50 pixel reference kernels. Although the rock has a uniform colouration, the dominant features are the steeply dipping dark line from top left to bottom right, which marks the edge between Planes 2 and 10 (an enclosed angle of about 66º), and the bottom left to top right dark crack that is the trace of Plane 3 across both the rock faces.

Variations in the correlation coefficient *r* with reference kernel size are given in Figure 6.16. The correlation coefficient *r* is highly variable at small sizes, but with

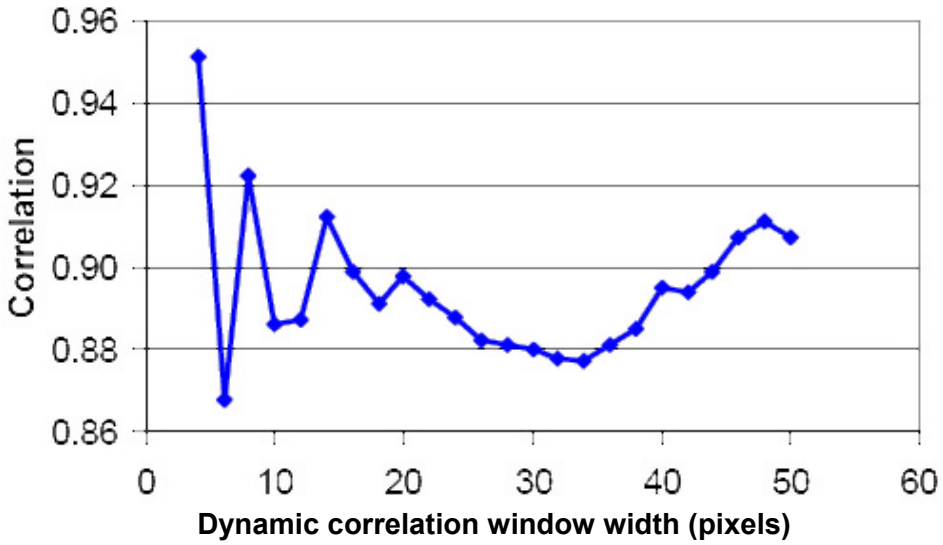

Figure 6.16 Variation in image correlation coefficient with window width within a sharp concavity

decreasing fluctuations as the reference kernel increases from 4 to 20 pixels. Observation of the image details centred on the junction between the two linear features does not suggest any immediate cause as to the local correlation minimum (*r* = 0.877) at 34 pixels, but is probably related to the dimensions of the feature as compared to the reference kernel.

6.6 Discussion

The results of this investigation demonstrate that acceptable measurement precision can be achieved using both multi-image and stereo photogrammetry. Multi-image modelling was carried out using PhotoModeler software (version 5.1.1; http://www.photomodeler.com), and stereo softcopy photogrammetry using the uSMART system (version 8.16.0; http://www.smarttech.co.za). The main constraints on the precision of the resulting planar orientations are: accuracy of the absolute orientations of the images; image resolution and separation; 3D distribution of points used to define each plane, and camera calibration.

Under normal photogrammetric measurement using topographic survey quality equipment, Read and Graham (2002) quote the 'typical' measurement accuracy as $1{:}10^4$, i.e. one part in 10,000. With an object distance in the quarry of 42m (Figure 6.1), this would give an expected RMSE of 4.2mm. Figure 6.17 has been compiled using the equation for δ_z from Kraus (2000; Equation 2.7-1). This gives the range of

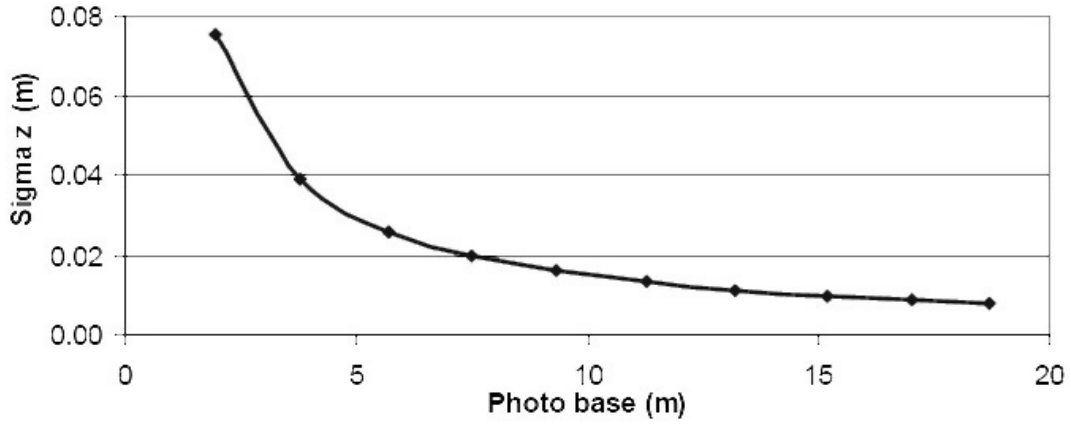

Figure 6.17 Variation of measurement accuracy with photobase in the Quarry survey

mean square accuracies for δ_z as ranging from 75mm for the 2m photobase, to 8mm for the 18.7m photobase. The RMSE of all the points used in the PhotoModeler model was 0.129m, but this included the control points outside the mapped rock face. If only the points forming the measured planes are used, the RMS reduces to 0.040m, similar in magnitude to the δ_z value as determined using the Kraus equation.

The variability of point measurement as demonstrated by the length of residuals from the measured points to the estimated plane is considerably higher than this (Table 6.7), ranging from 24mm for Plane 7 with uSMART, to 293mm for PhotoModeler on Plane 1 (Plane 3 is excluded as it is very long and the offset is not as closely related to individual point measurement as for the smaller planes. This variability is also due to the local roughness of the planes in addition to the individual point measurement accuracy.

Table 6.7 Summary of offset results, PhotoModeler, uSMART and TLS

Plane	Offset lengths (m)			Ratio of offset to project distance		
	Photo-Modeler	uSmart	Laser scanner	Photo-Modeler	uSmart	Laser scanner
1	0.293	0.173	0.152	143	243	276
2	0.151	0.099	0.093	278	424	452
3	0.377	0.608	N/A	111	69	N/A
4	0.109	0.073	0.099	385	575	424
5	0.063	0.076	0.068	667	553	618
6	0.126	0.070	0.033	333	600	1273
7	0.033	0.024	0.035 *	1273	1750	1200
8	0.065	0.058	0.078 *	646	724	538
9	0.076	0.078	0.147	553	538	286
* Results are unreliable						

6.7 Chapter Summary: Landform Measurement

This Chapter has described the results of an investigation into the practical use of two photogrammetric methods for the measurement of rock surface orientation within a complex rock face. Multi-image photogrammetry, as applied using the PhotoModeler software, uses a block bundle adjustment of all the measured points digitised from many photographs to build the oriented 3D model. The method has the advantage of being able to incorporate photographs from many different viewing

directions into a single model, but has the relative disadvantage of relying on manual identification of corresponding object points. The alternative methodology, stereo photogrammetry, builds independent models from stereo pairs but can allow the semi-automated capture of points and lines using image matching algorithms operating in real time. If the ground control and the camera calibration models are weak, the independent models determined by spatial resection can yield slightly different measurements for the 3D object points. When used solely for the purposes of feature orientation, such as for use in landslide hazard analysis, these small spatial variations are likely to fall within the range of acceptable measurement precision.

Chapter 7 describes the results for a more detailed investigation into the use of stereo photogrammetry to map landslides on the hillsides around One Rise More in Hong Kong. The description of the use of multi-image photogrammetry to locate and map the main landslide at One Rise More is given in Chapter 8.

Chapter 7

STEREO PHOTOGRAMMETRICALLY-ASSISTED LANDSLIDE MAPPING

Landslide inventory studies carried out in Hong Kong since 1978 record that the majority of the shallow debris flow type slope failures occur on steep slopes. Styles and Hansen (1989) note that 1.2% of the Territory's 1090km^2 contains well-defined landslips and coastal instability, and that a further 20.4% of the terrain shows evidence of relict or recent landsliding. More detailed inventory studies such as the Natural Terrain Landslide Inventory (Evans, 1998; Evans et al. 1999; King, 1999), interpretive studies partly based on these data (Dai et al., 1999, 2001; Fuchu et al., 1999; Dai and Lee, 2001, 2002), and detailed area studies such as Franks (1998; 1999) record that around 90% of these landslides occur on slopes with gradients of 30º or steeper, and with scar lengths of between five and 20m, widths between three and 18m and depths of less than 2m. Surrounding hillsides may be densely vegetated, and the failure scars and transported debris also tend to become revegetated in the months and years after failure. The distinct landforms that facilitate recognition of past landslides degrade over timescales of tens to thousands of years (Chapter 2.6.1, Figure 2.12; McAlpin, 1984; Wieczorek, 1984; Sewell and Campbell, 2005). These conditions present challenges to the use of photogrammetric techniques in the production of detailed geomorphological maps, particularly at scales where component elements of the landslides and the factors promoting instability need to be identified.

Multi-parametric methods of landslide hazard assessment require the sources of various terrain attributes and environmental data to be correctly correlated spatially. With regard to the acquisition of photogrammetric data, the salient factors are location, dimensions and relevant attributes. The precision required for each of these three components varies, commensurate with the scale of the feature in relation to its surroundings. Consider the hillside shown in Figure 7.1 that is approximately 110m and 180m wide. Locating the landslide with a single point either at its centre or at the crest of the 14.1m wide landslide scar indicated on Figure 7.1a for use in a landslide inventory with reproduction at a scale of 1:10,000 for example, may require accuracy in the order of ±5 to ±10m. Determining the width and height dimensions

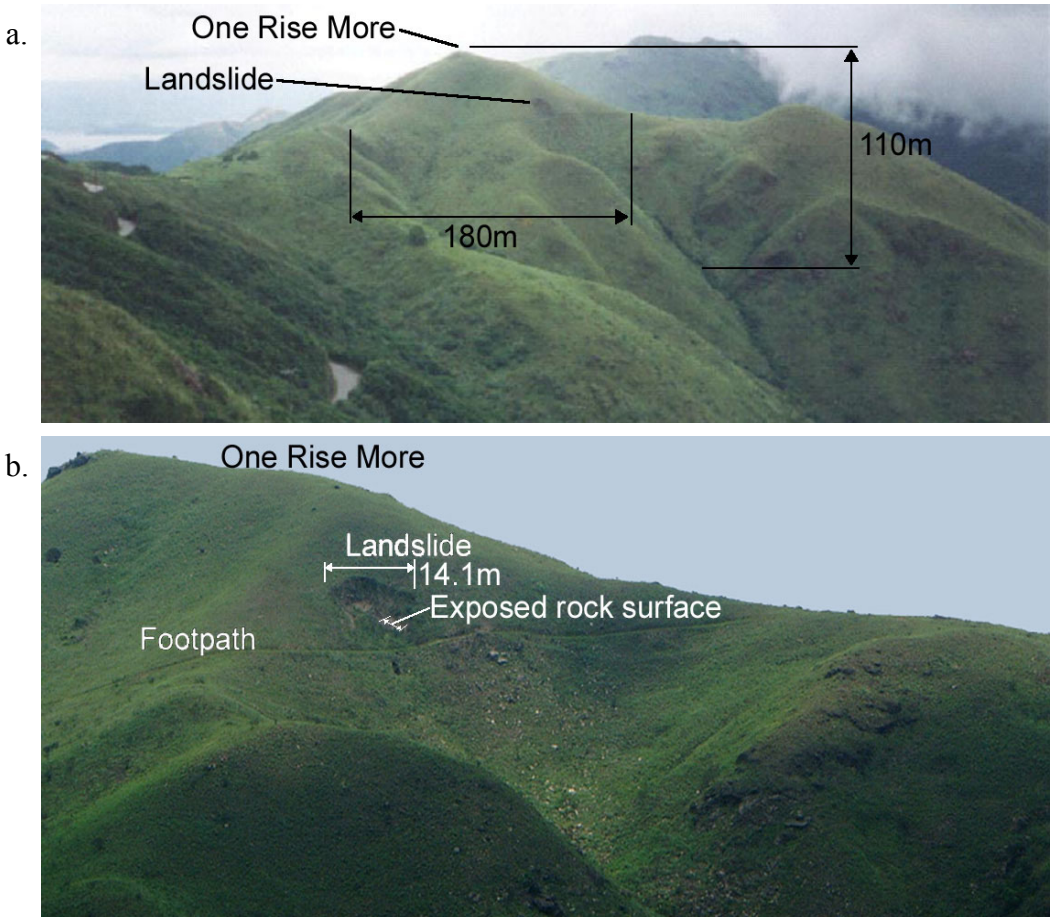

Figure 7.1 One Rise More landslide in Hong Kong
a. View to NNE; b. View to N

of the feature more clearly visible on the closer photograph in Figure 7.1(b) may require accuracy in the order of ±0.5 to 1m. An intermediate resolution of ±1 to 5m would be required for the bounding convex edge of the landslide to be identified on a DEM. Attribution of component landforms such as rock outcrops or sections of exposed failure surface needs the smallest DEM spacing, in the order of ±0.1 to 0.5m. When considering the first derivative attributes of elevation including gradient and aspect for the small rock surface identified in Figure 7.1(b), the DEM spacing would need to be less than 1m, and the precision of point measurement ±0.1m. If an estimate of the radius of curvature of the convex bounding edge of the landslide is required, for example for estimation of the age of this landslide by reference to its stage of degradation (e.g., Figure 2.12), the point spacing would need to be less than 0.1m, with a precision around ±0.03m; the radius of curvature in this case may be <0.1m for recent landslide features identified as being <1000 years old (Sewell and Campbell, 2005).

These varying precisions need to be considered in relation to the internal and external factors relating to the orientation of the imagery and individual point measurement. Orientation of the photogrammetric model is commonly achieved through the identification of ground control points (GCPs). Signalised pre-marks such as painted crosses on urban roads may have coordinates determined to a precision of ±10mm but these are rarely available in open hillsides, and on aerial photography that predates the establishment of a photogrammetric survey network. GCPs extracted from a topographic map may have a relatively low precision as compared to signalised pre-marks, for example, around ±2m for the intersection of two footpaths identified on a 1:1000 scale topographic map. While this may limit the absolute precision of mapping results, the accuracy of individual points relative to a nearby point is dependent on the measurement precision at each point. Consequently, measurement of feature dimensions and determining the various first and second derivatives of elevation, gradient, aspect and various curvatures, are less affected by the precision of GCPs than by the resolution of the imagery.

The implications of these factors are investigated in this Chapter and Chapter 8, with studies on two debris flow scars and the surrounding terrain in Hong Kong. These landslides were surveyed photogrammetrically to investigate the constraints and opportunities to map morphometric and geomorphometric content that could be resolved and interpreted from the resulting DEMs generated by stereo and multi-image techniques. This Chapter describes investigations performed using stereo photogrammetry with vertical aerial photographs on a partly revegetated landslide that took place over forty years ago at One Rise More, and on several older features on nearby hillsides. Mapping at One Rise More involved both stereo aerial and terrestrial multi-image photogrammetry; while satisfactory mapping results were obtained from the 1963 vertical aerial imagery obtained at a flying height of 676m above the landslide (scale 1:4450; ground pixel size 5.6mm), dense vegetation cover limited the success of the multi-image photogrammetry. Consequently, a second study was carried out at a landslide that took place in 2000 at Cloudy Hill in Hong Kong that was limited to the use of terrestrial multi-image techniques for detailed mapping of the failure scar. The multi-image photogrammetric studies at One Rise More and Cloudy Hill are discussed in Chapter 8.

7.1 Introduction to the One Rise More Study

Hong Kong has an extensive archive of historical aerial photography dating back to 1924 (Geotechnical Control Office, 1984), which allows the identification and approximate dating of the landslides by year of first recognition on the aerial photograph archive (Styles and Hansen, 1989; Evans, et al., 1997). Although the landslide on the southern slopes of One Rise More (also named Tung Yeung Shan; Figure 7.1) is first recognised in the poor-resolution 1954 vertical aerial photography (frame 0133, run V81A RAF552; 29,00ft, 14" lens, dated 18.11.54), it is clearly visible in the 1963 vertical aerial photography (extract shown in Figure 6.2). The landslide and surrounding terrain were surveyed photogrammetrically using vertical aerial photographs, supplemented by a ground topographic survey and multi-image photogrammetry. Some details of the landform features within the landslide scar were partially obscured by vegetation, and consequently are poorly defined in the resulting 3D models.

This landslide has been measured using three techniques:

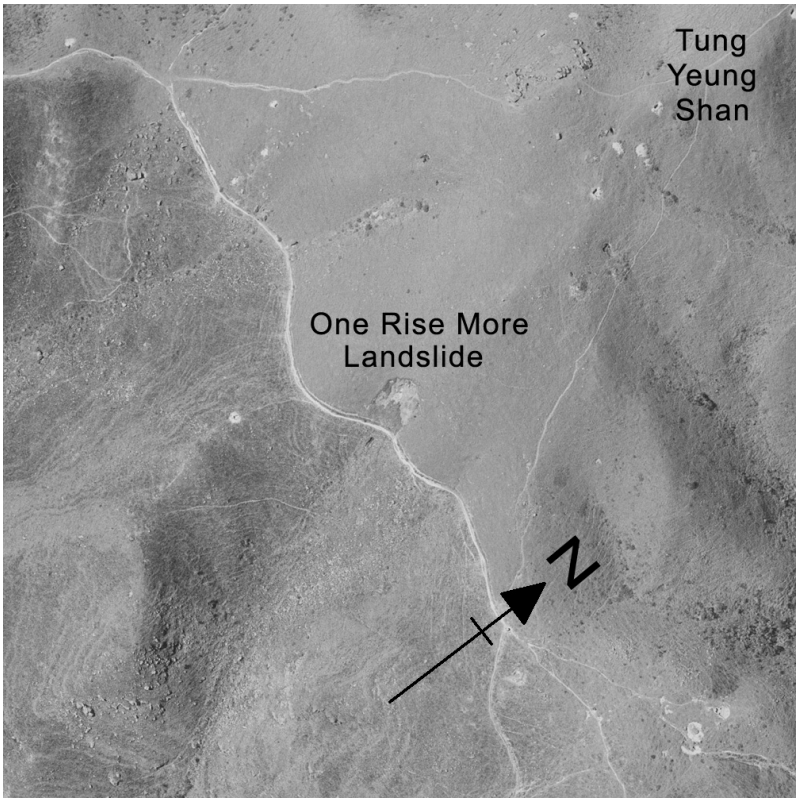

Figure 7.2 Section of 1963 aerial photograph frame 9647 around the One Rise More landslide. Image is 230m wide.

(a) A Total Station ground survey to collect DTM data for use in testing the photogrammetric results. The ground survey included feature surveys around the crest and base of the rear landslide scarp, and measurements at approximately 8, 4 and 2m grid patterns across the landslide and surrounding terrain;

(b) Stereo photogrammetric surveys were carried out using vertical aerial photography flown in 1963, with the aim of testing the accuracy and characteristics of automated and semi-automated image correlation in steeply-sloping terrain for the collection and mapping of high-resolution ground detail. The stereo pairs were flown at 3900ft, 4200ft, 7000ft and 12,500ft altitudes (1189m, 1280m, 1838m and 3810m respectively) with the flight lines passing upslope and downslope of the landslide;

(c) Multi-image photogrammetric surveys was performed using images taken at a range of distances using consumer-grade digital cameras; this model was oriented using longer range terrestrial images that included the local hillside from the ridge line to near the valley floor. This investigation is described in Chapter 8.

Stereo photogrammetric processing of the aerial photography was performed using the uSMART software package, while the terrestrial images were processed using PhotoModeler software.

7.2 Description of the One Rise More Landslide

The One Rise More landslide can be seen in the centre of the image in Figures 7.2 and 7.3. Study of the catalogue of aerial photographs held in the Aerial Photograph Library of the Geotechnical Engineering Office, Hong Kong Government, revealed that this landslide is first visible in 1954, although only limited ground detail is discernable due to the 1:25,000 scale of the photographs. Details of the landslide scar are most clearly visible in the low altitude 1963 aerial photography (Figures 7.2 and 7.3), by which date both the landslide scar and debris remaining within the base of the scar have become partly revegetated. The photo scale at the landslide is 1:4449 from a flying altitude of 1169m (3835ft), only 676m above the feature.

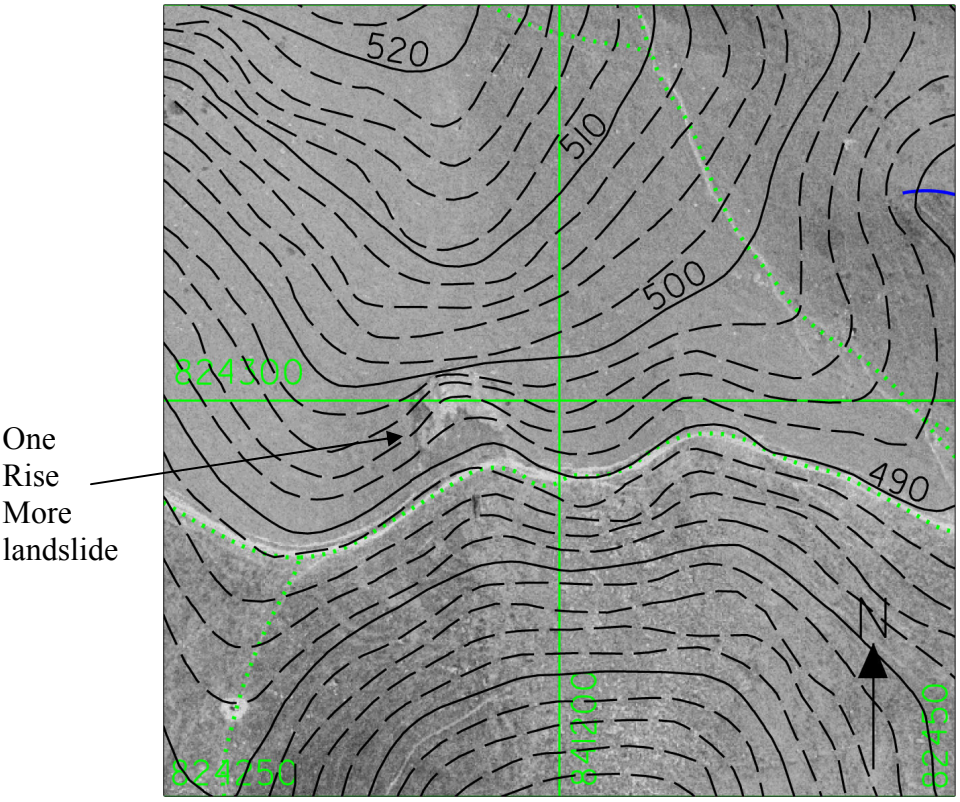

Figure 7.3 Orthophoto of part of the 19 February 1963 aerial photograph frame 9647 around the One Rise More landslide. Rectified to 0.1m pixels with the 1:1000 scale topographic map information superimposed.

The crown of the landslide consists of a near vertical, mostly bare soil and regolith slope above a weathered rock slope, with the central and lower parts of the failure scar containing debris covered by dense, low vegetation. This feature was selected for study because:

(a) The landslide scar contains several distinct landform elements forming photographically-contrasting topographic features that should facilitate detailed photogrammetric measurement;

(b) The surrounding terrain has a vegetation cover of low grasses that does not obscure details of the landslide or its morphological boundary;

(c) In the 1963 aerial photography, the terrain downslope of the footpath at the toe of the landslide had suffered a bush fire, leaving parallel streaks of wind-blown ash that provides a strong photo-texture contrast with the smooth textured grasses upslope of the footpath. This is clearly visible in Figures 7.2 and 7.3.

The vertical aerial photography used in this investigation was supplied by the Lands Department through the Geotechnical Engineering Office, Civil Engineering Services Department, Government of Hong Kong SAR.

7.3 Vertical Stereo Models

7.3.1 Sources of Imagery

The most detailed aerial photography exists for 1963 and 1964, covering a range of flying altitudes from 1189m (3900ft) to 3810m (12,500ft). The One Rise More landslide lies between 488 and 500m elevation (Figure 7.3); with the lowest aerial photography of this landslide being flown at 1169m, the flying height above the landslide is approximately 676m (2217ft) giving a photo scale of 1:4449 at the elevation of the landslide. The photographs were supplied as digital images scanned at 12.5μm from the original film negatives using the Hong Kong Government's DSW500 scanner. Paper prints of some of the frames were also supplied which were scanned by the author using a 1200dpi HP5300 A4/US Letter-size desktop scanner and a 700dpi Agfa Horizon Plus A3 desktop scanner.

7.3.2 Camera Calibration

Camera calibration certificates were obtained from Hunting Surveys Ltd. (1963; 1964) for the low, medium and high altitude flights in 1963 and 1964. These large format camera calibration reports state that lens distortions are less than 0.007 to 0.011mm within 100mm radial distance from the image centre (Principal Point), increasing to over 0.020mm for the outer parts of the image at radial distances over 130mm from the Principal Point. Except for the outer edges of the photographs, this distortion is negligible compared to the dimensional stability of paper prints and the paper photograph scanning process, particularly if A4/US Letter format desktop scanners are used.

7.3.3 Orienting the Photogrammetric Models

Photogrammetric models were built using vertical aerial photography obtained at high-, medium- and low-altitude, as detailed in Table 7.1. The footprints of the flight

lines relative to the study area are depicted in Figure 7.4. Although the ground control points around the study from the Hong Kong Government's photogrammetric network were supplied, few of these were found to be visible on the stereo models. Consequently, GCPs were identified from the 1:1000 scale digital topographic data sets of the area around the One Rise More landslide, also supplied by the Lands Department, Government of Hong Kong SAR. These data sets contain the elevation-attributed 2m-interval contours and spot heights, but all the non-topographic detail were supplied with 0m elevation, and some of the contours and spot heights had been attributed with incorrect elevations; these were corrected before use.

a.

b.

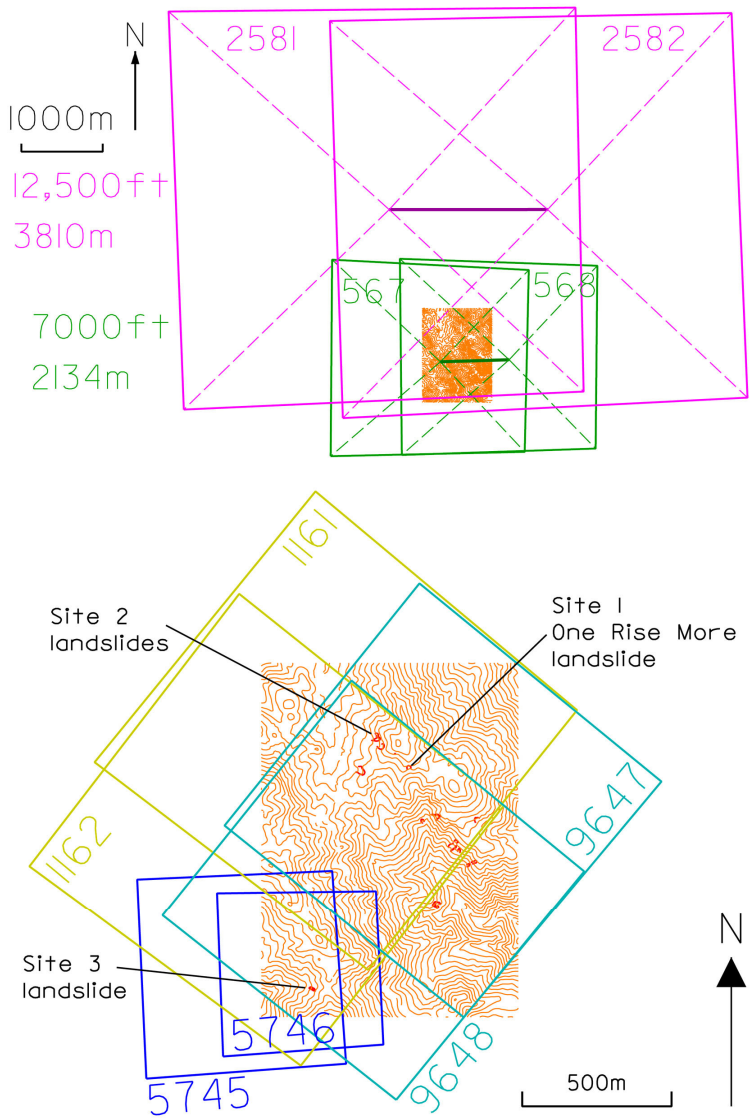

Figure 7.4 Image footprints for a. the high- and medium-altitude flight lines, b. low altitude flight lines, with the study area shown by the contoured region (2m contour interval)

As the softcopy photogrammetry system used allows superimposition of 3D vector data within the stereo visualisation, the non-topographic vectors were translated vertically to a surface formed from a TIN model constructed using the 2m contour and spot height data. Figure 7.5 depicts the flight line and footprint of the two images 9647 and 9648 over the contours within the study area and the non-topographic detail over a wider area. The major advantage of using this form of vector data was that once an initial three 3D GCPs had been identified, the stereo model could be visually compared to the 3D non-topographic data, and suitable GCPs identified and incorporated into the absolute orientation of the stereo model. This was particularly valuable when visually assessing the suitability of potentially non-permanent features such as footpath intersections and old buildings.

Table 7.1 Stereo model quality results for the models used in the One Rise More landslide study

Model	9648-47	9648-47	1162-61	567-68	2581-82	5746-47
Scanning resolution (µm)	12.5	21.17	12.5	12.5	12.5	12.5
Flying altitude (m)	1169	1167	1288	2140	3933	830
Flying altitude (ft)	3835	3829	4226	7021	12904	2723
Landslide elevation (m)	493	493	493	493	493	480
Difference (m) (target distance)	676	674	795	1647	3440	350
GCPs	9	9	9	15	18	8
Max. residual X (m)	-0.456	-1.265	-0.849	-0.768	1.847	-0.440
Scale number at seal level	7693	7680	8476	14083	25882	5462
Scale number at landslide	4449	4435	5232	10838	22638	2303
Ground pixel size (m)	0.056	0.094	0.065	0.135	0.283	0.029
Max. residual Y (m)	0.857	-1.647	1.075	0.915	2.691	0.503
Max. residual Z (m)	-0.813	-1.949	1.579	1.019	3.844	0.745
RMSE X (m)	0.236	0.854	0.668	0.375	0.813	0.258
RMSE Y (m)	0.522	0.862	0.531	0.399	1.05	0.294
RMSE Z (m)	0.488	1.299	0.961	0.559	1.207	0.404
Accuracy: target distance / RMSE Z	1385	519	827	2946	2850	866
Focal length of lens (m)	0.15196	0.15196	0.15196	0.15196	0.15218	0.15196

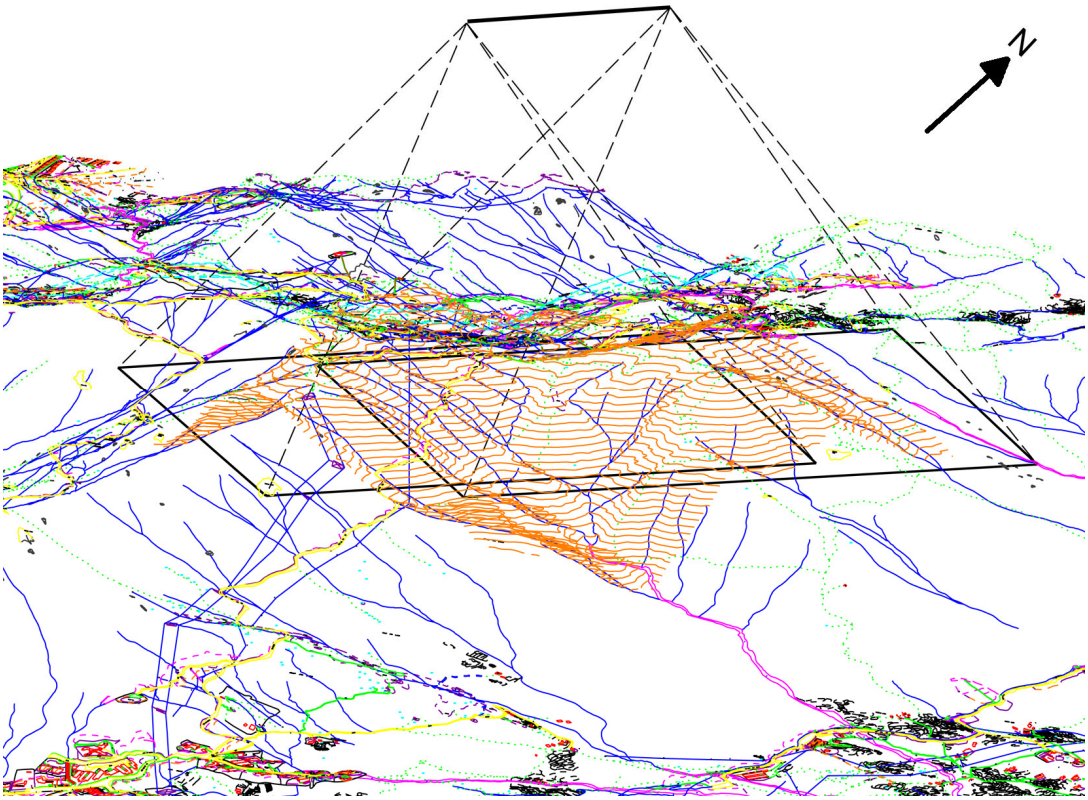

Figure 7.5 Isometric view of the image footprints for frames 9647 and 9648 over the 2m interval contours for the One Rise More study area. Also included, are the non-topographic details from the 1:1000 scale digital map series, warped to the ground surface represented by a TIN derived from the 1:1000 scale topographic detail (contours and spot heights). 1:1000 scale digital data © Government of Hong Kong SAR, reproduced with permission

Table 7.1 contains data on the relative accuracy of the various stereo models used in this study, including the low-, medium- and high-altitude photography scanned at 12.5µm and model 9648-47 scanned at both 12.5 µm and 21.17 µm. Of particular note is the relative increase in accuracy for the medium- (model 567-68) and high-altitude (model 2581-82) stereo models, defined in terms of the ratio of the target distance to the RMSE of vertical measurements. This is attributed to two factors: (i) the ability to include control points from the urban area at the foot of the hill masses that are more clearly defined both visually and spatially, and (ii) accuracy of control points derived from the topographic maps increases relative to altitude as the flying height increases.

7.3.4 Discussion of Error Sources and Effects

Table 7.2 compares the results of the spatial resection to derive the camera location and orientation data for the two images used in stereo model 9648-47 between the high quality 2032dpi (12.5µm) and desktop 1200dpi (21.17µm) scanning. The differences between perspective centre coordinates derived by spatial resection between the two models averages 2.7m in X, 1.7m in Y and 1.03m in Z, as compared to variations in the ground control point data for the same two models (Table 7.1) ranging from 0.236 to 1.299m. This occurs as the spatial resection incorporates some of the distortion errors due to the use of a paper print and desktop scanner. If stereo models are built using exterior orientation data only (for example, as applied in the use of vertical aerial photography for Mountain Quarry in Chapter 6), the degradation of measurement accuracy due to the use of paper prints and desktop scanners will be higher.

Table 7.2 Comparison of exterior orientation results between photogrammetric (12.5µm) and desktop (21.17µm) scanning for stereo model 9648-47

Exterior orientation parameter	12.5µm scanning		21.17µm scanning		Difference		
	9648	9647	9648	9647	9648	9647	Ave.
X (m)	841077.727	841295.642	841075.100	841292.866	2.627	2.776	2.702
Y (m)	823863.015	824165.531	823861.465	824163.608	1.550	1.923	1.737
Z (m)	1169.425	1167.565	1167.844	1167.077	1.581	0.488	1.035
ω (°)	0.9218	0.8566	1.0326	1.0520	-0.1108	-0.1954	0.153
φ (°)	0.4537	-0.1995	0.3285	-0.4104	0.1252	0.2109	0.168
κ (°)	39.0382	39.2107	39.0960	39.2504	-0.0578	-0.0397	0.049

The camera calibration charts for the 1963 and 1964 photography record that the image resolution varies from approximately 37 line pairs per mm (lp.mm^{-1}; pixel size = 0.0135mm) around the centre of the image, to about 22 lp.mm^{-1} near the outer edges (pixel size = 0.0227mm). Scanning with a pixel size of 0.0125mm slightly exceeds the resolution of the film and ensures the maximum ground resolution data are obtained. Using the concept of the Nyquist Sampling Criterion (Nyquist, 1924; Castleman, 1996, Wolf and Dewitt, 2000), the sampling interval should be half the wavelength of the smallest spatial frequency in the object being measured. In practice, the smallest discretely identifiable object is about three pixels wide to allow for some misalignment of pixels between the object and image, and between two

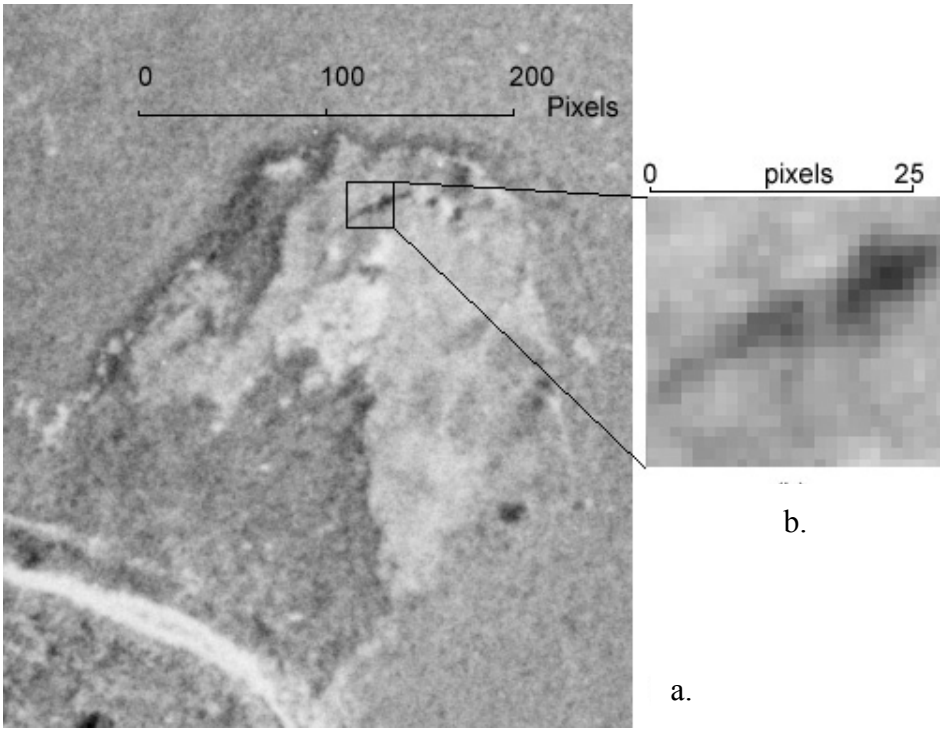

Figure 7.6 Enlargement of Frame 9647, One Rise More landslide, scanned at 12.5µm pixel resolution.
a. enlarged from 4.2mm wide block of the source image
b. further enlargement of the, dark near-vertical face

images if viewed in stereo, as demonstrated in the two enlargements of the One Rise More landslide in Figure 7.6. It will also depend on the amount of contrast or colour variation between adjacent pixels and the background noise in both the images and introduced by the scanning process. The pixels in Figure 7.6 are about 5.6cm wide; therefore the near-vertical linear feature in Figure 7.6b has a horizontal dimension of between 10cm at the southwest end to approximately 25cm at the higher northeast end.

On open hillsides, the vegetation pattern may form an irregular texture with a very high spatial frequency, as the leaves and plant stems are usually smaller than the ground pixel size. Reflectance will vary with wind movement and shading, introducing high-frequency noise with consequent poor representation on the image. Larger objects including individual boulders, bushes, tracks and other higher contrast features may be present across many parts of the terrain which allow automated image correlation routines to function on open hillside landforms; examples of these are visible in the northern part of Figure 7.2. The variability of the photo texture has

a significant impact on the function of the automated image matching algorithm, which is investigated further in the next section.

7.4 Results of Softcopy Photogrammetry

Figure 7.7 shows the operation of the DEM measurements in the uSMART softcopy photogrammetry system. The contour interval on the stereo base-map is 2m. Note that the photographs are oriented with the flight line forming the X axis, and the north direction is towards the upper right. Three morphological lines have been

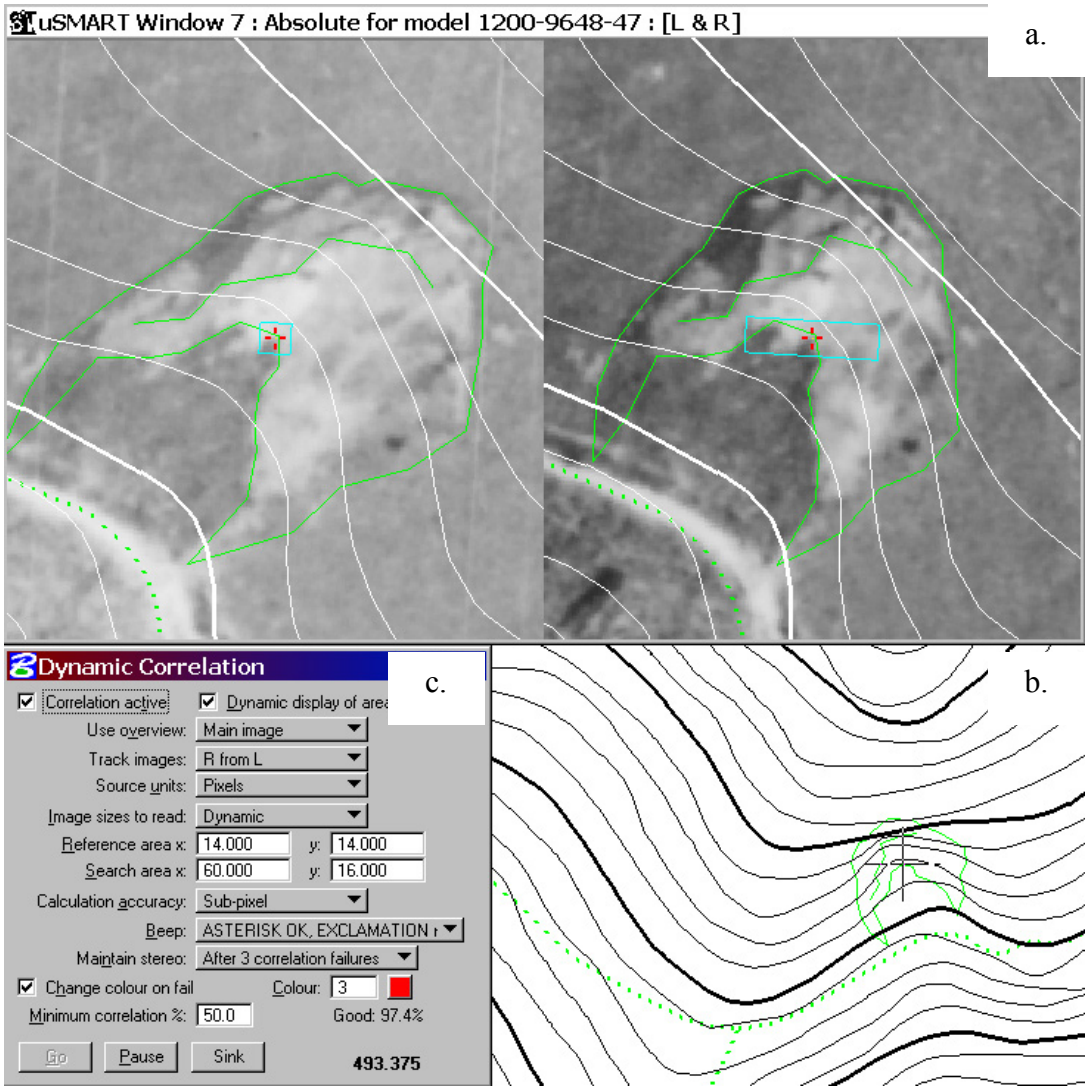

Figure 7.7 Automated measurement using image correlation.
a. Stereo viewing window with reference (pale blue square on left) and search (pale blue rectangle on right) windows, flight line orientation; b. cross-hair cursor on target; map orientation
c. Dynamic Correlation parameter window.
Left image 9648, right image 9647 © Government of Hong Kong SAR, reproduced with permission.

mapped that are visible on both the stereo aerial photographs and the topographic base map in Figure 7.7c. 3D vectors mark the boundaries of the landslide scar and the revegetated debris within the base of the landslide depression, and an intermediate line marks the base of a steeper slope within the landslide scar.

The two red crosses within the landslide scar in Figure 7.7a are the stereo cursor, which has been placed on the upper limit of debris within the landslide, and the window marked 'DYNAMIC CORRELATION' shows the measured ground level at 493.375m (referenced to the Hong Kong datum). While the contours appear to approximate the ground surface within the landslide scar, the mapped vectors are misaligned as compared to the contours along the top and base of the edge of the scar. This is due firstly, to mis-alignment of the photogrammetric model resulting from the use of poorly-defined ground control on open hillsides, and secondly, to smoothing of the contours that appears to have been applied during the data capture or cartographic processes.

Semi-automated image correlation can increase the rate of mapping for the capture of 3D points over that achievable by manual operation (Chandler, 1999; Schenk, 1999). This procedure measures the conformity between the target patch of one image, and all the possible permutations of the same sized patch within the search window on the second image. The 'Dynamic Correlation' window of Figure 7.7b contains the text 'GOOD 97.4%', referring to the correlation achieved by the software between the two image patches for this location. Correlations are usually highly variable, depending on the range of pixel values (contrast) within and between the two patches, and the variation in the distribution of bright and dark pixel values.

In steeply-sloping terrain, there can be a significant variation between the two image patches caused by changes in ground geometry relative to the two camera positions. Consequently, the use of a small image 'reference' area (the size of the patch being measured) which is moved across the larger 'search' window, improves the level of correlation where this can be achieved. However, using small image patches (up to 10 pixels in each dimension) was found to reduce the number of successful correlations due to increased relief-induced distortion between images, and an increased number of false positive correlations giving rise to errors in elevation (Chapter 6).

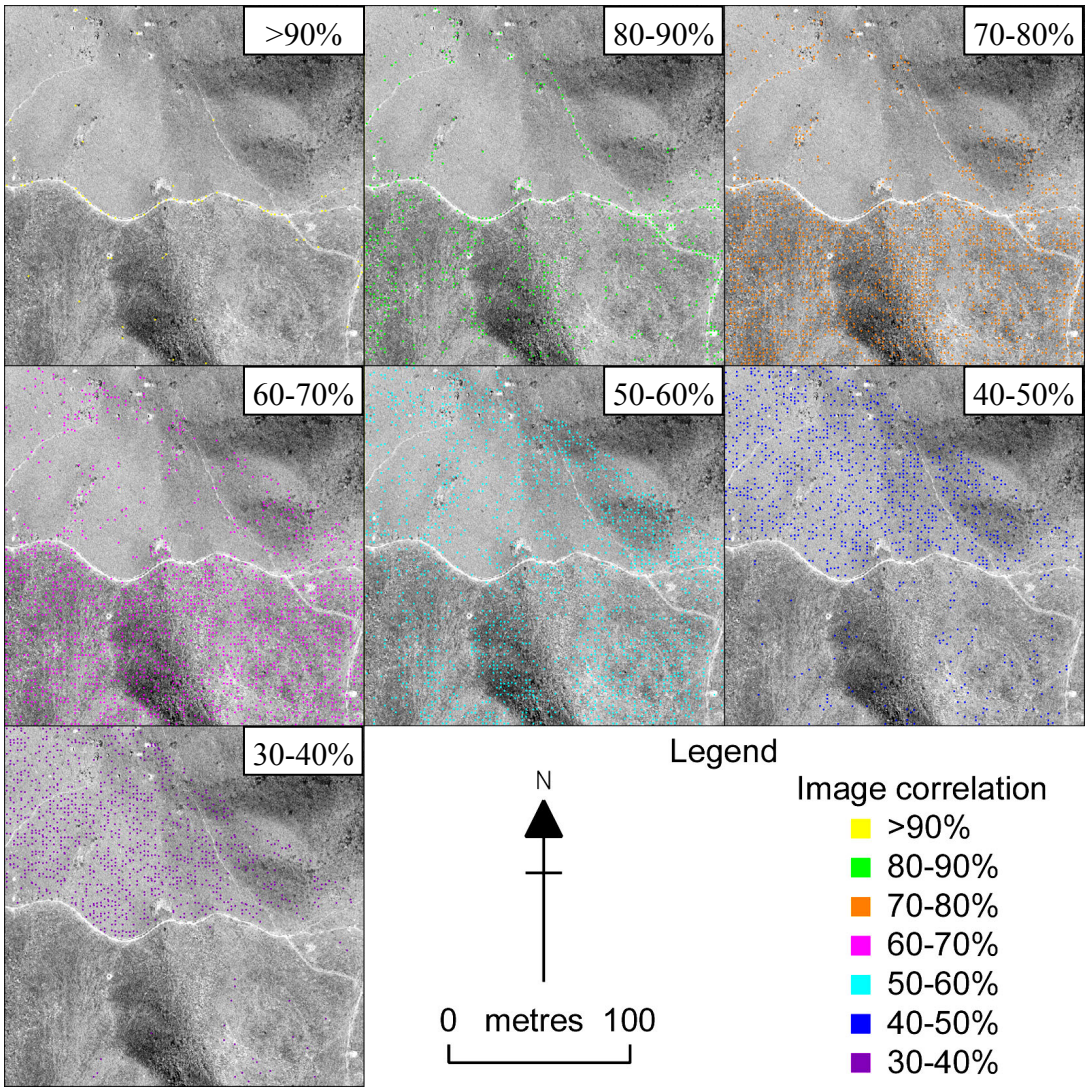

Figure 7.8 Variations in image correlation values for a 2m DEM automatically generated across part of the study area. Rectified image 9647. © Government of Hong Kong SAR, reproduced with permission

The confidence in feature identification also depends on the amount of texture (consisting of contrasting patterns) present within the image patch. Figure 7.8 shows the distribution of points photogrammetrically captured on the hillside in and around the One Rise More landslide in Figure 7.2. The most striking result is the variation of successful correlations across the study area. Areas around the boundaries of the landslide scar show correlations >60%, together with other locations outside the landslide that correspond to the footpath, eroded drainage lines, boulders or small, dark areas of vegetation, plus the terrain downslope of the footpath that appears to be streaked from the distribution of ash from a grass fire. Upslope of the footpath, the image contains low contrast features where the dynamic correlation algorithm

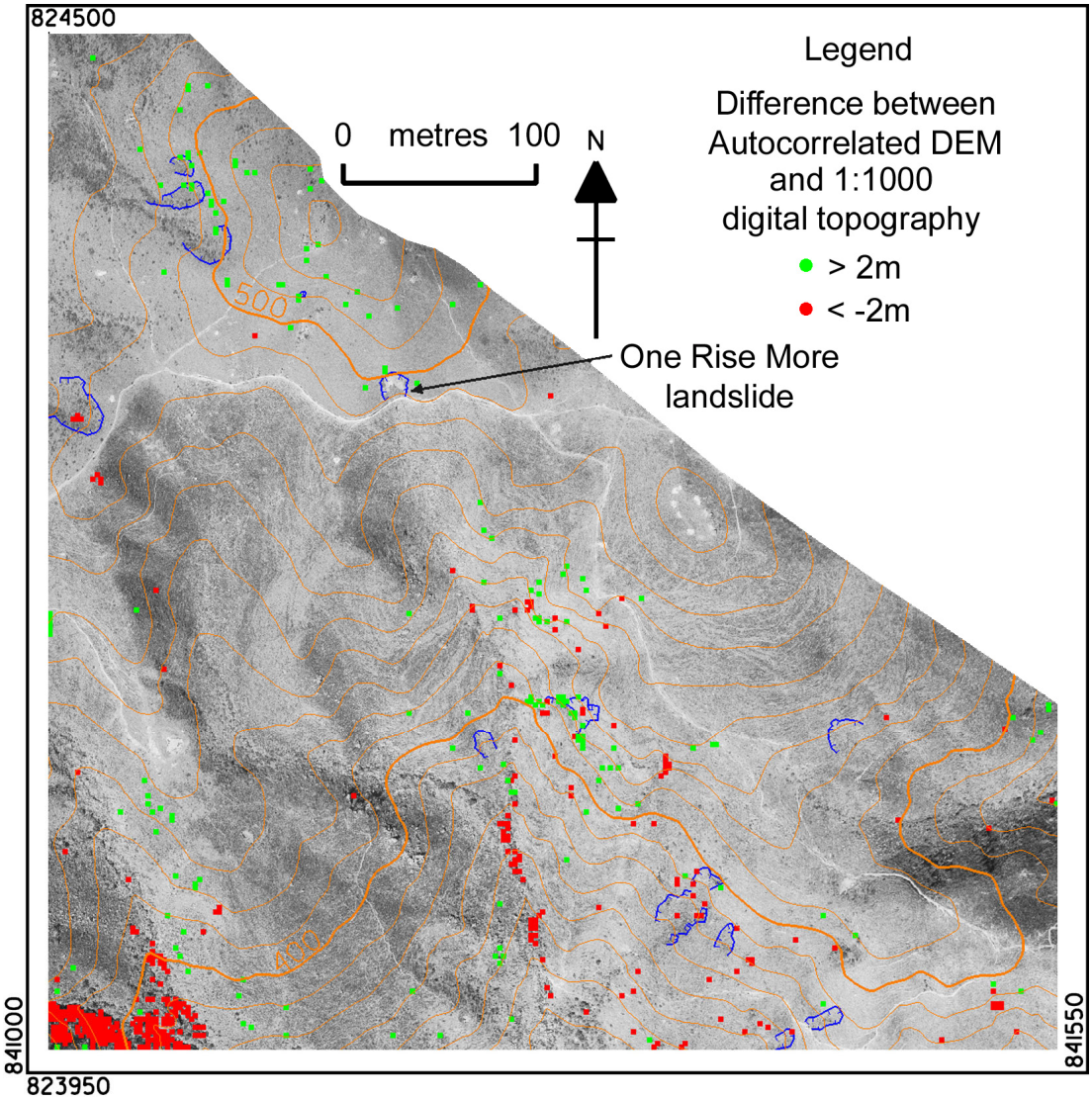

Figure 7.9 Variations >±2m in DEM elevations automatically measured for a 2m grid on stereo pair 9647-9648 compared to the 1:1000 scale digital topography. Landslide locations are shown (blue), together with the 10m contours; TIN based on 2m interval contours. Part of image 9647, cropped to stereo overlap with image 9648.

recorded lower values, mostly in the range 30 to 60%. Editing of the auto-correlated points was necessary, with between 2 and 5% of the points being deleted because of incorrect correlations; greater proportions of incorrect correlations were generated for the lower minimum acceptable correlation threshold. These results are similar to those for the quarry rock face measured in Chapter 6.

Figure 7.9 shows the distribution of erroneous points varying by more than >±2m from a TIN generated from the 2m contours and spot height data on the digital

1:1000 scale topographic data supplied by the Lands Department, Government of Hong Kong SAR. Although many of the erroneous data points are located in the valley floors which are generally densely vegetated with similarly-shaped tall bushes and trees, the low-contrast hillside to the north of the One Rise More landslide contains almost exclusively points measured by the autocorrelation routine as being >2m higher than the digital topography.

Table 7.3 Differences in measured ground elevations at each of three DEMs on the hillside around the One Rise More landslide.

		Grid spacing		
		8m	4m	2m
Photogrammetry – Ground survey	Sample size	68	81	72
	Average difference (m)	0.456m	0.497	0.366
	Standard deviation (m)	0.540	0.502	0.619
	Ave. absolute diff.(m)	0.606	0.578	0.580
	RMS (m)	0.703	0.704	0.715
Photogrammetry – 1:1000 scale contours	Sample size	81	81	72
	Average difference (m)	-0.073	-0.080	-0.181
	Standard deviation (m)	0.541	0.447	0.682
	Ave. absolute diff.(m)	0.429	0.353	0.548
	RMS (m)	0.541	0.450	0.701
Ground survey – 1:1000 scale contours	Sample size	68	81	72
	Average difference (m)	-0.509	-0.577	-0.546
	Standard deviation (m)	0.695	0.571	0.622
	Ave. absolute diff.(m)	0.716	0.669	0.670
	RMS (m)	0.857	0.808	0.824

7.4.1 Comparison of Photogrammetrically-derived Elevations with Ground Survey

An analysis was conducted of the reliability of automated softcopy measurements under different terrain conditions around the landslide. The locations of these measurements are shown by the regular grid patterns around the landslide visible in Figure 7.10. The 2m grid formed an 8x9 pattern; the 4m and 8m grids formed 9x9 patterns, but the northeast and southwest corners were not included in the ground survey because of line-of-sight obstructions. The three grids overlapped in the area around the landslide. Elevations were compared at each location between the ground survey, the photogrammetric survey using 12.5μm resolution high quality scanned images, and the published digital 1:1000 topographic data, for each of the 2m, 4m and 8m grids; the results are summarised in Table 7.3. Note that the 8m and 4m

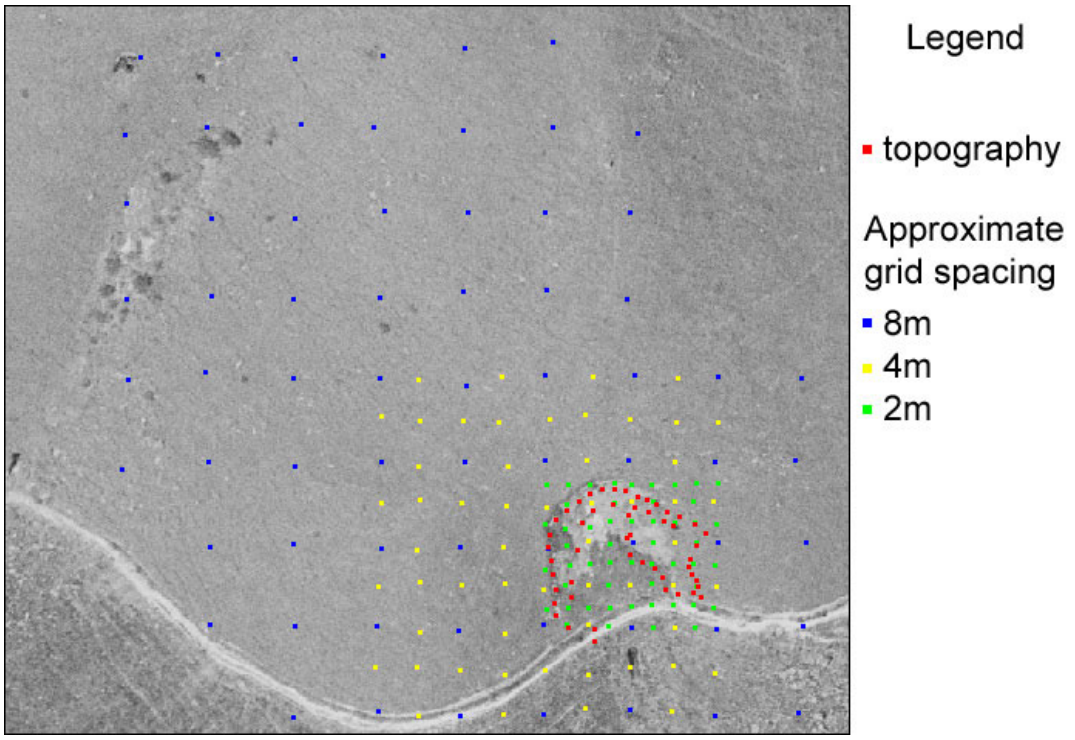

Figure 7.10 Locations of ground survey points on rectified image 9647

grids extend largely across open, grass-covered hillsides, whereas the 2m grid is located within and around the landslide (Figure 7.10).

The variations in RMS error between the three surveys range between 0.450m and 0.857m, with a mean of 0.700m. The distribution of measured points shown on Figure 7.10 shows that there is a translation error of approximately 0.5m in the Easting (Y) and Northing (X) coordinates between the rectified aerial photo and the ground survey points, which is attributed to difficulties in orienting the Total Station on an open hillside. For aerial photographs obtained at an elevation above the landslide of approximately 676m, this gives a vertical precision of one part in 966 of the flying height. This value is approximately an order of magnitude less accurate than 'typical' working accuracies quoted in photogrammetric textbooks; for example Wolf and Dewitt (2000) quote a vertical accuracy of one part in 10,000 for routinely locating pass points between photographs. This reduction is explained by the use of ground control points extracted from the 1:1000 digital data, where the spatial precision of horizontal control identified from these data on poorly-marked open hillsides is estimated to be ±2m.

Table 7.4 records the type of ground cover for the measurements around the edge and within the landslide for the 2m component of the grid survey. In general, the low contrast, grassy ground cover gives the highest variation in height measurements, while high contrast boundaries give much lower variation. From this assessment, the repeatability of measurements over low contrast, grassy hillsides gives a standard deviation of 0.18m and RMSE of 0.37m.

Table 7.4 Variation in automated correlation results between photogrammetric and ground surveys for 32 points at the One Rise More landslide

Height difference (m)	<0.05	0.05 -0.15	0.15 -0.25	0.25 -0.35	0.35 -0.45	0.45 -0.55	0.55 -0.65
Number of measurements and location type	11	5	6	3	4	2	1
	9B 1G	4B 1G	3B 3G	1G 2R	1G 2S	1B G	1G -

Legend for measurements

B	Boundary (high contrast edge, including boulders)
G	Grass (low contrast, some feint linear features)
R	Revegetated landslide debris
S	Steep slope (near-vertical side slope of landslide scar)

7.4.2 Comparison of Photogrammetrically-derived Elevations with Digital Topographic Data

When the contour vectors from the digital topographic data are projected onto the stereo imagery, variations between the ground and the vectors are clearly seen; note for example, the smoothing of the contours visible crossing the landslide in Figure 7.7. Contour smoothing is commonly applied to topographic maps as a cartographic enhancement; it can also occur due to the photogrammetric mapping process in operator-driven contouring with analogue plotters, where the pair of spots is kept on the ground surface at a given elevation by traversing across the surface using hand and foot-operated rotating wheels.

Figure 7.11 shows the positive and negative variations between the autocorrelated DEM and the TIN derived from the 2m contours in the 1:1000 digital topographic data supplied by the Lands Department. Two forms of discrepancy can be observed:

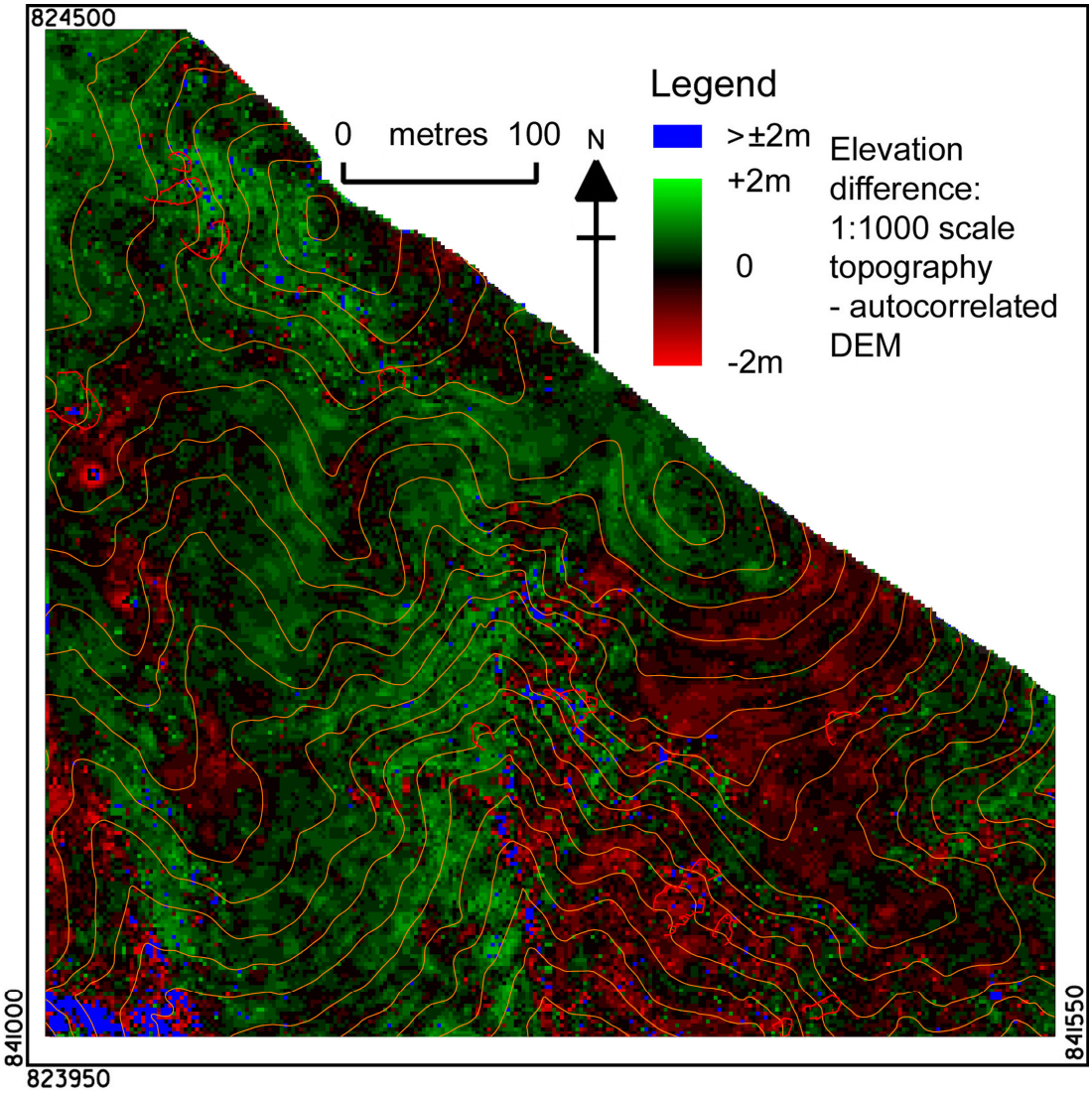

Figure 7.11 Variations in DEM elevations automatically measured for a 2m grid on stereo pair 9647-9648 compared to the 1:1000 scale digital topography. Coordinates are Hong Kong metric grid.

(a) a north-south oriented diffuse edge between the green positive and red negative differences; and

(b) striping that approximates the direction of the local contours.

The north-south variation coincides with the edge between maps sheets 7SE23C and 7SE23D of the Hong Kong Government's 1:1000 scale topographic map series, indicating some variation between the orientation of the photographs used to compile these two data sets.

The second artefact appears to be due to the manual mapping process noted above. Figure 7.12 contains two 1m resolution shaded relief models; Figure 7.12a. was

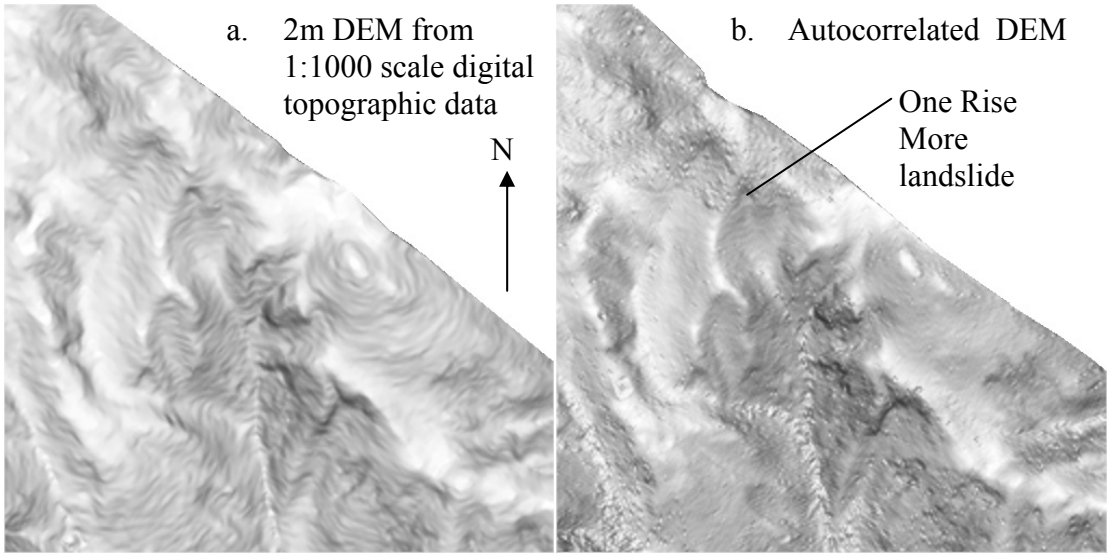

Figure 7.12 Shaded relief models of a. 2m DEM from 1:1000 digital topographic data and b. autocorrelated 2m DEM of the hillside around the One Rise More landslide. Sun azimuth 90º (non-directional), same area as Figures 7.9 and 7.11, 512m x 512m.

generated from the 1:1000 scale digital topographic data, and Figure 7.12b. from the autocorrelated DEM. While the digital topographic data TIN contains the contour-spacing artefacts, the autocorrelated DEM does not, although the latter also contains small pits and hummocks due to variations in the autocorrelated elevations from a smooth surface. This is especially noticeable in the smooth-textured terrain around the upper slopes to the north of the One Rise More landslide.

The presence of the contour-artefact has implications when the 1:1000 scale topographic data are used to generate derivative attributes to assist in morphological mapping of landforms that contain elements up to 10m in size, as the contour spacing artefact generates zones of high concave and convex curvature along slope profiles. As has been demonstrated in the synthetic model in Chapter 5, zones with high values for convex curvature can be indicative of the boundary of a landslide scar.

7.4.3 Relative Accuracies of the Source Data

The One Rise More landslide was measured using the terrain-following cursor on seven different photogrammetric models, and compared to the results of the ground survey. The results are shown in graphically in Figure 7.13 and in Table 7.5. The landslide boundary that deviates most from the manual placement is that carried out using the high altitude aerial photography, 12500ft (3440m above the landslide); this

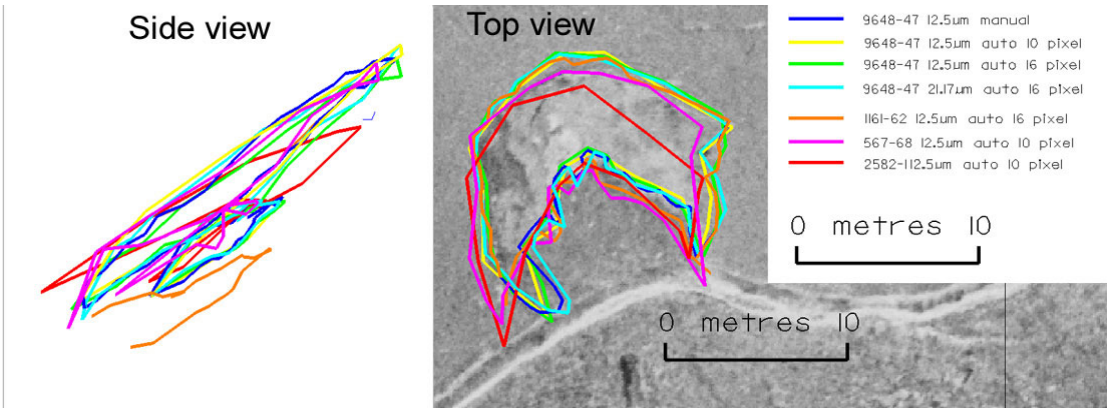

Figure 7.13 Boundaries of the One Rise More landslide, plotted for different photogrammetric models

is both because of an unfavourable orientation of the landslide in relation to the perspective centre, and the scale as the pixel size on this image is approximately 0.28m (Table 7.1). With the exception of the high altitude stereo pair, the gradient of the rear scar is consistently estimated to 49º ±2º, and the standard deviations of the X, Y and Z coordinates are 0.88m, 0.80m, and 1.32m respectively.

7.5 Automated Feature Extraction from DEM Data

Maximum convexity was identified in Chapter 5 as the most suitable curvature parameter to identify the boundaries of landslide scars on open hillsides. Autocorrelated DEMs have been prepared from two sites shown on Figure 7.4b on the hillsides around One Rise More, to test the effectiveness of using this curvature parameter for feature identification. The first group of sites is located around the One Rise More landslide, extending from the western flanks of the One Rise More hill south-eastwards within the area of stereo coverage for model 9648-47. The western part of the site contains five landslide scars, three of which have large-radius curvatures to the boundary convexity, typical of old, partially degraded features. The area southeast of the One Rise More landslide is deeply dissected by a steep-sided valley and contains more than twelve complex landslides and rockfalls.

The second site is located southeast of One Rise More where a landslide is located within the stereo coverage of very low level vertical aerial photography flown at an altitude 350m above the landslide; this landslide is also completely revegetated, but the debris trail clearly forms an elevated mound in the valley downslope of the erosion scar.

Table 7.5 Landslide measurements from different photogrammetric models

Attribute		3900ft				4200ft	7000ft	12500ft	Survey
		9648-47 12.5µm manual	9648-47 12.5µm auto 10 pixel	9648-47 12.5µm auto 16 pixel	9648-47 21.17µm auto 16 pixel	1162-61 12.5µm auto 10 pixel	567-68 12.5µm auto 10 pixel	2582-1 12.5µm auto 10 pixel	
Crown	X	185.742	185.752	185.208	185.469	184.636	185.625	182.894	186.602
	Y	305.970	305.385	305.399	305.351	305.114	304.359	302.433	303.713
	Z	500.312	500.999	499.472	500.973	498.525	499.272	496.821	500.631
Debris	X	187.300	187.126	187.110	187.391	186.948	187.302	186.832	187.286
	Y	299.888	299.725	300.150	299.782	299.381	298.737	299.149	298.470
	Z	493.684	493.344	493.482	493.482	491.169	493.392	493.527	493.886
Max Width	X1	181.265	181.263	181.486	180.846	181.384	180.952	180.360	181.663
	Y1	296.335	297.562	297.965	298.983	300.139	297.566	298.308	299.226
	Z1	494.600	495.947	495.117	496.923	494.265	495.230	495.395	497.843
	X2	194.807	194.395	194.395	194.755	193.820	193.322	193.366	196.338
	Y2	301.542	301.150	301.888	301.269	301.594	301.207	298.313	299.503
	Z2	497.336	496.780	496.956	496.958	495.367	497.571	492.971	496.384
Width Bowl	X	194.200	193.264	193.868	193.214	193.646	192.705	193.137	194.971
	Y	300.206	299.689	298.582	299.783	300.319	299.535	297.494	297.008
	Z	495.924	495.100	493.330	494.986	493.241	495.120	492.605	494.232
Max Width (m)		14.764	14.212	13.617	14.096	12.569	13.105	13.230	14.750
Bowl Width (m)		13.567	12.217	12.525	12.544	12.306	11.917	13.103	13.966
Scar Grad.	δx	-1.558	-1.374	-1.902	-1.922	-2.312	-1.677	-3.938	-0.684
	δy	6.082	5.660	5.249	5.569	5.733	5.622	3.284	5.243
	δz	6.628	7.655	5.990	7.491	7.356	5.880	3.294	6.745
	Horiz. dist.	6.278	5.824	5.583	5.891	6.182	5.867	5.128	5.287
	angle (º)	46.552	52.734	47.014	51.817	49.958	45.064	32.717	51.907

Landslides in the local area as mapped within the stereo coverage of vertical stereo pair 9648-47aerial photography are shown on Figures 7.9 and 7.14. These were used to compare the effectiveness of using curvature algorithms to identify landslide locations on steeply-sloping terrain. The 1:1000 scale digital topographic data have been used as a control to establish the effects of using the maximum convexity algorithm to identify possible landslide features; the results are shown in Figure 7.14a, with processing carried out within the ER Mapper program (version 6.3), using ER Mapper's '**maximum convexity in any plane**' routine (MAXIC).

Automated image correlation routines were used to prepare approximately 1m grid spacing DEMs using both paper prints scanned at 21.17µm, and photogrammetric quality scans with a pixel size of 12.5µm. Consequently, the topographic data DEMs were also prepared at 1m spacing. Before the maximum convexity in any curvature algorithm was applied to the data, various Gaussian filters were inserted into the processing stream to smooth the local effects of contour spacing noted in Chapter 7.4.2, and the random variation due to point measurement precision; The Gaussian filters available in ER Mapper (version 6.3) cover 0.391, 0.625, 1.0 and 1.6 standard deviations, covering areas 3, 5, 9 and 11 pixels wide respectively, providing a centre-weighted averaging function. While the Gaussian filters reduce the effects of noise in the data, they also remove spatial variation between closely-spaced features; this is significant at One Rise More, where the crest of the landslide lies close to an interfluve, it is geomorphologically important to separately identify these two landforms. Looking at the results on Figure 7.14a to c, the upper boundary of the One Rise More landslide forms the strongest line on the hillside, and remains separated from the convex interfluve (wider, with slightly less intense white colour) to the northeast on both the 1m DEM convolved with the 1.6sd Gaussian filter, and the 2m DEM processed with the 0.625sd filter. However, on the 2m DEM convolved with the 1.6sd filter, the two features have merged to form one strong linear feature.

This demonstrates the problem of trying to identify component features within small landforms such as the debris flow landslide scars in Hong Kong and other sub-tropical climates; high fidelity ground elevation information is required if any form of semi-automated feature identification is to be performed.

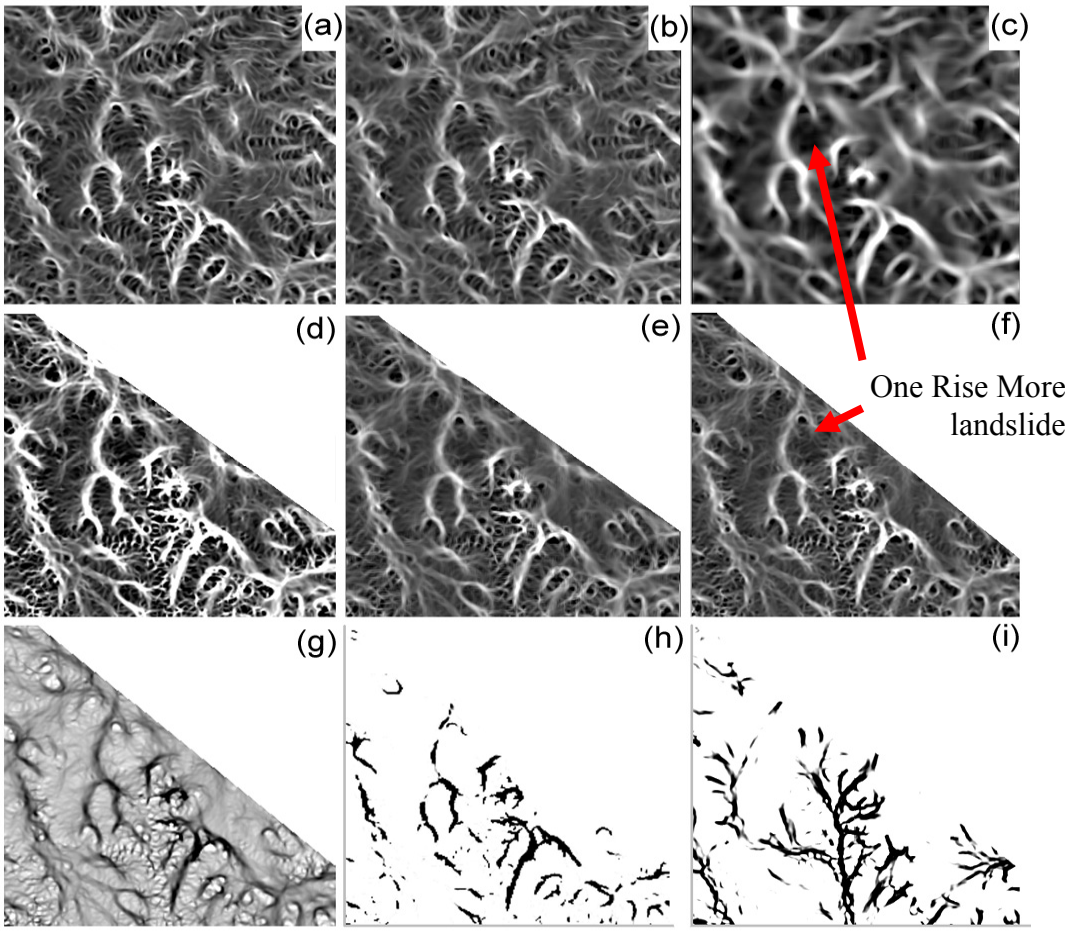

a., b. and c.: DEMs compiled from the 1:1000 scale digital topographic maps, 2m contour interval;
d. and e.: DEMs compiled by automated image correlation, from desktop scanning of paper prints at 1200 dpi (21.17µm pixel size);
f., g., h. and i. DEMs compiled by automated image correlation from photogrammetric quality 12.5µm scans of film negatives.

a 2m DEM, 0.625sd Gaussian filter followed by maximum convexity
b 1m DEM, 1.6sd Gaussian filter followed by maximum convexity
c. 2m DEM, 1.6sd Gaussian filter followed by maximum convexity
d. 2m DEM, 0.625sd Gaussian filter followed by maximum convexity
e. 1m DEM, 1.6sd Gaussian filter followed by maximum convexity (paper print)
f. 1m DEM, 1.6sd Gaussian filter followed by maximum convexity (film negative)
g. Same content as figure f. but with the greyscale reversed
h. Figure g. modified by selecting only part of the greyscale ready for vectorising
i. Same process as h. but using the minimum convexity function to identify concave slopes

Figure 7.14 Results from applying the 'maximum convexity in any plane' kernel to DEM data around the One Rise More hillside

Comparing images 7.14a and d shows that the topographic data are more affected by the contour separation issue than the photogrammetric data, although both data

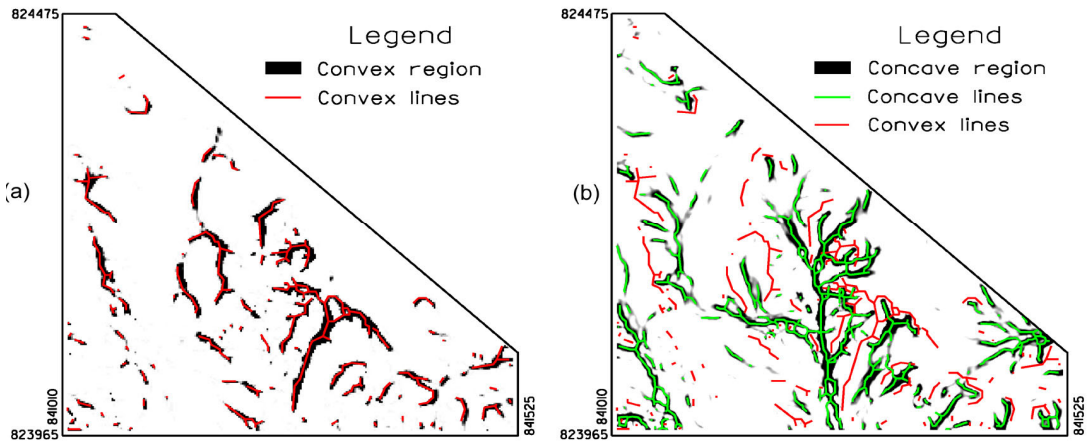

Figure 7.15 Results of vectoring the areas of maximum convexity and minimum convexity (concavity). Coordinates are Hong Kong metric grid (m).

sources are able to differentiate between the interfluve and the edge of the landslide provided that the processing stream maintains sufficient resolution. Using a 2m DEM with 0.625sd Gaussian filter has an equivalent effect to a 2m DEM with a 0.625sd filter (Figures 7.14 e and 7.14d, respectively). The results from the models built using desktop scanning of paper prints and photogrammetric scanning of film negatives also produce very similar results (Figures 7.14e and f).

The final three parts of Figure 7.14, parts g, h and i show the processing required to generate the linework for the lines of maximum convexity and maximum concavity. The curvature images are thresholded to emphasis the significant curvatures and then vectorised, in this case using the R2V vectorising routine (Figure 7.15). Once vectorised, the linework is imported into the MicroStation CAD package, either for direct superimposition onto the rectified aerial photograph, or onto a shaded relief model to assist in visualising the locations of the regions of high curvature. Alternatively, the 2D vectorised lines can be transposed to the TIN representing the ground surface using the appropriate routine within uSMART (Figure 7.16). The results of the vectoring are discussed in Chapter 7.5.1.

Once the raster results of the curvature algorithms have been converted to 3D vectors, and transposed to the ground surface, they can be viewed by stereo superimposition on the aerial photography, and checked against the visual interpretation of landforms. This is described in Chapter 7.5.1.

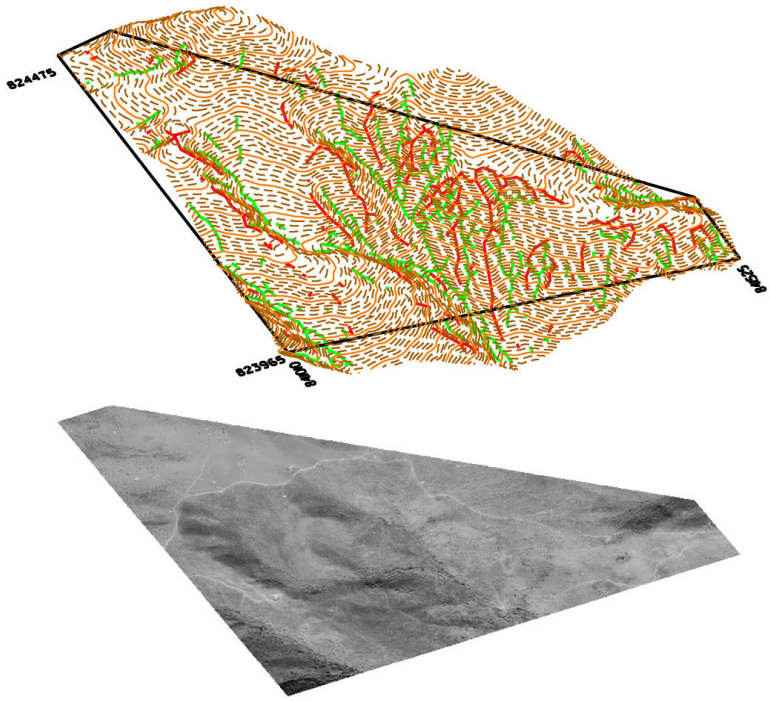

Figure 7.16 Transposing the 2D linework to the TIN surface for 3D visualisation; red lines are the convex edges, and green lines are the concave edges.

7.5.1 One Rise More Hillside

The shaded relief model shown in Figure 7.17 demonstrates that the photogrammetrically-sourced data do not generate the contour-separation problem noted in the supplied digital data. Photogrammetric data have their own problems, including extensive data editing to remove points located too high or low as compared to the ground. Although extensive editing has been performed on the source data, erroneous points can be seen as some of the isolated peaks and pits in the shaded surface. Some of the peaks are due to trees and bushes, or boulders. The illustration in Figure 7.18 provides an alternative perspective view of the relationship between the mapped edges and the landslide bowls.

Figure 7.17 includes approximately 25 landforms that appear to be the result of rapid mass movement processes on steep hillslopes. Many of the features, especially on the steeper slopes, are the result of multiple small slope failures, sometimes including rockfalls. Fourteen of the mapped features also include part of an edge highlighted

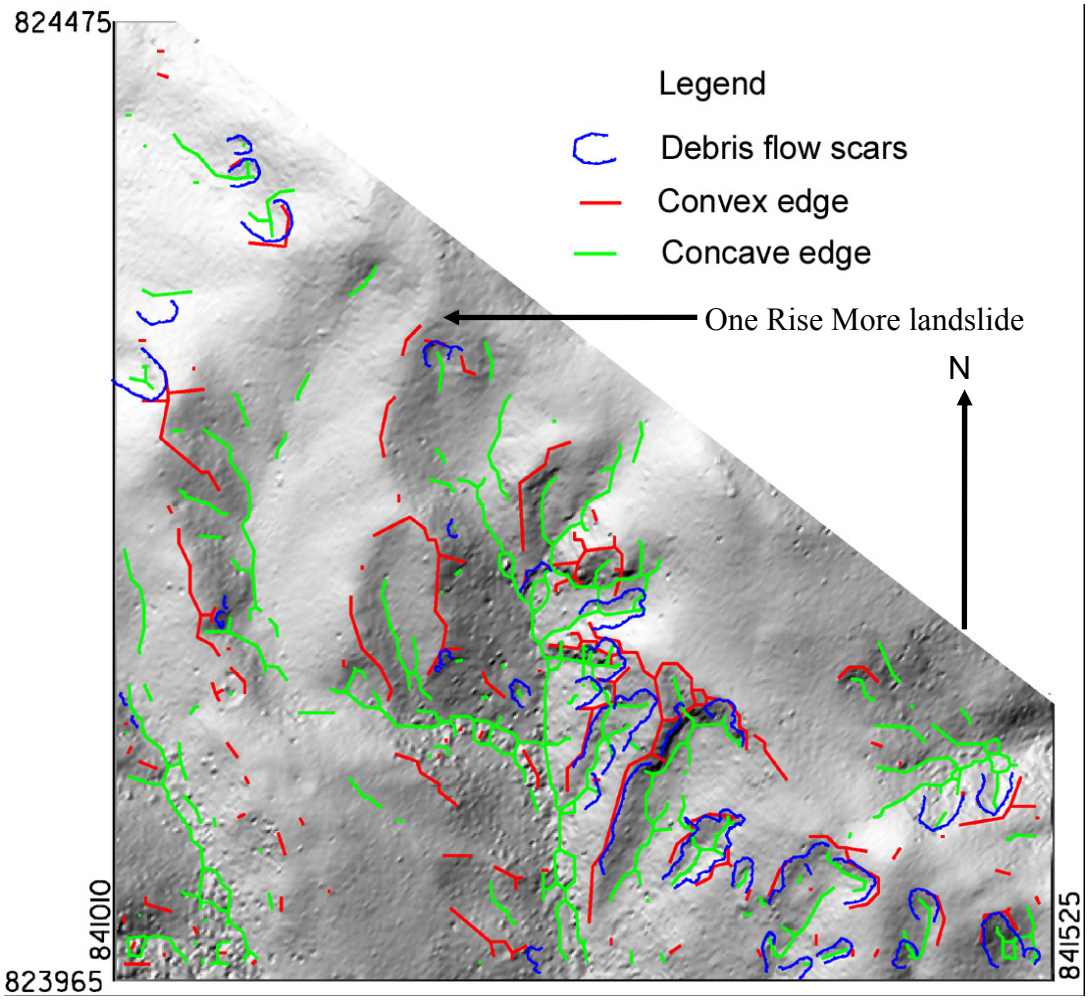

Figure 7.17 Vertical sunshaded relief view of the landslide scars on the hillsides around One Rise More, mapped by an experienced observer (blue), as compared to the convex and concave edges. Coordinates are Hong Kong metric grid (m).

by the red convex line. In some of them the location of the edge corresponds closely, within a few metres of the mapped location. When viewed stereoscopically, the red edges frequently lie within 5m of the mapped feature, however, they rarely are coincident. This is the result of the vectorisation process, which did not produce linework that followed the highest density of line. This may be a constraint of the vectorisation product, R2V, and may not apply to other software solutions. Some of the longer red lines mark the major interfluves; identification of this class of feature is now common among GIS packages such as Grass and ArvView and will not be examined further.

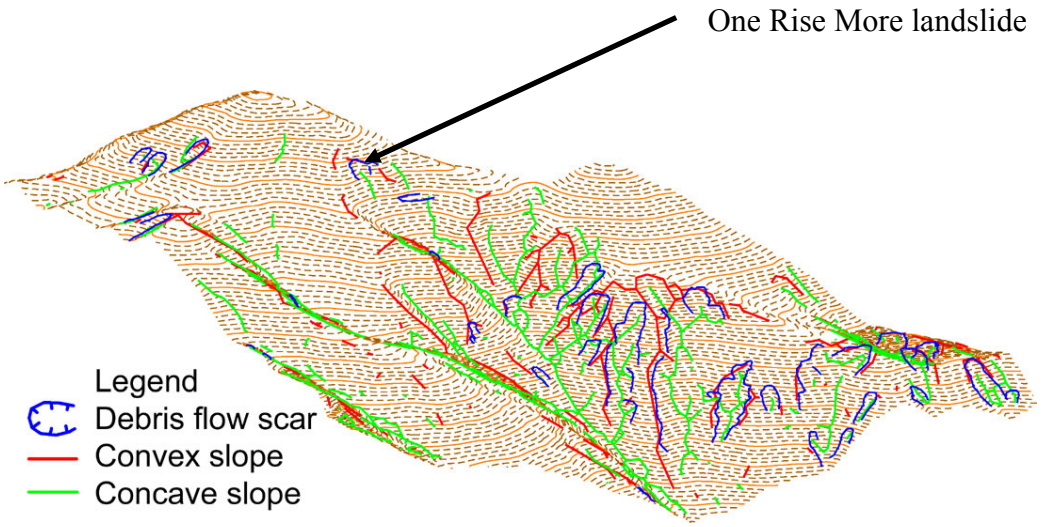

Figure 7.18 Perspective view of the landslide scars on the hillsides around One Rise More, mapped by an experienced observer (blue), as compared to the convex and concave edges. Note the southwest slopes are obscured by the perspective view.

The results for the concave edges are much less satisfactory. This is probably because the floors of the valleys and landslide bowls are frequently covered by debris and sediments, and support a more dense vegetation growth than the open hillsides. One major consequence of this is a greater local variability in recorded elevations than compared with a manual operator who is able to ignore isolated plants and bushes. Note the circular patterns around the lower central parts of Figures 7.14d, e and f which were derived by autocorrelation routines; these areas follow the valley floors. Part of the reason why the concave edges were poorly represented is because the slope failures in this area rarely deposit their debris in the nearby valley floor. To investigate the problem of concave features in more detail, a further study has been carried out on a small landslide to the southwest of One Rise More, shown as Site 3 in Figure 7.4.

7.5.2 Southwest Hillside: Detailed Photogrammetric Mapping

The lowest aerial photography available for 1963/64 in Hong Kong in the general area around One Rise More includes the 2700ft altitude run across the foothills of the urban area of northern Kowloon. This flight line passes over the Fei Ngo Shan ridge about 1km south of One Rise More (Figure 7.4) at an altitude of only 350m above the ground. A small landslide is visible on the 1963 aerial photography, which is

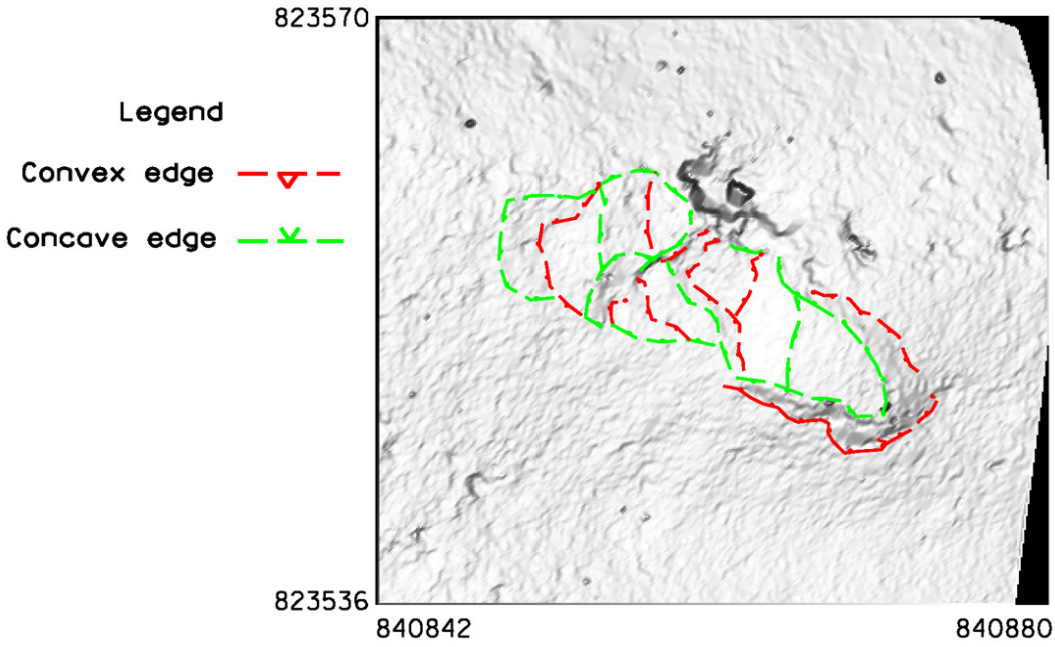

Figure 7.19 Morphological map of the Site 3 landslide prepared manually with line placement controlled visually within the stereo viewing environment of the uSMART photogrammetry system, superimposed over the shaded relief model derived from the DEM. Coordinates are Hong Kong metric grid (m).

approximately 27m long, from the top of the crown to the downslope end of a lobe of debris deposited at the toe of the failure. The failure scar is approximately 7m wide. The ground pixel size of this 12.5µm high resolution scanned imagery is about 3cm. Although the landslide scar is largely covered by low, grassy vegetation in the 1963 imagery, the morphology of the feature can be clearly seen. Two automated DEMs have been produced for this feature, a local one measuring 105 by 114m with a ground resolution of 1m, and a detailed 0.1m grid DEM of the landslide site covering 38 by 34m. This feature was initially mapped manually using a set of geomorphological mapping symbols purpose-written for use in within MicroStation, with the results shown in Figure 7.19.

The DEMs were run using the autocorrelated grid routine within the uSMART package using a minimum correlation of 70%. The resulting DEMs were then edited to remove most of the points that were observed to be placed either above or below the ground surface. The resulting points were imported into ER Mapper for production of the curvature images. As with the One Rise More area before, the images produced used the ‘maximum convexity in any plane’ kernel for the convex

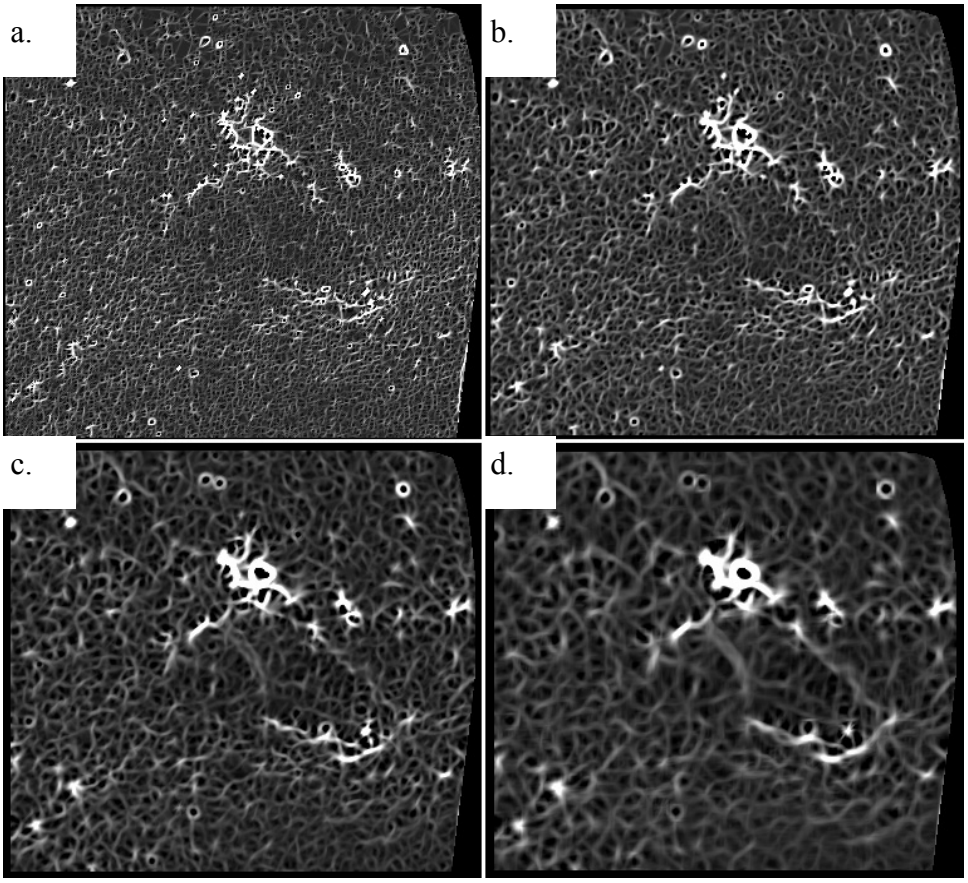

Figure 7.20 Maximum convexity generated from 0.1m photogrammetric DEM. The excessive noise in a. is due to the use of no smoothing filters. b. has a 0.625sd Gaussian filter applied, while c. uses the 1.0sd filter and d. uses the 1.6sd filter.

edges and the 'minimum convexity in any plane' for the concave edges. Gaussian filters were placed before the curvature kernel to reduce unwanted noise from the DEM measurements. The output images were checked for georeferencing, imported into R2V for vectorisation and the linework was exported via DXF into MicroStation, where the 2D lines were converted to 3D and transposed to the photogrammetric TIN surface.

Figure 7.20 shows four stages of noise removal using the Gaussian filter. While the results are less random than the noise experiments using the synthetic model, the effect of the noise reduction is similar, as the basic shape of the feature is discernable in Figure 7.20d.

The best results were obtained when the output from ER Mapper was further blurred using a 3.0 pixel Gaussian filter and the grey scale inverted in Photoshop. The

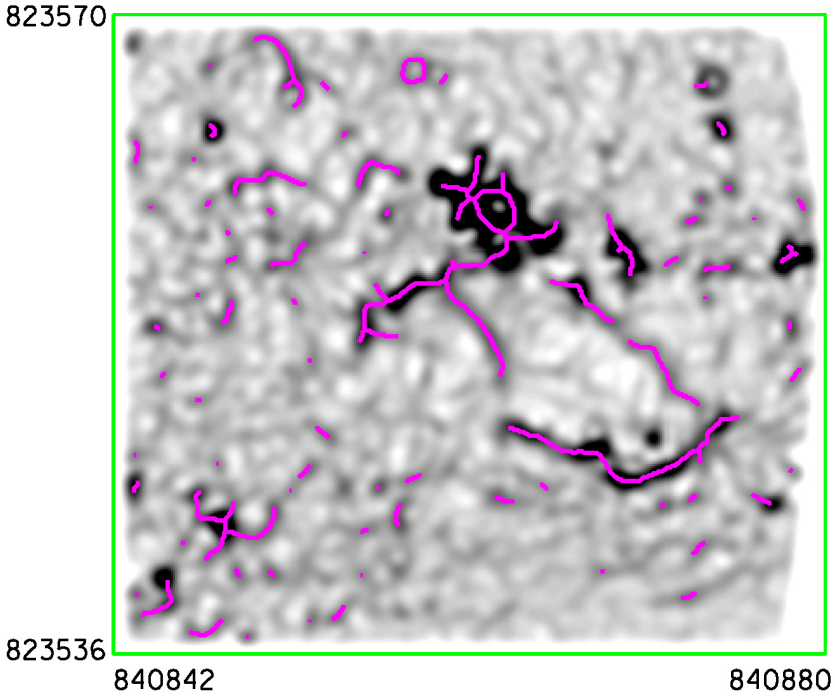

Figure 7.21 Convex edges generated as a result of vectorising using the 0.1m DEM 1.6sd Gaussian filter plus maximum convexity kernel. The result was further blurred using a 3 pixel Gaussian filter in Photoshop. Coordinates are Hong Kong metric grid (m).

vectors are shown in Figure 7.21. Similar results were obtained for the concave edges when the 'minimum convexity in any plane' kernel was used.

Figure 7.22 shows the results of the convex and concave vectorising compared to the manual mapping. There is a close correspondence between the convex and concave edges of the landslide scar. The terrain morphology of the debris is more complex, consisting of undulating terrain due to deposition of failed debris and subsequent fluvial erosion of surface and possibly subsurface materials. The edges highlighted by the curvature algorithms include the major convexity at the crest of the failed debris and the toe of the primary debris fan. The algorithm has failed to identify the more subtle secondary lobe that extends further downslope than the primary lobe, but this is not surprising, as recognition of this feature requires consideration of factors such as texture of the material where the surface of the lobe is devoid of boulders, in contrast to the surrounding terrain. However, the concave edge processing has identified several shallow drainage channels that had not been identified in the manual mapping.

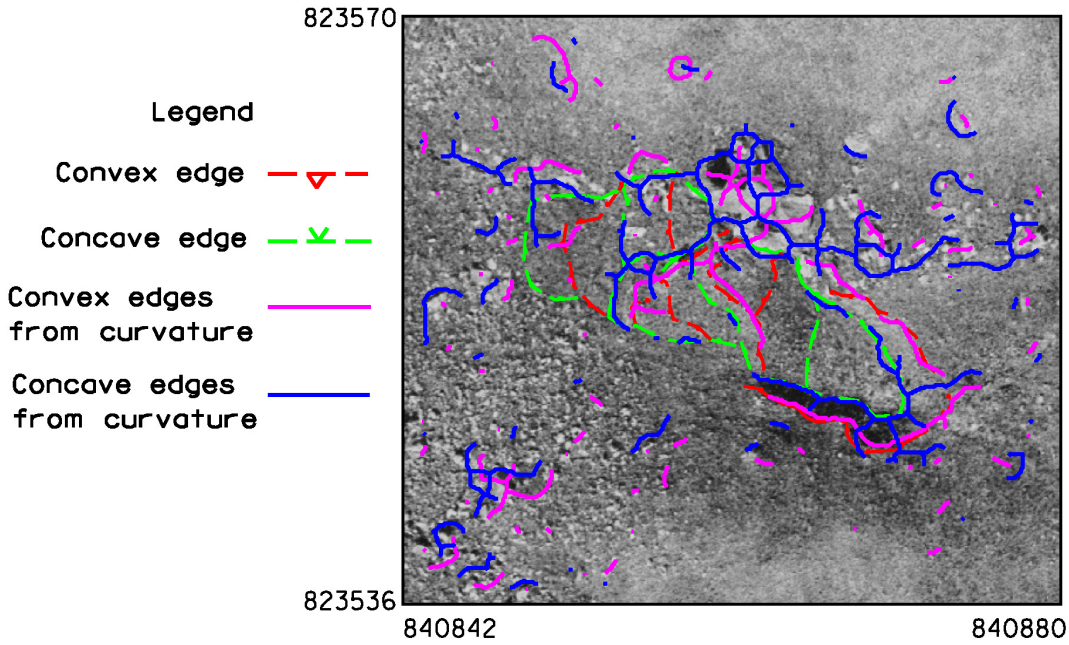

Figure 7.22 Concave and convex edges generated as a result of vectorising using the 0.1m DEM. Coordinates are Hong Kong metric grid (m).

7.6 Geomorphological Mapping Example

The investigations conducted in this Chapter have demonstrated that it is feasible to perform automated identification of slope morphology as part of geomorphological mapping. However, the requirements are a very detailed DEM, with significant amounts of editing to remove irregular points, as the curvature algorithms are more sensitive to irregularities than first derivatives of elevation such as slope and aspect. As a side benefit, the curvature images are useful to aid in identification of these erroneous points.

Sewell and Campbell (2005) have recommended that landslide chronologies should be extended by examining the relative degradation of relict and natural terrain landslides. The edges of landslide scars generally form the most prominent landform by which landslides can be identified both in the field and by API. As the radius of curvature forms an essential element of this landform degradation, very high resolution DEMs would be required to quantify this feature. High resolution scanning of low altitude aerial photography would be needed to facilitate this type of investigation.

The complexity of the morphological components of the terrain requires skilled interpretation to convert the morphology into a geomorphological map. Routines are available within the CAD software (MicroStation, version 8 was used for this study) to add symbology to the linework, either as the addition of graphic cells to existing lines (as would be generated by vectorising the georeferenced curvature images), or by direct placement of symbology using the terrain-following cursor of the photogrammetric software. The uSMART system used in this study runs within the MicroStation environment and all the normal CAD functions are available.

The main benefit of the curvature algorithms is the identification of target landforms for subsequent interpretation during stereoscopic observation. In this study, the high resolution DEMs have been generated photogrammetrically; however, the curvature algorithms function equally well with similar high resolution DEMs generated from other sources such as airborne laser scanning. Under these circumstances, the 3D vectorised curvature lines can be viewed superimposed onto the stereo aerial photography for subsequent conversion by interpretation into geomorphological boundaries and features as shown in Figures 7.23 and 7.24.

Figure 7.23a shows the shaded relief depiction of a sample LiDAR dataset supplied by AAMHatch for the northern and eastern slopes of Mt. Parker, Hong Kong. This has been processed using the methodology as described in this Chapter to derive convex curvature regions as shown in Figure 7.23b; only the convex regions have been identified in this example, a similar processing sequence can be performed to extract the concave lines. Vectorising of the 2D raster dataset is shown in Figure 7.23c, and the resulting high curvature lines are warped to the LiDAR-based 3D ground surface as shown in Figure 7.23d, where the photo-texture has been obtained from the georeferenced vertical aerial photography. The processing sequence depicted in this sequence is predominantly automated; manual intervention is required to determine the limits of the curvature algorithm applied within ER Mapper to highlight suitable regions.

At this stage, existing data sets can be imported into the 3D model for visual comparison and checking. Figure 7.24a shows the photo-textured 3D hillside model to which the 2D vector data from the Hong Kong Government's landslide inventory (King, 1999; Ng et al., 2000, 2003; 1:5000 scale data available on the Slope

a. Sun-shaded relief image of AAMHatch Hong Kong SAR LiDAR Sample of the northern and eastern slopes of Mount Parker; acquired between 17.12.2006 and 20.12.2006. Expected accuracy: 0.15m vertical, <0.55m horizontal (AAMHatch, 2007).

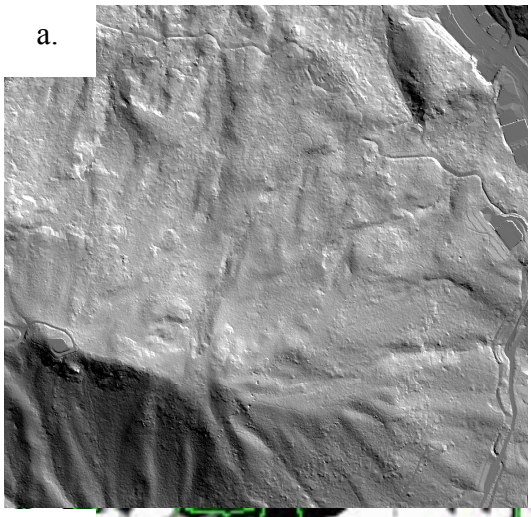

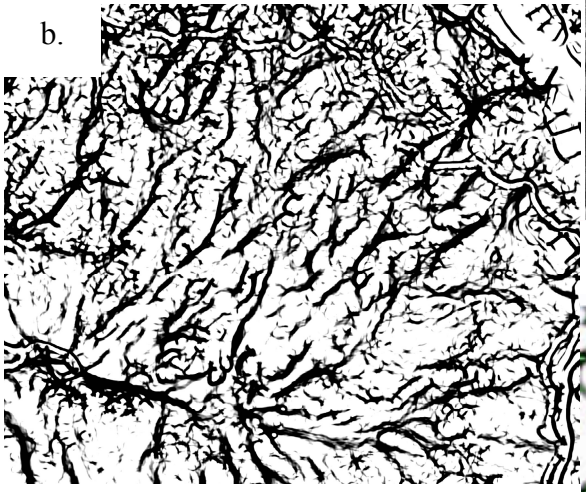

b. Zones of high terrain convex curvature (dark tones) derived from the AAMHatch HK SAR LiDAR Sample DEM

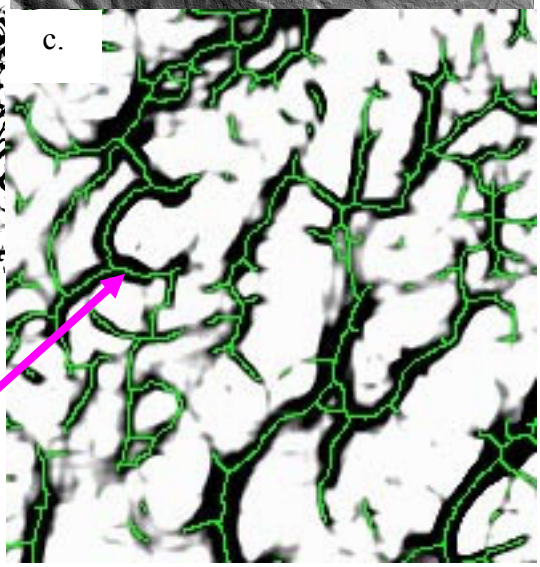

c. Convex curvature zones are vectorised (green linework), imported into the 3D photogrammetric mapping environment for warping to LiDAR-defined ground surface

d. Completed derivative processing of LiDAR data: contours and high curvature zones are draped across the LiDAR-defined ground surface. High curvature forms the basis for interpretation of terrain morphology and experience-based API of engineering geomorphology.

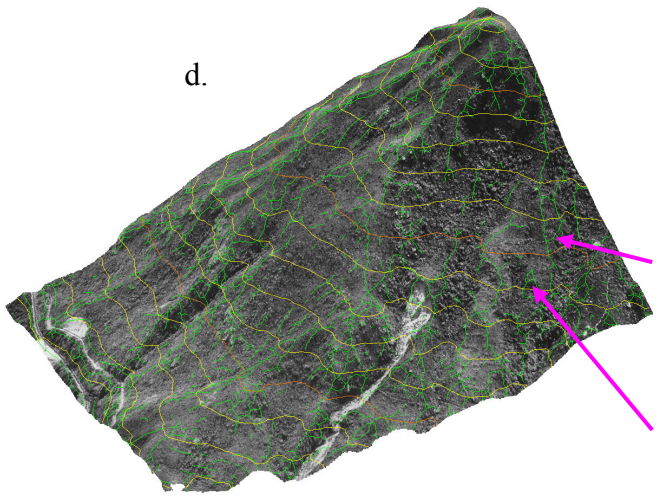

Note contours help identify steep-sided valleys obscured by the dense tree canopy while curvature helps highlight the boundaries of concave depressions.

Figure 7.23 Terrain morphology identified from LiDAR data

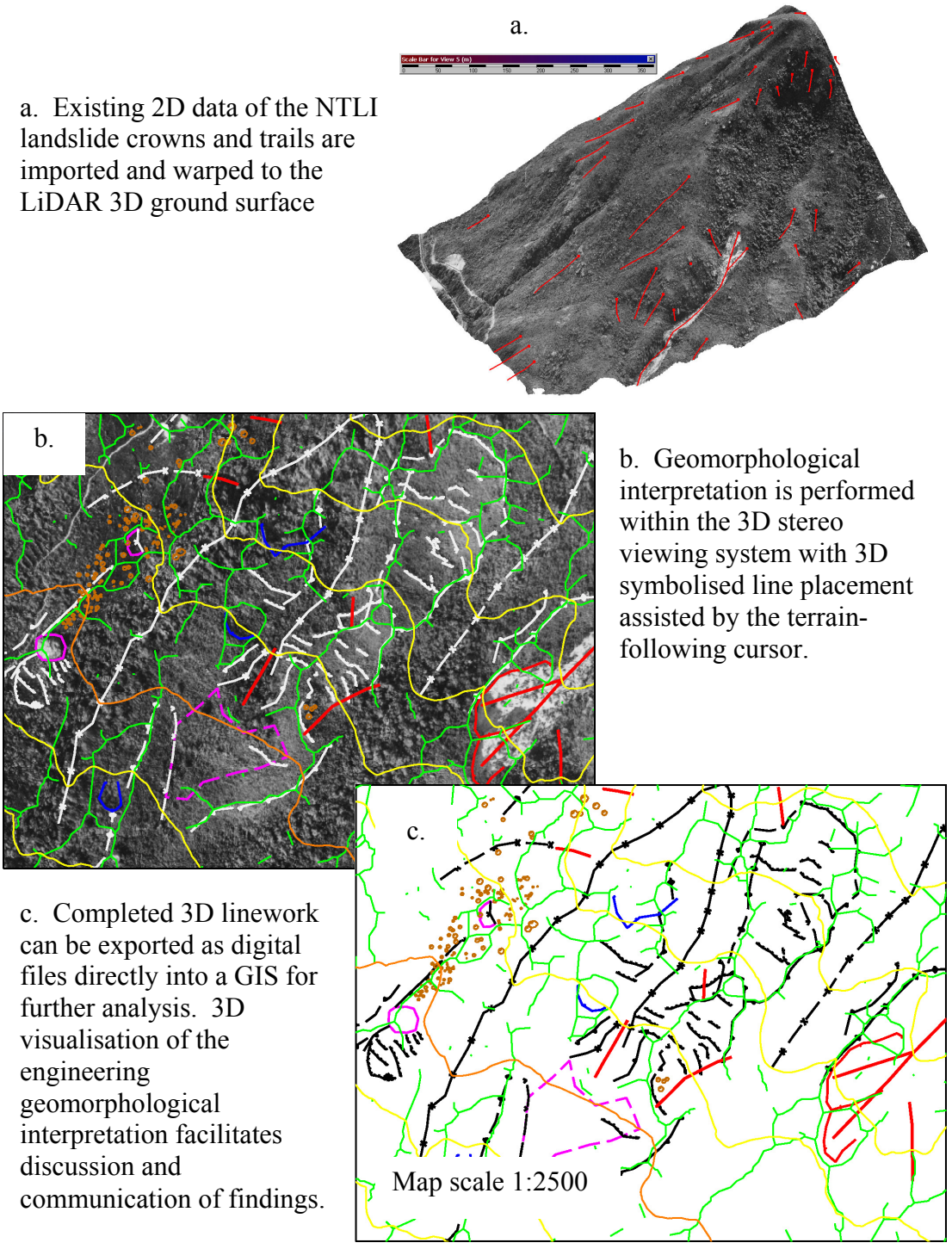

a. Existing 2D data of the NTLI landslide crowns and trails are imported and warped to the LiDAR 3D ground surface

b. Geomorphological interpretation is performed within the 3D stereo viewing system with 3D symbolised line placement assisted by the terrain-following cursor.

c. Completed 3D linework can be exported as digital files directly into a GIS for further analysis. 3D visualisation of the engineering geomorphological interpretation facilitates discussion and communication of findings.

Figure 7.24 3D geomorphological mapping process

Information System at http://hkss.ced.gov.hk;) have been warped to the LiDAR-based ground surface. Further conversion of the automated morphological mapping into geomorphologically-classified features and identification of other geological, geomorphological and hydrological entities not highlighted by the curvature linework is performed within the stereo-viewing environment. This allows

interactive line placement and editing, depending on the cognitive interpretation of the geomorphological model of the terrain.

Results from the comparison of the manual and semi-automated line placement on stereo pairs at different scales demonstrates that the use of moderately high altitude aerial photography coupled with high resolution scanning can prove adequate for feature mapping using a terrain-following cursor; low altitude photography with paper prints captured with a desktop scanner generated similar results. When the nature of image matching is considered, this result is not be surprising; correlation of image patches requires matching the pixel value patterns across the area of the kernel. When using a square minimum patch ten pixels wide, the correlation will be based on 100 pixels in the reference kernel. Consequently, small features with an area in the order of five to ten pixels will only be identified if they present a significant contrast. Linear or gently curving landform boundaries such as the edges of landslide scars will be adequately sampled provided they show some reflectance or colour contrast and that the sampling interval for placement of vector nodes in the mapped linework is at least half the width of the kernel.

7.7 Chapter Summary: Measuring Landslide Morphometry

This Chapter describes photogrammetric mapping at the One Rise More landslide in Hong Kong and on the adjacent open hillside terrain. Stereo models were set up using vertical aerial photography obtained between 1169 and 3933m altitude in 1963, and converted to digital images at 12.5µm pixel resolution from the negatives with a photogrammetric quality scanner, and from paper prints captured at 21.7µm with a desktop scanner. Ground control for the models was obtained from existing digital 1:1000 topographic survey data, with RMS errors on the residuals ranging from 0.2m on the low altitude photography to 1m on the higher altitude photography. The precision of the higher altitude photography was over 1:2800, whereas for the low altitude photography this reduced to approximately 1:1000; this is attributed to the use of only poorly-defined ground control on hillsides for the low altitude photography, where the high altitude photography extended coverage into the adjacent urban areas where well-defined control was obtained from the 1:1000 scale topographic plans.

Comparisons of point and vector mapping derived from ground Total Station survey, the digital maps, and stereo photogrammetry using the vertical imagery produced close agreement in derivative parameters including landslide dimensions and internal slope gradients, although the models contained mis-alignments of about 0.5m, largely due to the poorly-defined ground control.

The automated image correlation function was used to generate high ground resolution DEMs ranging from 0.2 to 2m spacing. The quality of the DEMs was strongly controlled by the texture of the images, with rough, boulder-strewn terrain producing image matching correlations generally between 50 to 90% with low contrast, grassy hillsides generating correlations of <60%. Sun-shaded relief visualisations of the photogrammetrically-generated DEMs assist in the identification of falsely-correlated elevations for editing and did not contain the horizontal striping consistently present in DEMs generated from the existing 1:1000 scale digital topographic survey data.

Maximum convex curvature vectors generated from the 2m resolution DEMs were found to compare closely with about 50% of the vectors representing landslide boundaries compiled manually using the terrain-following cursor; maximum convex curvature did not represent the boundary of the landslide, especially on degraded landslides, although this may be a function of the vectorising software used to extract the vectors from the curvature images. Maximum concave curvature was less successful at delineating features within the landslide scars, especially degraded features where dense vegetation was present. A second DEM was compiled at 0.1m resolution across a landslide that was less degraded; the resulting maximum convex and maximum concave curvature vectors agreed closely with the manually-derived morphological features of the landslide prepared using the terrain-following cursor.

Chapter 8 investigates the extent to which the geomorphological mapping process can be automated using multi-image photogrammetry. This presents a different set of opportunities and constraints due to the operational differences between stereo and multi-image photogrammetric techniques.

Chapter 8

USING MULTI-IMAGE PHOTOGRAMMETRY TO MEASURE LANDSLIDE MORPHOLOGY AND GEOMORPHOMETRY

Multi-image photogrammetric systems have developed a wide customer base, especially for building 3D models of architectural features and manufactured objects where visualisation can be an important criterion (see Chapter 3.4.4). Geomorphological mapping has a strong interpretive element, and techniques that can assist in visualising the relationships between landform elements may improve the quality and consistency of the final products.

Two landslide-prone hillsides in Hong Kong were photogrammetrically modelled to:

(a) Assess the suitability of hand-held digital photogrammetry as an input to multi-image photogrammetry for recording landslide locations for inventory purposes;

(b) Identify the opportunities and constraints of using this comparatively low cost photogrammetric solution to obtain simple morphometric information for inclusion in geomorphological maps; and

(c) Create 3D visualisations to assist geomorphological interpretation and mapping of the landforms.

The two sites selected included the partially revegetated landslide at One Rise More discussed in Chapters 7.1 to 7.4, together with several less-distinct, relict slope failure features further downslope, and a recent landslide at Cloudy Hill where measurements within the landslide scar were less obstructed by vegetation regrowth. Both sites were photographed at multiple locations from surrounding hillsides to map the landslides by comparison with ground control derived from major landform and anthropogenic features identified on the published 1:1000 topographic maps. Target distances ranged from over 1km to less than 10m within the landslide scars. These variable scale image sets were combined in multi-image photogrammetric models by bundle adjustment using the PhotoModeler softcopy system.

PhotoModeler is an example of a multi-image photogrammetric system that is able to incorporate points identified on a set of photographs taken in different directions, at

varying distances from the target, and using multiple cameras. The advantages and limitations of multi-image photogrammetric systems have been listed in Table 3.2 and discussed in Chapter 3.3. The investigations described in this Chapter have used multi-image photogrammetry to determine the spatial location and internal morphology of landslides at One Rise More and Cloudy Hill, both in Hong Kong.

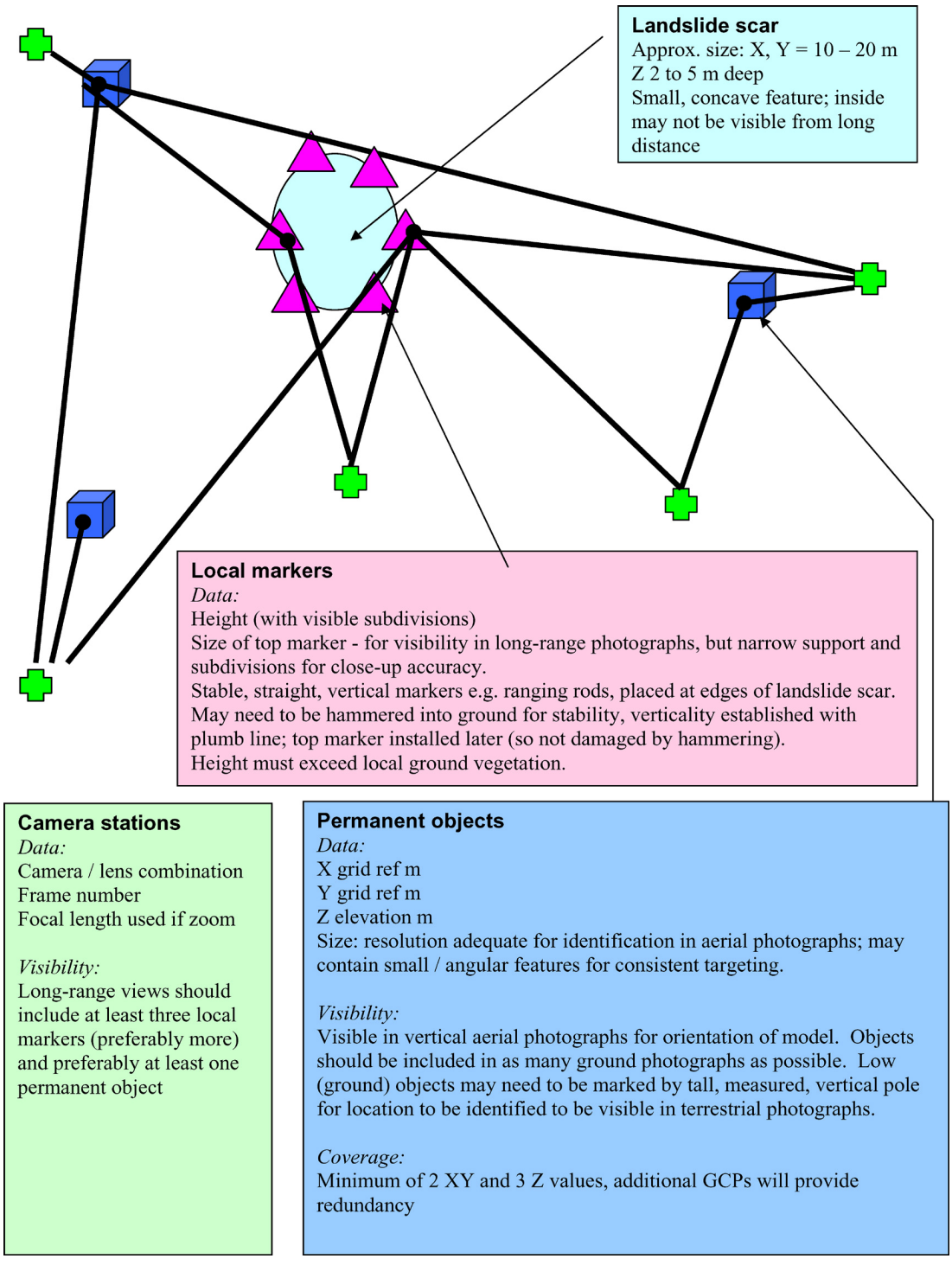

Figure 8.1 Design of external ground control

8.1 Creating the Multi-image Photogrammetric Models

8.1.1 Orientation and Landslide Location

In addition to prominent features in the landscape, two types of pre-marks were used to tie the wide-ranging scale imagery into one coherent model. Figure 8.1 shows the schematic layout of the larger pre-marks for external control; at the One Rise More site, black A4 polystyrene mounting boards with white, 18cm diameter circular targets were used for the longest distances across the valley. Figure 8.2 shows the target configuration for photography taken from the adjacent hillslopes to tie the pre-marks around the edges of the landslide into the external framework; 2m ranging

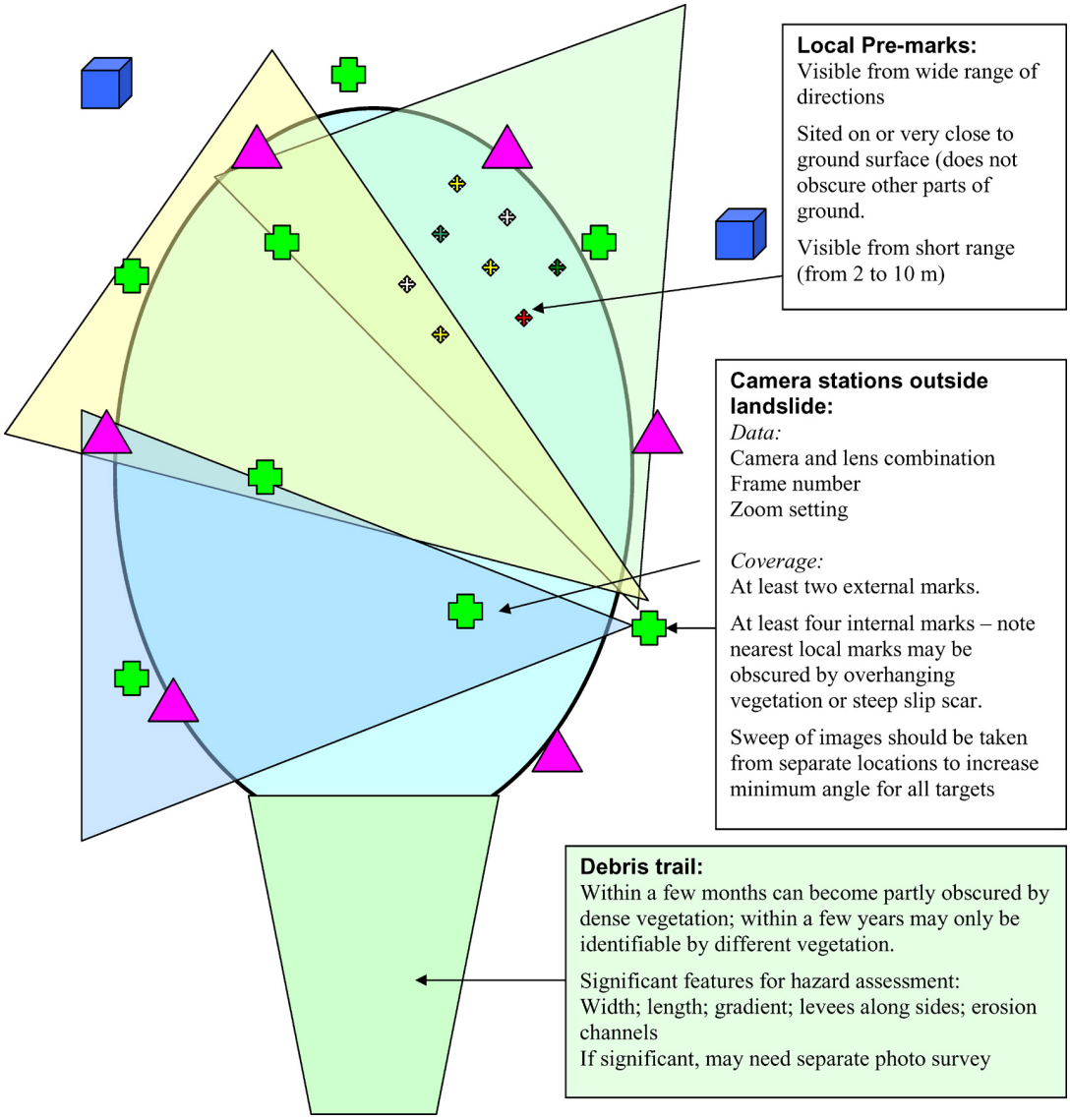

Figure 8.2 Transferring photogrammetric control onto the landslide

poles were used in the initial photography at One Rise More and the second set of photography at Cloudy Hill. Alternatively, black A5 and A6 polystyrene mounting boards with white circular targets were placed along the footpath and on rock outcrops on both hillsides to tie the intermediate distance photographs with those taken within the landslide. Yellow 60mm diameter self-adhesive paper targets were

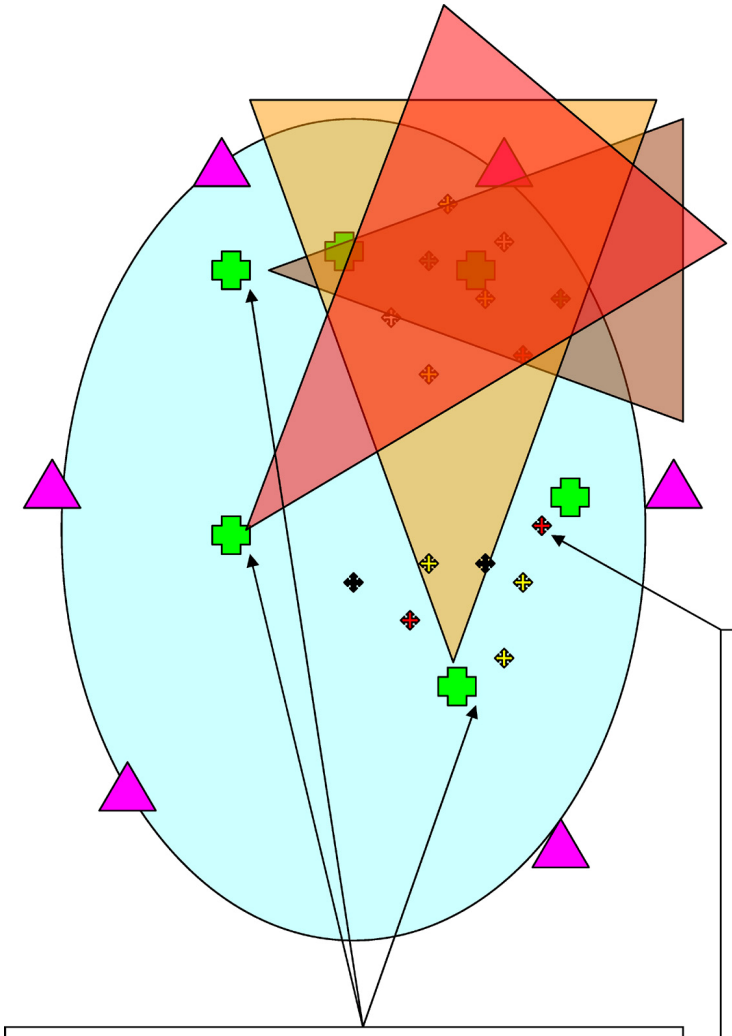

Local Pre-marks:
Sited on or very close to ground surface (does not obscure other parts of ground.

Visible from short range (from 2 to 10 m).

Visible in at least three images from wide range of directions – at least 45 degrees.

Marks should be a range of colours and shapes to ensure unique identification in complex areas with only local visibility.

Sized to match resolution of camera – at least 3 pixels wide for local photographs.

Local marks can be widely-spaced where there are high-contrast small natural features, but the features must be uniquely identifiable.

Camera stations within landslide:
Data:
Camera and lens combination
Frame number
Zoom setting

Coverage:
At least four local pre-marks, at least one must be uniquely identifiable

Possibly one or more external marks

Must differentiate surfaces obscured at certain view directions (e.g. debris mounds, bedrock pinnacles)

Figure 8.3 Images required to transfer the orientations within the landslide scar

fixed to rock outcrops and on prominent boulders within the landslide and around the edges, at locations visible above the surrounding grassy vegetation.

Figure 8.3 shows the specifications for photography within the landslide scar for detailed measurements. Self-adhesive paper circles were found to work very well, two sizes were used: 6 and 8mm, in fluorescent orange, yellow and white colours. As seen in Figure 8.10, these small targets proved very effective.

8.1.2 Sources of Imagery

The photography at One Rise More and Cloudy Hill was carried out using three consumer grade digital cameras, a Leica 4300, Fuji Finepix 6800 and an Olympus 3030 (Table 8.1). Although the Olympus camera has a lower resolution image format with regard to the number of pixels in the image X and Y dimensions, the quality of the images for measurement purposes was potentially higher when using the option to save the images in lossless TIFF format.

Table 8.1 Specifications of the cameras used for multi-image photogrammetry at One Rise More and Cloudy Hill

Camera	Leica 4300 zoom	Fujifilm FinePix 6800 zoom	Olympus 3030 zoom
Calibrated lens focal lengths (mm)	8.788	10.745	10.370 – 30.720
Format width (pixels; mm)	2400, 7.846mm	2832, 9.417mm	2048, 11.261mm
Format height (pixels, mm)	1800, 4.001mm	2128, 3.696mm	1536, 8.448mm
Image format and file size (maximum quality)	JPEG: 1.8MBytes	JPEG: 2.4MBytes	TIFF: 9.2 MBytes

An initial set of photographs was taken from along the footpath and around the outside boundaries of the landslide using the Fuji Finepix 6800 camera. Problems arose when trying to correlate the images, which were attributed to three factors:

(a) Inconsistent focal length settings;

(b) Uncalibrated camera;

(c) Loss of quality due to internal JPEG compression when storing the images within the camera as the medium quality setting had been used;

(d) Loss of resolution due to the design of the SuperCCD used in both the Leica and FujiFilm cameras (Chapter 3.5.3 and Figure 3.6).

The first problem was due to the use of a consumer-grade camera with a zoom lens. Although an attempt was made to take all the photographs with the zoom lens set to 'wide angle', it appears that for some of the images, the focal length setting had drifted from the limit. When these images were added to the model, the measures of variability increased significantly or in extreme cases, processing to orient the model failed to reach a solution. A field calibration using Australis software (Fraser and

Figure 8.4 Transferring orientation from external control into the landslide. Points marked on at least 2 images are shown in white.

Edmunson, 2000) was attempted using ranging poles for scale, but this also failed to solve, most likely due to the same variable focal length issue.

The JPEG compression problem was observed when enlarging the images sufficient to view small groups of pixels, where the images demonstrated the 'blockiness' typical of highly-compressed JPEG format. It was not always possible to distinguish the exact location of the target within one of the JPEG image blocks, due to the change in colour between adjacent blocks. The resulting model achieved precision for individual points of about 1/800 of the distance between the camera stations located around the edges of the landslide and object, which was considered inadequate for orientation of planes within the landslide, and a second photographic survey was undertaken to improve the consistency of the photographs.

A second set of photographs was taken using the Olympus and Leica cameras (Figure 8.4 and Table 8.1), with careful use of the wide angle setting. When the Olympus camera was used, the images were stored in TIFF format to improve the model resolution. The limitation of the TIFF format is the larger image file size, but this was offset in the field by downloading the images into a laptop computer. The variously scaled images were incorporated into a single photogrammetric model by co-identifying points on at least two images. Once the set of images had been oriented between each other, the whole set was scaled, rotated and translated into the local coordinate system by the use of three ground control points (Figure 8.5).

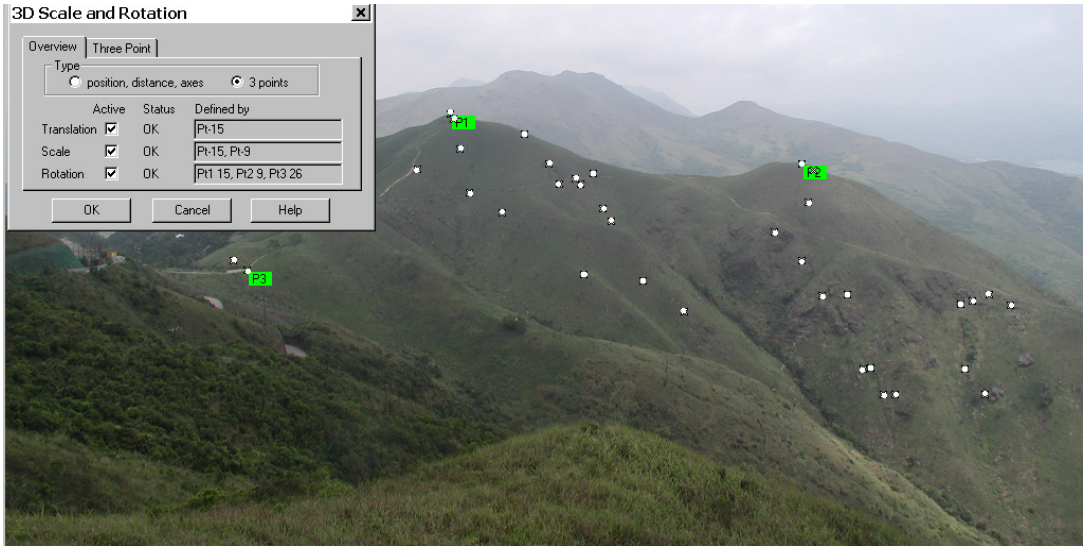

Figure 8.5 Three point scale to orient the photogrammetric model to the ground control.

8.1.3 Three-dimensional Model

The second set of digital images were used to build a single model that included both the external component to transfer orientation from features co-located on the published 1:1000 scale topographic map and the distant photographs (Figure 8.5) to the pre-marks located around the landslide. The distribution of the camera stations and the external control points is shown in Figure 8.6.

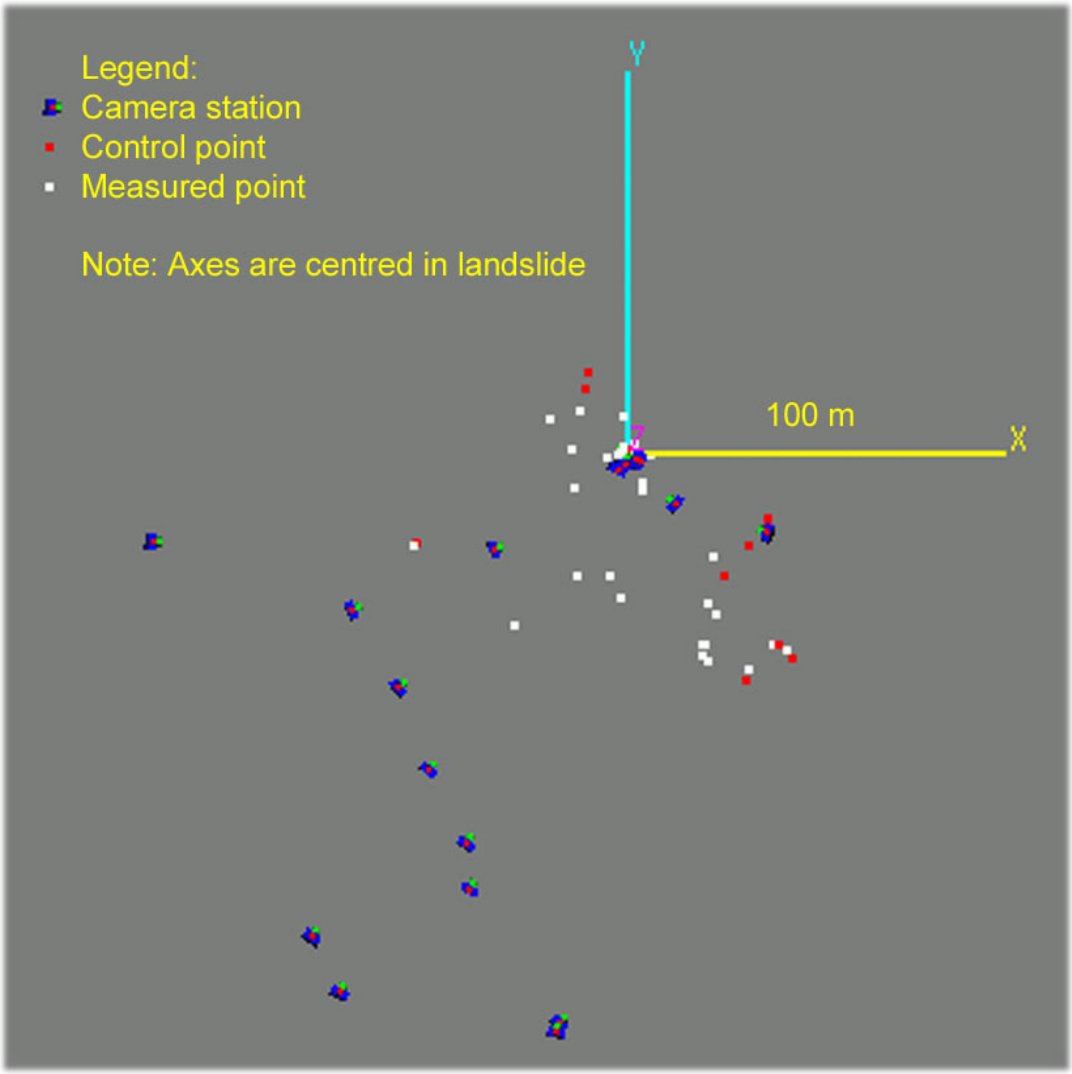

Figure 8.6 Distribution of camera stations relative to the landslide

Within the landslide scar, the major rock surfaces and selected stones within the soil matrix were pre-marked with highly visible, fluorescent yellow and orange adhesive, eight and 16mm diameter paper disks (Figures 8.4 and 8.7). Compared to the initial model, the precision improved to range, for individual points, to between 1:1500 and 1:4000 of the camera to target distance, with the greatest precision for the pre-marks.

Figure 8.7 Small rock joint exposed on the base of the landslide scar

These results are still lower than typical results from aerial photogrammetry (Chapter 3.4), which appears to be the result of the camera calibration curve determined for each of the cameras not adequately representing the larger lens distortion that typically occurs close to the margins of the images (Chapter 3).

Figure 8.7 shows one rock plane highlighted within the basal failure surface of the landslide. The 3D coordinates of the points on the highlighted plane, which forms part of the basal failure surface, are included in Table 8.2. The graphic result for Plane 1 as generated by the MatLab LSP least squares orientation routine (Chapter 5.5) is shown in Figure 8.8; the plane dips at 50.6° with a strike of 76.5°N. The length across strike is 0.32m, down dip it is 1.10m long and the maximum length of the maximum positive and negative residuals is 0.12m. Note the increased visibility of the coloured pre-marks; the largest is 60mm, the smaller ones are 8mm diameter.

Table 8.2 Multi-image photogrammetry results for Plane 1

Id	Coordinates (m)			Precision (m)			Angle (deg.)	Precision Vector Length (m)
	X	Y	Z	X	Y	Z		
67	841190.42	824296.95	487.53	0.064	0.050	0.011	83.99	0.082
68	841190.39	824297.04	487.69	0.062	0.054	0.013	26.78	0.083
72	841190.28	824297.55	488.35	0.053	0.049	0.013	26.35	0.073
73	841190.24	824297.53	488.25	0.054	0.049	0.013	26.39	0.074
74	841190.20	824297.32	487.92	0.057	0.051	0.014	26.71	0.078
75	841190.42	824297.22	487.85	0.060	0.053	0.013	26.45	0.081
76	841190.33	824296.93	487.44	0.064	0.055	0.014	26.98	0.086
122	841190.44	824297.69	488.28	0.052	0.050	0.013	25.72	0.073
Minimum	841190.20	824296.93	487.44	0.052	0.049	0.011	25.72	0.073
Maximum	841190.44	824297.69	488.35	0.064	0.055	0.014	83.99	0.086
Range	0.23	0.76	0.91	0.012	0.006	0.002	58.27	0.012

8.1.4 Comparison with Vertical Stereo Photogrammetry

Table 8.3 gives the length and direction of the misplacement vector between the multi-image model and the stereo photogrammetry. A significant factor in this error is the co-identification of suitable ground control points in the landscape. Features were chosen as control points if they could be co-identified on both the topographic map and the photographs. Measurement of the coordinates for the features chosen, large rock outcrops and spot heights on ridge crests and along footpaths, plus the location of intersections between two footpaths, has errors approaching this magnitude. In terms of the assessment of slope stability, however, it is the orientation of the model axes that is more important.

Table 8.3 Difference between landslide locations determined from multi-image and stereo photogrammetry

Feature	X (m)	Y (m)	Z (m)
Multi-image photogrammetry landslide crown	841188.5	824301.1	493.5
Stereo photogrammetry landslide crown	841185.4	824305.0	501.5
Difference	3.1	-3.9	-7.9
Total length	9.4		

8.2 Suggestions for Improvement

The stereo measurements demonstrated that high density ground surveys can be obtained from suitable photography, but that care must be taken to ensure that the

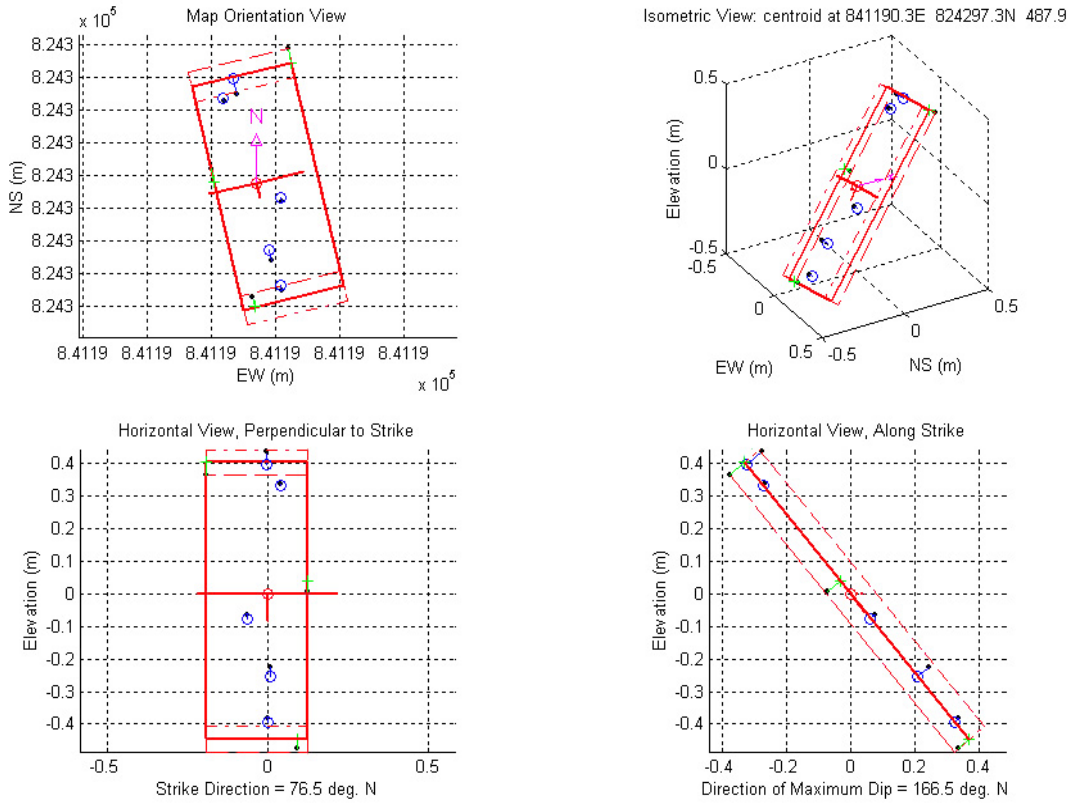

Figure 8.8 Graphic display of the orientation results for Plane 1

photographs chosen are optimised in relation to the view direction. The 3D point and vector data must be checked for consistency and edited where necessary.

The multi-image survey could be improved by better choice of both external and internal ground control. The preferred method would be to use GPS or other survey technique. Although the ±4m achieved in the present survey for measurement of Eastings and Northings is satisfactory for orientation of features within the landslide relative to the regional coordinate system (Hong Kong metric grid), this error was disappointing. The major problem within the landslide in the multi-image survey was the vegetation that obscured much of the basal surface. This limited the number of photographs in which details of the surface were visible. The use of ranging poles would help to reduce this problem due to the greater vertical extent which increases visibility from a wide range of vantage points.

A second case study was carried out at a recent landslide on Cloudy Hill to try and improve on the results of the One Rise More study.

8.3 Visualisation of a Landslide Scar for Geomorphological Interpretation

A second landslide was photographed with the aim of building a detailed 3D model with less ground obscured by vegetation. The feature chosen was located on a moderately steep hillside on the northern side of Cloudy Hill in the northern New Territories, Hong Kong. An initial set of terrestrial photography was obtained in January 2002 and a more detailed set of photographs were taken in April 2002. While the landslide scar remained substantially clear of vegetation, by the dates of the photography, the debris trail downslope of the landslide scar had become partially revegetated. This second case study has allowed greater detail to be modelled within the landslide scar.

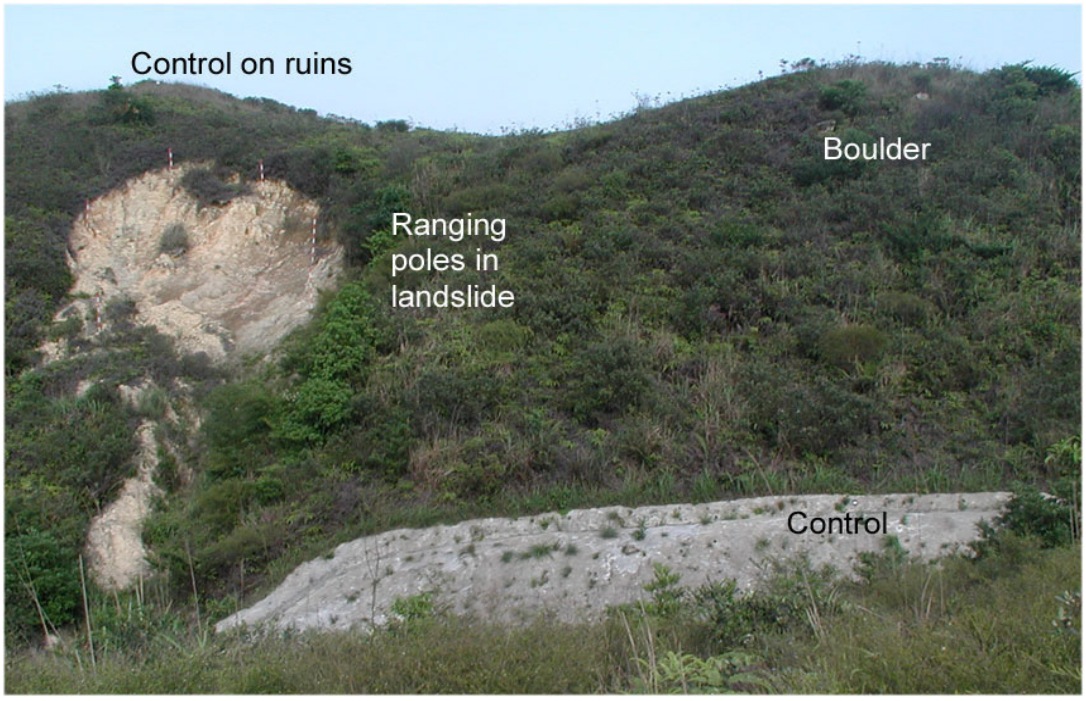

Figure 8.9 Recent landslide on the northern slopes of Cloudy Hill

8.3.1 Description of the Landslide and Surrounding Terrain

The 2001 landslide is located within a valley-side depression that can be seen in the 1963 aerial photographs to have failed previously. The recent failure extended the pre-existing landslide scar further upslope. The terrain around the landslide is shown in Figure 8.9; the sideslopes have a dense but low vegetation cover. Upslope of the landslide, a footpath runs along the ridge, with the ruins of small military trenches that are visible in the aerial photography (Figure 8.11). A second ridge runs on the

opposite side of the valley, providing a vantage point for photography of the landslide and adjacent hilltops.

Two 3D models were built, both using images from the same consumer grade Olympus 3030 digital zoom camera with a maximum frame size of 2048x1536 pixels. Semi-automatic camera calibration was performed with the PhotoModeler software (version 4). The calibration images were taken at a shorter distance than the approximate infinity focal length of the field images as the calibration was performed in the laboratory. Due to space restraints and the A0 size of the calibration target, the wide angle images were taken at a distance of about 2m from the centre of the calibration chart, and the telephoto images at a distance of about 3m.

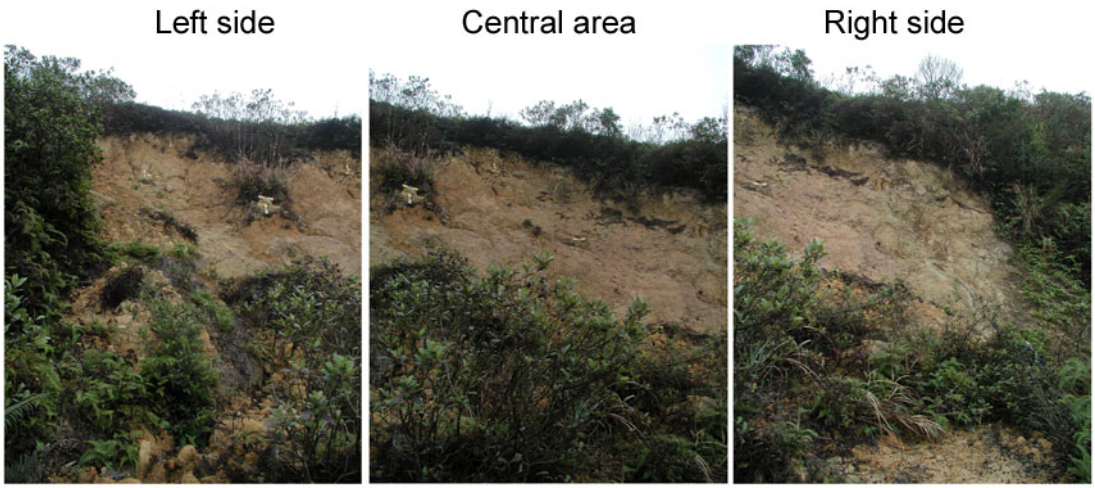

Figure 8.10 Three photos taken from the left toe of the landslide

8.3.2 First Model

The first model was built using a set of images was taken by Mr J.P. Thompson in Hong Kong. The model used existing landforms for external control with scale provided inside the landslide by four 0.6m long paper targets, each consisting of two strips of grey and white bars (Figure 8.10). Photographs inside the landslide were taken from three locations: at the two sides of the toe of the scar and one in the middle of the toe, with the camera facing three directions each time. A second set of photographs were taken traversing the ridge on the opposite side of the valley, a distance of approximately 70m. The 3D visualisation model was successful, but the

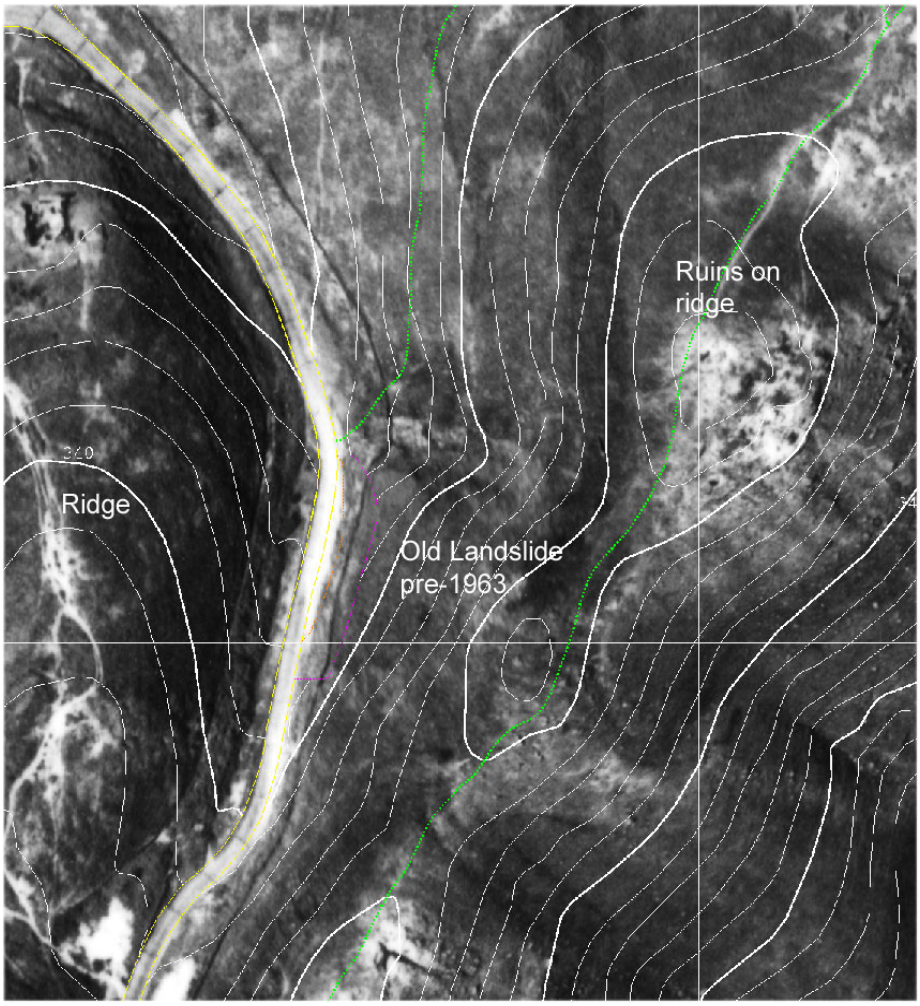

Figure 8.11 Orthophoto using 1963 aerial photograph

measurement precision was poor as the photographs had been collected using the medium compression JPEG setting of the Olympus 3030 digital camera (Table 8.1).

8.3.3 Second Model

A second set of photographs were collected in April 2002, using the same camera but saving the images in TIFF format. A laptop computer was used to download the images in the field to allow more high quality images to be obtained. The photographs were taken at many locations within the landslide, with improved coverage of the sides and rear of the failure. External control was provided by black A4 sized polystyrene mounting boards with 15cm white circular disks. These were located at the edges of landmarks on the ridge identifiable on an orthophoto (Figure 8.11) made of the 1963 aerial photography. Coordinates of the features marked by the targets were obtained to an accuracy of ±1m relative to the Hong Kong metric

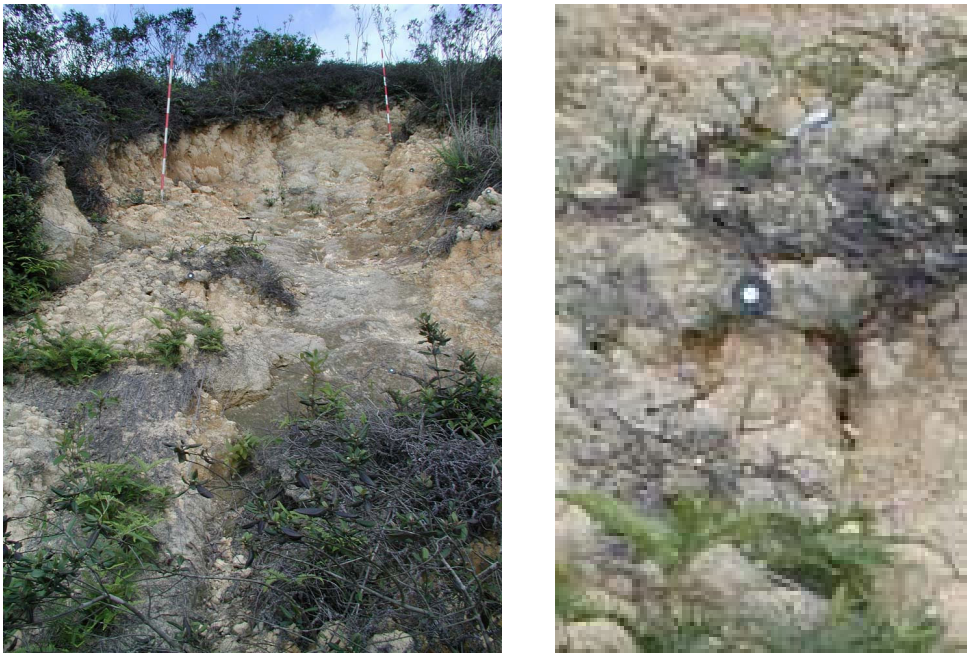

Figure 8.12 Internal control by ranging poles and adhesive disks

grid. Internal control was provided by placing forty 8mm diameter, orange self-adhesive paper targets on the sides and floor of the landslide scar. Control was passed from the external to internal networks by four ranging poles (Figure 8.12). These additional control measures improved the ground resolution and precision of the second 3D model.

8.3.4 3D Photorealistic Model

A detailed, 3D model (Figure 8.13) was constructed of the whole landslide using the first set of photographs, consisting of over 1500 points. Visualisation can be

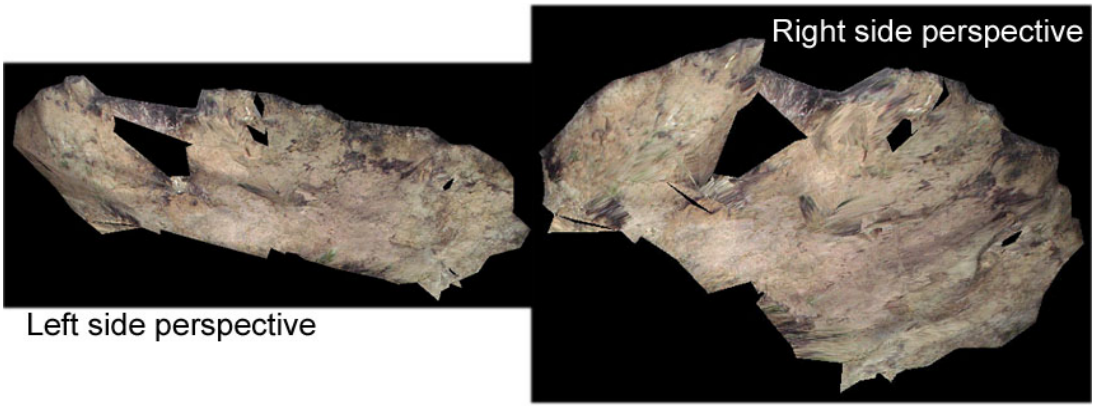

Figure 8.13 3D photo textured visualisation of the Cloudy Hill landslide

achieved by constructing a triangular network of surfaces across the model with user-selected points and applying a photo texture to each surface. The holes in the model illustrated in Figure 8.13 are due to the mound of debris in the rear centre of the scar which was not possible to model in the original set of photographs taken from the toe of the landslide. The 3D model can be rotated within PhotoModeler, or exported in a number of external 3D graphics formats.

8.3.5 Use of the Model for Interpretation

The 3D visualisation of the landslide can be extended by adding an interpretation to each surface of the model. For example, in the Cloudy Hill landslide, the sides of the scar show the soil profile and the junction with the underlying bedrock can be observed. The bedrock surfaces are subdivided into those forming the base of the pre-existing landslide, and those created by the recent failure. Applying different symbology to lines and surfaces within the model provides an alternative visualisation that is geologically and geomorphologically enhanced. The white surface on the edge of the landslide scar shown in Figure 8.14 marks the downslope extent of the soil profile that has been interpreted from the short range imagery used to build this part of the model.

Figure 8.14 Soil profile at the side of the landslide

8.4 Chapter Summary: Multi-image Photogrammetry

Multi-image photogrammetric methods were the first ones to be tried in the course of the present dissertation. The problems experienced in satisfactorily performing orientation of the early images collected for these two detailed case studies demonstrated that great care needs to be given to keeping the camera parameters stable; this is particularly true for low cost digital cameras. With care, point accuracies can be obtained in the order of one part in 1000 of the camera to target distance. This is lower than the results normally achievable with digital photogrammetry and can be attributed to the difficulties in identifying ground features of similar appearance in images obtained as widely differing scales and imaging direction.

As with conventional vertical aerial photogrammetry, the major constraint on the accuracy of the results is the choice and co- identification on the ground and on the images, of suitable ground control points. This can be made more difficult because of the lack of stereo viewing and the potentially extreme variations in view directions and scale across the image.

In 2000, the strength of the multi-image software was in the ability to build 3D visualisations such as the landslide model created for this dissertation. These facilities are increasingly being incorporated into the generally more expensive photogrammetric software. This is demonstrated by the final case study which forms Chapter 9 in this dissertation, of the landslide at Chainage 23+800 along the Pos Selim to Lojing Highway in Malaysia.

Chapter 9

CASE STUDY: LANDSLIDE AT CHAINAGE 23+800, SIMPANG PULAI – LOJING HIGHWAY, MALAYSIA

The techniques investigated in Chapters 5 to 8 have applied photogrammetric measurement and mapping regimes to small rock slopes and discrete landslide features covering areas up to approximately 2000m^2. This Chapter describes the photogrammetric and aerial photograph interpretation techniques used to carry out semi-automated geomorphological mapping on a large, deep-seated landslide in Malaysia (Figure 9.1), covering an area over 100,000m^2, and approximately 190m vertical extent. The landslide is located upslope of chainage Ch23+800 of the Simpang Pulai – Lojing Highway, a major East-West route linking the Cameron Highlands with Ipoh on the west coast. The results of this study are being used as part of on-going slope stability investigations at the site. The results described here are limited to the geomorphological mapping components of the investigation; other parts of the study cover the geological, engineering geological and geotechnical

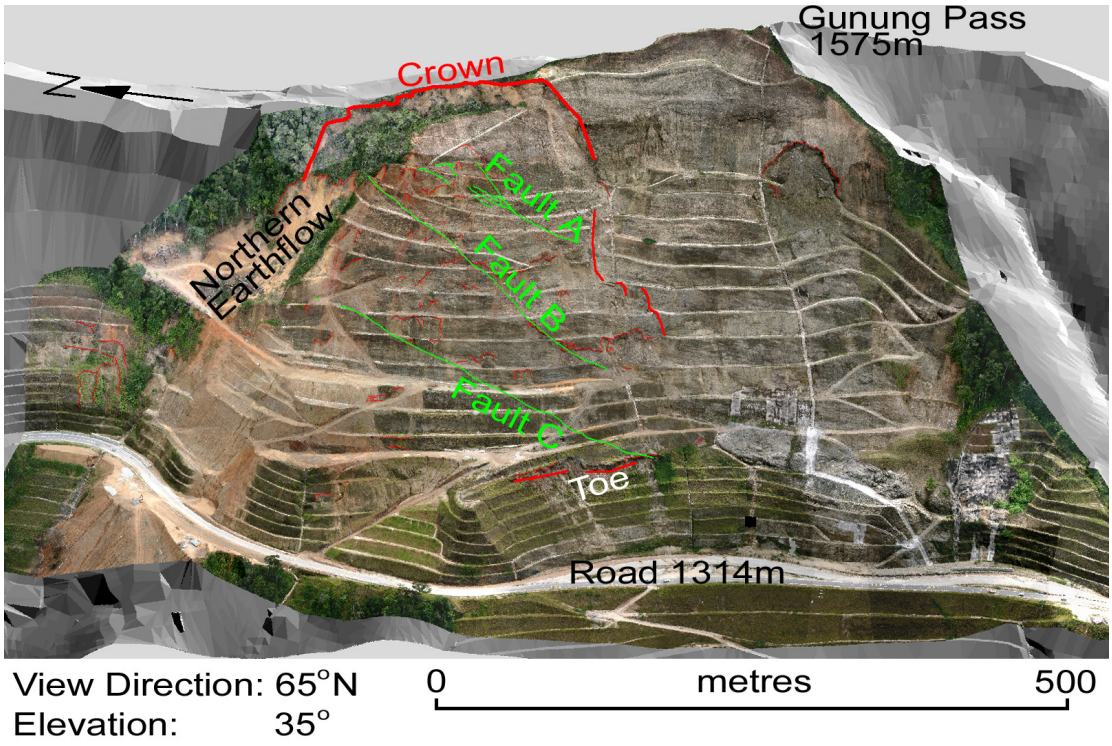

Figure 9.1 Composite oblique view of the landslide and adjacent hillside. Sun-shaded relief model with superimposed orthophoto mosaic from the helicopter-borne aerial photography.

components of the investigation and are published elsewhere (Andrew Malone Ltd., 2007). The uSMART photogrammetric system (ver. 8.51.1 to 9.03.B) was used for all the photogrammetric modelling and mapping and ER Mapper (ver. 6.3) was used for DEM analysis and the production of derivative products such as the shaded relief models. MatLab routines were written to convert the conventional 2D orthophoto products into 3D photorealistic models with a voxel (3D equivalent of a 2D pixel) size of 10cm per side.

This investigation is described in three sections:

(a) aerial photography and establishment of the photogrammetric model;
(b) morphological and geomorphological mapping; and
(c) measuring components of landslide movement and ground disturbance.

The final part of this Chapter discusses the benefits and limitations of using semi-automated photogrammetric techniques for geomorphological mapping of large landslides.

9.1 Oblique Aerial Photography and Establishing the Photogrammetric Model

9.1.1 Oblique Digital Aerial Photography

The landslide upslope of chainage Ch23+800 lies within the left half of the hillside visible in Figure 9.1; it consists of several massive blocks exhibiting a backward rotation of approximately 4º with a broadly rotational failure mode, slightly elongate downslope. Backtilting of the low gradient platform at the crest of the hill has created a depression in front of the 15m high main scarp and crown of the landslide (defined on Figure 2.12a); three upslope-facing counterscarps are present in the main body of the landslide possibly due to forward rotations of the failed mass as it moves downslope, with movement occurring along pre-existing, steeply-dipping fault planes. In order to assist in defining the complex failure mechanism, the detailed components of the landslide needed to be defined and identified, together with an assessment of the relative displacements between the various parts of the landslide.

Mapping was carried out using a block of oblique photographs taken with a calibrated Canon EOS D10 digital camera, fitted with a 28mm lens (as used for the

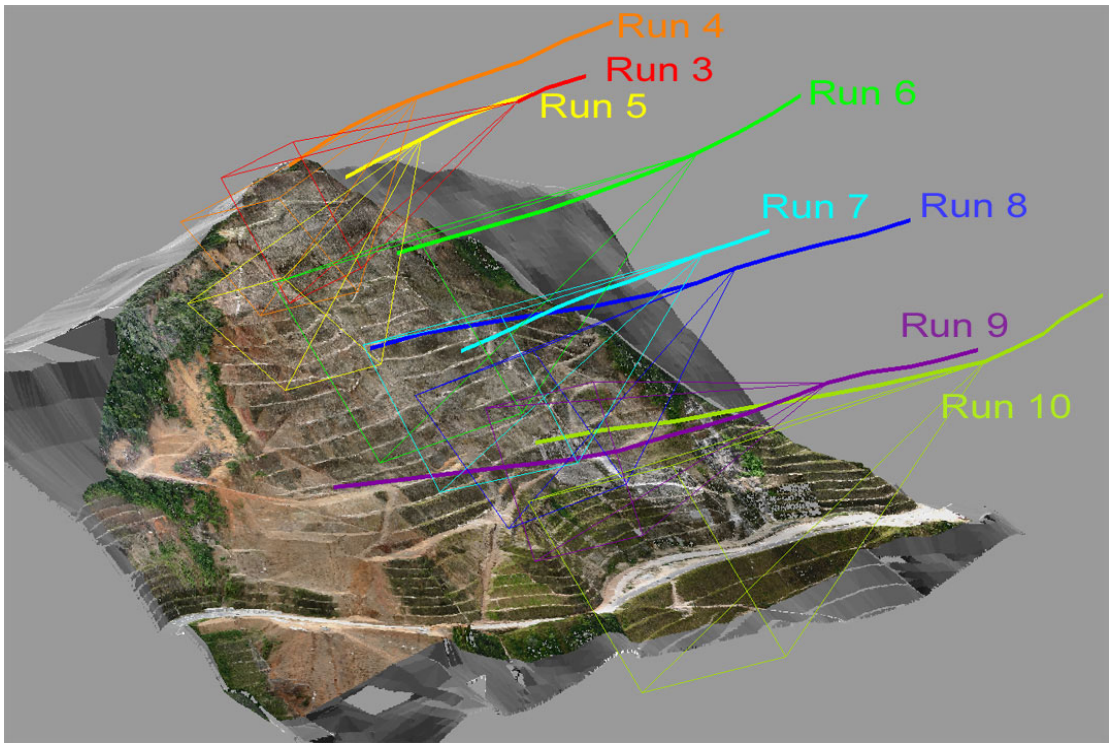

Figure 9.2 Oblique view of the eight sub-parallel flightlines used for mapping (only coverage of one frame from each run is shown).

Mountain Quarry study at Boya). Figure 9.2 shows eight flightlines taken to cover the hillside at varying ranges and altitudes; the flight direction was designed to be parallel to the general orientation of the hillside. For the mapping photography, the design object distance perpendicular to the hillside was 200m, which would give a pixel size on the ground of 5.3cm. Additional runs were obtained at greater distances (Table 9.1) to provide wider ground coverage but at a lower resolution, and one run was also obtained vertically above the crest of the hill. The runs were specified to the pilot as a flight direction and altitude, with the distance from the hillside estimated by reference to features on the ground vertically beneath the flightpath. Due to the mildly turbulent wind conditions on the day of the aerial photography, the resulting flight lines were not straight, and the object distances ranged between 220 and 330m.

The ground pixel size for the six closest runs ranged from about 6cm to 9cm, with a minimum ground coverage of approximately 180m by 120m, a stereo overlap between 60 and 75%, and airbase:object distance ratios ranging from of approximately 0.12 to 0.29 (Table 9.1).

Table 9.1 Summary of the configuration of the aerial photography

Run	Object distance (m)	Airbase (m)	Airbase:object distance ratio	Stereo overlap	Ground Pixel width (m)	Ground coverage (width, m)	Od:sdR	sdR (expected, m)
1	901	105	0.12	86 %	0.238	731	1484	0.61
2	507	80	0.16	81 %	0.134	412	1979	0.26
3 *	231	53	0.23	72 %	0.061	188	2845	0.08
4 *	219	63	0.29	65 %	0.058	178	3587	0.06
5 *	221	49	0.22	73 %	0.059	180	2721	0.08
6 *	334	66	0.20	75 %	0.088	271	2474	0.14
7 *	265	57	0.22	67 %	0.070	216	2721	0.10
8 *	266	72	0.27	68 %	0.070	216	3340	0.08
9 *	247	63	0.26	71 %	0.065	200	3216	0.08
10 *	334	78	0.23	61 %	0.088	271	2845	0.12
						Mean (mapping runs)	2970	0.09

* Runs used for mapping

Od:sdR Object distance: standard deviation of residuals (obtained from Figure 4.12)

sdR(expected) expected standard deviation of residuals

9.1.2 Ground Control and Establishing the Photogrammetric Models

Ground control for the project consisted of 20 pre-marks, 12 displacement monitoring markers and 81 points identified on an existing 3D CAD drawing.

Pre-mark control consisted of twenty boards manufactured and placed on the hillside by the local site staff (Figure 9.3); each was made from approximately 1.2m wide plywood boards painted black, with a white 0.7m diameter circle painted in the middle. Ground coordinates for these targets were obtained by the civil engineering contractor's site survey team using a Sokkia SET5E Total Station. Displacement monitoring surveys had commenced in October 2003, using the same Total Station equipment and prism reflectors, to record the changing positions of 11 markers within the landslide mass and one prism reflector located 8m south-east of the crown

of the landslide; the location of the monitoring points on the date of the aerial photography as interpolated from the movement records were also used as ground control points.

81 additional control points were identified from features visible on both the oblique aerial photographs and a 3D CAD drawing showing the edges of the man-made berms and drainage channels (referred to as the 'As Built Drawing'). Points were selected outside the area known to form the body of the main landslide. Approximately 200 additional pass points were identified on the aerial photographs across the whole site, including within the landslide area. A block bundle adjustment was performed within uSMART on the full set of control and pass points to determine the camera orientations of the photographs. Several of the control points exhibited anomalously large residuals (>1m) and were excluded from the bundle adjustment; one was overturned and others appeared to have been inadequately immobilised.

The As Built Drawing was used to identify 56 check points on ground considered not

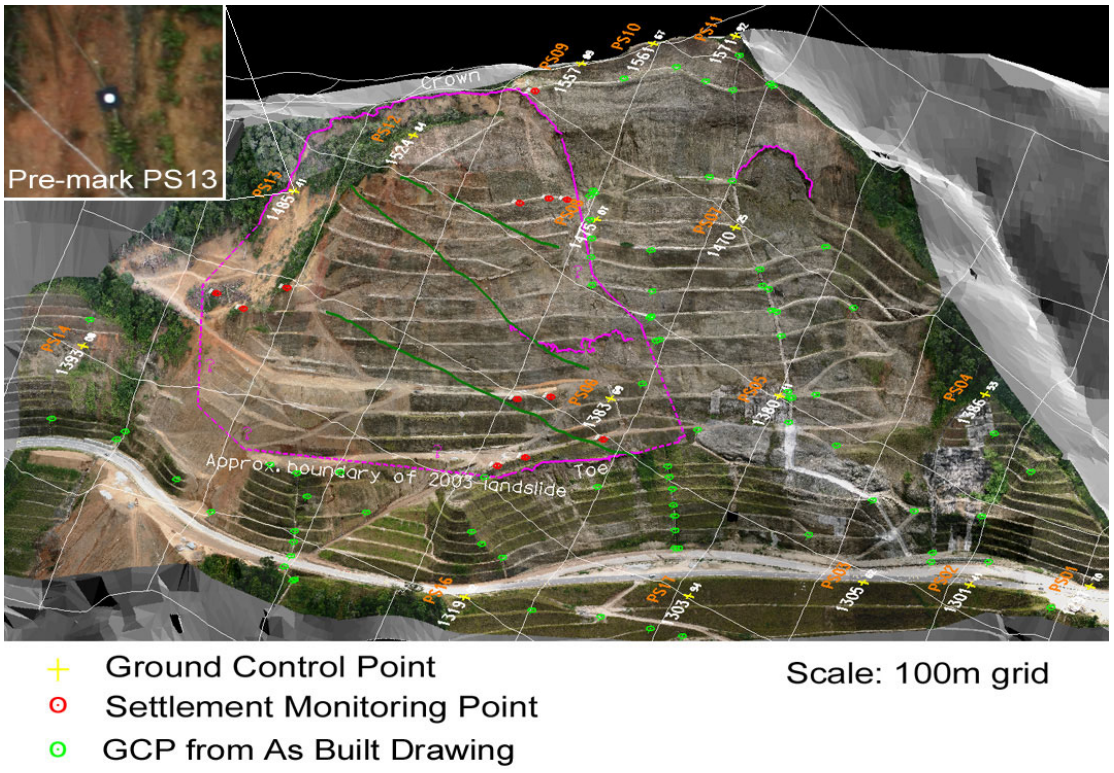

Figure 9.3 Ground control from pre-marked targets, settlement monitoring points and features extracted from the As Built Drawing located around the hillside

to have moved between 2003 and 2005 on the photogrammetric models used for the mapping. A summary of the check point results is given in Table 9.2. Features used were clearly identifiable drainage channels and angles in the berm edges.

Table 9.2 Error parameters for the check points

metres	X (Easting)	Abs(X)	Y (Northing)	Abs(Y)	Z (Elevation)	Abs(Z)	Correction vector
Mean	-0.044	0.147	-0.027	0.147	-0.018	0.179	0.323
RMSE	0.208		0.185		0.263		0.384
Minimum	-0.916	0.008	-0.414	0.006	-0.782	0.003	0.061
Maximum	0.569	0.916	0.490	0.490	0.749	0.782	0.941
Standard deviation	0.265	0.186	0.195	0.265	0.140	0.211	0.204

With a minimum variation of 0.061m and maximum variation of 0.941m for the XYZ (3D) correction vector, the root mean square error (RMSE) was 0.384m and the standard deviation 0.204m. The variations for the height component were 0.003m minimum, 0.749m maximum and an RMSE of 0.263m, standard deviation 0.140m. The values for the standard deviation of the residuals in each of the X Y and Z axes are broadly similar, which is expected as the photography was taken at an oblique elevation (Figure 9.2) rather than vertical.

Using the parameter 'object distance/standard deviation of residuals' for single pixel operations, as determined in Chapter 4.1.5 and shown in Figure 4.12, the expected accuracy in the direction of the lens axis is shown in Table 9.1. For the seven closer runs used for mapping, this varies between one part in 2474 and one part in 3587 of the object distance. Based on this ratio, the expected mean standard deviation of the residuals for the mapping runs would be 0.09m.

The values obtained as shown in Table 9.2 are larger than anticipated. At least four factors will have contributed to this:

(a) Unspecified errors in the identification of the pre-marks due to target movement and poor orientation of the pre-marks relative to the imagery;

(b) Low relative precision for some of the features identified on the As Built Drawing (e.g., eroded berm edges);
(c) Accuracy of the ground surveys used to compile the As Built Drawing and define the pre-marks (no audit of the surveys was available);
(d) Systematic error within the measurement system due to the parameters used for the terrain-following cursor; these have been described in Chapter 4.

A fifth possible factor is the low resolution in the image due to the design of the CCD array, although this is likely to be an order of magnitude smaller than the other four listed above (see Chapter 3.5.3).

9.2 Semi-automated Geomorphological Mapping

Three types of mapping were carried out across the hillside: (i) symbolic geomorphological mapping, (ii) high resolution (20cm) DEM, and (iii) landslide displacement vector mapping.

9.2.1 Geomorphological Feature Mapping

The initial process involved 3D geomorphological mapping of the landform boundaries using symbolic linework drawn within the CAD environment of the uSMART/MicroStation photogrammetric system. Figure 9.4 shows the section of the geomorphological map around the main landslide.

Mapping of terrain morphology and man-made features such as drainage channels was carried out mostly assisted by the terrain-following cursor. This was found to allow much faster mapping rates for routine line drawing, such as for the morphological lines. Additional symbology was prepared to show the locations of the convex and concave components of the upward-facing counter scarps, tension cracks and landslide debris visible on the hillside. However, the small counterscarps and tension cracks had to be mapped using visual placement of the 3D cursor in the stereo imagery, as the size of the deformed features were similar to the smallest practical correlation window, about 8 to 12 pixels across. Auto-placement was found to be unstable, and it was not possible to draw separate lines on each side of the smaller translated blocks as the terrain-following cursor averaged elevations across the kernel. Part of this instability may be due to the single pixel phase-wrapping

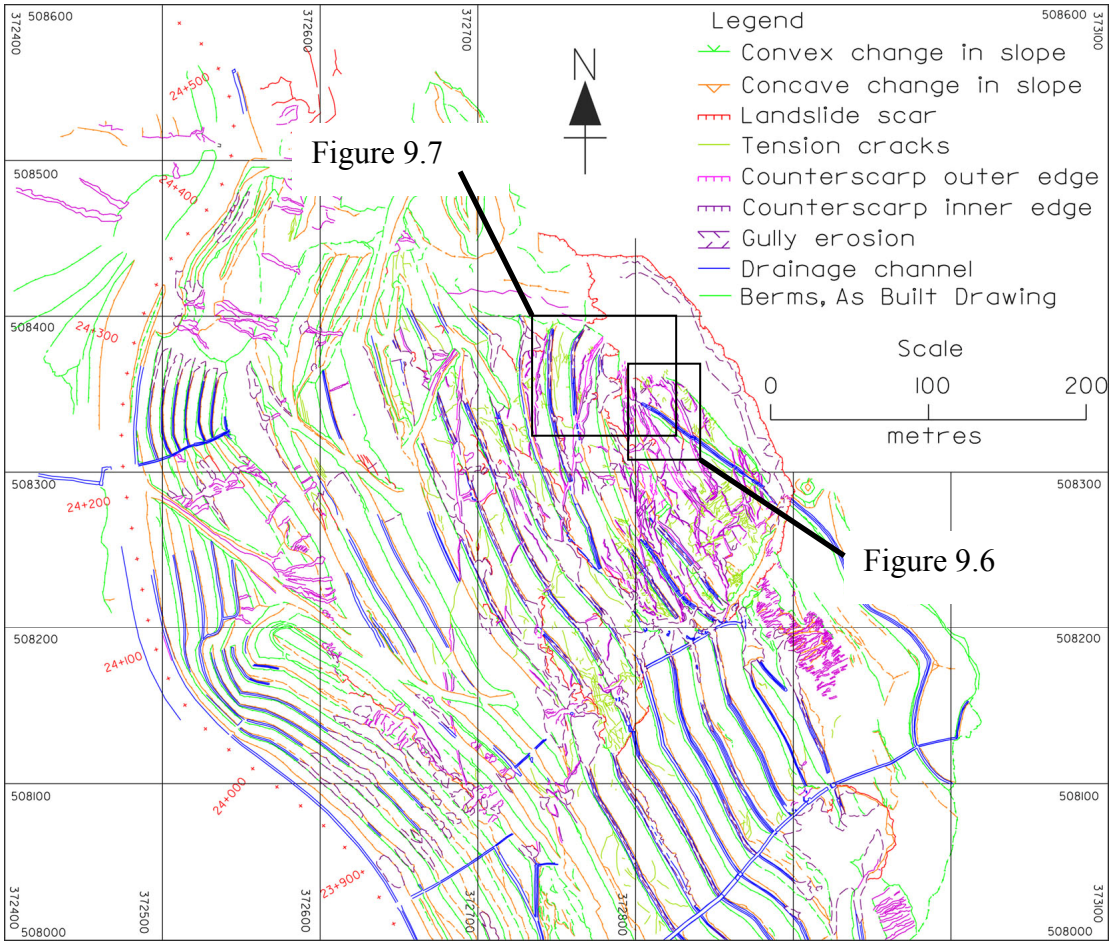

Figure 9.4 Geomorphological map of the landslide and surrounding terrain

effect described in Chapter 4, but this issue had not been identified at the date of the mapping.

A section from the upper part of the main landslide mass is shown in Figure 9.5. The complex array of tension cracks and counter scarps is clearly seen, superimposed over the oblique imagery. Mapping this complex array of landslide features would have been very difficult on the ground, and the use of oblique aerial photos under stereo viewing with interpretation-driven mapping carried out by an experienced observer is very time-efficient.

9.2.2 High Resolution DEM

USMART, similar to many GIS and photogrammetry packages, define the location of automatically-generated DEM posts by reference to an XY coordinate grid, although the angle of the grid and grid spacing can be defined differently in each

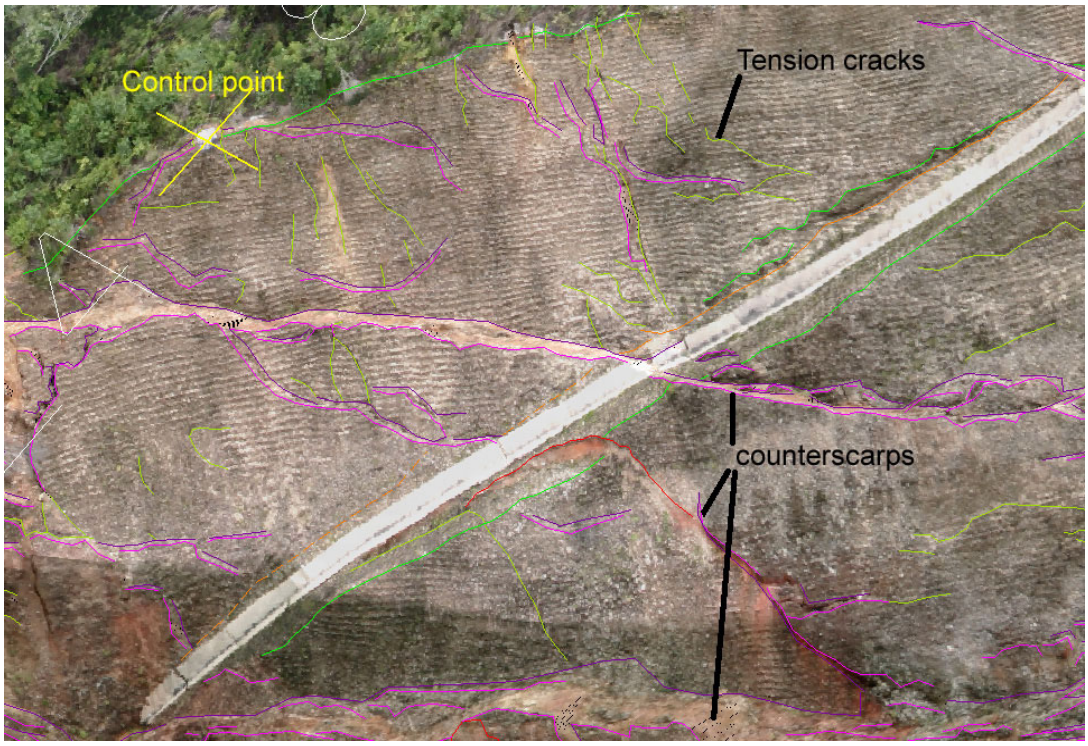

Figure 9.5 Detailed oblique view of the northern part of the 3D geomorphological map (see Figure 9.4 for location)

orthogonal axis. In the context of slope stability, the steeply sloping batters and rock faces are particularly important as these form zones of high hazard from rockfall and small landslide initiation. In addition, the hillside contains some overhanging rock faces forming the upper parts of rock falls and landslide scars. Conventional horizontally-oriented sampling distributions may not adequately record these areas, and TIN models created from the DEMs may form erroneous triangles from mis-association of adjacent DEM posts which appear to overlap in a 2D projection of the XY plane.

Consequently, the photogrammetric models were re-oriented so that the Z axis was approximately perpendicular to the average slope across the hillside. This entailed a standard seven-parameter transform involving a unit scale factor, translation to bring the origin into the centre of the study area, and finally rotations to bring a vector representing the general slope of the hillside to the negative Y axis. The transformed feature boundaries were imported as initial points in the DEM, with automated image matching used to density the DEM up to the required 0.2m resolution. Once checked and edited, the DEM was transformed back to the original coordinate system before

being imported into ER Mapper to prepare shaded relief visualisations. Two 10cm resolution orthophotos were produced, one in each of the coordinate systems.

Version 9 of the uSMART photogrammetric software, released in November 2006, also has the facility for storing and visualising laser scan cloud data for visual display in conjunction with the MicroStation CAD file. The 3D visualisations shown in this Chapter were prepared using a 3D photo-coloured point cloud containing approximately 60 million points, viewed interactively with the conventional 3D CAD linework. The point cloud was initially generated as ASCII text files containing the XYZ coordinates of points on the transformed DEM, resampled to a grid spacing of 10cm, and adding the RGB colour values from the corresponding pixel on the 10cm resolution orthophoto. To ensure that maximum coverage was included on the steeper slopes and overhangs, the DEM and orthophoto used were those from the transformed model parallel to the overall slope and orientation of the hillside.

This form of visualisation is very effective, especially for steeply-sloping terrain such as in this case study, and needs to be investigated further, but this is beyond the scope of the present dissertation. The present 3D visualisation suffers from holes in the 3D point cloud where the orientations of the triangles in the TIN are laterally extensive where the normal to the local TIN triangle is highly oblique to the normal to the plane of the transformed model. This can be corrected by creating the point cloud directly by using the TIN triangles to identify the point spacing and sampling the most appropriate image. This is a slightly different approach from the normal method of draping photo textures across the surfaces of TINs, as is available in PhotoModeler, for example, as it allows more dynamic data structures such as octrees to be accessed with the potential for more flexible viewing and faster zooming and image resizing.

Appendix B contains a CD with an animation of the landslide displacement vectors draped over the 3D photorealistic model.

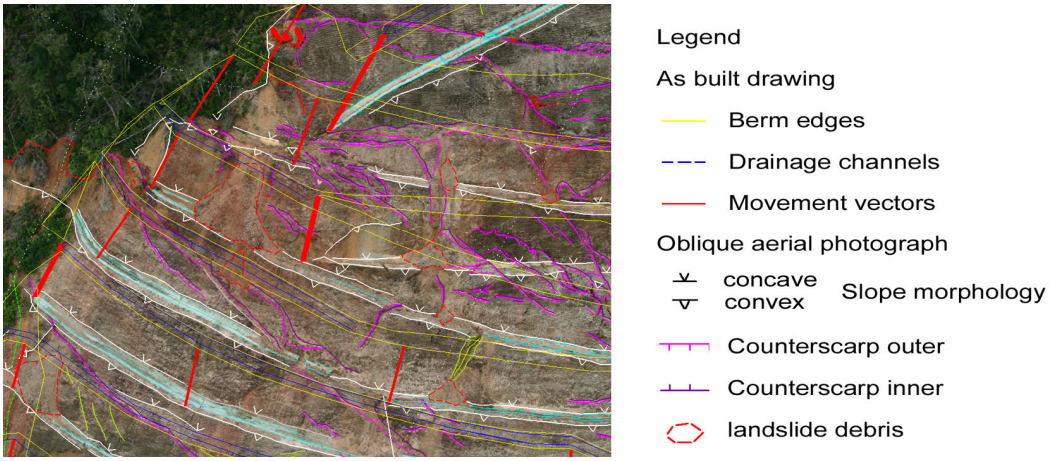

Figure 9.6 Landslide displacement vector mapping around the end of the upper sloping drain (see Figure 9.4 for location)

9.2.3 Landslide Displacement Vector Mapping

3D visualisation allows rapid comparison of the past and present ground configurations, and hence the placement of vectors showing the landslide displacement through time. The landslide displacement vectors were identified by comparing prominent features of the As Built Drawing such as the terminations and intersections of drainage channels and angular berm edges, with the same features visible in the stereo models. Figure 9.6 shows in yellow, the berm edges from the As Built Drawing and dark blue the drainage structures. The positions of the berm edges and geomorphological features as of the date of the aerial photography are also shown as interpreted from the stereo imagery. Bold red lines mark the change vectors between the two data sets; increasing line thickness represents greater confidence in the measurement. The accuracy of the displacement is not uniform in all directions; accuracies downslope and horizontally across the berms are generally higher than that parallel to the edge of the berms due to possible misidentification of the corresponding points along the berm edge. Some features, such as the downslope termination of the major sloping drain in the upper part of Figure 9.6, are clearly identified on both the As Built Drawing and the project mapping.

Over 150 displacement vectors were mapped across the landslide as shown in Figure 9.7. Also shown are the total displacement contours that help define the nature of the movement. The toe of the landslide daylights at the steep overhang located about seven berms above the road, and the movement appears to be greater along the

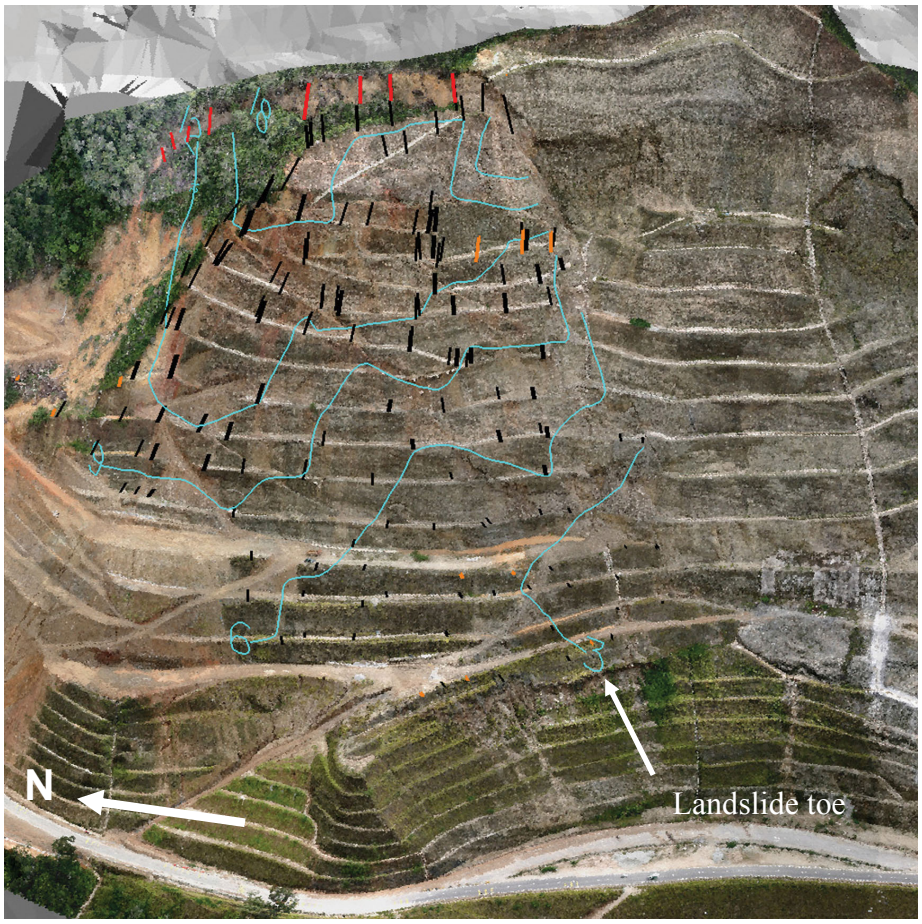

Figure 9.7 Oblique view from East of the hillside with total displacement vectors and contours (m)

northern section. The greatest movements recorded ranged from 24.5m near the crest to 3.1m near the toe.

One of the significant advantages of drawing the maps in 3D is that other view directions can be rapidly compiled. Figure 9.8 shows two cross sections of the hillside; Figure 9.8a shows the hillside as it was configured at three stages in development, including (i) pre-development, (ii) As Built Drawing stage (mid-2003), and (iii) date of the oblique aerial photography, 1st September 2005. Figure 9.8b also includes a set of normals extending from the upper end of the displacement vectors. While there is no clear centre to the distribution of normals, this is expected as the landslide mass is traversed by three major counterscarps showing some lateral displacement, and the distribution of displacement vectors suggests some translational component in the middle part of the failure surface. A circle radius 300m drawn roughly through the centre of the cloud of normals approximates the

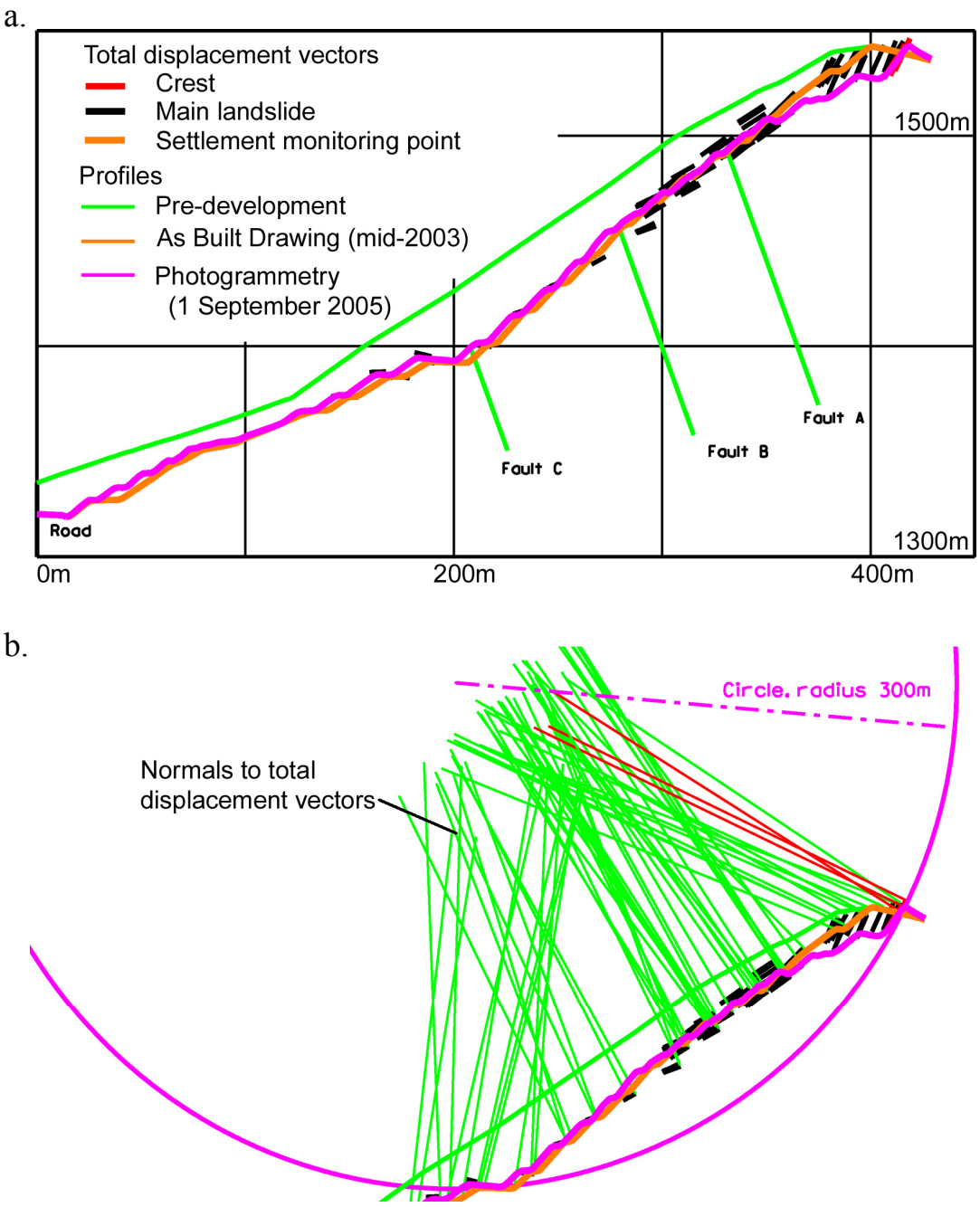

Figure 9.8 Profile view of the hillside showing a. three stages of slope development and b. normals and 300m radius circle around estimated centre of displacement vectors.

direction of the displacement vectors in the upper, middle and lowest sections of the hillside profile, and provides an estimate of the maximum depth of the probable failure surface. The translational component of downslope movement results in the intersection of the normals forming a zone extending for approximately 250m parallel to the slope surface (Figure 9.8b), which would suggest that the basal slip surface may lie at a depth of less than the 40m implied by the circle.

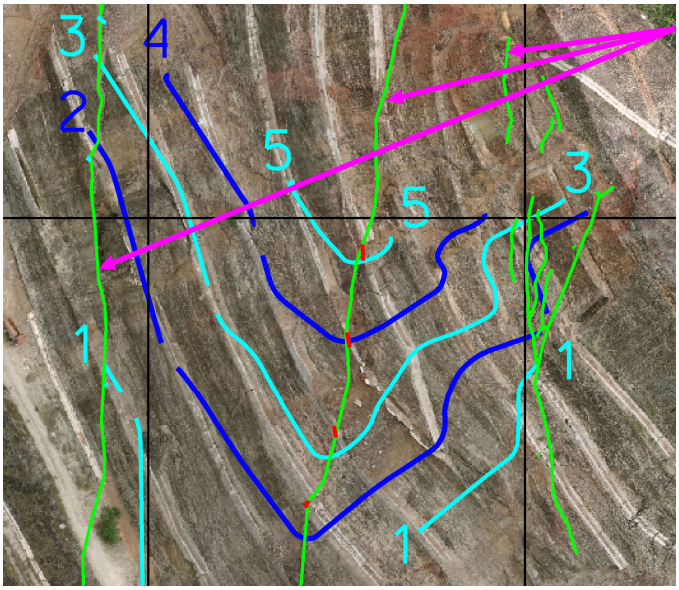

Major pre-existing faults reactivated by the landslide movement (Andrew Malone Ltd, 2007)

Red: Local displacement vectors

Blues: Contours of local counterscarp displacement (m)

Scale: 100m grid

Figure 9.9 Landslide displacement vector mapping along the three main counterscarps in the central part of the landslide

The dynamics of the landslide movement have also been indicated by the southward movement across the direction of the overall landslide displacements, as shown by the contours of local displacement shown in Figure 9.9 which follow the trend of three reactivated faults (labelled Faults A, B and C on Figure 9.1) . The magnitude of these small relative displacements is approaching that of the overall model accuracy as demonstrated by the checkpoints. However, these refer to local displacements measured within stereopairs and are therefore independent of the As Built Drawing. These short distance measurements were made by manual stereo-placement and the possible effects of the single pixel phase-wrapping artefact is not considered to have affected these results.

9.3 Results

The distribution of total displacement vectors shows a clearly radial pattern outward downslope. In addition to the subsidence at the crest, the toe areas are bulging outward, indicative of broadly rotational movement; however, the body of the landslide appears to be suffering a significant amount of internal disruption both as large scale cross-movement along pre-existing steeping-dipping faults and downslope rotational movement creating the outward displacements of the upward-facing counterscarps.

The possible error in the measurements is smaller than the displacements estimated from the comparison between the As-built survey and the photogrammetry. The smallest recorded displacement defined by photogrammetry, located near the toe of the landslide, is 3.4m, which is almost ten times greater than the RMS error established by comparison of checkpoints.

9.4 Discussion

Figures 9.6 and 9.7 demonstrate the clarity of visualisation possible with softcopy systems, allowing the operator to concentrate effort on interpretation, and with a known degree of confidence in the reliability of the measurements on which any interpretation is based. In this case, it has been possible to measure the complex array of displacements in varying directions occurring both between a known configuration at an earlier date, and the date of aerial photography, as well as locally between each pair of boundary lines across the counterscarps. 3D representation allows the spatial distribution of displacement vectors to be visualised, which can be difficult to do through ground mapping where access is time-consuming and potentially hazardous. As is usual with any form of aerial photograph interpretation (Chapter 2), the resulting maps must be subject to careful field checking to ensure the accuracy and consistency of the observations. For this project, the orthophotos and geomorphological mapping were used for extensive walk-over surveys by members of the investigation team, and contributed to the engineering geological and lithological maps accompanying the project report (Andrew Malone Ltd., 2007).

As with most forms of scientific investigation, the value of the products is only realised when the results are conveyed to decision-makers and they in turn are able to act upon it. The management guru, Peter Drucker, (et al., 1998) defines knowledge as ‘Information that changes something or somebody – either by becoming grounds for actions or by making an individual (or an institution) capable of different or more effective action.’ Large landslides can be complex entities, with potentially variable driving and resisting forces. Methods that can help the decision-makers appreciate the complexity of the landforming processes and changing landforms are extremely valuable. Softcopy technology has reached the stage where 2D and 3D photorealistic models can be constructed from comparatively low-cost camera equipment, applied directly by Earth scientists to aid their interpretation, and to produce graphic

visualisations to help portray the results of their investigations. The CD in Appendix B contains a two minute animation of the landslide displacement vectors superimposed over the 3D photorealistic model created from the 10cm resolution 3D voxel model.

9.5 Chapter Summary: Semi-automated 3D Geomorphological Mapping

This Chapter has demonstrated both the feasibility of capturing a block of oblique aerial photography using a small format, hand-held digital camera and building an oriented photogrammetric model for use by an experienced geomorphological interpreter. While the measurement accuracy is lower than that normally achieved using a large format metric camera, the accuracy was suitable for this project where the smallest landslide movement appears to be about ten times greater than the magnitude of the uncertainty in positional accuracy of the model. The flexibility of softcopy systems for small projects may allow the wider adoption of this technology, especially among Earth scientists. This flexibility is especially valuable when approaching complex slope stability problems, where steep terrain, including overhangs, may limit the ability of conventional GIS systems to handle the datasets.

Stereo visualisation of DEMs and shaded relief models can give a general impression of the terrain. However, photography generally contains more fine detail than a DEM, and measurements made directly from the stereo photography will be enhanced by the added confidence in geomorphic, hydrologic and geologic contributions to the interpretation.

Chapter 10

CONCLUSIONS AND RECOMMENDATIONS

This dissertation has investigated the application of softcopy photogrammetry to geomorphological mapping, with specific reference to mapping steeply sloping terrain prone to landsliding. Two forms of softcopy technology was covered, stereo and multi-image photogrammetry, and considered the benefits and limitations of each in regard to the issues relating to improving both the quantitative and qualitative accuracy and mapping rates. This Chapter contains (i) a summary of the findings of this research, (ii) makes recommendations for the practical application of digital photogrammetry to geomorphological applications, especially on steep terrain, and (iii) identified future directions where these investigations can be extended.

10.1 Summary of Results

Geomorphological mapping is a two-stage process of landform analysis and representation. Traditional geomorphological mapping involves delineating and classifying landforms through a combination of field study and photographic observation commonly using paper photographs viewed through mirror stereoscopes, with the results drawn by hand onto topographic base maps. In recent years, digital databases and orthophotos stored within GIS systems have been integrated into the mapping component of this workflow although most photographic interpretation is still carried out using mirror stereoscopes. Softcopy photogrammetry presents a mature technology developed for topographic mapping that is also appropriate for the task of stereoscopic observation and interpretation. Softcopy systems generally incorporate the placement of geometric entities within a CAD system, or to export digital files of these entities in standard formats, and can form an appropriate data collection front-end to further decision analysis using GIS systems. The capabilities of softcopy systems include visualisation functions that can be used to enhance specialist interpretation in geomorphology and other Earth sciences.

The major benefits of softcopy mapping are:

(a) Stereopairs of digital images and blocks of regularly spaced or uncontrolled imagery can be oriented to a coordinate system using ground control points;

(b) Landforms can be viewed in 3D if suitably constrained images are available;

(c) Coordinates of individual points can be determined and joined to form higher geometric entities and all can be viewed superimposed over the photographs, often in 3D in the stereoscopic systems;

(d) Automated and semi-automated softcopy systems use image correlation and to create high density DEMs that can be exported for further processing outside the softcopy system;

(e) Existing graphic data can be imported into the softcopy systems and visualised in conjunction with the landform and other thematic mapping.

The findings of this research are summarised in relation to the objectives stated in Chapter 1.3.1.

10.1.1 Evaluate Sources of Digital Terrain Images

Digital images imported into the softcopy systems can be obtained from scanning of existing negatives or paper photographs, or captured directly in digital cameras. Calibration of the camera format and lens distortion parameters can significantly improve the accuracy of resulting measurements, especially with low cost, small and medium format cameras. With appropriate design of the photographic sequences and camera parameters, complex terrain mapping tasks can be satisfactorily achieved using low cost photographic equipment in highly irregular terrain.

Low pass noise filtering of the source imagery improves area-based image correlation both for manual feature mapping using a terrain-following cursor and the automated measurement of DEMs.

10.1.2 Process DEMs to Identify Landforms Relevant to Slope Stability

Curvature algorithms applied to high resolution DEMs have been found suitable for the delineation of landforms that may be recent or relict landslide scars, and other morphologically distinct elements of landforms; improved results are obtained if the DEMs are smoothed with low pass filters prior to applying curvature algorithms. Raster-based curvature maps are vectorised and warped to the DEM for input and viewing within the softcopy systems. Stereoscopic viewing of the terrain in

conjunction with these curvature vectors allows an experienced observer to classify the associated landforms according to their likely genetic origins.

10.1.3 Evaluate Softcopy Technology for Practical Geomorphological Mapping Applications

The major benefits of softcopy systems in the context of geomorphological mapping applications are:

(a) Visualisation of the terrain and interactive placement of user-defined landform classificatory symbology; stereo-visualisation makes this procedure highly efficient, but it is possible to accomplish under single image viewing with multi-image softcopy systems;

(b) Stereo softcopy systems have been found to be more practical for the majority of geomorphological mapping applications where suitable (stereo-capable) imagery exists;

(c) Multi-image systems can produce good orientation results from random and highly convergent imagery but they lack the image matching capability for automatically generating high density DEMs although these can be derived manually;

(d) While planar surfaces can be adequately delineated using both stereo and multi-image softcopy techniques, this research has identified limitations in the expected accuracy achievable from using image correlating technologies to capture points on the surface of the planes; these limitations refer to the angle between the camera stations and the target, and the orientation of the target plane in relation to the lens axes.

In addition, the research has identified the presence of phase-wrapped surfaces in image correlation results that may reduce the expected accuracy of results. These image artefacts appear to be a quantisation effect due to the image correlation systems functioning at a single pixel resolution. Other related artefacts may be present when the correlation parameters are not optimised. The use of smooth planar surfaces as test targets is recommended for performance testing of the softcopy systems.

10.1.4 Develop CAD Technologies for Use in Conjunction with Softcopy Photogrammetry for the Depiction of Landforms Relevant to Slope Stability

CAD systems can be very flexible for the cartographic production of geomorphological maps with variable view perspectives, including horizontal or even upward. This is particularly valuable for steeply sloping terrain with overhanging rock faces. A technique has been developed to incorporate 3D photorealistic ground models with the CAD symbolised linework to aid visualisation and the communication of results without the aid of the softcopy system.

10.2 Recommendations for Good Practice

Softcopy photogrammetry is a flexible and valuable addition to the measurement and analysis tools available to Earth scientists, but satisfactory data collection is possible only if certain minimum requirements are met. These requirements can apply to field or laboratory conditions.

The camera or imaging system must have an adequate ground resolution to identify the features; complex shapes cannot be identified from single pixels. Pixels in the image may already be interpolated as a result of the structure of the capturing CCD, and this should be allowed for in the design of targets and ground resolution.

Consideration needs to be given to minimising the amount of geometric variation occurring within the camera system, preferring single focus over zoom lenses, and temporary or permanent fixing of moving parts of the lenses by taping or cementing.

While parallel camera axes maintain the optimum image configuration for automated image matching to function efficiently, the matching algorithms function adequately for convergent imagery. The design of image capture networks should take this into account. This is less of an issue for multi-image photogrammetry which thrives on highly convergent image networks.

Target design should take cognisance of the capabilities of the softcopy system. If high contrast target centroiding is available, the targets should be made of high contrast circles with wide borders, and oriented on the ground so as not to catch reflections from the sky.

10.3 Future Directions

This research has identified a number of areas where further investigation is required.

(a) The causes of the phase-wrapped surfaces found in high density DEMs produced by area-based image correlation routines need to be further investigated. This may become critical to the operation of some of the new forms of combined terrestrial laser scanner / digital imaging devices. This can be extended to the formulation of a set of calibration and testing procedures to ensure adequate functionality of softcopy and other software that uses image correlation functions such as terrain-following cursors within GIS packages;

(b) Area-based image correlation algorithms are often used to capture points on sloping surfaces – this may apply to vertical as well as terrestrial photogrammetry. This research has demonstrated that there are potentially severe limitations on the accuracy of these results, especially for planes oriented at large angles from the perpendicular to the lens axes of stereopairs and for moderately- to highly-convergent imagery. The limitations of these techniques should be addressed further in relation to various imaging and image correlation parameters;

(c) The present research has imported vectorised curvature maps for visualisation within the photographic stereo models. There is scope for incorporating rasters directly into such models through the application of the collinearity equations.

REFERENCES

AAMHatch (2007) *Personal Communication*, Stuart Flowers, 108 Stirling Street, Perth, Australia, 6th February 2007.

Ahmad, A. and Chandler, J.H. (1999) Photogrammetric Capabilities of the Kodak DC40, DCS420 and DCS460 Digital Cameras, *Photogrammetric Record*, Vol. 16, No. 94, pp. 601-615.

Aleotti, P. and Chowdury, R. (1999) Landslide Hazard Assessment: Summary Review and New Perspectives, *Bulletin Engineering Geology and Environment*, Vol. 58, No. 1, pp. 21-44.

Allen, S. (2004), *Personal Communication*, CEO, SmartTech, 34 Constantia Hills, Cape Town, South Africa, http://www.smarttech.co.za

Allen, S. (2007), *Personal Communication,* CEO, SmartTech.

Anderson, M.G. and Burt, T.P. (1981) Methods of Geomorphological Investigation, in *Geomorphological Techniques*, Goudie, A.S. (Ed.), George Allen and Unwin, London, pp. 3-11.

Anderson, M.G. and Richards, K.S. (Eds.) (1987) *Slope Stability: Geotechnical Engineering and Geomorphology*, John Wiley and Sons, Chichester, 648p.

Andrew Malone Ltd., (2007) *Landslide Study at Ch23+800 Simpang Pulai-Lojing Highway, Malaysia,* Andrew Malone Ltd., 50p. (Contributors: Malone, A.W., Fletcher, C.J., Hansen, A., and Hencher, S.J.)

Anon (1972) The Preparation of Maps and Plans in Terms of Engineering Geology, *Quarterly Journal of Engineering Geology,* Vol. 5, pp. 297-367.

Anon (1982) Land Surface Evaluation for Engineering Practice, *Quarterly Journal of Engineering Geology,* Vol. 15, pp. 265-316.

Ardizzone, F., Cardinalli, M., Carrara, A., Guzzetti, F. and Reichenbach, P. (2002) Impact of Mapping Errors on the Reliability of Landslide Hazard Maps, *Natural Hazards and Earth System Science*, Vol. 2, pp. 3-14.

Atkinson, K.B. (Ed.) (1996) *Close Range Photogrammetry and Machine Vision*, Whittles Publishing, Caithness, Scotland, 371p.

AutoDesk (2005) http://usa.autodesk.com/

Axelsson, P. (1999) Processing of Laser Scanner Data - Algorithms and Applications, *ISPRS Journal of Photogrammetry and Remote Sensing,* Vol. 54, No. 2-3, pp. 138-147.

Bailey, B., Collier, P., Farres, P., Inkpen, R. and Pearson, A. (2003) Comparative Assessment of Analytical and Digital Photogrammetric Methods in the Construction of DEMs of Geomorphological Forms, *Earth Surface Processes and Landforms*, Vol. 28, pp. 307-320.

Baltsavias, E.P. (1994) Test and Calibration procedures for Image Scanners, *International Archives of Photogrammetry and Remote Sensing*, Vol. 30, No. 1, pp. 163-170.

Barton, N. (1971) A Model Study of the Behaviour of Steep Excavated Rock Slopes, *Ph.D. Thesis*, University of London.

Beaumont, T.E. (1979) Remote Sensing Survey Techniques, *Journal of the Institution of Highway Engineers,* Vol. 26, No. 4, pp. 2-14.

Beerenwinkle, R., Bonjour, J-D., Hersch, R.D and Kolbl, O. (1986) Real Time Stereo Image Injection for Photogrammetric Plotting, *International Archives of Photogrammetry*, Edinburgh, Scotland, Vol. 26, No. 4, pp. 99-109.

Bentley (2005) http://www.bentley.com/en-US/

Beven, K.J. (1977) *TOPMODEL – A Physically-based Variable Contributing Model of Catchment Hydrology*, School of Geography Working Paper No. 183, University of Leeds.

Beven, K. (1997) TOPMODEL: a Critique, *Hydrological Processes*, Vol. 11, No. 9, pp. 1069-1085.

Bishop, A.W (1955) The Use of the Slip Circle in the Stability Analysis of Slopes, *Geotechnique*, Vol. 5, No. 1, pp. 7-17.

Bjerrum, J. (1967) Progressive Failure in Slopes of Overconsolidated Plastic Clay and Clay Shales, *Journal of Soil Mechanics and Foundation Engineering, American Society of Civil Engineers,* Vol. 93, pp. 1-49.

Bonham-Carter, G.F. (1994) *Geographic Information Systems for Geoscientists: Modelling with GIS*, Pergamon, Kidlington (Oxfordshire, UK).

Bosi, C. (1978) Considerazioni e Proposte Metodologiche Sulla Elaborazione di Carte di Stabilita, *Geologia Applicata e Idrogeologia,* Vol. 13, pp. 245-281.

Brabb, E.E. (1995) The San Mateo County GIS Project for Predicting the Consequences of Hazardous Geologic Processes, in *Geographic information Systems in Assessing Natural Hazards*, Carrara, A. and Guzzetti, F., (Eds.) Kluwer Academic Publishers, Dordrecht, the Netherlands, pp. 299-334.

Brabb, E.E. and Harrod, B.L. (Eds.) (1989) *Landslides: Extent and Economic Significance*, Balkema, Rotterdam, 385p.

Brabb, E.E., Pampeyan, E.H. and Bonilla, M.G. (1972) Landslide Susceptibility in San Mateo County, California, *U.S. Geological Survey Miscellaneous Field Studies Map, MF360, Scale 1:62,500*.

Brecher, H.H. (1986) Surface Velocity Determination on Large Polar Glaciers by Aerial Photogrammetry, *Annals of Glaciology*, Vol. 8, pp. 22-26.

Brecher, H.H. and Thompson, L.G. (1993) Measurement of the Retreat of the Qori Kalis Glacier in the Tropical Andes of Peru by Terrestrial Photogrammetry, *Photogrammetric Engineering and Remote Sensing*, Vol. 59, No. 6, pp. 1017-1022.

Bromhead, E.N. (2000) *The Stability of Slopes*, Taylor and Francis, 411p.

Brunsden, D., Doornkamp, J.C., Fookes, P.G., Jones, D.K.C. and Kelly, J.M.H. (1975) Large Scale Geomorphological Mapping and Highway Engineering Design, *Quarterly Journal of Engineering Geology,* Vol. 8, pp. 227-253.

Burrough, P.A. and McDonnell, R. (1998) *Principles of Geographical information Systems*, Oxford University Press, Oxford , UK, 333p.

Butler, J.B., Lane, S.N. and Chandler, J.H. (1998) Assessment of DEM Quality Characterising Surface Roughness Using Close Range Digital Photogrammetry, *Photogrammetric Record*, Vol. 16, No. 92, pp. 271-291.

Butler, J.B., Lane, S.N., Chandler, J.H. and Parfiri, E. (2002) Through-water Close Range Digital Photogrammetry in Flume and Field Environments, *Photogrammetric record*, Vol. 17, No. 99, pp. 419-439.

Canon (2004), http://www.canon.com

Carbonneau, P.E., Lane, S.N. and Bergeron, N.E. (2003) Cost-effective Non-metric Close-range Digital Photogrammetry and its Application to a Study of Coarse Gravel River Beds, *International Journal of Remote Sensing*, Vol. 24, No. 14, pp. 2837-2854.

Carrara, A., Cardinali, M. and Guzzetti, F. (1992) Uncertainty in Assessing Landslide Hazard and Risk, *ITC Journal*, Vol. 1992-2, pp. 172-183.

Carrara, A., Cardinali, M., Guzzetti, F. and Richenbach, P. (1995) GIS Technology in Mapping Landslide Hazard, in *Geographic Information Systems in Assessing*

Natural Hazards, Carrara, A. and Guzzetti, F., (Eds.), Kluwer Academic Publishers, Dordrecht, the Netherlands, pp. 135-175.

Carter, J.R. (1992) The Effect of Data Precision on Calculation of Slope and Aspect Using Gridded DEMs, *Cartographia,* Vol. 29, No. 1, pp. 22-34.

Castleman, K.R. (1996) *Digital Image Processing*, Prentice Hall, New Jersey, 667p.

Chandler, J.H. (1989) The Acquisition of Spatial Data from Archival Photographs and Their Application to Geomorphology, *PhD Thesis*, City University, London,

Chandler, J.H. (1999) Effective Application of Automated Digital Photogrammetry for Geomorphological Research, *Earth Surface Processes and Landforms*, Vol. 24, No. 1, pp. 51-63.

Chandler, J.H. (2001) Terrain Measurement Using Automated Digital Photogrammetry, in *Land Surface Evaluation for Engineering Practice*, Griffiths, J.S. (Ed.), Geological Society Engineering Geology Special Publication No. 18, Geological Society Publishing House, Bath, UK, pp. 13-18.

Chandler, J.H., Clark, J.S., Cooper, M.A.R. and Stirling, D.M. (1987) Analytical Photogrammetry Applied to Nepalese Slope Morphology, *Photogrammetric Record*, Vol. 12, pp. 443-458.

Chandler, J.H. and Cooper, M.A.R. (1989) The Extraction of Positional Data from Historical Photographs and their Application to Geomorphology, *Photogrammetric Record,* Vol. 13, No. 78, pp. 69-78.

Chandler, J.H., Cooper, M.A.R., and Robson, S. (1989) Analytical Aspects of Small Format Surveys Using Oblique Aerial Photography, *The Journal of Photographic Science*, Vol. 37, pp. 235-240.

Chandler, J.H. and Moore, R. (1989) Analytical Photogrammetry: a Method for Monitoring Slope Instability, *Quarterly Journal of Engineering Geology*, Vol. 22, No. 2, pp. 97-110.

Chandler, J.H. and Brunsden, D. (1995) Steady State Behaviour of the Black Ven Mudslide - the Application of Archival Analytical Photogrammetry to Studies of Landform Change, *Earth Surface Processes and Landforms,* Vol. 20, No. 3, pp. 255-275.

Chandler, J.H., Shiono, K., Rameshwaren, P., and Lane, S.N. (2001) Measuring Flume Surfaces for Hydraulic Research Using a Kodak DCS460, *Photogrammetric Record*, Vol. 17, No. 97, pp. 39-61.

Chandler, J.H., Buffin-Belanger, T., Rice, S., Reid, I, and Graham, D.J. (2003) The Accuracy of a River Bed Moulding/Casting System and the Effectiveness of a Low-cost Camera for Recording River Bed Fabric, *Photogrammetric Record*, Vol. 18, No. 103, pp. 209-223.

Chandler, J.H., Fryer, J.G. and Jack, A.(2005) Metric Capabilities of Low-cost Digital Cameras for Close Range Surface Measurement, *Photogrammetric Record*, Vol. 20, No. 109, pp 12-26.

Christian C.S. and Stewart, G.A. (1968) Methodology of Integrated Surveys. *Proceedings of Conference on Aerial Surveys and Integrated Studies*, Toulouse, UNESCO, pp. 233-280.

Chorley, R.J. (1962) Geomorphology and General Systems Theory, *U.S. Geological Survey Professional Paper,* Vol. 500-B, pp. 1-10.

Chorley, R.J. (1966) The Application of Statistical Methods to Geomorphology, in *Essays in Geomorphology*, Dury, G.H. (Ed.), Heinemann, London, pp. 275-387.

Chorley, R.J. and Kennedy, B.A. (1971) *Physical Geography: a Systems Approach*, Prentice-Hall, London, 370p.

Chowdhury, R.N. (1978) *Slope Analysis*, Elsevier, New York, 423p.

Collin, R.L. and Chisholm, N.W.T. (1991) Geomorphological Photogrammetry, *Photogrammetric Record,* Vol. 13, No. 78, pp. 845-854.

Collins, S.H. and Moon, G.C., (1979) Stereometric Measurement of Streambank Erosion, *Photogrammetric Engineering and Remote Sensing*, Vol. 45, No. 2, pp. 183-190.

Cooke, R.U. and Doornkamp, J.C. (1974) *Geomorphology in Environmental Management*, Clarendon Press, Oxford, 413p.

Cooper, M.A.R. (1998) Datums, Coordinates and Differences, in *Landform Monitoring, Modelling and Analysis*, Lane, S.N., Richards, K.S. and Chandler, J.H. (Eds.), John Wiley and Sons, Chichester, pp. 21-35.

Cooper, M.A.R. and Robson, S. (1996) Theory of Close Range Photogrammetry, in *Close Range Photogrammetry and Machine Vision*, Atkinson, E.B. (Ed.), Whittles Publishing, Caithness, pp. 9-51.

Cotecchia, V. (1978) Systematic Reconnaissance Mapping and Registration of Slope Movement, *International Association of Engineering Geology, Bulletin,* Vol. 17, pp. 5-37.

Crofts, R.S. (1981) Mapping Techniques in Geomorphology, in *Geomorphological Techniques*, Goudie, A.S. (Ed.), pp. 66-75.

Crozier, M.J. (1973) Techniques for the Morphometric Analysis of Landslips, *Zeitscrift für Geomorphologie,* Vol. 17, pp. 78-101.

Cruden, D.M. and Varnes, D.J. (1996) Landslide Types and Processes, in *Landslides: Investigation and Mitigation*, Turner, A.K. and Schuster, R.L. (Eds.), Special Report 247, National Academy Press, Washington, D.C., pp. 36-75.

Dallas, R.W.A. (1996) Architectural and Archaeological Photogrammetry, in Atkinson, K.B. (Ed.) *Close Range Photogrammetry and Machine Vision*, Whittles Publishing, Caithness, Ch. 10, pp. 283-302.

Dalrymple, J.B., Blong, R.J. and Conacher, A.J. (1968) A Hypothetical Nine-Unit Land Surface Model, *Zeiscrift für Geomorphologie,* Vol. 12, pp. 60-76.

Damjanovski, V. (2000) *CCTV*, Butterworth Heinemann, Boston, 385p.

Davis, W.M. (1899) The Geographical Cycle, *Geographical Journal*, Vol. 14, pp. 481-504.

Darwin, C.R. (1859) *The Origin of Species By Means of Natural Selection; or, the Preservation of Favoured Races in the Struggle for Life*, John Murray, London.

Dearman, W.R. (1991) *Engineering Geological Mapping*, Butterworth-Heinemann, Boston, MA, 387p.

de Graaff, L.W.S., de Jong, M.G.G., Rupke, J. and Verhofstad, J. (1987) A Geomorphological Mapping System at Scale 1:10,000 for Mountainous Areas, *Zeiscrift für Geomorphologie N. F.,* Vol. 31, No. 2, pp. 229-242.

Demek, J. (Ed.) (1972) *Manual of Detailed Geomorphological Mapping*, Academia, Prague.

Demek , J. and Embleton, C.E. (1978) *Guide to Medium-Scale Geomorphological Mapping*, International Geographical Union, Stuttgart.

Dikau, R. (1989) The Application of a Digital Relief Model to Landform Analysis in Geomorphology, in *Three Dimensional Application in Geographic Information Systems*, Raper, J. (Ed.), Taylor and Francis, London, pp. 51-77.

Dikau, R., Cavallin, A. and Jäger, S. (1996) Databases and GIS for Landslide Research in Europe, *Geomorphology*, Vol. 15, pp. 227-239.

Dissart, O. and Jamet, O. (1995) 3D Reconstruction of Buildings from Stereo-images using Both Monocular Analysis and Stereomatching: an Assessment within the Context of Cartographic Production, *Proceedings of the Society of Photo-Optical Instrument Engineers*, Vol. 2486, pp. 255-266.

Dixon, L.F.J, Barker, R., Bray, M., Farres, P., Hooke, J., Inkpen, R., Merel, A., Payne, D. and Shelford, A. (1998) Analytical Photogrammetry for Geomorphological Research, in *Landform Monitoring, Modelling and Analysis*, Lane, S.N, Richards, K.S. and Chandler, J.H. (Eds.), John Wiley and Sons, Chichester, Chapter 4, pp. 63-94.

DPReview (2004) http://dpreview.com/

Drennon, C.B. and Schleining, W.G. (1975) Landslide Hazard Mapping on a Shoestring, *Proceedings of the American Society of Civil Engineers, Survey and Mapping Division,* Vol. SU1, pp. 107-114.

Drucker, P.F., Garvin, D., Leonard, D. and Straus, S. (1998) *Harvard Business Review on Knowledge Management,* Harvard College, 223p.

Duran, J. and Grant, G.E. (2000) Shallow Landslide Delineation for Steep Forest Watersheds Based on Topographic Attributes and Probability Analysis, in *Terrain Analysis: Principles and Applications*, Wilson, J.P. and Gallant, J.C. (Eds.), John Wiley and Sons, Chichester, pp. 311-329.

Elfick, M.H., Fryer, J.G., Brinker, R.C. and Wolf, P.R. (1994) *Elementary* Surveying, 9th Edn., Harper Collins, London.

EOS (2003) PhotoModeler Pro 5 User Manual, EOS Systems Inc., Vancouver, 488p. URL: http://www.photomodeler.com/index.htm

ESRI (2005) http://esri.com/

ER Mapper (2005) http://ermapper.com/

Evans, I.S. (1972) General Geomorphometry, Derivatives of Altitude, and Descriptive Statistics, in *Spatial Analysis in Geomorphology*, Chorley, R.J. (Ed.), Methuen and Co., London, pp. 17-90.

Evans, I.S. (1975) The Effect of Resolution on Gradients Calculated from an Altitude Matrix, *Report 3 on Grant DA-ERO-591-73-G0040, Statistical Characterisation of Altitude Matrices by Computer*, Department of Geography, University of Durham, 24p.

Evans, I.S. (1979) *An Integrated System of Terrain Analysis and Slope Mapping, Final Report (Report 6) on Grant DA-ERO-591-73-G0040*, Department of Geography, University of Durham.

Evans, I.S. (1980) An Integrated System of Terrain Analysis and Slope Mapping, *Zeitschrift fur Geomorphologie, Supp. Bd.,* Vol. 36, pp. 274-295.

Evans, I. (1981) General Geomorphometry, in *Geomorphological Techniques*, Goudie, A.S. (Ed.), pp. 31-37.

Evans, I.S. (1998) What Do Terrain Statistics Really Mean? In *Landform Monitoring, Modelling and Analysis*, Lane, S.N., Richards, K.S. and Chandler, J.H. (Eds.), John Wiley and Sons, Chichester, pp. 119-138.

Evans, N.C. (1998) The Natural Terrain Landslide Study, in *Slope Engineering in Hong Kong*, Li, K.S., Kay, J.N. and Ho, K.K.S. (Eds.), Balkema, Rotterdam, pp. 137-144.

Evans, N.C., Huang, S.W. and King, J.P. (1999) The Natural Terrain Landslide Study, Phases I and II, *GEO Report* No. 73, Geotechnical Engineering Office, Hong Kong SAR, 128p. plus 2 drgs.

Felicísimo, A.M. (1994) Parametric Statistical Method for Error Detection in Digital Elevation Models, *ISPRS Journal of Photogrammetry and Remote Sensing,* Vol. 49, No. 4, pp. 29-33.

Fellinius, W. (1927) *Erdstatische Berechnungen mit Reibung und Kohasion*, Ernst, Berlin.

Filin, S. and Doytsher, Y. (1998) Estimating Accuracy of Photogrammetric Data - Mechanisms and Implementation, *Journal of Surveying Engineering-ASCE,* Vol. 124, No. 4, pp. 156-170.

Finsterwalder, S. (1897) Der Vernagtferner, *Wissenschafliche Erganzungshefte zur Zeitscrift der Deutschen und Osterreichen Alpenvereins*, Gratz, Vol. 1, pp. 1-96, [quoted in Chandler J.H. and Moore, R. (1989)]

Florinsky, I.V. (1996) Quantitative Topographic Method of Fault Morphology Recognition, *Geomorphology,* vol. 16, pp. 103-119.

Florinsky, I.V. (1998) Accuracy of Local Topographic Variables Derived from Digital Elevation Models, *International Journal of Geographical Information Science,* Vol. 12, pp. 47-61.

Florinsky, I.V., Eilers, R.G., Manning, G. and Fuller, L.G. (2002) Prediction of Soil Properties by Digital Terrain Modelling, *Environmental Modelling and Software,* Vol. 17, pp. 295-311.

Fookes, P.G., Dale, S.G. and Land, J.M. (1991) Some Observations on a Comparative Aerial Photography Interpretation of a Landslipped Area, *Quarterly Journal of Engineering Geology*, Vol. 24, pp. 249-265.

Förstner, W., Wrobel, B., Paderes, F., Craig, R, Fraser, C. and Dolloff, J. (2004) Analytical Photogrammetric Operations, in *Manual of Photogrammetry, ASPRS,* 5th Edn., McGlone, J.C. (Ed.), pp. 763-948.

Fox, A.J. and Gooch, M.J. (2001) Automatic DEM Generation for Antarctic Terrain *Photogrammetric Record*, Vol. 17, No. 98, pp 275-290.

Fraser, C.S., (1983) Photogrammetric Monitoring of Turtle Mountain: a Feasibility Study, *Photogrammetric Engineering and Remote Sensing*, Vol. 49, pp. 1551-1559.

Fraser, C.S. (1997) Digital Camera Self-calibration *ISPRS Journal of Photogrammetry and Remote Sensing*, Vol. 52, pp. 149-159.

Fraser, C.S. (1998) Some Thoughts on the Emergence of Digital Close Range Photogrammetry, *Photogrammetric Record*, Vol. 16, No. 91, pp. 37-50.

Fraser, C.S. and Edmunson, K.L. (2000) Design and Implementation of a Computational Processing System for Off-line Digital Close-range Photogrammetry, *ISPRS Journal of Photogrammetry and Remote Sensing*, Vol. 55, No. 2, pp. 94-104.

Fraser, C.S. and Gruendig, L. (1985) The Analysis of Photogrammetric Deformation Measurements on Turtle Mountain, *Photogrammetric Engineering and Remote Sensing*, Vol. 51, No. 2, pp. 207-216.

Fraser, C.S. and Stoliker, P.C. (1983) Deformation Monitoring of a Landslide Area by High-precision Photogrammetry, Presented Paper, *FIG XVII International Congress*, Sofia, Bulgaria, June 19-28.

Fraser, C.S., Shortis, M.R. and Ganci, G. (1995) Multi-sensor System Calibration, *Proceedings of the Videometrics VI Conference SPIE,* Vol. 2598, Philadelphia, 25-27 Oct. 1992, pp. 2-18.

French, J.R. (2003) Airborne LiDAR in Support of Geomorphological and Hydraulic Modelling, *Earth Surface Processes and Landforms*, Vol. 28, No. 3, pp. 321-335.

Fryer, J.G. (1986) Distortion in a Zoom Lens, *Australian Journal of Geodesy, Photogrammetry and Surveying*, Vol. 44, pp 49-59.

Fryer, J.G. (1996) Camera Calibration, in *Close Range Photogrammetry and Machine Vision*, Atkinson, K.B. (Ed.), Whittles Publishing, Caithness, Scotland, pp. 156-179.

Fryer, J.G. and Brown, D.C. (1986) Lens Distortion for Close-range Photogrammetry, *Photogrammetric Engineering and Remote Sensing*, Vol. 52, No. 1, pp. 51-58.

Fryer, J.G. and Mitchell, H.L. (1987) Radial Distortion and Close Range Stereo-photogrammetry, *Australian Journal of Geodesy, Photogrammetry and Surveying*, Vol. 46/47, pp. 123-138.

Fryer, J.G., Chandler, J.H. and Cooper, M.A.R. (1994) On the Accuracy of Heighting from Aerial Photographs and Maps - Implications to Process Modellers, *Earth Surface Processes and Landforms,* Vol. 19, No. 6, pp. 577-583.

Fuji Photo Film Co. Ltd. (2001) *Super CCD* (accessed 17 January 2001). http://www.fujifilm.com/about/technology/super_ccd/index.html.

Gabet, E.J., Burbank, D.W., Putkonen, J.K., Pratt-Sitaula, B.A. and Ojha, T. (2004) Rainfall Thresholds for Landsliding in the Himalayas of Nepal, *Geomorphology*, Vol. 63, pp. 131-143.

Gabet, E.J. and Mudd, S.M. (2006) The Mobilization of Debris Flows from Shallow Landslides, *Geomorphology*, Vol. 74, pp. 207-218.

Gagnon, P.A., Agnard, J.P., Nolette, C. and Boulianne, C. (1990) A Microcomputer-based General Photogrammetric System, *Photogrammetric Engineering and Remote Sensing*, Vol. 56, pp. 623-625.

Gao, J. (1992) Modeling Landslide Susceptibility from a DTM in Nelson County, Virginia: a Remote Sensing - GIS Approach, *Ph.D. Thesis*, University of Georgia.

Gao, J. (1993) Identification of Topographic Settings Conducive to Landsliding from a DEM in Nelson County, Virginia, USA, *Earth Surface Processes and Landforms,* Vol. 18, No. 7, pp. 579-591.

Gao, J. (1997) Resolution and Accuracy of Terrain Representation By Grid DEMs at a Micro-scale, *International Journal of Geographical Information Science,* Vol. 11, No. 2, pp. 199-212.

Gao, J. (1998) Impact of Sampling Intervals on the Reliability of Topographic Variables Mapped from Grid DEMs at a Micro-Scale, *International Journal of Geographical Information Science,* Vol. 12, No. 8, pp. 875-890.

Garner, H.F. (1974) *The Origin of Landscapes: a Synthesis of Geomorphology*, Oxford University Press, New York.

Gauss, C.F. (1827) Disquisitiones Generales Circa Area Superficies Curvas, *Gott. Gel. Anz.,* Vol. 177, pp. S1761-S1768. [English translation available as Morehead, J.C. and Hiltebeitel, A.M. (translators) (1902) *General Investigations of Curved Surfaces of 1827 and 1825*, The Princeton University Library, 126p.]

Ghosh, S.K. (1988) *Analytical Photogrammetry*, 2nd Edn., Pergamon, New York, 308p.

Gilewska, S. (1976) Different Methods of Showing Relief on Detailed Geomorphological Maps, *Zeiscrift für Geomorphologie*, Vol. 11, No. 4, pp. 481-490.

Gooch, M. and Chandler, J. (1998) Optimization of Strategy Parameters used in Automated Digital Elevation Model Generation, *International Archives of Photogrammetry and Remote Sensing*, Vol. 32, No. 2, pp. 88-95.

Gooch, M.J., Chandler, J.H. and Stojic, M. (1999) Accuracy Assessment of Digital Elevation Models Generated using the ERDAS Imagine OrthoMAX Digital Photogrammetric System, *Photogrammetric Record,* Vol. 16, No. 93, pp. 519-531.

Gooch, M.J. and Chandler, J.H (2001) Failure Prediction in Automatically Generated Digital Elevation Models, *Computers and Geosciences*, Vol. 27, pp. 913-920.

Goodrich, D.C. (1982) A Simple 35-mm SLR Photogrammetric System for Glacier Measurements, *Photogrammetric Engineering and Remote Sensing*, Vol. 48, No. 9, pp. 1477-1485.

Graham, R. and Koh, A. (2002) *Digital Aerial Survey: Theory and Practice*, CRC Press/Whittles Publishing, Boca Raton, Fl., 248p.

Grainger, P. and Kalaugher, P.G. (1987) Intermittent Surging Movements of a Coastal Landslide *Earth Surface Processes and Landforms*, Vol. 12, No. 6, pp. 597-603.

Granshaw, S.I., (1980) Bundle Adjustment Methods in Engineering Photogrammetry, *Photogrammetric Record*, 10, No. 56, pp. 181-207.

Griffiths, J. S. (Ed.) (2001) *Land Surface Evaluation for Engineering Practice*, Geological Society, London, Bath, U.K.

Griffiths, J.S. and Edwards, R.J.G. (2001) The Development of Land Surface Evaluation for Engineering Practice, in *Land Surface Evaluation for Engineering Practice*, Griffiths, J.S. (Ed.), Geological Society Engineering Geology Special Publication No. 18, Geological Society, London, Bath, pp. 3-9.

Griffiths, J.S. and Hearn, G.J. (1990) Engineering Geomorphology: a UK Perspective, *Bulletin of the International Association of Engineering Geology,* Vol. 42, pp. 39-44.

Gruen, A. and Baltsavias, E.P. (1988) Geometrically Constrained Multiphoto Matching, *Photogrammetric Engineering and Remote Sensing,* Vol. 54, No. 4, pp. 633-641.

Grussenmeyer, P., Hanke, K. and Streilein, A. (2002) Architectural Photogrammetry, in *Digital Photogrammetry*, Kasser, M. and Egels, Y. (Eds.), Taylor and Francis, London, pp. 300-339.

Guth, P.L. (1995) Slope and Aspect Calculations on Gridded Digital Elevation Models: Examples from a Geomorphometric Toolbox for Personal Computers, *Zeiscrift für Geomorphologie N.F., Supp. Bd.,* Vol. 101, pp. 31-52.

Guzzetti, F., Cardinali, M. and Reichenbach, P. (1994) The AVI Project: a Bibliographical and Archive Inventory of Landslides and Floods in Italy, *Environmental Management,* Vol. 18, No. 4, pp. 623-633.

Guzzetti, F. and Tonelli, G. (2004) Information System on Hydrological and Geomorphological Catastrophes in Italy (SICI): a Tool for Managing Landslide and Flood Hazards, *Natural Hazards and Earth System Science,* Vol. 4, No. 2, pp. 213-232.

Haala, N. and Brenner, C. (1999) Extraction of Buildings and Trees in Urban Environments, *ISPRS Journal of Photogrammetry and Remote Sensing,* Vol. 54, No. 2-3, pp. 130-137.

Hancock, G. and Willgoose, G. (2001) The Production of Digital Elevation Models for Experimental Model Landscapes, *Earth Surface Processes and Landforms,* Vol. 26, No. 5, pp. 475-490.

Hanke, K. and Ebrahim, M.A.-B. (1997) A Low-Cost 3D Measurement Tool for Architectural and Archaeological Applications, *International Archives of Photogrammetry and Remote Sensing,* Vol. 31, pp. 113-120.

Hansen, A. (1984a) Landslide Hazard Analysis, in *Slope Instability*, Brunsden, D. and Prior, D. B. (Eds.), John Wiley and Sons Ltd., Chichester, pp. 523 -602.

Hansen, A. (1984b) Engineering Geomorphology: the Application of an Evolutionary Model of Hong Kong's Terrain, *Zeiscrift für Geomorphologie, Supp. Bd.,* Vol. 51, pp. 39-50.

Hansen, A., Franks, C.A.M., Kirk, P.A., Brimicombe, A.J. and Fung, J. (1995) Application of GIS to Hazard Assessment, with Particular Reference to Landslides in Hong Kong, in *Geographic information Systems in Assessing Natural Hazards*, Carrara, A. and Guzzetti, F. (Eds.), Kluwer Academic Publishers, Dordrecht, The Netherlands, pp. 273-298.

Hattori, S., Akimoto, K, Fraser, C.S. and Imoto, H. (2002) Automated Procedures with Coded Targets in Industrial Vision Metrology, *Photogrammetric Engineering and Remote Sensing*, Vol. 68, No. 5, pp. 441-446.

Hartlén, J. and Viberg, L. (1988) General Report: Evaluation of Landslide Hazard, in *Fifth international Symposium on Landslides*, Bonnard, C. (Ed.), A.A. Balkema, Rotterdam, Lausanne, pp. 1037-1057.

Heritage, G.L., Fuller, I.C., Charlton, M.E., Breweer, P.A. and Passmore, D.P. (1998) CDW Photogrammetry of Low Relief Fluvial Features: Accuracy and Implications for Reach-scale Sediment Budgeting, *Earth Surface Processes and Landforms*, Vol. 23, pp. 1219-1233.

Heuvelink, G.B.M. (1998) *Error Propagation in Environmental Modelling with GIS*, Taylor and Francis, London, 127p.

Higgins, C.G. (1975) Theories of Landscape Development: a Perspective, in *Theories of Landform Development, Proceedings of the 6th Annual Geomorphology Symposia Series, Binghampton, New York, 26-27 September 1975*, Melhorn, W.N. and Flemal, R.C. (Eds.), George Allen and Unwin, London, pp. 1-28.

Hoek, E. and Bray, J. (1981) *Rock Slope Engineering*, 3rd Edn., Institute of Mining and Metallurgy, London, 358p.

Hoveland, H.J. (1977) Three-dimensional Slope Stability Analysis Method. *Journal of the Geotechnical Engineering Division, Proceedings of the American Society of Civil Engineers*, Vol. 103, No. GT9, pp. 971-986

Hunter, G.J. and Goodchild, M.F. (1997) Modeling the Uncertainty of Slope and Aspect Estimates Derived from Spatial Databases, *Geographical Analysis,* Vol. 29, No. 1, pp. 35-49.

Hunting Surveys Ltd (1963) *Calibration Certificate for Wild Aviogon Serial No. 15Ag141*, Boreham Wood, Herts. UK, 26th September, 6p.

Hunting Surveys Ltd (1964) *Calibration Certificate for Wild Aviogon Serial No. 15Ag168*, Boreham Wood, Herts. UK, 12th November, 6p.

Hussain, M. and Bethel, J. (2004) Project and Mission Planning, in McGlone, J.C. (Ed.), *Manual of Photogrammetry, ASPRS,* 5th Edn., pp. 1105-1122.

Hutchinson, J.N. (1988) General Report: Morphological and Geotechnical Parameters of Landslides in Relation to Geology and Hydrogeology, in *Fifth*

International Symposium on Landslides, Bonnard, C. (Ed.), A.A. Balkema, pp. 3-35.

Hutchinson, M.F. and Gallant, J.C. (1999) Representation of Terrain, in *Geographical Information Systems, Vol. 1: Principles and Technical Issues*, 2nd Edn. Longley, P.A., Goodchild, M.F., Maguire, D.J. and Rhind, D.W. (Eds.), John Wiley and Sons, New York, Ch. 9, pp. 105-124.

Hutchinson, M.F. and Gallant, J.C. (2000) Digital Elevation Models and Representation of Terrain Shape, in *Terrain Analysis: Principles and Applications*, Wilson, J.P. and Gallant, J.C. (Eds.), John Wiley and Sons, New York, pp. 29-50.

IAEG Commission on Landslides (1990) Suggested Nomenclature for Landslides, *Bulletin of the International Association of Engineering Geology,* Vol. 41, pp. 13-16.

Irvin, B.J., Ventura, S.J. and Slater, B.K. (1997) Fuzzy and Isodata Classification of Landform Elements from Digital Terrain Data in Pleasant Valley, Wisconsin, *Geoderma,* Vol. 77, No. 2-4, pp. 137-154.

Janbu, N. (1954) Application of Composite Slip Surface for Stability Analysis, *European Conference on the Stability of Earth Slopes*, Vol. 3, pp. 43-49.

Jania, J., Lipert, C. and Mechlinski, Z. (1984) The Ice Mass Loss in the Front Zone of the Werenskiold Glacier From 1957 to 1978 Determined using Terrestrial Photogrammetry, *Polish Polar Research*, Vol. 5, pp. 207-216

Kang, M.S., Park, R.H. and Lee, K.H. (1994) Recovering an Elevation Map by Stereo Modelling of the Aerial Image Sequence, *Optical Engineering*, Vol. 33, No. 11, pp. 3793-3802.

Kalaugher, P.G., Grainger, P., and Hodgson, R.L.P. (1987) Cliff Stability Analysis using Geomorphological Maps Based upon Oblique Aerial Photographs, in *Planning and Engineering Geology, Engineering Geology Special Publication*, No. 4, Culshaw, M.G., Bell, F.G., Cripps, I.C. and O'Hara, M. (Eds.), pp. 155-161.

Kasser, M. and Egels, Y. (2002) *Digital Photogrammetry*, Taylor and Francis, London ; New York.

Keaton, J.R. and de Graff, J.V. (1996) Surface Observation and Geologic Mapping, in *Landslides: Investigation and Mitigation*, Turner, A.K. and Schuster, R.L. (Eds.), Special Report 247, National Academy Press, Washington, D.C., pp. 178-230.

Keinholz, H. (1977) Kombinierte Geomorphologische Gefahrenkarte 1:10,000 von Grindelwald, *Catena,* Vol. 2, pp.265-294.

Keinholz, H. (1978) Maps of Geomorphology and Natural Hazards of Grindelwald, Switzerland, Scale 1:10,000, *Arctic and Alpine Research,* Vol. 10, pp. 169-184.

Kenefick, J.F., Gyer, M.S. and Harp, B.F. (1972) Analytical Self-calibration, *Photogrammetric Engineering and Remote Sensing*, Vol. 38, pp. 1117-1126.

King, J.P. (1999) Natural Terrain Landslide Study: the Natural Terrain Landslide Inventory, *GEO Report* No. 74, Geotechnical Engineering Office, Hong Kong SAR, 127p.

King, L.C. (1953) Canons of Landscape Evolution, *Geological Society of America, Bulletin,* Vol. 64, pp. 721-752.

King, L.C. (1962) *The Morphology of the Earth,* 2nd Edition 1967, 726p. Oliver and Boyd, Edinburgh.

Kirby, R.P. (1991) Measurement of Surface Roughness in Desert Terrain by Close Range Photogrammetry, *Photogrammetric Record*, Vol. 13, No. 78, pp. 855-875.

Kirkby, M.J. (1971) Hillslope Process-Response Models Based on the Continuity Equation, *Institute of British Geographers, Special Publication,* Vol. 3, pp. 15-30.

Kirkup, L. (1994) *Experimental Methods: an Introduction to the Analysis and Presentation of Data*, Jacaranda Wiley, Milton, Queensland, 216p.

Klimazewski, M. (1956) The Principles of Geomorphological Survey of Poland, *Przeglad Geograficzny*, Vol. 28 (Supp.), pp. 32-40

Klimazewski, M. (1982) Detailed Geomorphological Maps, *ITC Journal*, 1982-3, pp. 265-272.

Klingmann, S. and Blackwell, G.H. (2003) The Application of Digital Video Plotter (DVP) Systems to the Location and Orientation of Open Pit Wall Slope Features, *CIM Bulletin*, Vol. 96, No. 1071, pp. 72-75.

Koike, K., Nagano, S. and Kawaba, K. (1998) Construction and Analysis of Interpreted Fracture Planes through Combination of Satellite-Image Derived Lineaments and Digital Elevation Model Data, *Computers and Geosciences,* Vol. 24, No. 6, pp. 573-583.

Koike, K., Nagano, S. and Ohmi, M. (1995) Lineament Analysis of Satellite Images Using a Segment Tracing Algorithm (STA), *Computers and Geosciences,* Vol. 21, No. 9, pp. 1091-1104.

Korup, O. (2004) Geomorphometric Characteristics of New Zealand Landslide Dams, *Engineering Geology*, Vol. 73, No. 1, pp. 13 -35.

Kraus, K. (1994) Visualization of the Quality of Surfaces and their Derivatives, *Photogrammetric Engineering and Remote Sensing,* Vol. 60, No. 4, pp. 457-462.

Kraus, K. (1997) *Photogrammetry: Volume 2 Advanced Methods and Applications,* English Edition, 1997, Translation of 3rd Edn., 1996, Dümmler, Bonn.

Kraus, K. (2000) *Photogrammetry: Volume 1 Fundamentals and Standard Processes,* English Edition, Revised Translation of 4th Edn., 1997, Dümmler, Bonn.

Kuhn, T.S. (1970) *The Structure of Scientific Revolutions,* 2nd Edn., University of Chicago Press.

Lam, K.W.K., Li, Z.L. and Yuan, X.X. (2001) Effects of JPEG Compression on the Accuracy of Digital Terrain Models Automatically Derived from Digital Aerial Images, *Photogrammetric Record,* Vol. 17, No. 98, pp. 331-342.

Lambe, T.W. and Whitman, R.V. (1979) *Soil Mechanics, SI Version*, John Wiley and Sons, New York, 553p.

Lane, S.N. (1994) Monitoring and Modelling Morphology, Flow and Sediment Transport in A Gravel Bed Stream, *Ph.D. Thesis*, University of Cambridge, U.K.

Lane, S.N. (2005) Roughness – Time for a Re-evaluation? *Earth Surface Processes and Landforms*, Vol. 30, pp. 251-253.

Lane, S.N. and Chandler, J.H. (2003) The Generation of High Quality Topographic Data for Hydrology and Geomorphology: New Data Sources, New Applications, New Problems, *Earth Surface Processes and Landforms*, Vol. 28, No. 3, pp. 229-230.

Lane, S.N., Chandler, J.H. and Richards, K.S. (1998) Landform Monitoring, Modelling and Analysis: Land Form in Geomorphological Research, in

Landform Modelling, Monitoring and Analysis, Lane, S. N., Richards, K. S. and Chandler, J.H. (Eds.), John Wiley and Sons, Chichester, pp. 1-17.

Lane, S.N., James, T.D. and Crowell, M.D. (2000) Application of Digital Photogrammetry to Complex Topography for Geomorphological Research, *Photogrammetric Record*, Vol. 16, No. 95, pp. 793-821.

Lane, S.N., Richards, K.S. and Chandler, J.H. (1993) Developments in Photogrammetry - the Geomorphological Potential, *Progress in Physical Geography,* Vol. 17, No. 3, pp. 306-328.

Lane, S.N., Richards, K.S. and Chandler, J.H. (Eds.) (1998) *Landform Monitoring, Modelling and Analysis*, John Wiley and Sons, Chichester.

Lane, S.N., Hardy, R.J., Elliott, L. and Ingham, D.B. (2005) High Resolution Numerical Modelling of Three-dimensional Flows Over Complex River Bed Topography, *Hydrological Processes*, Vol. 16, No. 11, pp 2261-2272.

Lee, E.M. (2001) Geomorphological Mapping, in *Land Surface Evaluation for Engineering Practice*, Griffiths, J.S. (Ed.), Geological Society Engineering Geology Special Publication No. 18, Geological Society Publishing House, Bath, pp. 53-56.

Lee, E.M. and Moore, R. (2001) Land Use Planning in Unstable Areas: Ventnor, Isle of Wight, in *Land Surface Evaluation for Engineering Practice*, Griffiths, J.S. (Ed.), Geological Society Engineering Geology Special Publication No. 18, Geological Society, London, Bath, pp. 189-192.

Leica (2007) http://www.leica.com/

Leroi, E. (1996) Landslide Hazard – Risk Maps at Different Scales: Objectives, tools and Developments, in *Landslides, Proceedings 7th International Symposium on Landslides*, Senneset, (Ed.), Trondheim, Norway, 17-21 June 1996, Balkema, Rotterdam, pp. 35-51.

LH Systems (2007) http://gi.leica-geosystems.com/default.aspx

Li, Z.L. (1992) Variation of the Accuracy of Digital Terrain Models with Sampling Interval, *Photogrammetric Record,* Vol. 14, No. 79, pp. 113-128.

Li, Z.L. (1994) A Comparative Study of the Accuracy of Digital Terrain Models (DTMs) based on Various Data Models, *ISPRS Journal of Photogrammetry and Remote Sensing,* Vol. 49, No. 1, pp. 2-11.

Li, Z., Yuan, X. and Lam, K.W.K. (2002) Effects of JPEG Compression on the Accuracy of Photogrammetric Point Determination, *Photogrammetric Engineering and Remote Sensing*, Vol. 68, No. 8, pp. 847-853.

Lichti, D.D. and Chapman M.A. (1997) Constrained FEM Calibration, *Photogrammetric Engineering and Remote Sensing*, Vol. 63, No. 9, pp. 1111-1119.

Lichti, D.D., Gordon, S.J. and Stewart, M.P. (2002a), Ground-Based Laser Scanners: Operation, Systems and Applications, *Geomatica*, Vol. 56, No. 1, pp. 21-33.

Lichti, D.D., Gordon, S.J., Stewart, M.P., Kranke, J. and Tsakiri, M. (2002b) Comparison of Digital Photogrammetry and Laser Scanning, In *CIPA WG 6 International Workshop on Scanning Cultural Heritage Recording* Corfu, Greece, 1-2 September 2002. pp. 39-44 [On CD-ROM].

Lillesand, T.M. and Kiefer, R.W. (1979) *Remote Sensing and Image Interpretation*, John Wiley and Sons, New York.

Lo, C.P. (1978) Landslide Mapping with the CP1 Plotter, *Photogrammetric Record*, Vol. 9, No. 51, pp. 377-389.

Lo, C.P. and Wong, F.Y. (1973) Microscale Geomorphology Features, *Photogrammetric Engineering and Remote Sensing*, Vol. 39, pp. 1289-96.

Mark, B.G. and Seltzer, G.O. (2005) Evaluation of Recent Glacier Recession in the Cordillera Blanca, Peru (AD 1962-1999): Spatial Distribution of Mass Loss and Climatic Forcing, *Quaternary Science Reviews*, Vol. 24, No. 20-21, pp. 2265-2280.

McAlpin, J. (1984) Preliminary Age Classification of Landslides for Inventory Mapping, in *Proceedings of the 21st Engineering Geology and Soils Engineering Symposium*, University of Idaho, Moscow, pp. 99-120.

McGlone, J.C. (Ed.) (2004) *Manual of Photogrammetry*, 5th Edn. American Society for Photogrammetry and Remote Sensing, Bethesda, Maryland, 1151p.

McCullagh, M.J. (1998) Quality, Use and Visualisation in Terrain Modelling, , in *Landform Monitoring, Modelling and Analysis*, Lane, S.N, Richards, K.S. and Chandler, J.H. (Eds.), John Wiley and Sons, Chichester, Chapter 5, pp. 95-117.

McConchie, J.A (1986) Earthflows: Measurement and Explanation: an Investigation into the Problems of Instrumentation and Measurement of Earthflow Properties and their Application to the Explanation of Mass Movement, *Ph.D. Thesis*, Victoria University of Wellington, New Zealand, 577p.

Meentemeyer, R.K. and Moody, A. (2000) Automated Mapping of Conformity between Topographic and Geological Surfaces, *Computers and Geosciences,* Vol. 26, No. 7, pp. 815-829.

Meyerhoff, H.A. (1940) Migration of Erosional Surfaces - Walther Penck's Contribution to Geomorphology, *Association of American Geographers, Annals,* Vol. 30, No. 4, pp. 247-254.

Meyerhoff, H.A. (1975) The Penckian Model - with Modifications, in *Theories of Landform Development, Proceedings of the 6th Annual Geomorphology Symposia Series, Binghampton, New York, 26-27 September 1975*, Melhorn, W.N. and Flemal, R.C. (Eds.), George Allen and Unwin, London, pp. 45-68.

Mikhail, E.M. (1976) *Observations and Least Squares*, IEP, New York, 497p.

Mikhail, E.M., Bethel, J.S. and McGlone, J.C. (2001) *Introduction to Modern Photogrammetry*, John Wiley and Sons, New York, 479p.

Miliarensis, G.C. (2001) Geomorphological Mapping of Zagros Ranges at Regional Scale, *Computers and Geosciences*, Vol. 27, pp. 775-786.

Miliarensis, G.C. and Argailas, D.P. (1999) Segmentation of Physiographic Features from the Global Digital Elevation Model/GTOPO30, *Computers and Geosciences*, Vol. 25, pp. 715-728.

Mills, J.P., Newton, I, and Graham, R.W. (1996) Aerial Photography for Survey Purposes with a High Resolution, Small Format, Digital Camera, *Photogrammetric Record*, Vol. 15, No. 88, pp. 575-587.

Moffitt, F.H. and Mikhail, E.M. (1980) *Photogrammetry*, 3rd Edn. Harper and Row, Cambridge, 649p.

Moore, I.D., Grayson, R.B. and Ladson, A.R. (1991) Digital Terrain Modelling: a Review of Hydrological, Geomorphological and Biological Applications, *Hydrological Processes,* Vol. 5, No. 1, pp. 3-30.

Nathani, K.K. (1990) Can Satellite Images Replace Aerial Photographs? A Photogrammetricist's View, *ITC Journal*, Vol. 1, pp. 29-31.

Norman, J.W., Leibowitz, T.H. and Fookes, P.G. (1975) Factors Affecting the Detection of Slope Instability with Air Photographs in an Area Near Sevenoaks, Kent, *Quarterly Journal of Engineering Geology*, Vol. 8, No. 3, pp. 159-176.

Ng, K.C., King, J.P., Franks, C.A.M. and Shaw, R. (2000) *Natural Terrain Hazard Study: Interim Guidelines*, Planning Division, Geotechnical Engineering Office, Hong Kong SAR, PRC, Special Project Report SPR 5/2000.

Ng, K.C., Parry, S., King, J.P., Franks, C.A.M. and Shaw, R. (2003) Guidelines for Natural Terrain Hazard Studies, *GEO Report* No. 138, Geotechnical Engineering Office, Hong Kong SAR, 138p.

Nyquist, H. (1924) Certain Factors Affecting Telegraph Speed, *Bell Systems Technical Journal*, Vol. 3, pp. 324-346.

Oka, N. (1998) Application of Photogrammetry to the Field Observation of Failed Slopes, *Engineering Geology*, Vol. 50, pp. 85-100.

Onorati, G., Poscolieri, M., Ventura, R., Chiarini, V. and Crucilla, U. (1992) The Digital Elevation Model of Italy for Geomorphology and Structural Geology, *Catena,* Vol. 19, pp. 147-178.

Osterkamp, W.R. and Hupp, C.R. (1996) The Evolution of Geomorphology, Ecology and Other Composite Sciences, in the *Scientific Nature of Geomorphology. Proceedings of the 27th Binghampton Symposium in Geomorphology, 27-29 September 1996*, Rhoads, B.L. and Thorn, C.E. (Eds.), John Wiley and Sons, Chichester, pp. 415-441.

Paola, J.D. and Schowengerdt, R.A. (1995) The Effect of Lossy Image Compression on Image Classification*, IEEE International Geoscience and Remote Sensing Symposium (IGARSS)*, Vol. 1, pp. 118-120.

Parry, S., Ruse, M.E. and Williamson, S.J (2005) Discussion of Chau and Lo (2004): Hazard Assessment of Debris Flow for Leung King Estate of Hong Kong by Incorporating GIS with Numerical Simulation, *Natural Hazards and Earth Systems Sciences*, Vol. 5, pp. 23-24. SRef-ID: 1684-9981/nhess/2005-5-23

Penck, W. (1924) *Die Morphologische Analyse*, J. Englehorn, Stuttgart.

Pennock, D.J., Zebarth, B.J. and de Jong, E. (1987) Landform Classification and Soil Distribution in Hummocky Terrain, Saskatchewan, Canada, *Geoderma*, Vol. 40, pp. 297-315.

Petrie, G. (1990) Developments in Analytical Instrumentation, *ISPRS Journal of Photogrammetry and Remote Sensing*, Vol. 45, pp. 61-89.

Pike, R.J. (1988) The Geometric Signature: Quantifying Terrain Types from Digital Elevation Models, *Mathematical Geology,* Vol. 20, No. 5, pp. 491-511.

Pike, R.J. (1993) A Bibliography of Geomorphometry, *United States Geological Survey Open-File Report 93-262-A*, p. 132.

Pike, R.J. (1995) Geomorphometry - Progress, Practice and Prospect, *Zeitschrift für Geomorphologie, Supplementband,* vol. 101, pp. 221-238.

Pike, R.J. (2000) Geomorphometry - Diversity in Quantitative Surface Analysis, *Progress in Physical Geography,* Vol. 24, pp. 1-20.

Radbruch-Hall, D.R., Edwards, K. and Batson, R.M. (1979) Experimental Engineering Geologic Map of the Conterminous Uniter States Prepared Using Computer Techniques, *International Association of Engineering Geology, Bulletin,*, Vol. 19, pp. 358-363.

Ray, R.G. (1960) Aerial Photographs in Geologic Interpretation and Mapping, *U.S. Geological Survey Professional Paper,* Vol. 373, pp. 1-230.

Read, R.E. and Graham, R. (2002) *Manual of Aerial Survey: Primary Data Acquisition,* CRC Press/Whittles Publishing, Boca Raton, Fl., 408p.

Rees, W.G. (2000) The Accuracy of Digital Elevation Models Interpolated to Higher Resolutions, *International Journal of Remote Sensing,* Vol. 21, No. 1, pp. 7-20.

Reigl (2004) http://www.riegl.co.at/

Rendel Geotechnics (1995) *The Undercliff of the Isle of Wight: a Review of Ground Behaviour*, South Wight Borough Council, UK.

Rengers, N., Soeters, R. and van Westen, C.J. (1992) Remote Sensing and GIS Applied to Mountain Hazard Mapping, *Episodes*, Vol. 15, No. 1, pp. 36-45.

Robinson, C., Montgomery, B. and Fraser, C.S. (1995) The Effects of Image Compression on Automated DTM Generation, in *Photogrammetric Week '95*, Fritsch, D. and Hobbie, D. (Eds.), Wichmann Verlag, Heidelberg, pp. 255-262.

Rollei (2005) http://www.rollei.com/files/RolleiMetricCDW.pdf

Ruhe, R.V. (1975) *Geomorphology. Geomorphic Processes and Surficial Geology*, Houghton Muffin, Boston.

Ruxton, B.P. and Berry, L. (1957) Weathering of Granite and Associated Erosional Features in Hong Kong, *Geological Society of America, Bulletin*, Vol. 68, pp. 1263-1292.

Salomé, A.I. and van Dorsser, H.J (1982) Examples of 1:50,000 Scale Geomorphological Maps of Part of the Ardennes, *Zeiscrift für Geomorphologie, Bd.,* Vol. 26, No. 4, pp. 481-489.

Salomé, A.I. and van Dorsser, H.J (1985) Some Reflections on Geomorphological Mapping Systems, *Zeiscrift für Geomorphologie, Bd.,* Vol. 29, No. 3, pp. 375-380.

Savigear, R. (1965) A Technique of Morphological Mapping, *Annals of the Association of American Geographers,* Vol. 55, pp. 514-538.

Schenk, T.F. (1999) *Digital Photogrammetry*, TerraScience, Laurelville, OH, Vol. 1, 428p.

Schoorl, J.M., Sonneveld, M.P.W. and Veldkamp, A. (2000) Three-Dimensional Landscape Process Modelling: the Effect of DEM Resolution, *Earth Surface Processes and Landforms,* Vol. 25, No. 9, pp. 1025-1034.

Schumm, S.A. (1973) Geomorphic Thresholds and Complex Response of Drainage Systems, in *Fluvial Geomorphology*, Morisawa, M. (Ed.), State University of New York, Binghampton, New York, pp. 299-310.

Schumm, S.A., (1976) Episodic Erosion: a Modification of the Geomorphic Cycle, in *Theories of Landform Development*, Melhorn, W.N. and Flemal, R.C. (Eds.), Publications in Geomorphology, State University of New York, Binghamton, New York, pp. 69-85, reprinted by Allen and Unwin, London.

Schumm, A.A. and Lichty, R.W. (1965) Time, Space and Causality in Geomorphology, *American Journal of Science,* Vol. 263, pp. 110-119.

Selby, M.J. (1982) *Hillslope Materials and Processes*, Oxford University Press, Oxford, 264p.

Shary, P.A. (1995) Land Surface in Gravity Points Classification by a Complete System of Curvatures, *Mathematical Geology,* Vol. 27, No. 3, pp. 373-390.

Shary, P.A., Sharaya, L.S. and Mitusov, A.V. (2002) Fundamental Quantitative Methods of Land Surface Analysis, *Geoderma,* Vol. 107, No. 1-2, pp. 1-32.

Shih, T.-Y. and Liu, J.-K. (2005) Effects of JPEG 2000 Compression on Automated DSM Extraction: Evidence from Aerial Photographs, *Photogrammetric Record*, Vol. 20, No. 112, pp. 351-365.

Shortis, M.R., Ogleby, C.L., Robson, S., Karalis, E.M. and Beyer, H.A. (2001) Calibration Modelling and Stability Testing for the Kodak DC200 Series Digital Still Camera, in *Videometrics and Optical Methods for 3D Shape Measurement*, El-Hakim, S.F. and Gruen, A. (Eds.) Proceedings of the SPIE, Vol. 4309, pp. 148-153

Siragusa, M. and McDonnell, D.J. (2002) Indirect Digital Images: Limit of Image Compression for Diagnosis in Endodontics, *International Endodontic Journal*, Vol. 35, No. 12, pp. 991-995.

Skidmore, A.K. (1989) A Comparison of Techniques for Calculating Gradient and Aspect from Gridded Elevation Data, *International Journal of Geographical information Systems,* Vol. 3, No. 4, pp. 323-334.

Skempton, A.W.(1954) The Pore Pressure Coefficients A and B, *Geotechnique*, Vol. 4, pp. 143-147.

Skempton, A.W. (1964) Long-term Stability of Clay Slopes, *Geotechnique*, Vol. 14, pp. 77-102.

Slama, C.C. (Ed.) (1980) *Manual of Photogrammetry* 4th Edn., American Society of Photogrammetry, Falls Church, Va., 1056p.

SmartTech (2005) Using Correlation Routines, unpublished email to registered users, 17 June 2005, http://www.smarttech.co.za/index.htm

SmartTech (2007) http://www.smarttech.co.za/index.htm

Smith, G.R., Woodward, J.C., Heywood, D.I. and Gibbard, P.L. (2000) Interpreting Pleistocene Glacial Features from SPOT HRV Data using Fuzzy Techniques, *Computers and Geosciences,* Vol. 26, No. 4, pp. 479-490.

Stirling, D.M. (1982) Measuring Short Term Glacial Fluctuations by Aerial and Terrestrial Photogrammetry: a Comparative Study, *International Archives of Photogrammetry*, Vol. 24, pp. 484-496.

Soeters, R. and van Westen, C.J. (1996) Slope Instability: Recognition, Analysis and Zonation, in *Landslides: Investigation and Mitigation*, Special Report 247, Turner, A.K. and Schuster, R.L. (Eds.), National Academy Press, Washington, D.C., pp. 129-177.

Stojic, M., Chandler, J., Ashmore, P. and Luce, J. (1998) The Assessment of Sediment Transport Rates by Automated Digital Photogrammetry*, Photogrammetric Engineering and Remote Sensing*, Vol. 64, No. 5, pp. 387-395.

Strahler, A.N. (1950) Equilibrium Theory of Erosional Slopes, Approached by Frequency Distribution Analysis, *American Journal of Science,* Vol. 248, pp. 673-696 and 800-814.

Styles, K.A., and Hansen, A. (1989) *Geotechnical Area Studies Programme - Territory of Hong Kong*, Geotechnical Control Office, Civil Engineering Services Department, Hong Kong, GASP Report No. XII, 346p. plus 14 maps and 1 chart.

TapesG-ArcGIS (2005) http://arcscripts.esri.com/details.asp?dbid=13759

Terhorst, B. and Kirschhausen, D. (2001) Legends for Mass Movements in the MABIS-Project, *Zeiscrift für Geomorphologie N. F.,* Supp. Bd. 125, pp. 177-192.

Terzaghi, K., and Peck, R.B. (1967) *Soil Mechanics in Engineering Practice*, Wiley, New York, 729p.

Thompson, E.H. (1972) The CP1 Plotter: Setting Procedure and Results, *Photogrammetric Record*, Vol. 7, No. 39, pp. 323-333.

Thomson, G. (2004) Analytical Methods of Assessing the Image Quality Associated with Digital and Photographic Imaging Systems, *Photogrammetric Record*, Vol. 19, No. 107, pp. 237-249.

Thornes, J.B. and Brunsden, D. (1977) *Geomorphology and Time*, Methuen, London, 208p.

Tribe, A. (1991) Automated Recognition of Valley Heads from Digital Elevation Models, *Earth Surface Processes and Landforms,* Vol. 16, pp. 33-49.

van Westen, C.J. (1993) Application of Geographic Information Systems to Landslide Hazard Zonation, *Ph.D. Thesis*, Technical University Delft, ITC-Publication No. 15, International Institute for Aerospace Survey and Earth Science (ITC), Enschede, Netherlands, 245p.

van Westen, C.J., Rengers, N., and Soeters, R. (2003) Use of Geomorphological Information in Indirect Landslide Hazard Susceptibility Assessment*, Natural Hazards*, Vol. 30, pp. 399-419.

van Westen C.J., Seijmonbergen, A.C. and Mantovani, F. (1999) Comparing Landslide Hazard Maps, *Natural Hazards*, Vol. 20, pp. 137-158.

van Zuidam, R.A. (1986) *Terrain Classification*, ITC Textbook, International Institute for Aerospace Survey and Earth Science (ITC) Enschede, Netherlands

Varnes, D.J. (1978) Slope Movement Types and Processes, in *Special Report 176: Landslides and Engineering Practice*, Schuster, R.L. and Krizek, R.J. (Eds.), Highways Research Board, National Research Council, Washington, D.C., pp. 11-33.

Varnes, D.J. (1984) *Landslide Hazard Zonation - a Review of Principles and Practice*, Commission on Landslides of the IAEG, Natural Hazards, No. 3, UNESCO, Paris, 61p.

Ventura, S.J. and Irvin, B.J. (2000) Automated Landform Classification Methods for Soil-Landscape Studies, in *Terrain Analysis: Principles and Applications*, Wilson, J.P. and Gallant, J.C. (Eds.), John Wiley and Sons, Chichester, U.K., pp. 267-294.

Verstappen, H.T. (1983) *Applied Geomorphology: Geomorphological Surveys for Environmental Development*, Elsevier, Amsterdam.

Vertappen, H.T. and van Zuidam, R.A. (1968) I.T.C. System of Geomorphological Survey, in *I.T.C. Textbook of Photo-interpretation*, Vertappen, H. T. and Zuidam, R. A. (Eds.), I.T.C., Delft, Vol. 2.

Ward, T.J., Li, R.S. and Simons, D.B. (1978) Landslide Potential and Probability Considering Randomness in Controlling Factors, in *Proceedings of the International Symposium on Risk and Reliability in Water Resources*, McBean, E.A. (Ed.), University of Waterloo, Waterloo, Ontario, Canada, pp. 592-608.

Ward, T.J., Li, R.S. and Simons, D.B. (1982) Mapping Landslide Hazards in Forested Watersheds, *Transactions of the American Society of Civil Engineers,* Vol. 108, pp. 319-324.

Warner, W.S., Graham, R.W. and Read, R.E. (1996*) Small Format Aerial Photography*, Whittles Publishing, Caithness, 348p.

Waters, R.S. (1958) Morphological Mapping, *Geography,* Vol. 43, pp. 10-17.

Welsh, R. and Jordan, T.R. (1983) Analytical Non-metric Close-range Photogrammetry for Monitoring Stream Channel Erosion, *Photogrammetric Engineering and Remote Sensing*, Vol. 49, No. 3, pp. 367-374.

Weir, B.R. (2000) Dynamic Performance Testing of a Low Cost Scanner in the Application of Digital Photogrammetry, *M.Sc. Thesis*, Curtin University of Technology, Australia, 143p.

Wicken, E. and Barton, N.R. (1971) The Application of Photogrammetry to the Stability of Excavated Rock Slopes, *Photogrammetric Record*, Vol. 7, No. 73, pp. 46-54.

Wieczorek, G.F. (1984) Preparing a Detailed Landslide-inventory Map for Hazard Evaluation and Reduction, *Bulletin of the Association of Engineering Geologists,* Vol. 21, No. 3, pp. 337-342.

Wilson, J.P. and Gallant, J.C. (Eds.) (2000) *Terrain Analysis: Principles and Applications*, John Wiley and Sons, Chichester.

Wise, S.M. (1998) The Effect of GIS Interpolation Errors on the Use of Digital Elevation Models in Geomorphology, in *Landform Monitoring, Modelling and Analysis*, Lane, S.N., Richards, K.S. and Chandler, J.H. (Eds.), John Wiley and Sons, Chichester, pp. 139-164.

Wise, S.M. (2000) Assessing the Quality for Hydrological Applications of Digital Elevation Models Derived from Contours, *Hydrological Processes,* Vol. 14, No. 11-12, pp. 1909-1929.

Wolf, P.R. and Dewitt, B.A. (2000) *Elements of Photogrammetry: with Applications in GIS,* 3rd Edn., McGraw Hill, Boston, Mass., 608p.

Wood, J. (1996) The Geomorphological Characterisation of Digital Elevation Models, *Ph.D. Thesis*, University of Leicester, U.K.

Wright, R.H. and Nilsen, T.H. (1974) Isopleth Map of Landslide Deposits, Southern San Francisco Bay Region, California, in *U.S. Geological Survey Miscellaneous Field Studies Map MF550, Scale 1:25,000.*

Young, M. (1978) *Terrain Analysis: Program Documentation. Report 5 on Grant DA-ERO-591-73-G0040*, Department of Geography, University of Durham

Zevenbergen, L.W. and Thorne, C.R. (1987) Quantitative Analysis of Land Surface Topography, *Earth Surface Processes and Landforms,* Vol. 12, No. 1, pp. 47-56

Zaruba, Q. and Mencl, V. (1976) *Engineering Geology*, Elsevier, Amsterdam, 504p.

Zhou, G.Q. and Li, D.R. (2001) CAD-Based Object Reconstruction using Line Photogrammetry for Direct Interaction between GEMS and a Vision System, *Photogrammetric Engineering and Remote Sensing,* Vol. 67, No. 1, pp. 107-116

ZI Imaging (2007) http://www.intergraph.com/photogrammetry/

ZunZun (2007) http://www.zunzun.com, last accessed May 2007.

APPENDIX A

GLOSSARY

Batter	Side face of a man-made slope
Berm	A narrow ledge or shelf along the top or bottom of a slope, in the context of this dissertation, a man-made slope
Breaklines	Topographically-significant lines in the landscape, often forming landforms or boundaries of landforms, e.g. ridgelines or stream channels; often marked by regions of high curvature.
Cadastral surveys	Surveys for official registers of land ownership
Delaunay triangulation	Divides a topographic region into triangles where each point is connected to its natural neighbours
DEM	Digital Elevation Model formed of elevation values (sometimes called posts) across a regularly-spaced grid
DLI SkyView	Orthophoto produced by the Department of Land Information in Western Australia
DTM	Digital Terrain Model formed of elevation values (sometimes called posts) irregularly-spaced across a surface
Epipolar line/plane	The epipolar plane contains the two camera stations and a third point on the target/surface; epipolar lines are the loci of this plane on each image.
Ergodic	Statistical assumption that repeated observations of a process are equivalent to observing that process over a long period of time
Fiducal marks	Fixed points on the camera body that appear on the film image to identify the camera geometry; for a digital camera, the corners of the image array are often used.
Fourier transform	Converts a signal in the spatial domain (distribution of a parameter across the X and Y axes), to the frequency domain (distribution of that parameter in terms of frequency in the X and Y axes)
Georeference	Define the location of an object in terms of physical space, such as a local or national coordinate system
GCP	Ground Control Point with known Easting, Northing and/or elevation values used to georeference an image
GIS	Geographic Information System allows data to be captured, stored, managed and analysed with reference to georeferenced spatial attributes

Hyperfocal distance	For a camera, this refers to the closest distance at which objects at infinity also remain in acceptable focus
Isometric	A method for the visual representation of 3D objects in 2D space
Lossy, lossless	Lossless compression occurs when images are sequentially compressed then decompressed and the original data is completely recovered. If the decompressed data losses some component of the original (usually the high frequency component), it is said to be lossy.
Morphochronologic	Landform components defined by age relationships
Morphogenetic	Landform components defined by process relationships
Morphographic	Landform components where the shape is implicit in the name, e.g., drumlins
Morphometric	Landform components defined by shape relationships
Orthophoto	Photograph that has been transformed to remove distortions produced by the camera, lens and elevation, and is the photographic equivalent of a map; orthophotos usually contain a rectified image with topographic or thematic mapping overlaid
Phase wrapped	A signal forms a continuous surface up to a limit, beyond which it forms a different surface, possibly parallel to the first
Photo texture	High frequency contrast variations within an image, possibly forming an interpretable pattern
Photobase	Distance in object space between camera stations (equivalent to airbase for vertical aerial photography)
Rectified image	Image where the distortions have been removed, part of an orthophoto
Reference kernel	Patch of pixels in an image used as the template to identify a corresponding part of a search area in a second image during the process of area-based image matching
Remotely-sensed	Data captured about an object from a distance using non-contact methods
Resection	Finding the position of an object by reference to three known points
Softcopy	Analytical photogrammetry applied through a computer program
TIN	Triangulated Irregular Network composed of vectors forming discrete triangles between a set of 3D points; each triangle forms a planar surface. The triangles are typically based on a Delaunay triangulation.
Transferscope	Optical device used to project photographic images onto a planar surface such as a map; allows some projective scaling of the image to reduce distortion.

Warping	in the context of stereo viewing, warping is the process of modifying the zero elevation coordinate of a 3D digital map converted from 2D source to the surface obtained by a TIN forming the 3D ground model. This allows the 2D data to be viewed in a 3D visualisation system

APPENDIX B

VISUALISATION OF 3D LANDSLIDE DISPLACEMENT VECTORS AND GEOMORPHOLOGICAL MAPPING, LANDSLIDE AT CH23+800, SIMPANG PULAI – LOJING HIGHWAY, MALAYSIA

The attached CD contains 2 files:

3D Landslide Displacement plus Geomorphology HQ.avi (533Mbytes)

3D Landslide Displacement plus Geomorphology Small.wmv (13Mbytes)

The HQ (high quality) file should be downloaded to a hard disk before viewing, unless the host computer has a very fast file-read facility.